AETHERIA

Hydrogen-powered long-range eVTOL designed for crashworthiness

Group 11 - Final Report

Delft University of Technology

TU Delft AETH$_2$ERIA

This page is intentionally left blank.

AETHERIA

Hydrogen-powered long-range eVTOL designed for crashworthiness

by

Group 11 - Final Report

Delft University of Technology

Student Name	Student Number
W. Albers	5040019
J. Arends	5243637
B.A. van Battum	5100771
E. Hadzhiyski	5229022
C. Karaca	5211123
D.M. Keijzer	5303206
L. Middendorp	5067049
S. de Rijke	5109345
B. Sarıgöl	5252016
C. Simon Soria	5220491

Tutors:	S. Giovani Pereira Castro & F. Scarano
Coaches:	M. Barahona Lopez & J. Benad
Teaching Assistant:	K. Smit
Project Duration:	April 2023 - June 2023
Faculty:	Faculty of Aerospace Engineering, Delft

TU Delft AETH$_2$ERIA

Summary

In light of increasing research and development efforts exploring alternative modes of transportation, there has been a noticeable increase in the quest for faster, more efficient, and sustainable travel options. This has gained urgency due to the substantial increase in air pollution and traffic congestion. As one of the solutions, the Vertical Take-Off and Landing (eVTOL) aircraft may hold the key to this issue's resolution. Particularly, the addition of hydrogen-based propulsion to the eVTOL design has emerged as a significant enhancement, increasing the aircraft's potential range. Therefore, the goal of this Design Synthesis Exercise (DSE) is to implement hydrogen as a means to improve the performance of battery-powered long-range eVTOLs. The Mission Need Statement (MNS) of the project is formulated as follows:

Design a safe and sustainable long-range hydrogen eVTOL that can transport four passengers

The team has organized itself into both managerial and technical roles, with each team member connected to a specific department. The functional flow diagram (FFD) and the functional breakdown structure (FBS) were updated from the baseline report, and presented in more depth in order to demonstrate the tasks as they become clearer and more specific. Additionally, a project design and development logic diagram demonstrates the progression of the project beyond the preliminary design phase, including detailed design, prototype construction, testing, certification, mass production, commercialization, regular inspections, and eventual recycling and disposal.

Market Analysis
An in-depth market analysis was conducted to understand the market size and potential. The analysis identified six main sectors in order of promise: commercial travel, private usage/leisure, cargo transporting, structure inspection/maintenance, first responders, and military applications. The ranking was based on user requirements and the number of existing eVTOLs in each sector. Commercial travel was deemed the easiest to enter, with a four-passenger requirement. Four lift technology categories were identified: multirotor, lift + cruise, tilt wing, and tilt duct/rotor. Range calculation was crucial in determining design choices. Western Europe and the USA were identified as the primary markets, with cities within a certain range analyzed for potential connections. High-value connections, particularly with London, were seen as advantageous. Cost estimation was based on a mission involving three daily flights at maximum range with a full payload, operating for 200 days per year over a 15-year lifespan. The estimated total cost was 24.5 million euros. Cruise speed was determined to compete with high-speed trains, and a speed of 300 km/h was chosen. Market share projections varied by region, with the European market having the highest obtainable share (8%) and the North American market having the highest total market share potential (55%). The projected production size was 445 units, with a focus on the European and American markets. The preliminary mission profile included nine segments, accounting for energy consumption during taxi, hovering climb, transition, cruise, and loiter. The total energy consumption for a 400 km flight was calculated to be 534 kWh, resulting in a competitive energy efficiency of 333 Wh/passenger km.

Once the market analysis was performed, a trade-off was performed between three configurations where the J2 had been picked. Once a final configuration had been set, the technical aspects were designed.

Aerodynamics
Reflecting on the aerodynamics of the Aetheria aircraft, a number of parameters were sized. Firstly, an airfoil selection was performed which showed that the NACA2412 was most suitable for this particular aircraft. Next, the sizing of the wing planform gave an aspect ratio of 6.7 and a wing surface of 13 [m^2]. The low aspect ratio is due to the wing weight being optimized. A stall speed of 40 [m/s] was deemed appropriate since the aircraft is able to land horizontally during emergency landings. Furthermore, due to the large propellers in front of the wings, their influence on the wing's aero-

dynamic performance had to be investigated. Following this analysis, the C_L in cruise conditions increased by 25%. The wingtip-mounted propellers are also investigated as their rotating direction has a great influence on the sectional lift coefficient. The final L/D in cruise conditions is 18.3.

Flight Performance
The mission profile of the Aetheria has been edited to minimize the mission energy. First of all, the cruise altitude is increased to 2400 [m]. Secondly, the transition manoeuvres have been optimized such that the aircraft climbs and descends as efficiently as possible. For the first transition, following hovering the aircraft will start rotating its propellers which will increase its horizontal velocity. Due to this, the lift will start increasing therefore slowly making the aircraft wingborne. At a stall speed of 40 [m/s] the aircraft will be fully wingborne and will accelerate to climb velocity. For the second transition, from descent to landing, the aircraft will start with a gliding phase, in which the propellers will rotate up, followed by a leveling out phase where the propellers (now in vertical configuration) will provide the necessary thrust. After leveling out the aircraft will slow down and descend down to the landing pad. A more in-depth analysis of the separate propellers is also done to investigate stability in transition. From this analysis came that the propeller's maximum thrust is far below the maximum thrust which can be provided by the engines. The total mission energy can be lowered to 219 kWh, far lower than what was designed for in the Midterm report [1].

Control and Stability
The control and stability has been determined and assessed for Aetheria. Vertical stability and control is ensured by placing the rotors in such a way that they allow for vertical flight stability. A SAS and CAS systems have been designed to overcome the natural instability of the aircraft during hover conditions. For horizontal stability and control, an empennage in the form of a V-tail is established as the preferred option. Because of the high-wing configuration, the only feasible options are a T-tail or a V-tail. The use of a V-tail reduces structural loads, and hence the weight and cost are reduced. The V-tail is consequently sized for horizontal stability and control. The resulting design is placed at the end of the fuselage, with a surface area of 4.446 [m^2], a span of 4.99 [m] (V-wise), and a dihedral of 0.33 [rad]. Then, the stability derivatives are determined for the aircraft, followed by a dynamic analysis of the eigenmotions. A SAS system is designed to ensure the appropriate stability and control of Aetheria during horizontal flight.

Structures
The structural design of the project focused on four key aspects: the wingbox design for the V-tail and main wing, the safety of the hydrogen storage system, passenger safety, and vibrational analysis. For the wingbox design, a Python model was used to optimize weight while meeting constraints related to skin and stringer buckling, as well as yield and tensile stress failure. To ensure passenger safety, the aircraft was designed to land horizontally with one propeller inoperative, and an energy-absorbing structure was incorporated into the fuselage to handle crash loads during vertical flight. The fuselage size was determined using a crashed diameter coefficient, which considers the normal and safe cross-sectional areas after a crash. The hydrogen system was placed in the tail cone within the undeformed area based on this coefficient. Finally, a vibrational analysis was conducted to assess eigenfrequencies of the wing and tail, and to evaluate any coupling effects between them.

Propulsion and Power
The propulsion design of the eVTOL consists of choosing the number of blades, their radius, and their geometry. This design was based on a method by Eugene Larabee [2]. Once the design procedure was implemented, many iterations were performed to obtain the optimal parameters. Due to constraints from the control department, the propellers had to provide a thrust of 2.25 times the thrust required in vertical flight for controllability. Therefore, the propellers had to be sized for a thrust value as close as possible to cruise, while still meeting the maximum thrust requirements. This resulted in a radius of 1.05 [m], where the thrust produced in cruise, hover, and maximum con-

ditions is 0.26 [kN], 4.7 [kN], and 11 [kN], respectively, at 300, 1600, and 2300 revolutions per minute, respectively. This propeller's design thrust is 2.6 [kN], at 1000 rpm, using 6 blades, working at 83% efficiency. Noise emissions at cruise and hover, taken at 2,400 [m], and 30 [m], are 34 [dB] and 80 [dB].

83% of Aetheria's energy is stored in hydrogen and the rest is stored in batteries. Hydrogen is mostly for power generation during cruise as it provides 80 % of cruise power due to the energy density of hydrogen being substantially higher (33.3 kWh/kg) than the energy density of batteries (0.34 kWh/kg). The batteries are used to provide the high-power requirements associated with vertical take off and landing operations (VTOL). This resulted in an overall power system mass of 510 kg where the battery weighs 205 kg, the fuel cell 42 kg, and the hydrogen storage system including hydrogen weights 177 kg.

Sustainability

The concept of sustainability has taken a vital role in the design process. A Life Cycle Analysis (LCA) is conducted to evaluate the environmental impact of the Aetheria aircraft. The analysis considers the entire lifespan of the aircraft, from production to recycling and disposal. The study quantitatively analyzes the cradle-to-gate (CTG) and well-to-shaft (WTS) cycles, assessing the Global Warming Potential (GWP) in terms of CO2 emissions per VTOL produced and battery impact in terms of CO2 emissions per kilowatt-hour (kWh). The results estimate a total GWP of approximately 50 tons of equivalent CO2 emissions for Aetheria, considering a MTOM of 2500 kg, and a WTS GWP of around 70 kg of equivalent CO2 emissions for the US grid, based on a battery capacity of 70 kWh.

Secondly, in order to make sustainability a top priority, it has been integrated into each department. The aerodynamic department has integrated sustainability by selecting a commonly used airfoil and focussing on minimizing drag. For flight performance sustainability plays a role as the cruise altitude is designed such that the noise on the ground is minimized. The power department has focused on sustainability by maximizing the use of hydrogen and minimizing the use of batteries since these contain harmful materials. Furthermore, the structures and control & stability departments mainly focused on social sustainability, by providing a high level of crashworthiness and a stable aircraft.

Finance

In order to put a price on the production costs and operational costs of the eVTOLs, a financial analysis was conducted. The equations that were used to assess the costs were found in a textbook that conducted this research on GA aircraft [3], which were deemed close enough to eVTOLs to provide a preliminary cost analysis. This method showed that the unit variable cost is 920,000 dollars, at a yearly operational cost of 327,000 dollars. This would result in a break-even eVTOL number at 106, giving a total ROI of 14%.

Finally, once the design methodologies of each technical department were made clear, a code was run to converge on values, which were then optimized.

Parameter	Value
MTOM [kg]	2522
OEM [kg]	2012
Range [km]	400
Cruise speed [m/s]	300
Stall speed [m/s]	40
Max. power [kW]	875.4
h _2 Fuel Capacity [kg]	9.6

Parameter	Value
Number of Passenger	4
Wing span [m]	9.4
Wing area [m^2]	13.0
Fuselage length [m]	11.2
Lift to Drag ratio [-]	18.3
Price per eVTOL [million $]	2.0
Unit Variable Cost [thousands $]	925

Contents

List of Symbols

Abbreviations

$ACAI$	Available Control Authority Index
CAS	Control Augmentation System
CG	Center of Gravity
$EASA$	European Union Aviation Safety Agency
$eVTOL$	Electrical Vertical Take-Off and Landing (aircraft)
I	Integral (controller)
$LEMAC$	Leading Edge of the Mean Aerodynamic Chord
$MTOM$	Maximum Take-Off Mass
PD	Proportional-Derivative (controller)
PI	Proportional-Integral (controller)
PID	Proportional-Integral-Derivative (controller)
SAS	Stability Augmentation System
SF	Safety factor

Greek Symbols

α	Angle of Attack	rad
β	Blade Pitch Angle	rad
β	Crashed diameter coefficient	-
β	Prandtl-Glauert factor	-
β	Sideslip angle	rad
δ	Control surface deflection	rad
ϵ	Downwash angle	rad
ϵ	Heat exchanger effectiveness	-
ϵ	Strain	-
η	Propulsive Efficiency	-
η_{af}	Airfoil efficiency factor	-
$\frac{d\epsilon}{d\alpha}$	Downwash gradient	-
$\frac{d\sigma}{d\beta}$	Sideslip gradient	-
Γ	Dihedral	rad
γ	Climb angle	deg
λ	Taper ratio	-
$\Lambda_{0.25h}$	Horizontal tail quarter chord sweep	deg
$\Lambda_{0.5c_h}$	Half-chord sweep angle of the horizontal tail	rad
μ_b	Laterally dimensionless mass	-
μ_c	Longitudinally dimensionless mass	-
ν	Fuel cell cruise power fraction	-
ν	Poisson	-
ω	Rotational velocity	$rads^{-1}$
ϕ	Roll angle	rad
ϕ_{sys}	Control system phase	-
ψ	Yaw angle	rad
ρ	Density	kgm^{-3}
σ	Stress	N/m^2
τ	Control surface effectiveness	-
τ	Eigenmotion time constant	-
θ	Pitch angle	rad
ζ	Damping ratio	-
ζ	Displacement Velocity Ratio	-

Latin Symbols

$\bar{c}$	Mean aerodynamic chord	m

$\bar{x}_{ac}$	Non-dimensionalised aerodynamic centre location w.r.t. LEMAC	-
$\bar{x}_{cg}$	Non-dimensionalised CG location w.r.t. LEMAC	-
ΔL	Roll moment difference w.r.t. hover state	Nm
ΔM	Pitch moment difference w.r.t. hover state	Nm
ΔN	Yaw moment difference w.r.t. hover state	Nm
ΔT	Thrust difference w.r.t. hover state	N
$\dot{m}$	mass flow	kgs^{-1}
$\frac{V_h}{V}$	Ratio of velocities over horizontal tail and main wing	-
A	Aspect ratio	-
A	Cross-sectional area	m^2
a	Speed of sound	ms^{-1}
b	Wing span	m
C	heat capacity rate	JK^{-1}
c	Chord	m
C_L	Lift coefficient	-
C_l	Roll moment coefficient	-
C_m	Pitch moment coefficient	-
C_n	Yaw moment coefficient	-
c_r	Chord length at root	m
c_t	Chord length at tip	m
C_X	X-force coefficient	-
C_Y	Y-force coefficient	-
C_Z	Z-force coefficient	-
$C_{m_{ac}}$	Pitch moment coefficient around the aerodynamic centre	-
D	Diameter	M
E	E modulus	N/m
E	Energy	J
G	mass flux	$kgm^{-1}s^{-1}$
g	Gravity acceleration at sea-level	ms^{-2}
h	Height	m
h	altitude	m
I_{xx}	Moment of inertia around x-axis	kgm^2
I_{xz}	Moment of inertia around in xz-plane	kgm^2
I_{yy}	Moment of inertia around y-axis	kgm^2
I_{zz}	Moment of inertia around z-axis	kgm^2
K	Vertical tail aspect ratio reduction factor	-
K_d	Roll moment difference w.r.t. hover state	m
K_p	Gain of proportional controller	-
l	Distance between main wing's and stability surface's aerodynamic centres	m
M	Moment	Nm
m	Mass	kg
n	Load factor	-
p	Roll rate	$rads^{-1}$
Q	Heat	J
S	Wing surface area	m^2
T	Torsion	Nm
t	Thickness	m
T_2	Time to double the amplitude	s
v	Volume	m^3
v	velocity	ms^{-1}

V_s	Stall speed	ms^{-1}
W	Local Flow Velocity	ms^{-1}
w	Stringer pitch	m
w	Width	m
x	Aircraft x-location in body reference frame	m
x_{cg}	CG x-location	m
y	Aircraft y-location in body reference frame	m
z	Aircraft z-location in body reference frame	m

Subscripts

0	Trim condition (stability derivatives)
α	Derivative w.r.t. angle of attack
β	Derivative w.r.t. sideslip
δa	Derivative w.r.t. aileron deflection
δe	Derivative w.r.t. elevator deflection
δr	Derivative w.r.t. rudder deflection
$\dot{\alpha}$	Double derivative w.r.t. angle of attack
a	Parameter of aileron
$A-h$	Parameter of aircraft-less-tail
cr	Parameter of cruise condition
e	Parameter of elevator
eng	Engine
f	Parameter of fuselage
fus	Parameter of fuselage
h	Parameter of horizontal tail
k	Kinetic
max	Maximum
N	Parameter normal to surface
p	Derivative w.r.t. roll rate
$prop$	Parameter of propellers
q	Derivative w.r.t. pitch rate
r	Derivative w.r.t. yaw rate
r	Parameter of rudder
s	Parameter of wing section
s,eff	Parameter of slipstream
sk	Skin
sp	Spar
str	Stringer
T	Parameter of thrust
ult	Ultimate
v	Parameter of vertical tail
vee	Parameter of V-Tail
vt	Parameter of vertical tail
$vtail$	Parameter of V-Tail
x	About x-axis / in x-direction
y	About y-axis / in y-direction
z	About z-axis / in z-direction

1

Introduction

The growing demand for sustainable and fast means of transport has led to the development of a new type of aircraft: an electrical Vertical Take-Off and Landing (eVTOL) aircraft. This new promising revolution in the Urban Air Mobility (UAM) industry aims to compete with short-range regional transport to serve as a personal air taxi. However, this project aims to include hydrogen as a power source, making it a novel concept which very few have attempted to design yet. By harnessing the power of hydrogen, the range can be increased significantly compared to existing eVTOLs, making it possible to compete with international high-speed trains and short-range regional commercial flights. The innovative aircraft designed in this report, Aetheria, eliminates the problems of urban congestion while flying emission-free.

This report aims to present the final detailed design of Aetheria, extensively analyzing each system and subsystem after which the integration of all systems leads to a coherent and harmonized final design while complying with all requirements set previously at the beginning of the project. The different technical disciplines of the design cover structures, aerodynamics, performance, stability & control and and power & propulsion as the main technical elements. As sustainability is a driving factor in the design, each system carefully considers ways to optimize the design to ensure the most sustainable design possible after which the integration and optimization of the design aimed for a light aircraft and a mission energy as low as possible. Other non-technical aspects of the design such as market analysis, technical risk management operations & logistics, and financial analysis are also covered and carefully analyzed. Finally, conclusions are made on the feasibility of the design and concept based on the work performed throughout the report.

2

Project Plan & Organisation

The Project Plan includes the Functional Flow Diagram, Functional Breakdown Diagram, and Project Development & Logic Diagram. These diagrams provide a visual representation of the project's functions and logical flow of activities. Additionally, the Gantt chart offers a timeline view of tasks and dependencies, which aids in scheduling and time management.

2.1. Functional Flow Diagram

An updated version of the Functional flow diagram from the Baseline report [4] can be seen in Figure 2.1. The diagram analyses a nominal flight excluding any emergency procedures [4]. Compared to a conventional aircraft, there are no differences in such a diagram, except for the transition phase where a change from vertical to horizontal flight and vice versa, takes place [4].

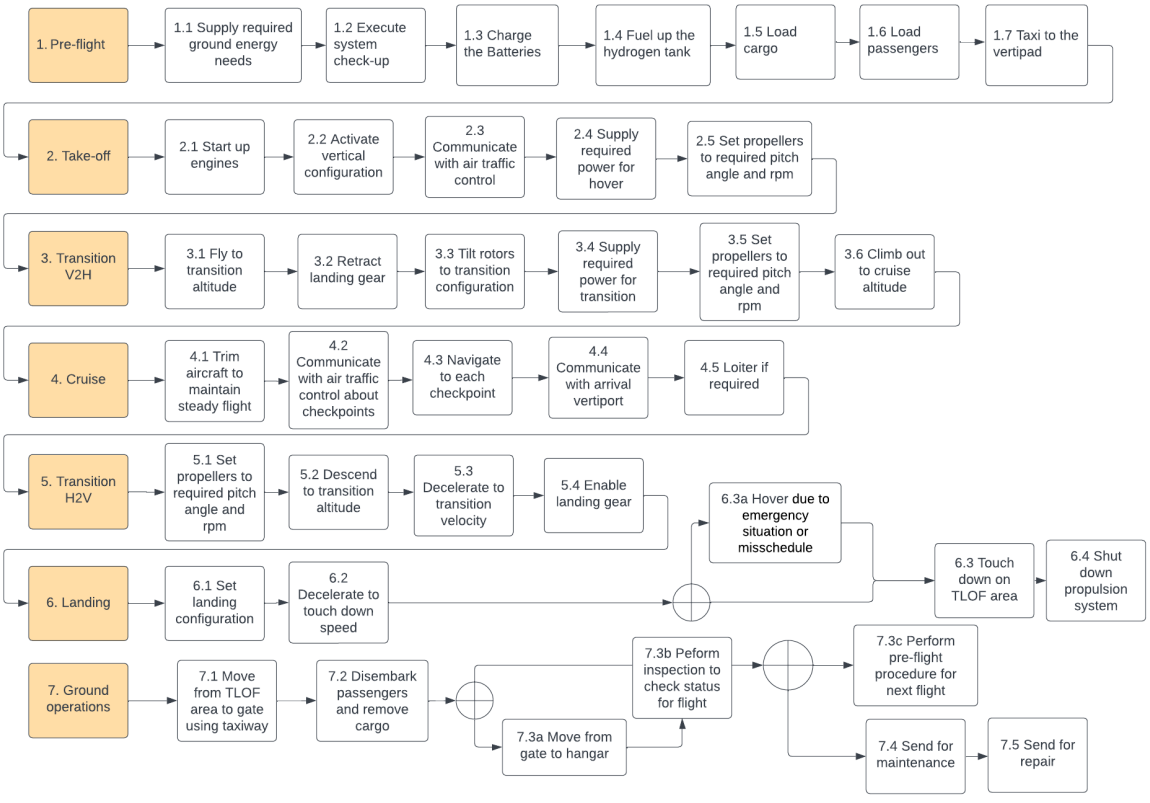

Figure 2.1: *Functional Flow Diagram*

2.2. Functional Breakdown Diagram

The functional breakdown structure updated from the Baseline report [4], is based more on the functions of the different subsystems rather than the operations of the eVTOL. Some levels of the functional breakdown structure flow from the functional flow diagram, like the ground operations segment. The functional breakdown structure can be seen below.

- eVTOL
  - Flight performance
    - Maintain structural integrity
      - Damp vibrations
        - Damp engine/propellor vibrations
        - Damp turbulence induced vibrations
      - Provide structural stability
        - Ensure VTOL is laterally stable
          - Ensure VTOL doesn't tip over
          - Ensure VTOL has ground clearance
        - Ensure VTOL is longitudinally stable
          - Ensure VTOL doesn't tip back
      - Provide required structural support
        - To sustain unexpected aerodynamic loads
        - To sustain nominal aerodynamic loads
    - Provide power
      - Store electrical energy
        - Convert electricity to correct voltage
        - Manage battery thermally
          - Expell 95kW of heat
        - Manage battery level
        - Apply redundancy in eletrical energy storage
      - Convert hydrogen to electricity
        - Provide filtered and compressed air
          - Provide use of compressor and filters
        - Manage fuel cell thermally
          - Expell 113kW of heat
        - Purge excess hydrogen
        - Apply redundancy in hydrogen conversion
      - Store hydrogen
        - Provide storage space for hydrogen
          - Provide 533L for Hydrogen
        - Provide optimal conditions for hydrogen
          - Provide 350 bar pressure
          - Provide ambient room temperature
    - Provide aerodynamic performance
      - Provide aerodynamic stability
        - Provide longitudinal stability
        - Provide lateral stability
      - Provide aerodynamic control
        - Execute roll, pitch and yaw manoeuvre
          - Determine Control Surface deflection
          - Deflect Control Surface
        - Provide altitude change
      - Provide Lift
    - Provide Propulsion
      - Provide 4,689 [N] for vertical flight
      - Provide 289 [N] for horizontal flight
      - Apply redudancy in thrust generation
    - Provide Communications and Control
      - Provide Control Capabilities
        - Provide roll control
        - Provide pitch control
        - Provide yaw control
        - Provide altitude control
      - Provide communication capabilities
        - Provide Navigation Capabilities
        - Provide internal Communication
        - Provide external Communication
          - Provide communication with Air traffic control
    - Emergencies
      - Cabin
        - Provide passenger protection systems
        - Provide fire extinguishing system
        - Provide Emergency breathing systems
        - Provide emergency exits
      - External
        - Maintain Structural Integrity during emergeny landing
        - Float on water
        - Provide lifevests for passengers
        - Autoland in case of low battery level / empty hydrogen tank
  - 7. Ground operations
    - 7.1 Taxiing
      - Provide means of ground movement through taxiways
    - 7.2 Load (on/off) Cargo and Passengers
      - Disembark Cargo and Passengers
    - 7.3b Inspection
      - Provide regular inspection
    - 7.3c Refuelling
      - Provide hydrogen to tanks after every flight
      - Re-charge the Lithium-ion Batteries after every flight
    - 7.4 Maintainance
      - Provide maintenance for parts that wear out before end of operational life
    - 7.5 Repair
      - Provide repair for needed parts
  - General Design
    - Provide maintenance access
      - Have latches in the wing-box
    - Carry Payload
      - Provide passenger accommodation
      - Provide cargo space
      - Provide loading / unloading of payload
  - Aircraft disposal
    - Dispose Parts
      - Recycle unusable parts
      - Reuse functioning parts
      - Dispose un-recyclable parts
    - Dismantle aircraft
      - Send aircraft to scrapeyard

Legend

- The Design - eVTOL
- Operations level
- Operations sub-level
- Requirements level
- Requirements sub-level
- Requirements sub-sub-level
- Proces

2.3. Project Development & Logic Diagram

The path the project will follow post DSE can be seen in a project development diagram in Figure 2.2. Initially, the preliminary design made during DSE will be iterated to check for feasibility. This can be done using wind tunnel experiments. Later a detailed design will be performed followed by the construction of a prototype which will be tested using various testing methods. Once these tests are successful, the eVTOL can be subjected to certification followed by mass production if successful. The mass-produced eVTOLs will then be commercialised and sold to customers for use. During their operational life, the eVTOLs will be inspected, maintained and repaired whenever necessary. Finally, at the end of the lifetime of the eVTOL, parts can be re-used and re-cycled prior to its complete disposal. A more detailed analysis of each of the steps of the project development diagram can be seen in the Midterm report [1].

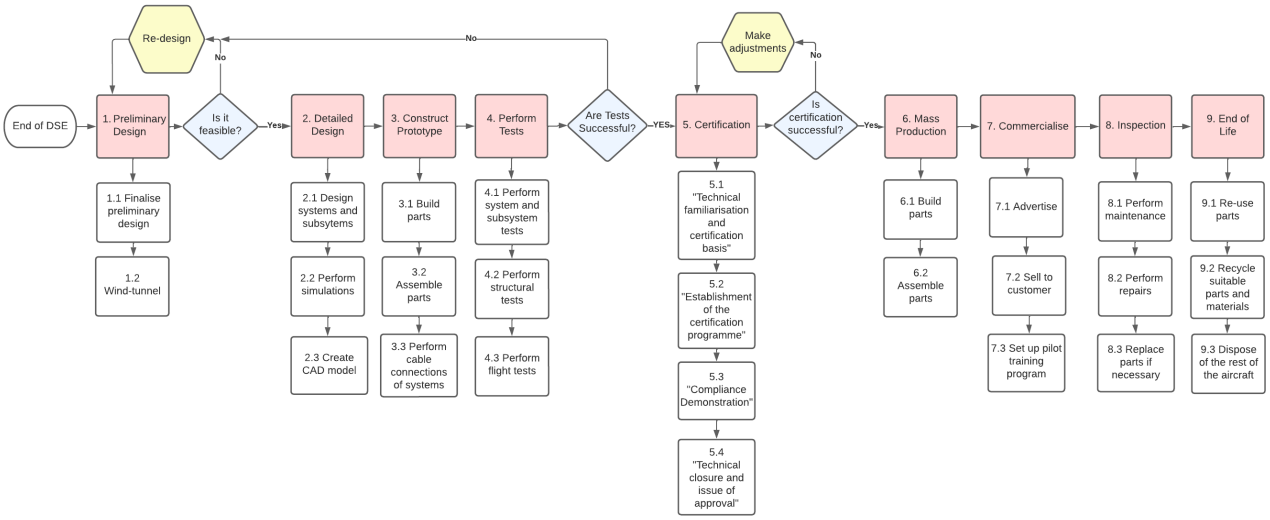

Figure 2.2: *Project Development Diagram*

In addition to the project development and logic diagram, a post-DSE Gantt chart was also constructed in order to show the detailed flow of events that will take place ranging from finalising the preliminary design all the way until the end of life of Aetheria. The Gantt chart can be seen below.

ID	TASK	DURATION (weeks)	START	FINISH
0	**Post DSE Gantt Chart**	**1176**	**01.07.2023**	**01.07.2045**
1	**1: Preliminary Design**	**26**	01.07.2023	31.12.2023
1	1.1: Finalise Preliminary Design	13	01.07.2023	01.10.2023
2	1.2: Perform Iterations	13	01.10.2023	31.12.2023
3	**2: Detailed Design**	**104**	**01.01.2024**	**31.12.2025**
4	2.1: Design Subsystems	40	01.01.2024	01.10.2024
5	2.1.1: Design Avionics System	40	01.01.2024	01.10.2024
6	2.1.2: Design Electrical Systems	40	01.01.2024	01.10.2024
7	2.1.3: Design Cabin Environment Control System	40	01.01.2024	01.10.2024
8	2.1.4: Design Cockpit Interface	40	01.01.2024	01.10.2024
9	2.1.5: Design Communication Systems	40	01.01.2024	01.10.2024
10	2.1.6: Design Lighting Systems	40	01.01.2024	01.10.2024
11	2.1.7: Design Emergency Systems	40	01.01.2024	01.10.2024
12	2.2: Perform Simulations	60	01.10.2024	01.12.2025
13	2.2.1: Perform Computational Fluid Dynamics (CFD)	60	01.10.2024	01.12.2025
14	2.2.2: Perform Finite Element Analysis (FEA)	60	01.10.2024	01.12.2025
15	2.2.3: Perform Aeroelasticity Analysis	60	01.10.2024	01.12.2025
16	2.2.4: Perform Stability Augmentation System (SAS) Analysis	60	01.10.2024	01.12.2025
17	2.3: Technical Drawings	4	01.12.2025	31.12.2025
18	2.3.1: Update CAD Drawings	4	01.12.2025	31.12.2025
19	**3: Prototype**	**52**	**01.01.2026**	**31.12.2026**
20	3.1: Hire Workers	4	01.01.2026	01.02.2026
21	3.1: Build Parts	22	01.02.2026	01.07.2026
22	3.2: Buy Parts	22	01.02.2026	01.07.2026
23	3.3: Assemble Parts	22	01.07.2026	01.12.2026
24	3.4: Perform Cable Connections	4	01.12.2026	31.12.2026
25	**4: Testing**	**104**	**01.01.2027**	**31.12.2028**
26	4.1: Perform System Tests	13	01.01.2027	01.05.2027
27	4.1.1: Perform Power System Tests	13	01.01.2027	01.05.2027
28	4.1.2: Perform Propulsion Tests	13	01.01.2027	01.05.2027
29	4.2: Perform Subsystem Tests	13	01.05.2027	01.08.2027
30	4.2.1: Perform Avionics Tests	13	01.05.2027	01.08.2027
31	4.2.2: Perform Electrical System Tests	13	01.05.2027	01.08.2027
32	4.2.3: Perform Communication and Navigation Tests	13	01.05.2027	01.08.2027
33	4.3: Perform Structural Tests	26	01.08.2027	01.02.2028
34	4.3.1: Perform Vibration Tests	26	01.08.2027	01.02.2028
35	4.3.2: Perform Flutter Tests	26	01.08.2027	01.02.2028
36	4.3.3: Perform Static Load Tests	26	01.08.2027	01.02.2028
37	4.3.4: Perform Fatigue Tests	26	01.08.2027	01.02.2028
38	4.4: Perform Flight Tests	32	01.02.2028	01.09.2028
39	4.4.1 Perform Previous (Sub) - System Tests	32	01.02.2028	01.09.2028
40	4.4.2: Perform Stability and Control Tests	32	01.02.2028	01.09.2028
41	4.4.3: Perform Aerodynamic Tests	32	01.02.2028	01.09.2028
42	4.5: Perform Crash Tests	20	01.09.2028	31.12.2028
43	**6: Finance**	**104**	**01.01.2028**	**31.12.2029**
44	6.1: Gather Investments		01.01.2028	31.12.2029
45	6.2: Gather Loans from Banks		01.01.2028	31.12.2029
46	6.3: Gather Product Pre-Orders		01.01.2028	31.12.2029
47	**5: Certification**	**52**	**01.01.2029**	**31.12.2029**
48	5.1: EASA Technical Familiarisation	13	01.01.2029	01.04.2029
49	5.2: EASA Certification Programme Establishment	13	01.04.2029	01.07.2029
50	5.3: EASA Regulations Compliance Demonstration	13	01.07.2029	01.10.2029
51	5.4: EASA Approval	13	01.10.2029	31.12.2029
52	**7: Factory Set-UP**	**104**	**01.01.2028**	**31.12.2029**
53	7.1: Decide on Factory Location	10	01.01.2028	01.03.2028
54	7.2: Contact Local Authorities	8	01.03.2028	01.05.2028
55	7.3: Perform Law Arrangements	21	01.05.2028	01.10.2028
56	7.4: Build Factory	56	01.10.2028	31.10.2029
57	7.5: Hire Workers	9	31.10.2029	31.12.2029
58	**8: Supply Chain**	**52**	**01.01.2028**	**31.12.2028**
59	8.1: Decide Part Suppliers	10	01.01.2028	01.03.2028
60	8.2: Establish Just-in-Case Supply Chain	8	01.03.2028	01.05.2028
61	8.3: Establish Supply Routes	21	01.05.2028	01.10.2028
62	8.4: Establish Delivery Dates	13	01.10.2028	31.12.2028
63	**9: Mass Production**	**364**	**01.01.2029**	**31.12.2035**
64	9.1: Set-up Production Line	4	01.01.2029	01.02.2029
65	9.2: Build Parts	360	01.02.2029	31.12.2035
66	9.3: Import Parts	360	01.02.2029	31.12.2035
67	9.4: Assemble Parts	360	01.02.2029	31.12.2035
68	9.5: Component Assembly	360	01.02.2029	31.12.2035
69	9.6: Sub-Assembly	360	01.02.2029	31.12.2035
70	9.7: Final Assembly (Aetheria)	360	01.02.2029	31.12.2035
71	**10: Commercialise**	**104**	**01.01.2029**	**31.12.2030**
72	10.1: Advertise	104	01.01.2029	31.12.2030
73	10.2: Sell to Customers	104	01.01.2029	31.12.2030
74	10.3: Set-up Pilot Training Program	104	01.01.2029	31.12.2030
75	**11: Inspection**	**832**	**01.01.2030**	**31.12.2045**
76	11.1: Perform Regular Inspections	832	01.01.2030	31.12.2045
77	11.2: Perform Maintenance	832	01.01.2030	31.12.2045
78	11.3: Perform Repairs	832	01.01.2030	31.12.2045
79	**12: End of Life**	**6**	**01.01.2046**	**14.02.2046**
80	12.1: Re-Use Parts	2	01.01.2046	14.01.2046
81	12.2: Recycle Suitable Parts	4	01.01.2046	28.01.2046
82	12.3: Dispose of the remaining eVTOL	2	28.01.2046	14.02.2046

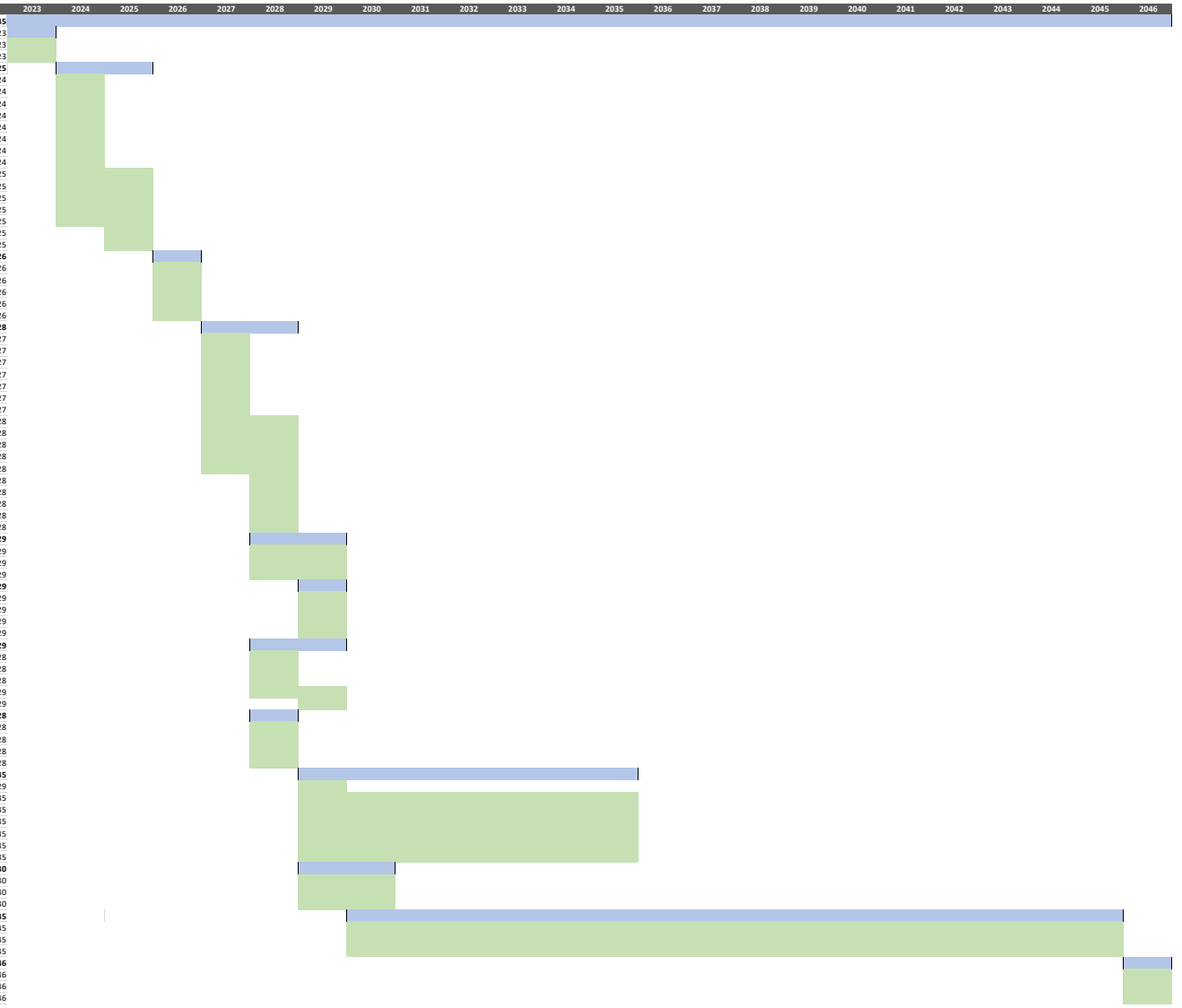

3

Trade-off Summary

In the midterm stage, four possible design configurations were identified: J1, J2, W1 and L1 based on existing designs. The J1 resembled the Joby eVTOL with its 6 tilt rotor engines and wing+tail configuration. However, in the J1 design, it was determined that achieving controllability during vertical flight under the one engine inoperative condition was nearly impossible. For this reason, a new design J2 was made that differed from the J1 only in the fact two motors powered each rotor instead of one. The W1 was a tandem tilt wing design with 12 engines and was inspired by the Wigeon design. The L1 featured a tandem fixed-wing, which was inspired by the existing Lilium jet. Its propulsion system comprised of 36 ducted fans, which were placed in pods that could be actively rotated to stabilize the aircraft during hover. The designs are presented in Figure 3.1.

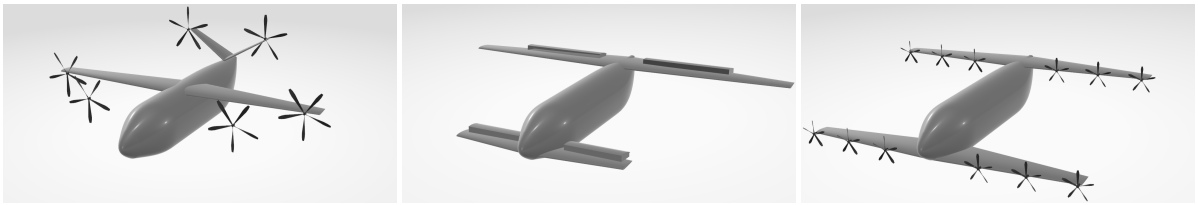

(a) *J1 & J2* **(b)** *L1* **(c)** *W1*

Figure 3.1: *Sketches of the different configurations*

To compare these designs, several trade-off criteria were defined which were assigned weights out of 100%. The criteria were scored from 0 to 3. The score 0 indicated by red in Table 3.1 indicates an unacceptable design that leads to the design automatically being discarded. Score 1 (indicated with orange) indicates that the configuration has correctable deficiencies. The scores 2 and 3 (indicated by yellow and green respectively) indicate a good and excellent design configuration that will meet or exceed any requirements related to that particular criteria respectively. This resulted in each design configuration obtaining a final score out of 3 shown in the 'Weighted Total' column of Table 3.1. The scores of different configurations for particular criteria and their overall score can also be seen in Table 3.1. Due to the J2 design receiving the highest score, the J2 configuration was chosen, for which the detailed subsystem design is performed in this report.

Table 3.1: *Final Trade-off Table*

Criteria / Design	Mission Energy (30%)	Stability & Controllability (20%)	Crashworthiness (20%)	Production cost (10%)	Operational cost except Fuel (10%)	Noise (10%)	Weighted Total
J1	204kWh (3)	cannot be made stable and controllable (0)	1.59m crash floor required for 3.25m cabin, high wing (2)	1.01 M $ / VTOL (3)	159k $ / year (3)	86dB at 30m (2)	DISCARDED
J2	204kWh (3)	large flexibility in terms of wing positioning and trim (3)	1.59m crash floor required for 3.25m cabin, high wing (2)	1.01 M $ / VTOL (3)	159k $ /year (3)	86dB at 30m (2)	2.4
W1	326kWh (2)	allowable cg range just meets required cg travel (2)	2.65m crash floor required for 3.25m cabin, not high wing (2)	1.68 M $ / VTOL (2)	294k $ / year (2)	94dB at 30m (2)	1.8
L1	547kWh (1)	large flexibility in terms of wing positioning and trim (3)	3.63m crash floor required for 3.25m cabin (can be fixed), not high wing (1)	3.12 M $ / VTOL (1)	614k $/ year (1)	56dB at 30m (3)	1.5

4

Market Analysis

In order to assess the market size and potential of the product within the industry, a market analysis was performed. The analysis is based on the current market trends, with an evaluation of potential developments regarding the industry in the future. The market analysis in this report was taken from the Baseline report [4] in order to produce a stand-alone final report.

4.1. Target Sectors & Market Trends

To start designing the eVTOL, the target demographic must be known. A list was made of demographics ranked from most promising to least. This means the eVTOL would be tailored toward that sector. The team decided on the following:

1. Commercial Travel
2. Private Usage/Leisure
3. Cargo Transporting
4. Structure Inspection/Maintenance
5. First Responders (Police, Ambulance, Firefighters, Natural Disaster)
6. Military Applications

The ranking was determined based on user requirements and the number of eVTOLs/helicopters in each sector. Commercial travel was deemed the most important sector because of the 4-passenger requirements, this is followed by leisure use by private individuals or companies. Cargo transportation ranked a bit lower due to its limited payload capacity of 500kg. Structure inspection for highways and offshore wind farms ranked higher due to the long distances involved, while first responders and military applications were ranked lowest due to their specific requirements and accreditation needs[1].

4.1.1. Market Trends

Markets and Markets has done an analysis of the eVTOL market and found the trends listed below. Note that CAGR stands for compound annual growth rate, a measure of the projected annual growth [2]:

1. The hydrogen-electric hybrid eVTOLs are projected to see the highest CAGR
2. The piloted segment is projected to see the highest CAGR
3. The last mile delivery segment is projected to see the highest CAGR
4. The 100-1,000 kg segment is projected to see the highest CAGR
5. The segment with a range longer than 200km is projected to see the highest CAGR

[1] Accessed May 2nd 2023, https://english.defensie.nl/topics/military-aviation-authority/accredit

[2] Accessed April 26th 2023, https://www.marketsandmarkets.com/Market-Reports/evtol-aircraft-market-28054110.html?gclid=CjwKCAjwl6OiBhA2EiwAuUwWZSjathr3v3yT_0HA4NXnApe3kRqR-TDThvEFZOwEi1txO0UzggDgshoC-twQAvD_BwE

When looking at the trends, it is clear that three of these trends comply with the user requirements, namely trends 1, 2, and 5. Trend 3 does not match the user requirements, as our goal is to satisfy passengers looking for a travel time of 1-3 hours, and a range up to 400 km while the last mile delivery focuses on short-range (0-30km). Our mass will also be a lot larger due to the long-range requirement meaning trend 4 also does not match. The user requirements matching most of the market trends indicate that the team's eVTOL can hold quite a substantial market share.

4.2. Range and Speed Analysis

Range has a significant impact on the total market share of the UAM industry [5], therefore finding a both suitable and feasible range is paramount. In order to do, the assumption was made that the amount of travel to and from a city is proportional to the Gross Metropolitan Product (GMP), the validity of this assumption is high as GMP is often used in computing passenger flow [6, 7]. Additionally, Brons et al. mentions that demand for air transport is largely determined by the spending capacity of the customer [8, pg. 1]. The analysis will mainly be limited to West Europe for reasons which will follow in this section. For this purpose, the cities in Table 4.1 were used, where all cities have a GMP higher than €159.2 billion. An evaluation of the North American market has also been performed together with a discussion on how compatible the markets are.

Table 4.1: *List of cities with a GMP higher than €159.2 used in Figure 4.1* [3].

Major Cities in Europe					
Paris	Madrid	Milan	London	Dortmund	Rome
Munich	Berlin	Amsterdam	Barcelona	Hamburg	Dublin

Europe

Using the Python script, the accessibility of each major city in Europe was mapped. In Figure 4.1, radii are drawn around the cities listed in Table 4.1. All cities included in the map have a GDP higher than €159.2 billion. Colour-coded radii indicate the cities that are within range of other cities, with a variety of colours for better distinction but no other intrinsic meaning. The black radii indicate that an isolated city is not able to fly to another city in Table 4.1.

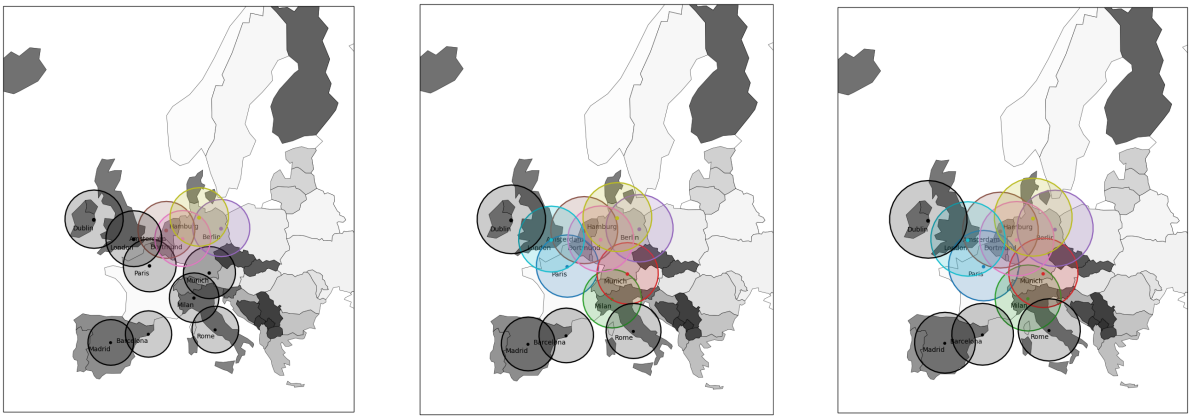

(a) *300 km Range* **(b)** *350 km Range* **(c)** *400 km Range*

Figure 4.1: *Visualization of cities listed in Table 4.1 with their corresponding radii.*

[3] Accessed May 4 2022, https://ec.europa.eu/eurostat/databrowser/view/met_10r_3gdp/default/table?lang=en

From Figure 4.1a it can be seen that using a range of 300 [km] severely limits the number of cities the VTOL would be able to fly to. Hence, the 300 [km] range requirement would severely limit the market for Aetheria. By increasing the range from 300 [km] to 350 [km], it can be seen in Figure 4.1b that Central Europe opens up. Further increasing the range to 400 [km] has no effect on the isolated cities. Madrid, Barcelona and Rome are still isolated and hence the further increased range does not add to the usage of Aetheria.

However, from an accessibility point of view increasing the range to 400 [km] range allows for more high-value direct routes. Meaning, that instead of flying Amsterdam-London via Brussels one directly flies from Amsterdam to London. Direct flights are invaluable to the success of the project as direct flights significantly increase the block speed, also interchanges/transfers form a hard barrier for commuters and decrease ridership [9, 10]. Significant direct routes that would be achieved when increasing the range from 300 to 400 [km] are listed in Table 4.2. The combined GDPs of all trips are substantial and thus would be worth considering increasing the range to accommodate these flights. Additionally, considering the fact that Europe is relatively not a large market for eVTOLs, being able to establish oneself in these major cities as an eVTOL company early on would give the company an advantage.

Table 4.2: *Direct flights with a combined GDP higher than €800 billion made possible by increasing the range from 300 [km] to 400 [km]*

Trip	Range	Combined GDP [€ billions]
Paris - London	342	€ 1544
Amsterdam - London	359	€ 984
Brussels- London	320	€ 949
Paris - Lyon	393	€ 831

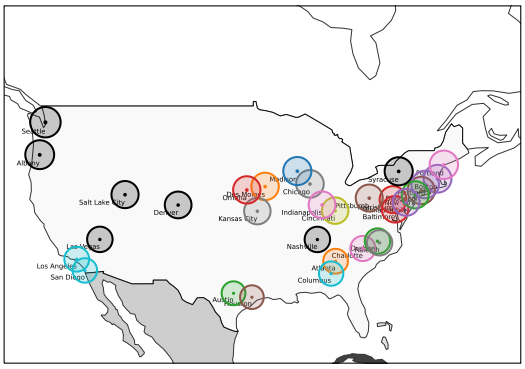

Figure 4.2: *Visualization of relevant cities in America with their corresponding radii indicating their reachability within a 300km range (circles are at half scale for clarity reasons).*

North America

The same can be considered for North America. In Figure 4.2, the sizes of the circles have been made smaller for clarity reasons. In the 300 [km], 350 [km], and 400 [km] range, there are 17,14,12 isolated cities respectively. The cities introduced are relatively small and would not significantly increases the market share of the eVTOL.

The East Coast of North America seems the most promising. Major cities like Boston, Washington, and New York lie in close vicinity to each other. The GDP of these cities is gigantic, e.g. New York has a GDP of €1.44 trillion. In contrast to Europe, increasing the range in North America is not as effective as for the European market due to the close vicinity and large market share of the major cities on the East Coast.

An exception on the general non-viable distances is the route between Los Angeles and Las Vegas, it is the busiest flight route in the US. The route has an average of 352 flights between them each

week[4]. The travel distance of this route is 366 [km], thus an eVTOL route between these cities could have a substantial influence on the size of the commercial market for Aetheria. This is another reason why increasing the range to 400 [km] would be advantageous.

Conclusion on Range Estimation

The decision was made to size the aircraft based on the European market as this market is more suitable for long-range UAM. As was seen in Table 4.2 from the European market case, a large benefit was acquired in direct trips and decreasing the number of isolated cities when increasing the range. Building on this, the trip Amsterdam - London was chosen as the limit case, while Paris - London will be the champion case. The reason for this limit case is that Amsterdam and London have second highest combined GDP but are still within an attainable range. Whereas, increasing the range to 393 [km] in order to serve Paris-Lyon would not be worth it. This would mean the final design range should be 359 kilometres. However, the accuracy of this distance might not be exact due to the vertiport being at the outskirts of the city or any deviations from the optimal trajectory, meaning contingencies should be utilized. A contingency of 10% was chosen, arriving at a final range of 400 [km].

Table 4.3: *Table containing the conclusions on the range analysis of the market*

Parameters	Value
Preliminary Range	360 [km]
Contingency	10%
Final Range	400 [km] [5]

4.2.1. Cruise Speed

Cruise speed is an important mission parameter as it is the main parameter with which the block speed can be controlled. The block speed is crucial to leverage the market according to Hae Choi and Park, as larger fare prices can be charged for a larger reduction in travel time compared to normal public transport/taxi services [5, pg. 275].

Table 4.4 displays many eVTOLs and their respective cruise speeds. Based on a range of 400 [km], and a user requirement that the duration of the trip may take between 1 and 3 hours, a range of cruise speeds of 133 [km/h] to 400 [km/h] is obtained. The eVTOLs with the largest market share are Lilium, Joby, Archer, and Vertical Aerospace. Hence, Aetheria's cruise speed should be competitive with these companies. These speeds are 280, 322, 241, and 322 kilometres per hour. Besides competition from the eVTOL market, the current best solution for sustainable travel, High-speed rail (HSR), will be the main competitor as HSR have similar missions, have high-capacity and are likely to be cheaper. Both the Eurostar and the Thalys reach speeds of 320[6] and 300[7] kilometres per hour respectively.

Thus, in order to stay competitive with HSR and existing eVTOLs, a cruise speed of 300 [km/h] was decided upon. The reason is that Aetheria would be significantly faster than HSR due to the similar speed and our advantage in a straight trajectory. Additionally, Aetheria would fly at the same speeds as competing eVTOLs and finally, with current technology, a speed of approximately 300 kilometres per hour should be feasible.

[4] Accessed May 1st 2023, https://simpleflying.com/what-are-the-usas-busiest-domestic-air-routes/
[5] Obtained by rounding 396 [km] up to 400 [km]
[6] Accessed May 3rd 2023, https://www.eurostar.com/us-en/about-eurostar/our-company
[7] Accessed May 3rd 2023, https://www.nsinternational.com/france/thalys-to-paris

4.3. Current eVTOL Market & Competition

From studying relevant literature, comparable products were found, based on which an estimate for the production costs as well as the cost per passenger mile could be made. Examples of products with similar user specifications are among others the Lilium Jet, Joby Aviation, Archer Midnight, Volocopter, Vertical Aerospace VX4, and the Terrafugia TF-X. Moreover, the literature serves as a feasibility study of the user requirements as well.

Another big player in the VTOL market which can't be overlooked is the helicopter market. Helicopters currently dominate the market for VTOLs with a market size of roughly 56.9 billion USD in 2022[8]. However, the CAGR is only 3.7% which is significantly lower compared to the eVTOL market, which has a CAGR between 13%-27%. The VTOL market will also face more regulations related to sustainability as Europe gets closer to 2050, meaning there will be extra constraints that will make it difficult for VTOLs to prosper.

In Table 4.4, many different eVTOLs with specifications have been given. These values can help determine the expected production costs, range, MTOW, and cruise speed from an eVTOL this size. Its main purpose is that it assesses competition.

Table 4.4: *Similar Product Specifications*

eVTOL	Cost ($)	Type of eVTOL	Pax	Range (km)	MTOM (kg)	Cruise Speed (km/h)
Astro [9]	-	Multirotor	2	32	360	70
VRCO[10]	2,000,000	Tilt Rotor	2	120	450	338
Bartini [11]	-	Tilt Rotor	3	150	1,100	300
Joby [12]	1,300,000 [13]	Tilt Rotor	4	241	1815	322
XTI [14]	-	Tilt Rotor	6	700	2404	555
Lilium [15]	2,500,000	Tilt Duct	6	300	3,175	280
Archer [16]	-	Lift + Cruise	4	160	3,175	241
Bell [17]	-	Tilt Rotor	4	97	3,175	241
Alaka'i Skai (H_2-based) [18]	-	Multi-rotor	4	640	454 (Payload)	185

Table 4.4 displays many eVTOLs, with their respective information. These give an order of magnitude for each specification that can be compared with Aetheria. For the Alaka'i Skai hydrogen-based eVTOL, no MTOW was found but instead, a maximum payload mass of 454 [kg] was found. The limited information found on costs is still quite important to be able to determine the price of Aetheria.

As for the segmentation of the eVTOL market displayed in Table 4.4, there are hundreds of designs available already, which can all be categorized into 4 different lift technology categories: multirotor, lift + cruise, tilt wing, and tilt rotor (or tilt duct)[19]. Multirotors are drone-like designs with multiple rotors able to provide vertical lift and will remain in the same configuration for horizontal flight by

[8] Accessed April 26th 2023, https://www.globenewswire.com/en/news-release/2023/04/13/2645861/0/en/Helicopter-Market-to-Reach-USD-76-16-Billion-by-2030-Fortune-Business-Insights.html#:~:text=Pune%2C%20India%2C%20April%2013%2C,3.7%25%20during%20the%20forecast%20period.
[9] Accessed April 28th 2023, https://flyastro.com/features/
[10] Accessed April 28th 2023, https://evtol.news/vrco-neoxcraft/
[11] Accessed April 28th 2023, https://evtol.news/bartini/
[12] Accessed May 1st 2023, https://evtol.news/joby-s4
[13] Accessed May 1st 2023, https://verticalmag.com/features/joby-aviation-evtol-spac-merger-reinvent-technology/
[14] Accessed May 1st 2023, https://evtol.news/xti-aircraft/
[15] Accessed May 1st 2023, https://www.lilium.com
[16] Accessed May 1st 2023, https://www.archer.com/midnight
[17] Accessed May 1st 2023, https://evtol.news/bell-nexus-4ex/
[18] Accessed April 26th 2023, https://www.alakai.com/skai
[19] Accessed April 28th 2023, https://www.einfochips.com/blog/evtol-aircraft-future-of-elevated-aerial-transportation/

pitching them forward. This is a rather simple design which is usually designed for shorter-range flight. Next, lift + cruise eVTOLs are fixed-wing designs that have designated propellors for vertical flight and usually a single propellor for horizontal flight. An advantage of this is the reduction of complexity for no additional rotating structural elements have to be implemented. Then, tilt-wing eVTOLs have wings capable of rotating in their entirety, which is beneficial for aerodynamics in vertical flight as the wing is in a low-drag configuration. Finally, tilt rotor eVTOLs are similar to tilt wings except that the rotors or ducted fans have rotational freedom instead of the entire wing.

4.3.1. Costs

Regarding costs, another study showed that the cost of an eVTOL is expected to be approximately US$1.2 million per four-seater eVTOL aircraft depending on an annual production of 100 units, close to US$600,000 for an annual production of 500 units, and close to US$200,000 for an annual production of 5,000 units [11].

A large difference between the team's eVTOL and existing ones is the usage of hydrogen. This affects the cost in a negative way as hydrogen requires more infrastructure to accommodate[20]. Storing hydrogen in a liquid state would require smaller tanks, but more energy to cool, and vice versa for storing it in a compressed gaseous state. Therefore in the final cost estimation, a margin should be added for the usage of hydrogen.

There are three eVTOLs given in Table 4.4 with their costs, yet Lilium is the only one that is not a projection. Therefore, using Lilium as a cost estimator for Aetheria makes more sense. Lilium costs 2.5 million but can fit 6 passengers. This makes the Lilium slightly more expensive in terms of payload mass ability, as their fuselage needs to be bigger. Working with Lilium's cost and taking into account a lowering of the cost for a smaller fuselage while also increasing it due to the usage of hydrogen, Aetheria has been given a budget of 3 million euros. This is including contingencies for production costs with the aim of lowering the cost to 2 million euros once economies of scale can be achieved. Now that production costs have been determined, the operational costs can be determined.

Table 4.5: *Operational Costs of eVTOLs*

	Lilium	**Joby**	**Vertical Aerospace**	**Archer**
Operational Cost [$/passenger mile]	1.75	0.86	1.06	-
Price [$/passenger mile]	2.25	3.0	-	3.30

Table 4.5 demonstrates the operational costs, and charged price[21]. These values have been roughly calculated by each producer at 25 flights a day, 100 km per flight, flying 10 hours a day, and filling 4.5 seats out of 6, excluding a pilot. These values are important to note as to stay competitive, these values must be considered. Joby Aerospace has even given the breakdown of their operational cost of 86 cents. They expect 22 cents for the pilot, 19 cents for maintenance, 11 cents for vertiport support/landing fees, 13 cents for the battery and charging, 9 cents for the aircraft insurance, and 12 cents for the sundries.

A few aspects to take into account when determining the operational costs of a hydrogen eVTOL relative to an electric one are:

1. Hydrogen costs more than electricity. However, hydrogen fuel cells have higher energy density

[20] Accessed May 3rd 2023, https://simpleflying.com/electric-vs-hydrogen-winner/

[21] Accessed April 26th 2023, https://www.futureflight.aero/news-article/2021-11-15/counting-cost-urban-air-mobility-flights

than batteries[22] so their overall weight might be lower.

2. Hydrogen fuel cells are more complex and delicate than batteries, meaning more maintenance can be required [23].
3. Hydrogen fueling infrastructure is not as widespread, so more infrastructure could be required [24].
4. Hydrogen refuelling takes a shorter time than batteries, so less time needs to be spent at vertiports, thus reducing vertiport fees [25].

Using Lilium's operational cost of 1.75 dollars per passenger mile, and adding on a margin for hydrogen use, the operational cost for Aetheria will be roughly 2.5 euros per passenger mile or 1.56 euros per passenger kilometre. Assuming a maximum of 1500 flights per year of maximum range with a full payload [26], this produces an operational cost of 3.744 million euros a year. The operational lifetime of a single unit is also an important parameter for designs. Lilium gives their jet a lifetime of 8 years [27], and Joby gives their jet a lifetime of 15 years [28]. The user requirement for the team has already been given as 15 years, and considering the competition, it is enough to stay competitive in the market. Therefore, due to the production cost of 3 million euros, (at economies of scale) plus 3.744 million each year due to operational costs, the total cost of Aetheria becomes 57 million euros.

4.3.2. Weight

When looking at the types of eVTOLs, the Lilium comes closest to meeting the user requirement in terms of sizing, because of the hydrogen tanks. This is important to keep in mind because there is quite a large range between the MTOWs listed in Table 4.4. Therefore, for the weight estimation, Lilium will be used, but considering a weight reduction both for the number of passengers, but also since less/none of the electric batteries will be used [29]. Using this, a preliminary weight estimation (MTOW) of 2400-2800kg has been used. A range has been given because a specific value would be quite far off compared to the real MTOW that will be found.

4.3.3. Infrastructure

Looking beyond just the market analysis of the aircraft itself, feasibility considerations regarding the required infrastructure should also be taken into account. Companies such as Skyports, Ferrovial and Skyportz already have plans for building a vertiport network in Dubai[30], Florida[31] and Australia[32], respectively. Another example of a company pursuing a market share in vertiports is Bayard Vertiport Solutions, which uses its previously acquired knowledge of building helipads and heliports to now start building vertiports[33]. On the other hand, Andrade et al. conducted a study in São Paulo proving the feasibility of using the existing helipad infrastructure for eVTOL use[12].

[22] Accessed May 3rd 2023, https://www.petro-online.com/news/measurement-and-testing/14/breaking-news/lithium-ion-batteries-vs-hydrogen-fuel-cells-which-is-better/58898
[23] Accessed May 3rd 2023, https://www.twi-global.com/technical-knowledge/faqs/what-are-the-pros-and-cons-of-hydrogen-fuel-cells
[24] Accessed May 3rd 2023, https://simpleflying.com/electric-vs-hydrogen-winner/
[25] Accessed May 3rd 2023, https://www.lexology.com/library/detail.aspx?g=1bf1cbf0-ac2f-4b39-a3de-2df77a9a515e
[26] Accesssed May 4 2023, https://aviationweek.com/business-aviation/opinion-there-will-be-blood-dissecting-evtol-bus
[27] Accessed May 2nd 2023, https://ir.lilium.com/static-files/e1912f16-b455-4929-a7df-f8b4dd5c2446
[28] Accessed May 2nd 2023, https://www.sec.gov/Archives/edgar/data/1819848/000119312521053631/d135823dex992.htm
[29] Accessed May 3rd 2023, https://www.umicore.com/en/newsroom/fuel-cells-battery-difference/
[30] Accessed April 26th 2023, https://evtolinsights.com/2023/02/skyports-infrastructures-vertiport-design-for-dubai-app
[31] Accessed April 26th 2023, https://newsroom.ferrovial.com/en/news/ferrovial-aecom-agreement/
[32] Accessed April 26th 2023, https://www.businessnewsaustralia.com/articles/skyportz-partners-with-perth-s-electro-aero-to-power-plans-for-vertiport-network.html
[33] Accessed April 26th 2023, https://www.bayardsvertiports.com

Another advantage this study brought to light was the ability to alleviate traffic congestion in São Paulo. Although this case was specifically focused on São Paulo, it shows the potential of using the current helipad infrastructure to accommodate eVTOL traffic in combination with future vertiport networks. It should be noted that to be able to accommodate eVTOLs on any helipad, additional infrastructure must be built to allow for battery-swapping, fast-charging, or refueling the H_2 tanks, which will already be incorporated in any vertiport designs.

4.4. Market Share

The most relevant dates to look at, to assess market share, would be the end of the 2020s. This is when Aetheria can be projected to start being operational. Many sources were found that gave information about the projected market share. These have been summarized in Table 4.6.

Table 4.6: *Market Share Projections*

Market Share Projection Date	Market Share Projection Value ($B)
2027	20.72 [34]
2028	23.21 [35]
2028	24.1 [36]
2030	24.9 [37]
2030	30.8 [38]
2032	35.79 [39]

Table 4.7: *Market Shares per Region*

Region	Region Market Size [40]	Obtainable Market Share of Aetheria
North America	55%	4%
Pacific Asia	9%	2%
Europe	27%	8%
Rest of World	9%	2%

Based on these studies, the team can project that the market volume of eVTOLs will reach 28 billion dollars by 2030. After examining numerous sources, the team believes that Aetheria could obtain the market shares indicated in Table 4.7.

Europe would be the dominant market in which the team establishes itself, due to the smaller market size. eVTOLs are not as popular relative to North America, meaning there is less competition but, of course, is more difficult to sell. Having increased the range to be more accommodating of intercity travel between large cities, the team feels confident in a rough 8% market share in Europe. The North American market is very promising, yet is difficult to succeed in. However, the team believes that due to the long-range capabilities of Aetheria, it has quite a good chance of establishing itself, especially on the East Coast where many major cities are quite close together. The Pacific Asian market does not show promise in this context. Ehang is already present in this region, having had quite an impact, but their eVTOL has a range of 30 kilometres. This means that intracity travel could be dominated by them, but intercity travel could be very ready for Aetheria to step in. The rest of the world has been given value as well as the Middle East is known for displaying interest in advanced aerospace technologies.

[34] Accessed May 1st 2023, https://www.thebusinessresearchcompany.com/report/evtol-aircraft-global-market-report
[35] Accessed May 1st 2023, https://www.fortunebusinessinsights.com/evtol-aircraft-market-106298
[36] Accessed May 1st 2023, https://www.imarcgroup.com/evtol-aircraft-market
[37] Accessed May 1st 2023, https://www.linkedin.com/pulse/evtol-aircraft-market-size-trends-report-2023-2030-shraddha?trk=article-ssr-frontend-pulse_more-articles_related-content-card
[38] Accessed May 1st 2023, https://www.marketsandmarkets.com/Market-Reports/evtol-aircraft-market-28054110.html
[39] Accessed May 1st 2023, https://www.precedenceresearch.com/evtol-aircraft-market
[40] Accessed May 1st 2023, https://www.marketsandmarkets.com/Market-Reports/evtol-aircraft-market-28054110.html

Assuming that the average eVTOL costs 3 million euros as was assumed for us initially, there would be 10,000 eVTOLs by 2030, giving an insight into how many units would need to be produced by this date.

1. Europe: $10,000 \cdot 0.27 \cdot 0.07 = 189$
2. North America: $10,000 \cdot 0.55 \cdot 0.04 = 220$
3. Pacific Asia: $10,000 \cdot 0.09 \cdot 0.02 = 18$
4. Rest of the World: $10,000 \cdot 0.09 \cdot 0.02 = 18$

From this calculation, 445 units would need to be produced. This is a feasible amount as the cost per unit will decrease as unit production increases. The team would begin focusing on the European market as stated before, then focus on North America, and then the rest.

4.5. Proposed Business Case

To illustrate the use case of Aetheria, the route from London to Paris will be analyzed and compared to the current best sustainable solution for intercity travel, high-speed rail. More specifically, Deloitte and Morgan Stanley want to organize a real-life version in London of the "Winning in the Future of Health" online convention held in 2020 [41]. In order to do so, employees from Deloitte have to arrange the logistics together with employees from Morgan Stanley in London, therefore they will have to travel the route Paris-London multiple times in the coming weeks. Finally, the route for both rail and Aetheria will be divided into three phases: First Mile, In-Transit and Last Mile. It is important to note that this business case will be based on transporting 4 passengers adding up to a payload total of 510 [kg] for an operational lifetime of 15 years.

4.5.1. First Mile

An important factor in the first mile is the location of the vertiport. According to Kai et al., UAM networks are more efficient when using a few centralized vertiports as opposed to many scattered ones [13]. It is then assumed that La Dèfense would be one of these hotspots, this can be justified by the fact that La Dèfense is Europe's largest purpose-built business district [42]. Then a location, as well as the route from Deloitte was chosen using Google Earth as shown in Figure 4.3. The location of the water was chosen for multiple reasons; the amount of people bothered by take-off and landings is minimized and the water offers energy absorption to a certain impact speed. The travel time and amount of interchanges for the first mile using Aetheria can be found in Table 4.8. Regarding rail the first-mile route can simply be taken from google maps, the amount of travel time and interchanges can be found in the summary Table 4.8.

[41] Accessed May 9th 2023, https://www2.deloitte.com/cn/en/pages/life-sciences-and-healthcare/events/wuxi-healthcare-forum.html

[42] Accesed May 10th 2023, https://www.ville-courbevoie.fr/1469/la-defense-le-1er-quartier-d-affaire-europeen.htm

Figure 4.3: *The route from Deloitte to the vertiport includes an indication of where the vertiport would be situated. Where the "V" indicates the vertiport location.*

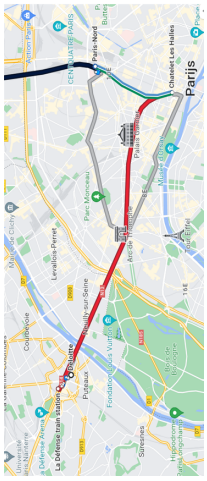

Figure 4.4: *The route required to travel from Deloitte to station Paris Nord where the Eurostar will leave from. Note figure is rotated by 90 degrees.*

Figure 4.5: *The In-Transit flight and route of the Aetheria and Eurostar, respectively*

4.5.2. In-Transit

The In-Transit phase for Aetheria and Eurostar are both visualized in Figure 4.5, as can be seen, Aetheria holds a significant advantage due to the fact that it can fly the Euclidean distance instead of being constrained by existing rail infrastructure such as the Eurostar. This results in the fact that the journey for Aetheria is twice as fast as compared to Eurostar. This is aided by the competitive cruise speed of 300 [km/h] of Aetheria as described in Subsection 4.2.1. The exact travel times can be seen in Table 4.9 and Table 4.8.

4.5.3. Last Mile

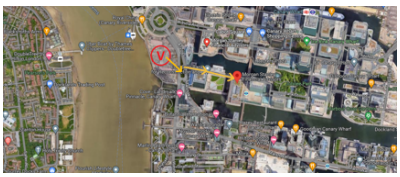

Figure 4.6: *The route from the vertiport in London to the office of Morgan Stanley includes an indication of where the vertiport would be situated. Where the "V" indicates the vertiport location.*

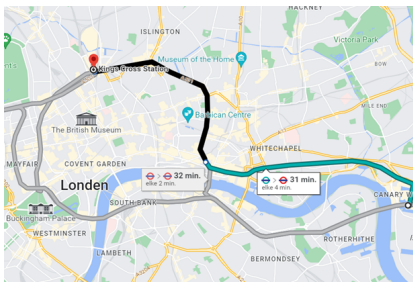

Figure 4.7: *The route required to travel from King's Cross station to the office of Morgan Stanley using public transit.*

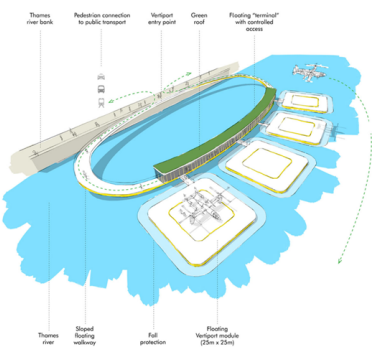

Figure 4.8: *Pascall+Watson's architect's concept ideas of a floating vertiport in the Waterloo area in London*

The last-mile concerns the trip from the arrival station of the in-transit phase to Morgan Stanley's office. To fulfil this trip, a vertiport location must be decided upon for Aetheria to land on. Similar reasoning as in Subsection 4.5.1 was utilized, and a location near Canary Wharf was chosen, as shown in Figure 4.6, indicated by the large V. Again, a location along the water was chosen. Concepts of this already exist, as seen in Figure 4.8. This concept was the result of a vertiport design

[42] Accessed on 11th May 2023 https://www.pascalls.co.uk/news/article/vertiport-design-competition/

competition by Pascall+Watson's architects. The vertiport allows for quick access to Canary Wharf compared to the last mile of the rail option, which requires two interchanges. The results of the last mile trip can be seen in Table 4.8 and Table 4.9.

4.5.4. Conclusion

The full journey has now been described for both the rail and Aetheria options. Aetheria is significantly faster due to the usage of the Euclidean distance but also the availability of landing at key hotspots comes to aid. This is because the Eurostar only arrives at the central station while the UAM is free in choosing its vertiport. So regardless of the location of interest, the Aetheria is statistically more likely to land closer to that location, therefore, decreasing the first and last-mile travel time.

However, an important factor that has not been taken into account yet is the customs control for boarding the VTOL in Paris. Feldhoff estimated the processing times based on the number of check-in counters and the category of the vehicle; Intracity, medium range or intercity. From the results, the most conservative estimation was used such that a contingency is already applied.

Table 4.8: *Summary of the trip from La Dèfense to Canary Wharf London using Aetheria*

Phase	Duration	Interchanges
First Mile	11 min	2
Customs Penalty	30 min	0
In-Transit	1h 10 min	0
Last Mile	5 min	0
Total	1h 56 min	4

Table 4.9: *Summary of the trip from La Dèfense to Canary Wharf London using Highspeed rail*

Phase	Duration	Interchanges
First Mile	23 min	3
In-Transit	2h 20 min	0
Last Mile	32 min	2
Total	3h 15 min	7

Taking the expected cost per passenger mile stated in Section 4.3 for eVTOLs, the price for a one-way trip from London to Paris (343 [km][43]) will range between €480 - €640 (calculated using Subsection 4.3.1) and will last approximately 1h to 1h15min. These prices do not really compete with the standard fares for the Eurostar, however, business seat tickets for the Eurostar trip cost €316,25 per trip. Although this is still cheaper than the eVTOL fare, one can now weigh the benefits of reduced travel time and exclusiveness against the slightly higher cost. Considering that the expected customers at first will most-likely be high-end businessmen looking for a swift commute, eVTOLs will probably be a highly appealing alternative travel option.

To conclude, Aetheria can compete with the market by addressing a majority of the largest barriers in public transit [10], which are the amount of interchanges, travel time and service frequency. Aetheria addresses the amount of interchanges by serving closer to your destination, travel time is reduced by a high cruise speed and a straight flight path and service frequency is addressed by offering on-demand service and a reasonable price range. Finally, Kai et al. concluded that UAM is most competitive on long-distance markets, therefore providing a more natural alternative to commuter rail and self-driving, further strengthening Aetheria's market position.

[43] Accessed May 1st 2023, https://nl.distance.to/Londen/Parijs

5

Technical Risk Management

As the project has stepped into the final design stage, new risks are introduced which have to be mitigated. These risks are identified by the design team of the different departments by using engineering judgement. This will again be done by identifying them, creating a risk map, and performing a mitigation analysis.

Below is a list of all the previous risks, which have already been identified and mitigated in the baseline and midterm reports so they will not be included in this report [1]. These risks are divided into their corresponding departments such as PP for power and propulsion, CS for control and stability, ST for structures and AD for aerodynamics. Furthermore, risks associated with operations (OP) of the eVTOL as well as during the development (DV) stage of the eVTOL are also divided. They will be shown in the risk map in Figure 5.1.

- TR-ST-01 - Underestimating the OEM weight.
- TR-ST-02 - Underestimating the loading of the wing and vtail.
- TR-ST-03 - Choosing an inadequate material
- TR-ST-04 - Over-designing the aircraft such that it becomes too heavy
- TR-ST-05 - Structural failure of wing-box
- TR-ST-06 - Structural failure of the fuselage
- TR-ST-07 - Corrosion damage of crucial design parts affecting flight performance and eVTOL structure
- TR-ST-08 - Delamination of composite parts
- TR-ST-09 - Failure of the landing gear
- TR-PP-01 - Underestimating the energy required during the transition phase.
- TR-PP-02 - Propulsive failure due to engine failure
- TR-PP-03 - Hydrogen fuel storage safety
- TR-PP-04 - Loss of hover abilities during flight because of transition failure
- TR-PP-05 - Overheating of the fuel cell
- TR-PP-06 - Loss of power
- TR-PP-07 - Not meeting hydrogen storage requirement in terms of volumetric space
- TR-PP-08 - Running out of hydrogen and energy during flight
- TR-PP-09 - Explosion of Hydrogen due to battery failure
- TR-PP-10 - Hydrogen boil-off loss underestimated
- TR-PP-11 - Leakage of ions from fuel cell through coolant liquid
- TR-PP-12 - Hydrogen fuel loading error
- TR-PP-13 - Corrosion of the fuel cell
- TR-PP-14 - Seal or joint failure of the hydrogen tank
- TR-PP-15 - Failure of the electrolyte in the fuel cell
- TR-PP-16 - Lithium-ion battery catches fire
- TR-PP-17 - Propeller blade breaking
- TR-PP-18 - Engines using more power than estimated
- TR-CS-01 - Center of gravity shift outside the acceptable region during flight

- TR-CS-02 - Aircraft too difficult to control
- TR-CS-03 - Operational cg range outside longitudinal stability & control and one engine inoperative hover limits
- TR-CS-04 - Aircraft maximum available power does not meet one engine inoperative hover power needs
- TR-AD-01 - Underestimating drag
- TR-AD-02 - Overestimating Lift
- TR-AD-03 - Using an inaccurate CFD method for validation
- TR-OP-01 - Damages during ground operations
- TR-OP-02 - Failing to meet noise requirements
- TR-OP-03 - Bird strike
- TR-OP-04 - Harder landing than structurally designed for
- TR-OP-05 - Hydrogen not being available at each vertiport
- TR-OP-06 - Operating cost too high
- TR-OP-07 - No available pilot
- TR-DV-01 - Numerical/model errors
- TR-DV-02 - Assumption is not accurate and/or correct
- TR-DV-03 - Underestimating power requirements during the transition phase
- TR-DV-04 - Inadequate market position establishment
- TR-DV-05 - Underestimating the development cost
- TR-DV-06 - Failure of certification
- TR-DV-07 - Aircraft is too expensive to develop

5.1. Additional Risks

Additionally, newly-found risks that the team discovered during the current design stage must be taken into account and effectively managed. The likelihood and consequence of these risks is given a value in a scale of 1 to 5. This information is used to quantify risk, which is calculated as likelihood times consequence. Using the same coding as the risks mentioned above, these risks are sorted into the respective departments.

TR-ST-10: Model is inaccurately verified
If the model is verified in an improper way this can lead to wrong results, from which an undersizing of the structure can be made resulting in a catastrophic accident.

TR-ST-11:The modal shape of the vibration between the V-tail and main wing has a prominent eigenfrequency
If a strong coupling exists between the V tail and wing structure, aerodynamics loads beyond the structural limit could occur leading to catastrophic failure. It should hence be verified this mode is not present.

TR-ST-12: The assumed value of the crashed diameter coefficient is too low to create a crashworthy design
Due to the lack of time and current resources, the crashed diameter coefficient could not be computed hence a value was assumed and the fuselage sized for that value. If later in production it turns out this value can not be met, the fuselage size would have to increase.

TR-ST-13:The firewall failing in a crash event and exposing the passengers to dangerous fumes and heat
The firewall will protect the passengers from any fires occurring in the rear of the fuselage where the hydrogen system is present. If during a crash event the firewall crumples and fails to fully seal the

cabin space, deadly fumes and flames could penetrate it.

TR-PP-19: Undersizing the cooling system
If the cooling system is undersized for the batteries, then the consequences due to this are the same reasons as the ones mentioned in TR-PP-20. If the cooling system is undersized for the fuel cell then, the fuel cell would overheat resulting in a higher degradation rate of the fuel cell. Furthermore, the fuel cell can experience thermal runaway and mechanical failure which can decrease the power generation significantly. This can reduce the power available for the eVTOL which can be catastrophic if it is below than required.

TR-PP-20: RPM set for hover and cruise is different from what is required. If it turns out that the rpm that is set for cruise and hover is too high, or too low, that could mean that the forces are not balanced and an acceleration or deceleration would take place.

TR-CS-05: Encountering higher external loads than designed for in vertical flight mode
When higher external loads than designed are applied during vertical flight, the stability and control of the aircraft is limited and may impede the desired performance.

TR-CS-06: Control surface is stuck during operation
If a control surface is stuck, the horizontal stability and control are affected, and the controllability space is reduced.

TR-CS-07: Stability augmentation system does not operate as intended
The SAS could not operate as intended, putting at risk the integrity of the aircraft and the safety of the passengers.

TR-AD-04: Choosing an airfoil with a thickness-to-chord ratio that is not suitable for eVTOLs
This may result in the airfoil being too slender for the wing box to fit in. Since the aircraft is an eVTOL, different loads may be present on the wing causing an increased wing box size.

TR-AD-05: Lack of validation due to lack of resources (i.e. wind tunnel testing)
A lack of resources limits the amount of validation that can be performed therefore causing uncertainty.

TR-OP-08: Tilt-rotor mechanism gets stuck
If this was to happen, then the transition from vertical to horizontal or vice versa would not happen, thus either cruising or vertical landing could not be executed. This would result in either an emergency landing in a gliding mode or, the eVTOL would have to land back right away after take-off if it can not transition to cruising. In both cases, the mission would be unsuccessful.

TR-OP-09: Inaccurate model used for transition phase
This may result in the transition phase being underestimated, therefore, the batteries and fuel cells might be undersized resulting in an unsuccessful transition due to lack of power.

TR-DV-08: Unsuccessful tests during the testing phase
If the eVTOL does not pass the tests performed during the testing phase such as structural, flight or system tests, then the design has to be changed and re-iterated. This will result in a delayed schedule.

Following the addition of these new risks per department seen in Table 5.1, the risk map from the Midterm report [1], can be updated. The new version of the risk map, prior to any mitigation can be seen in Figure 5.1.

Table 5.1: *Scoring per risk after risk mitigation*

Risk (TR)	ST10	ST-11	ST-12	ST-13	PP-19	PP-20	CS-05	CS-06
Likelihood	1	1	2	2	2	3	2	1
Consequence	5	5	4	5	4	1	4	4
Risk (TR)	**CS-07**	**AD-04**	**AD-05**	**OP-08**	**OP-09**	**DV-08**		
Likelihood	1	2	4	3	2	2		
Consequence	5	3	3	3	4	3		

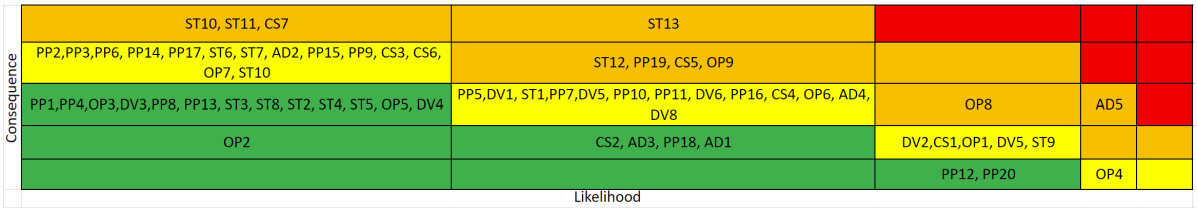

Figure 5.1: *Technical Risk matrix before mitigation*

5.2. Risk Prevention and Mitigation

For the risks visible in the orange and red sections of the risk map that corresponds to higher risk, a mitigation strategy will be applied in order to reduce these risks as much as possible. The prevention mitigation for these high risks can be seen below:

TR-ST-10: Model is inaccurately verified
Prevention measure: To prevent this, many different verification methods should be applied to verify the model accurately.
Contingency measure: A higher contingency factor can be applied, around 30% depending on how wrong the verification is. In addition, the model can also be validated.

TR-ST-11: The modal shape of the vibration between the V-tail and main wing has a prominent eigenfrequency
Prevention measure: A modal analysis can be performed to check and prevent this.
Contingency measure: If this was to take place, the stiffness of the wing-box and tail structures can be increased or decreased accordingly.

TR-ST-12: The assumed value of the crashed diameter coefficient is too low to create a crashworthy design
Prevention measure: To prevent this, a validation using crash testing can be performed to check for a more accurate value.
Contingency measure: The eVTOL should be re-designed with a higher crashed diameter coefficient.

TR-ST-13: The firewall failing in a crash event and exposing the passengers to dangerous fumes and heat
Prevention measure: Design a strong and hermetically sealed connection between the firewall and the cabin, so that if a crash takes place, the firewall will always be in between the fumes and the passengers thus preventing dangerous fumes from being exposed to passengers. **Contingency measure:** Have medical professionals on-site as fast as possible, and provide any means necessary to ensure the health and safety of the passengers. Furthermore, oxygen masks shall be deployed for the passengers to breathe preventing intake of dangerous fumes.

TR-PP-19: Undersizing the cooling system
Prevention measure: A higher safety factor can be applied to take into account possible higher heat generation than anticipated. In addition, a more accurate value for heat generation from the fuel cell and battery providers can be obtained to size the cooling system correctly.
Contingency measure: If this was to happen, it would be noticed during the flight testing period, therefore, the eVTOL cooling system can be redesigned to meet the higher thermal power prior to being commercialised.

TR-CS-05: Encountering higher external loads than designed for in vertical flight mode
Prevention measure: This can be avoided by weather conditions monitoring, and not landing or taking off during adverse weather conditions.
Contingency measure: If this was to happen, the eVTOL should transition back to horizontal flight mode to find another location for landing with better weather conditions.

TR-CS-07: Stability augmentation system does not operate as intended
Prevention measure: This can be avoided by thorough testing and certification.
Contingency measure: If this was to happen, all the eVTOLs should be grounded and the SAS should be re-designed.

TR-AD-05: Lack of validation due to lack of resources (i.e. wind tunnel testing)
Prevention measure: Input validation techniques can be used to check for dangerous inputs that can result in undesired outputs.
Contingency measure: Design the eVTOL with available resources and look for resources from possible sponsors.

TR-OP-08: Tilt-rotor mechanism gets stuck
Prevention measure: Perform regular checks on the tilt-rotor mechanism, to make sure it does not get stuck. It should be maintained regularly to prevent any wear. These inspection tests should be performed after every flight to ensure smooth operation of the mechanism
Contingency measure: If the rotor gets stuck during takeoff in vertical flight, land immediately. If it gets stuck during horizontal flight, land in a conventional horizontal manner.

TR-OP-09: Inaccurate model used for transition phase
Prevention measure: During the testing stage, prior to mass production, carefully monitor the compliance of the transition phase corresponding to the model.
Contingency measure: If the model for transition is inaccurate, re-design the model and perform adjustments so the model and reality match as much as possible.

Table 5.2: *Scoring per risk after risk mitigation*

Risk (TR)	ST10	ST-11	ST-12	ST-13	PP-19	CS-05	CS-07	AD-05	OP-08	OP-09
Likelihood	1	1	1	1	1	1	1	3	2	1
Consequence	4	4	4	3	3	3	4	2	3	4

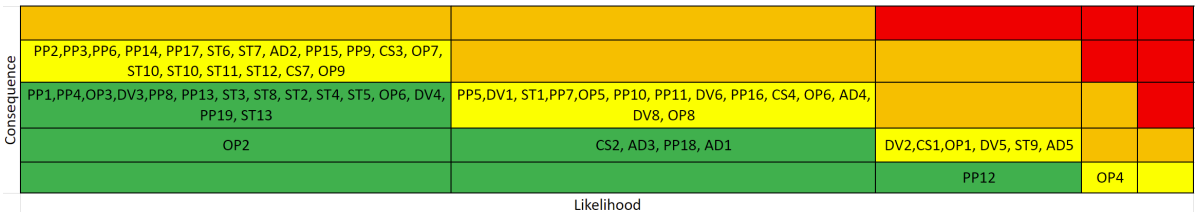

Figure 5.2: *Technical Risk matrix after mitigation*

6

Aerodynamics

This chapter explains the aerodynamic design choices for the Aetheria aircraft. First, an airfoil trade-off is performed in Section 6.1. Then, in autorefsec:wingplanform, the wing planform design is presented, followed by an analysis of the wing performance parameters presented in Section 6.3. The tail design is presented in the Control & Stability chapter (Chapter 8) because it is sized based on stability aspects. In Section 6.4, the propeller-wing interaction is described. Finally, the AVL method used for a wing loading diagram is discussed in Section 6.5 after which the chapter is concluded with a sensitivity analysis performed in Section 6.6.

6.1. Airfoil Selection

The initial phase of conducting a thorough aerodynamic analysis of the Aetheria design requires an airfoil analysis. The airfoils selected for the trade-off are explained below. A natural laminar flow (NLF) airfoil was considered a potential choice at first. However, due to the configuration of the propellers being positioned ahead of the wing, the laminarity of the flow is anticipated to be disrupted prior to reaching the leading edge. This is due to the presence of the propeller wake over the wing which has a high turbulence intensity. Hence, a NLF airfoil was not included in the trade-off.

NACA44017 The NACA44017 airfoil is the airfoil used in the Wigeon final design [15]. This airfoil will be included in the trade-off as it has also already been used in the trade-off of J1, L1 and W1 [1].

NACA2412 The NACA2412 airfoil is considered an option in the trade-off as it is used in small and lightweight aircraft, such as the Cessna 172.

NACA25112 A different type of airfoil included in the trade-off is the NACA25112. This is a reflex airfoil with very good C_L/C_D characteristics[1]. A reflex airfoil might also be useful as the $C_{m_{ac}}$ can be close to zero.

CLARK Y The CLARK Y is the final airfoil included in the trade-off. This is also a conventional airfoil.

The selection criteria for the trade-off are divided into three categories: C_L/C_D during cruise, stall characteristics and climb characteristics. The C_L/C_D during cruise is important as it greatly affects the mission energy. To accurately evaluate it, it is divided into three parameters. The first is C_d at $C_{l_{des}}$. This should be optimized to be as low as possible to optimize C_L/C_D. Furthermore, the C_l range at $C_{d_{min}}$ should be as close to $C_{l_{des}}$ as this would optimize the drag coefficient. This is combined with the third selection criterion, the drag bucket range, as both parameters indicate if and to what extent a change in C_l will affect the drag. The drag bucket range is taken as where the C_d is within 0.001 of the $C_{d_{min}}$. A large drag bucket is preferred, as a change in C_l will not have a huge effect on the C_d. The stall characteristics are important as the aircraft will transition close to stall speeds and to optimize time in vertical flight mode (as low as possible) the stall speed should be as low as possible. Next, the climb characteristics are evaluated by computing the $C_l^{1.5}/C_d$. The

[1] Accessed June 1st, http://airfoiltools.com/airfoil/details?airfoil=naca25112-jf

higher this is the better. This comes from the fact that one wants to minimize the power required which is equal to the drag multiplied by the velocity for optimum climb performance as shown in Equation 6.1. Finally, the thickness-to-chord ratio is taken as a parameter as it influences the structural weight of the airfoil.

$$(DV)_{min} = C_D \frac{1}{2}\rho V^3 S = C_D \frac{1}{2}\rho S \cdot \left(\frac{2W}{C_L \rho S}\right)^{1.5} = \left(\frac{C_D}{C_L^{1.5}}\right)_{min} W\sqrt{\frac{2W}{\rho S}} \tag{6.1}$$

The selection criteria are evaluated over a score of 1 to 5, in contrast to the trade-offs performed in previous reports[1]. The decision to increase the resolution of the scoring system was due to the small variations in the values of the parameters. A score of 5 indicates excellent performance gradually decreasing to a score of 1 indicating unacceptable performance. The values for the selected parameters can be found in Table 6.1 while the weights for the selection criteria and scores of the chosen airfoils are tabulated in Table 6.2.

Table 6.1: *Trade-off for the three chosen airfoils*

Selection criteria	**Reynolds no. [-]**	**NACA44017**	**NACA2412**	**NACA25112**	**CLARK Y**
C_d at $C_{l_{des}}$	7.00E+06	0.007	0.005	0.004	0.006
C_l range at $C_{d_{min}}$	7.00E+06	0.441-0.999	0.027-0.614	0.363-0.554	0.778-0.883
Drag bucket range	7.00E+06	1.40	1.27	0.486	1.17
$C_{l_{max}}$	3.00E+06	1.82	1.77	1.65	1
${C_l}^{1.5}/C_d$ (climb)	3.00E+06	24.1	24.8	25.9	2
(t/c)	-	0.17	0.12	0.12	2

Table 6.2: *Scores (out of five) for the different airfoils*

Selection criteria	**Weight [%]**	**NACA44017**	**NACA2412**	**NACA25112**	**CLARK Y**
C_d at $C_{l_{des}}$	50	2	4	5	3
C_l range at $C_{d_{min}}$ Drag bucket range	20	3	5	3	2
$C_{l_{max}}$	10	5	4	2	4
${C_l}^{1.5}/C_d$	10	3	4	5	3
(t/c)	10	5	4	4	4
Weighted average		**2.9**	**4.2**	**4.2**	**3.0**

To conclude the results performed in the trade-off, it can be seen that both the NACA2412 and NACA25112 show the biggest potentials. The NACA25112 receives a score of 2 for the $C_{l_{max}}$ criterion as the value for the $C_{l_{max}}$ would lead to a $C_{L_{max}}$ lower than the current value of 1.5. This would introduce the need for flaps on the wing, which is not uncommon but if a design can be created without the need for flaps this is favourable. Both the NACA44017 and CLARK Y airfoil suffer the most for the selection criteria related to cruise conditions, resulting in low final scores as the weight of these criteria are substantial. Considering the that reflex airfoils have a positive moment coefficent, these types of airfoils are used in tailless aircraft to ensure longitudinal stability. However, for an aircraft including a tail, it makes stability more difficult as the moments from the tail can be used to stabilize the aircraft. For this reason, it was decided that the NACA2412 is the best option for the airfoil of the final design, which is illustrated in Figure 6.1. In Figures 6.2 and 6.3, the airfoil performance graphs are illustrated for different performance parameters.

Figure 6.1: *NACA2412 airfoil*

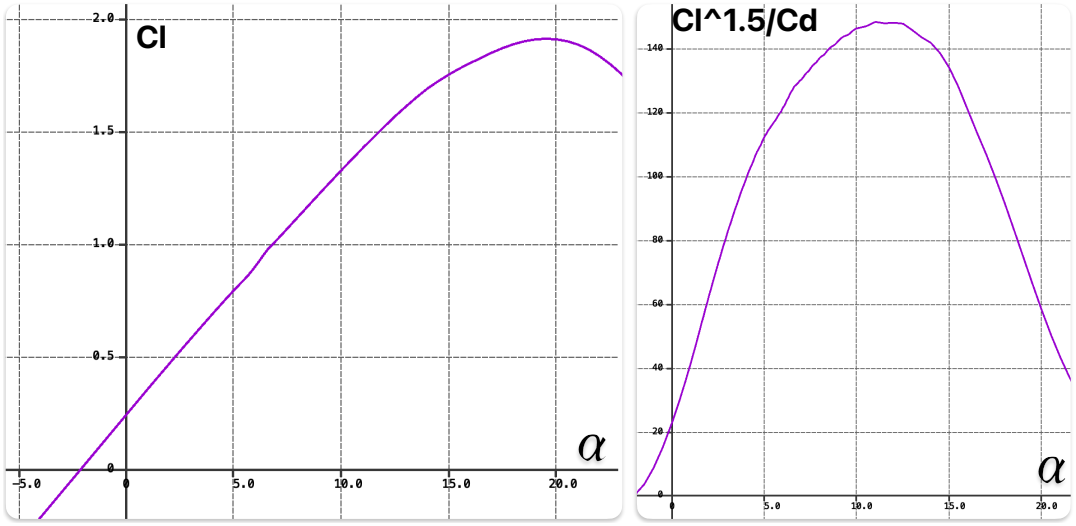

Figure 6.2: $C_l - \alpha$ *curve and* $C_l^{1.5}/C_d - \alpha$ *curve*

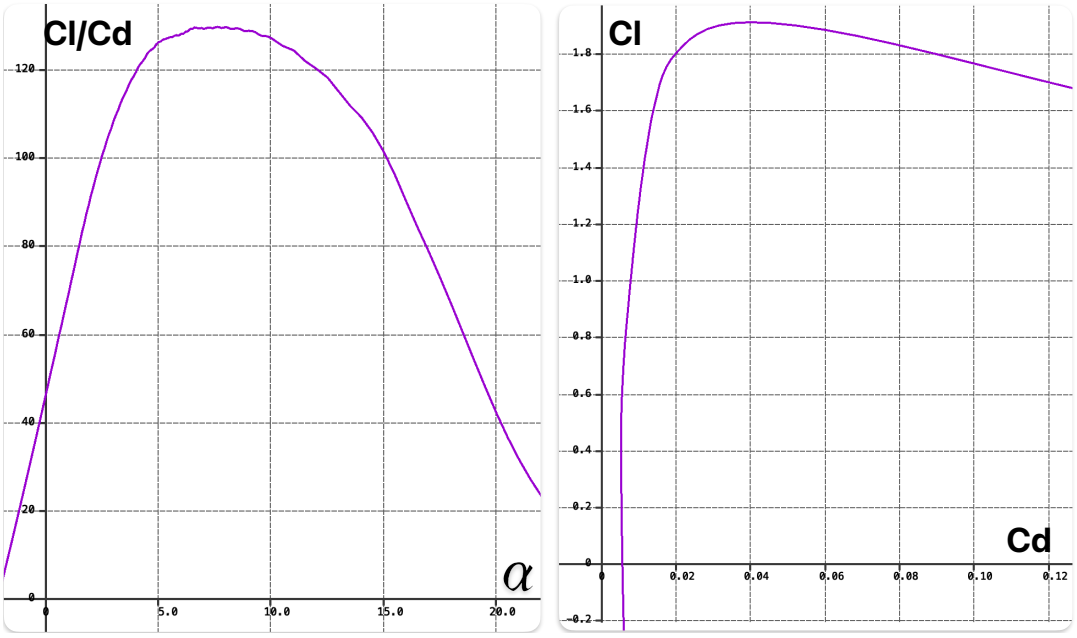

Figure 6.3: $C_l/C_d - \alpha$ *curve and* $C_l - C_d$ *- curve*

6.2. Wing Planform

In this section, the finalized wing planform is presented based on methods from Raymer [16], as well as methods described in the first and second year ADSEE courses of the Aerospace Engineering Bachelor [17, 18]. As the tail of the aircraft is a stabilizing surface, the sizing of it is done in Chapter 8 as this chapter discusses the control and stability of the aircraft.

Aspect ratio and surface area The aspect ratio AR is found through the optimization code performed towards the end of the project. The final optimized AR determined the weight and was optimized to have the lowest mission energy. Then, from the wing loading W/S and the converged MTOM, a wing surface area S was found.

Dimensions For the dimensions of the wing such as the span b, root and tip chord, basic formulas of [17] are used, based on optimal values for the taper ratio λ (0.4) and sweep angle Λ (0 deg at quarterchord)[17]. These parameters are calculated using Equations 6.2, 6.3 and 6.4.

$$b = \sqrt{S \cdot AR} \qquad (6.2) \qquad c_r = \frac{2S}{(1+\lambda)\cdot b} \qquad (6.3) \qquad c_t = \lambda c_r \qquad (6.4)$$

Oswald efficiency factor The Oswald efficiency factor e is calculated with Equation 6.5, which was obtained from [19].

Leading edge sweep The leading edge sweep angle Λ_{LE} is calculated using Equation 6.6 [1]. A summary of the final values for the wing planform is tabulated in Table 6.3.

$$e = 1.78 \cdot (1 - 0.045 \cdot AR^{0.68}) - 0.64 \qquad (6.5) \qquad \tan\Lambda_{LE} = \tan\Lambda_{x/c} + \frac{x}{c}\frac{c_r}{b}(1-\lambda) \qquad (6.6)$$

Table 6.3: *Wing planform parameters*

Parameter	Value
AR [-]	6.74
S [m^2]	13.1
b [m]	9.40
c_r [m]	1.99
c_t [m]	0.797
e [-]	0.847
Λ_{LE} [deg]	2.92

6.3. Wing Performance Parameters

In this section, the aerodynamic performance parameters will be analyzed and evaluated. As the results of these analyses can greatly influence the mission energy and therefore the sizing of other subsystems, accurate and valid methods are essential in acquiring reliable results.

6.3.1. Lift

Following the sensitivity analysis performed in Section 7.4, an optimum cruise altitude of 2400 [m] was found. This influences the design lift coefficient as the density decreases. For 2400 [m], a density of 0.967 [kg/m^3] can be obtained from the International Standard Atmosphere (ISA) model[2]. Maintaining the same wing loading and cruise velocity, a new $C_{L_{des}}$ of 0.56 was found. This is still within the drag bucket of the NACA2412 airfoil, meaning a higher C_L/C_D can be obtained as the C_d remains the same.

To continue, the same methods described in [1] to determine the values for $C_{L_{max}}$ and C_{L_α} are used. For other performance parameters such as the trim angle α_{trim}, stall angle α_{stall}, aerodynamic center moment coefficient $c_{m_{ac}}$ and the c_{m_α} the methods are explained below.

[2]Accessed June 5th, https://www.digitaldutch.com/atmoscalc/

Trim angle To calculate the trim angle, Equation 6.7 is used. The value for the zero-lift angle of attack is obtained from the XFLR5 software.

Stall angle For the stall angle, Equation 6.8 from Raymer's method as described in [16] can be used. Here, $\Delta C_{L_{max}}$ is a value that compensates for the non-linear segment of the lift curve near the stall angle for the high AR method and can be found to be 1.2 [deg]. This stall angle is taken for a clean configuration without flap deflection for which the $C_{L_{max}}$ is 1.59.

$$\alpha_{trim} = \frac{C_{L_{des}}}{C_{L_\alpha}} + \alpha_{L=0} \tag{6.7}$$

$$\alpha_{stall} = \frac{C_{L_{max}}}{C_{L_\alpha}} + \alpha_{L=0} + \Delta C_{L_{max}} \tag{6.8}$$

Moment coefficients To determine the moment coefficient about the aerodynamic center of the wing, the XFLR5 data for the wing is used. Then, using the XFLR5 data again from the c_m vs α curve, the slope was extrapolated to find c_{m_α}. The values of the final values are tabulated in Table 6.4.

Table 6.4: *Wing performance parameter values*

Parameter	Value
$C_{L_{des}}$ [-]	0.560
$C_{L_{max,clean}}$ [-]	1.59
C_{L_α} [deg^{-1}]	0.0853
$\alpha_{L=0}$ [deg]	-2.02
α_{trim} [deg]	4.16
α_{stall} [deg]	17.8
$c_{m_{ac}}$ [-]	-0.107
c_{m_α} [deg^{-1}]	-0.0279

In [1], it was assumed the main wing provided all the lift. However, since a V-tail has been designed in Chapter 8, the lift generated by this aerodynamic surface must also be taken into account. As the lift forces of the V-tail are not directed vertically upwards due to the large dihedral angle, the horizontally projected area is considered the reference surface area from which the produced lift can be determined. The lift and drag generated by V-tail as well as the propellers will be added to the lift of the wing and total drag yielding a final C_L/C_D. From Chapter 8, the methods of determining the lift coefficient of the V-tail are laid out in more detail. Moreover, the extra generated lift from the propellers is analyzed further in Section 6.4.

6.3.2. Drag

Determining the total drag for the aircraft is essential in optimizing its performance. Continuing upon the work done in [1], a more accurate drag estimation can be obtained. Similar as for the total lift, the influence of the tail on the total drag was not taken into account in [1]. The $C_{D_{tail}}$ can be found similar to $C_{D_{wing}}$ using the methods laid out in [1]. The drag estimation method used is the component drag method. The method consists of summing the parasite drag with the induced drag. The parasite and induced drag coefficients are defined by Equation 6.10 and Equation 6.9, respectively.

$$C_{D_i} = \frac{C_L^2}{\pi ARe} \tag{6.9}$$

$$C_{D_0} = \frac{1}{S_{ref}} \sum C_{f_e} \cdot FF_c \cdot IF_c \cdot S_{wet_c} + C_{D_{misc}} \tag{6.10}$$

Here, S_{ref} is the reference wing area, which is the same as the total wing area [1]. C_{f_e} is the flat plate skin friction coefficient, which depends on the flow. For turbulent flow, the C_{f_e} can be calculated using Equation 6.3.2 while for laminar flow Equation 6.3.2 holds. The assumption is done so that 5% of the flow around the fuselage is laminar, and 95% is turbulent [18]. Around the wing and tail

10% is laminar, 90% is turbulent. The effect of propellers on the flow has been neglected in the drag estimation. Using a Reynolds number of $4.5{\cdot}10^6$ for the calculations (cruise conditions), the values of C_{f_e} and $C_{f_{fus}}$ are $6.26{\cdot}10^{-4}$ and $3.40{\cdot}10^{-3}$ respectively.

$$C_{f_{turb}} = \frac{1.328}{\sqrt{Re}} \tag{6.11}$$

$$C_{f_{lam}} = \frac{0.455}{(\log_{10} Re)^{2.58}(1+0.144M^2)^{0.65}} \tag{6.12}$$

The form factor (FF) takes into account the form of the wing, tail and fuselage. t/c is the average thickness to chord ratio, $(x/c)_m$ is the position of maximum thickness, (l/d) is the slenderness ratio, Λ_m is the sweep angle at the position of the maximum thickness ($0.30c$ for NACA 2412 and NACA 0012) and M is the Mach number. The form factor of the wing and fuselage can be found in Equation 6.13 and Equation 6.14, respectively. The tail form factor is calculated using Equation 6.13 but using a different position of maximum thickness.

$$FF_w = \left(1 + \frac{0.6}{(x/c)_m}\left(\frac{t}{c}\right) + 100\left(\frac{t}{c}\right)^4\right)\cdot\left(1.34M^{0.18}\cos\Lambda_m{}^{0.28}\right) \tag{6.13}$$

$$FF_{fus} = 1 + \frac{60}{(l/d)^3} + \frac{l/d}{400} \tag{6.14}$$

Furthermore, IF is the interference factor, of which values range from 1.0 and 1.5. The S_{wet} is the wetted area of the aircraft, and $C_{D_{misc}}$ is the drag of other components, such as landing gear and fuselage upsweep [19]. The wetted area of the fuselage can be calculated using Equation 6.15. L1 is the length of the parabolic section, L2 is the length of the cylindrical section and L3 is the length of the conical section.

$$S_{wet_f} = \frac{\pi D}{4}\left(\frac{1}{3L_1^2}\left[\left(4L_1^2 + \frac{D^2}{4}\right)^{1.5} - \frac{D^3}{8}\right] - D + 4L_2 + 2\sqrt{L_3^2 + \frac{D^2}{4}}\right) \tag{6.15}$$

For $C_{D_{misc}}$ the upsweep drag was taken as the only component since the aircraft's gears fold in during cruise and the aircraft does not have a base area at the tail thus there is no base drag.

An overview of all the component drag coefficients is presented in Table 6.5.

Table 6.5: *Component drag coefficients*

Component	Value
Λ_m [deg]	-0.255
$C_{D_{upsweep}}$ [-]	0.00402
C_{D_0} [-]	0.0205
C_{D_i} [-]	0.0155
C_D [-]	0.0361
$(C_L/C_D)_{max}$[-]	18.3

6.3.3. High-Lift Devices

Following the analysis for the transition phases from horizontal to vertical flight and vice versa, it became clear that a stall speed of 45 [m/s] was too high to ensure a safe transition . Hence, high-lift devices (HLDs) must be designed to increase the $C_{L_{max}}$ and reduce the stall speed. Moreover, in the case of an emergency landing, it would be beneficial to reduce the stall speed as much as possible for a short landing. For a stall speed of 40 [m/s], the transition was feasible in terms of

thrust required, meaning a reduction of 5 [m/s] for the stall speed (45 to 40 [m/s]) is required. This can be accomplished by introducing high-lift devices such as trailing edge (TE) flaps or leading edge (LE) slats in the wing. For now, only TE HLDs are considered as the required reduction in stall speed is not as significant. For the same reason, plain flaps shall be implemented as these offer sufficient performance increases against the lightest mechanical structure for different types of flaps.

To lower the stall speed to 40 [m/s], $C_{L_{max}}$ must increase from 1.59 to 2.01, as the stall speed is inversely proportional to the root of $C_{L_{max}}$. Subsequently, knowing the $\Delta C_{L_{max}}$ is 0.42, Raymer's methods for designing HLDs can be used to find the required flap planform and type [16]. Following the targeted $\Delta C_{L_{max}}$, the next step is to choose a HLD type and choose the chord fraction of the flap c_f/c. For now, a plain flap with a c_f/c of 0.25 is chosen to keep the required structural weight as low as possible while still providing sufficient additional lift. Then, using Equation 6.16, values for $\Delta C_{l_{max}}$ and the sweep angle at the hinge line of the flaps $\Lambda_{0.75c}$ must be computed. $\Delta C_{l_{max}}$ follows from Raymer's methods and is 0.9 for plain flaps fully deployed at 60°. From Equation 6.6, a value of -7.45°can be obtained for $\Lambda_{0.75c}$. Finally, the ratio of the flapped wing surface area to the total wing area S_{wf}/S is 0.51, where the flapped wing surface area is the spanwise portion of the wing surface area. The wing planform including the flaps is shown in Figure 6.4 and the new performance parameters following the same methods as in Section 6.3 are presented in Table 6.6.

$$\Delta C_{L_{max}} = 0.92 \Delta C_{l_{max}} \frac{S_{wf}}{S} \cos \Lambda_{0.75c} \tag{6.16}$$

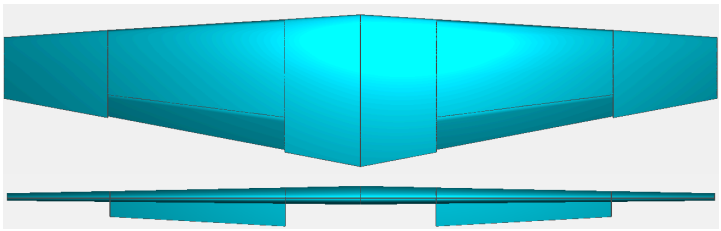

Figure 6.4: *Top and front view of wing planform including flaps*

Table 6.6: *Wing performance parameter values with 60 [deg] flap deflection*

Parameter	Value
$C_{L_{max,flaps}}$ [-]	2.01
α_{stall} [deg]	7.58

6.4. Propeller-Wing Interaction

The inclusion of propellers on the aircraft has significant effect on the lift and drag characteristics of the Aetheria. The increasing downwash and propeller thrust change the lift of the wing. The model of the propeller effect is based on the method of Bouquet et al. [20]. The method consists of the summation of the lift coefficient of the wing including slipstream effects, the lift due to the propeller normal force and a thrust component perpendicular to the free-stream direction. The thrust component is calculated using Equation 6.17.

$$C_{L_T} = C_T \cdot \sin \alpha \quad \text{with} \quad C_T = \frac{T}{\frac{1}{2}\rho V^2 S} \tag{6.17}$$

The normal force component is neglected [15] as is the swirl-effect generated by the angular momentum of the in-board propellers. The rotational velocity of the outboard propellers is taken into account in Subsection 6.4.1. The lift due to the propeller slipstream is found by incorporating the lifting line theory. It assumes the flow over the wing can be assumed a stream tube with a diameter equal to the span of the wing. The lift is then found by investigating the momentum resulting from the downwash (Equation 6.18). The effective area the propeller interacts with in the stream tube is

then subtracted from the total area. For the propeller slipstream a different equation is used, which incorporates the extra velocity generated by the propeller (Equation 6.19).

$$L_W = \rho \frac{\pi}{4} b_W^2 V_0^2 \sin\epsilon \tag{6.18}$$

$$L_S = n_e \rho \frac{\pi}{4} D^{*^2} (V_0 + \Delta V)^2 \sin\epsilon_S \tag{6.19}$$

The slipstream lift $C_{L_{W+S}}$ is then calculated using Equation 6.20[20].

$$C_{L_{W+S}} = \frac{2}{S}(\frac{\pi}{4} b_W^2 - \frac{\pi}{4} D^{*^2}) \sin\epsilon + n_e \frac{\pi D^{*^2}}{2S} \frac{(V_0 + \Delta V)^2}{V_0^2} \sin\epsilon_S \tag{6.20}$$

Where n_e is the number of engines, which is 4 in this case since there are 4 engines on the wing. δ V is the induced velocity due to the propeller thrust (Equation 6.21). Furthermore, D^* is the contracted slipstream diameter [20], calculated using Equation 6.22.

$$\frac{\Delta V}{V_0} = \sqrt{1 + C_T \frac{S}{n_e \frac{\pi}{4} D^2}} - 1 \tag{6.21}$$

$$D^* = D \sqrt{\frac{V_0 + \Delta V/2}{V_0 + \Delta V}} \tag{6.22}$$

The final parameters needed to compute the $C_{L_{W+S}}$ are the $\sin\epsilon$ and $\sin\epsilon_S$. These relate to the downwash created by the wing and the wing section in the slipstream. The downwash created solely by the wing is computed using Equation 6.23, where C_{L_W} is the lift coefficient of the wing and A_W is the aspect ratio, both these parameters exclude the wing section effect by the propeller slipstream. Equation 6.24 is used to compute the slipstream downwash. $C_{L_{\alpha_{s,eff}}}$ is calculated using the DATCOM method [1], while $A_{s,eff}$, the effective aspect ratio of the slipstream section, is calculated using the thrust coefficient [20].

$$\sin\epsilon = \frac{2C_{L_W}}{\pi A_W} \tag{6.23}$$

$$\sin\epsilon_S = \frac{2C_{L_{\alpha_{s,eff}}}}{\pi A_{s,eff}} \sin\alpha_S \tag{6.24}$$

The angle of attack for the slipstream section is different than that of the wing section. A few parameters influence this, as can be seen in Equation 6.25. The change in flow direction due to the propeller angle α^* is calculated with the Aetheria's angle of attack [20]. The wing angle compared to the fuselage centerline i_{cs} is calculated at 4.9 degrees [21]. During cruise, the propeller angle of attack is the same as i_{cs} as the propellers are placed in line with the wings. The zero-lift angle and the change in lift due to the flap angle are both taken from XFLR5 [22].

$$\alpha_S = \alpha^* + i_{cs} - \alpha_0 - \Delta\alpha_{0,f} \tag{6.25}$$

The model can compute different C_L values depending on the input. The outputs for both cruise and stall conditions were investigated. The cruise condition is important since the C_L/C_D will change, leading to a different power requirement, and therefore different mission energy. Furthermore, the stall C_L relates to the minimum airspeed possible to fly at. This is important for the transition phase and in case of emergency landing. Below the total C_L can be found. The C_{L_W} is the lift coefficient of the wing section that is not affected/behind the propellers. The C_{L_s} is the lift coefficient of the wing section (spanwise) that is behind the propellers, thus is affected by it. Adding these two together gives the total C_L of the wing. Finally, the C_{L_T} can be calculated which it also taken into account in the C_{L_tot}.

Table 6.7: *Propeller slipstream effect in cruise flight conditions: V = 83.3 [m/s], ρ = 1.18 [kg/m^3], angle of attack = 4.9 [deg], i_{cs} = 4.9 [deg], flaps = 0 [deg]*

Parameters	Values
C_{L_W} (wing section)	0.465
C_{L_S} (propeller section)	0.220
C_{L_T}	0.003
$C_{L_{tot}}$	0.688
Old C_L	0.55
Percentage increase	25%

Table 6.8: *Propeller slipstream effect in stall flight conditions: V = 40 [m/s], ρ = 1.224 [kg/m^3], angle of attack = 12.2, i_{cs} = 4.9 [deg], flaps = 60 [deg]*

Parameters	Values
C_{L_W} (wing section)	1.73
C_{L_S} (propeller section)	0.65
C_{L_T}	0.10
$C_{L_{tot}}$	2.49
Old C_L	2.01
Percentage increase	24%

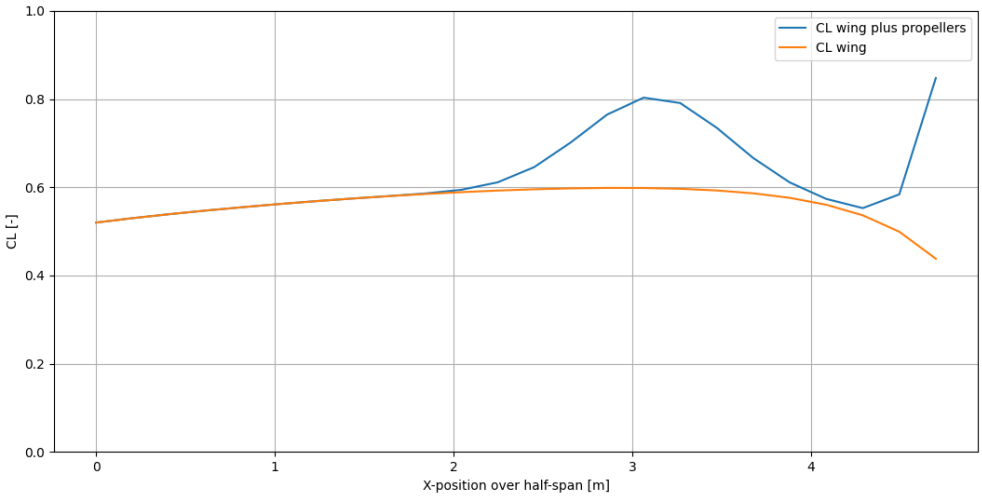

Figure 6.5: *Propeller Wing Interaction (Cruise)*

The results from the propeller wing interaction show a very significant increase in the lift coefficient due to the propeller interaction. This is mainly due to the increased C_L behind the propellers. The air is energized at these location giving it a higher velocity as it flows over the wing [20]. In Figure 6.5 the lift coefficient is displayed over the wingspan, starting at the fuselage (X=0). The peak at the wing tip comes from the fact that the propeller is located at the wing tip, as will be explained in the following section.

6.4.1. Wingtip-Mounted Propellers

These winglets increase the efficiency of the wing reducing the induced drag as the strength of the wingtip vortices are reduced. A study conducted by Sinnige et al. [23] shows great aerodynamic performance increases for wingtip-mounted propellers rotating inboard-up. Similar to winglets, the wingtip-mounted propellers can increase the sectional lift coefficient as well as reduce the induced drag due to the propellers rotating opposite to the direction of the wingtip vortices. Figure 6.6 nicely illustrates the increase in lift for different propeller advance ratios J. For $J = 0.7$, the greatest increase in lift and span efficiency factor were observed. Besides increasing the sectional lift coefficient and the span efficiency factor, the induced drag can be reduced up to 15%, and can be reduced even further for higher lift coefficients. The study also showed that for varying Reynolds numbers, the relative results were still similar. To be able to properly quantify the expected results for the

Aetheria design, windtunnel tests for the designed wing planform should be performed. However, comparing Figure 6.5 with Figure 6.6 shows quite some resemblance for the increase in sectional lift coefficient near the tip of the wing, giving some extra credibility to the method performed before.

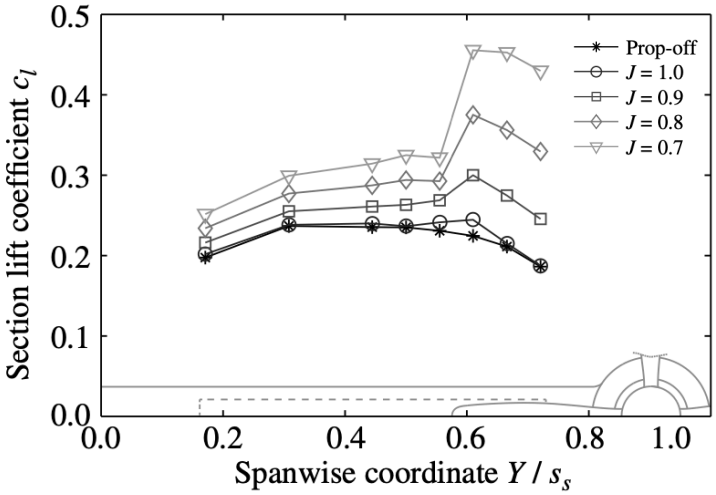

Figure 6.6: *Spanwise sectional lift coefficient with inboard-up rotating propeller [23]*

6.5. AVL

In addition to XFLR5, the software distribution Athena Vortex Lattice (AVL) by Mark Drela to retrieve the lift distribution was used. This decision was made as AVL has command line access and has readily available Python wrappers hence the lift distribution can be computed during runtime. This is of great importance to the structures department and the convergence of the aircraft as explained in Chapter 13. The run case was set up for cruise as required from the structures department. The model has three surfaces: the wing, V-tail and an elevator placed on the V-tail. The model is shown in Figure 6.7 and the run case is defined in Table 6.9.

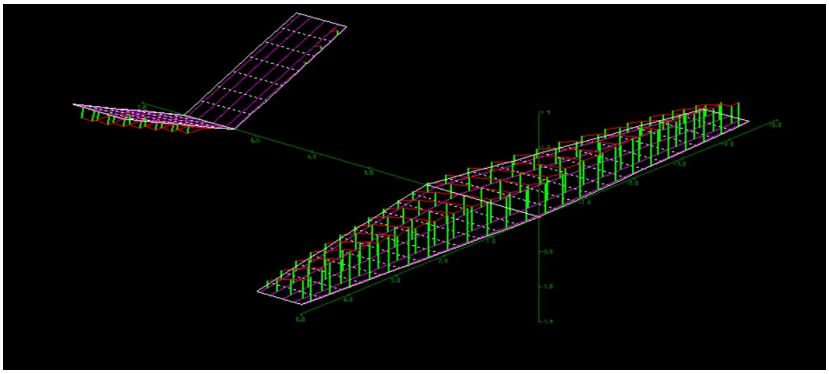

Figure 6.7: *The model of the final configuration in AVL including the loading on the lifting- and control surfaces.*

Table 6.9: *The run case used to define the lift distribution during cruise for the final configuration*

Constraints
$\alpha \rightarrow C_L = 0.56$
$\delta_e \rightarrow C_m = 0$
$V \rightarrow 83.3[ms^{-1}]$

6.6. Sensitivity Analysis

A sensitivity analysis of the propeller angle has been performed. As explained in Section 6.4, the wing trim angle is 4.16 degrees and the propellers are angled at the wing angle in cruise. Since this has not been investigated further, a sensitivity analysis should be performed to check whether this has a significant effect on the propeller interaction. In the analysis, the propellers (all 6) have been

angled from -6 [deg] to 10 [deg]. These angles are in correspondence to the fuselage, not the wing. Furthermore, different thrust coefficients (C_T) are plotted, to investigate their effect on C_L. The C_T is cruise conditions is 0.15 and in idle mode the propellers do not provide any thrust. In Figure 6.8 the results can be found, in regards to the total lift coefficient and thus the 6 propellers combined.

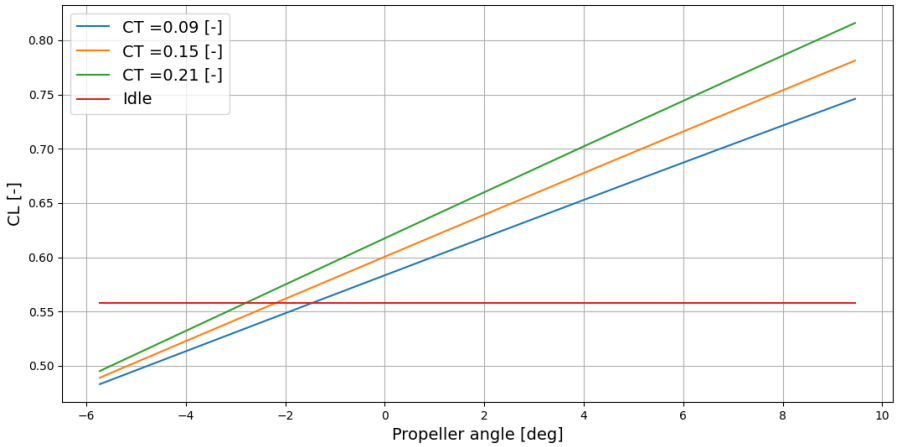

Figure 6.8: *Change in Lift Coefficient Due To Propeller Angle*

Figure 6.8 illustrates a clear correlation between the propeller angle and total lift coefficient, indicting that increasing the propeller angle causes a significant increase in the total lift coefficient. At the wing angle of 4.16 [deg] the lift coefficient at a C_T of 0.15 is indeed 0.70, matching previous research. What is remarkable is that at a negative angle of the propellers (until 2 [deg]) the propellers are still able to provide additional lift to the wing. This is due to the energy increase the propellers provide to the free-stream airflow [20].

7

Flight Performance

As was explained in the Midterm report [1], the most important aircraft performance parameter is the mission energy. An extended mission profile will be used to calculate the total mission energy. Furthermore, the transition from vertical to horizontal flight and from horizontal to vertical flight have been simulated such that their maximum power and total energy can be used for a more accurate estimation. Finally, the climb and cruise phases have been optimized to be as efficiently as possible while conforming to EASA regulations.

7.1. Mission Profile

When evaluating the flight performance of the Aetheria, the mission profile is required since it will determine the power and energy required for each mission.

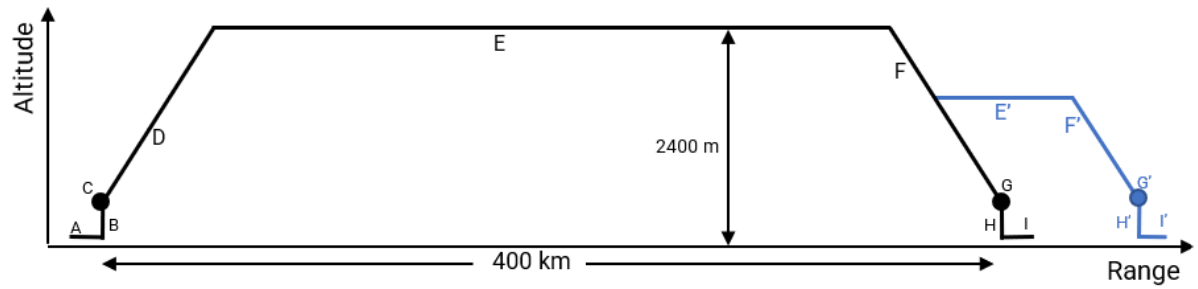

Figure 7.1: *Caption*

The mission profile seen in Figure 7.1 has been adapted from the one in the Midterm report [1]. The transitions are optimized as will be explained in the coming section.

A & I (I') - Taxi This represents the taxi segment. In this particular segment, the mission energy required is consider negligible due to its insignificant magnitude compared to the other segments.

B - Takeoff To Transition Altitude The takeoff segment of the mission should be as short as possible as the most efficient flight configuration is horizontal flight thus the transition should happen as soon as possible. From regulations set by EASA, a specified altitude 30.5 [m] (100 ft) was set for the minimum transition altitude [24]. Moreover, the rate of climb (ROC) is set at 2 [m/s] [1].

C - Transition To Horizontal Configuration The transition will happen after an altitude of 30.5 [m] is reached. In the next section (Section 7.2) the transition simulation is explained, including the results.

D - Climbing In segment D the Aetheria will climb to its cruising altitude of 2400 [m]. This has been optimized, as is explained in Subsection 7.2.2.

E - Cruise The cruise segment is the most essential segment to be optimized regarding mission energy. The mission energy is calculated using Equation 7.1, where the time in cruise is calculated by subtracting the distances in climb, descent and in the transition segments. The cruise speed is taken at 300 [km/h] to ensure the aircraft is competitive to high-speed rail [1].

$$E_{cr} = t_{cr} \cdot \frac{W V_{\infty}}{\eta_{cr}} \frac{C_D}{C_L} \tag{7.1}$$

F - Descent The descent segment occurs from an altitude of 2400 [m] till the transition altitude of approximately 100 [m]. The descent is optimized with a vertical rate of descent of 3 [m/s].

G (G') - Transition To Vertical Configuration The transition to vertical configuration will occur when the Aetheria aircraft descends to an altitude of approximately 100 [m]. The transition is further explained in Section 7.2.

H - Landing The landing of the Aetheria has been incorporated into the transition simulation. The rate of descent during landing is 2 [m/s] to conform to passenger comfort [1].

E' & F' - Horizontal Loiter Horizontal loitering time has been set to 20 [min]. This would occur during a holding procedure before landing. The altitude at which this may occur can differ from cruise altitude till the final descent altitude.

H' - Vertical Loiter In case the landing pad is not available for the aircraft to land on, a short loitering phase has been calculated into the mission segment. This phase is only 15 [sec] but should be enough for the landing pad to clear.

Segment	B Takeoff	C Transition	D Climbing	E Cruise	F Descent	G Transition	H Landing
Time [s]	15.3	45	466	3638	800	35	10

7.2. Transition Simulation

To accurately derive the power and energy needed in transition, a model has been set up for both the transition from hovering to climbing and from descent to landing (touch-down). The wing is kept at a constant angle of attack. For the hovering to climbing phase, this is at the optimal angle of attack for climb, while for the descent transition this is at the optimal descent angle. Therefore, the wing will start generating lift even at velocities below the stall speed. For both models the flight path angle γ is assumed to be zero when the aircraft is not yet airborne, i.e. the aircraft velocity is below the stall speed. Below, the two models are explained.

7.2.1. Hovering to Climb Simulation

The first transition model consists of the Aetheria aircraft when it has taken off vertically to an altitude of 30.5 [m] (EASA requirements [25]) till when the propellers have fully turned into the climbing configuration. This model is called the hovering-to-climb model. It is split up into three phases. The first phase is the hovering to transition phase, the second phase consists of the turning propellers and the third phase is when the aircraft has finished transition and the propellers are at the wing angle. The equations of motion (EOM) for this transition phase were determined based on the Free Body Diagram (FBD) presented in Figure 7.2. There are three EOM, namely the sum of forces in x-direction , y-direction and the moment equation (Equations 7.2, 7.3 and 7.4). The moment

equation was assumed to equal zero, meaning that the aircraft shall not experience any angular accelerations during transition. The feasibility of this assumption was checked by evaluating whether the maximum required thrust by a single propeller does not exceed the maximum available thrust per propeller. It is also assumed α_T is the same for all propellers. Moreover, the moments generated by the lift forces of the main wing and tail are assumed to cancel each other out from a longitudinal stability point of view (Section 8.3). These forces are not taken into account because of this, and due to the magnitude of the forces as well as the moment arm for the wing lift being small compared to moments generated from the thrust forces.

$$\Sigma F_x : (T_1 + T_2 + T_3)\cos\alpha_T - D = ma_x \tag{7.2}$$

$$\Sigma F_y : (T_1 + T_2 + T_3)\sin\alpha_T + L_{total} - W = ma_y \approx 0 \tag{7.3}$$

$$\Sigma M_{@c.g.} : T_1(-\sin\alpha_T \cdot x_1 + \cos\alpha_T \cdot y_1) + T_2(\sin\alpha_T \cdot x_2 + \cos\alpha_T \cdot y_2) + T_3(\sin\alpha_T \cdot x_3 + \cos\alpha_T \cdot y_3) = I\ddot{\theta} = 0 \tag{7.4}$$

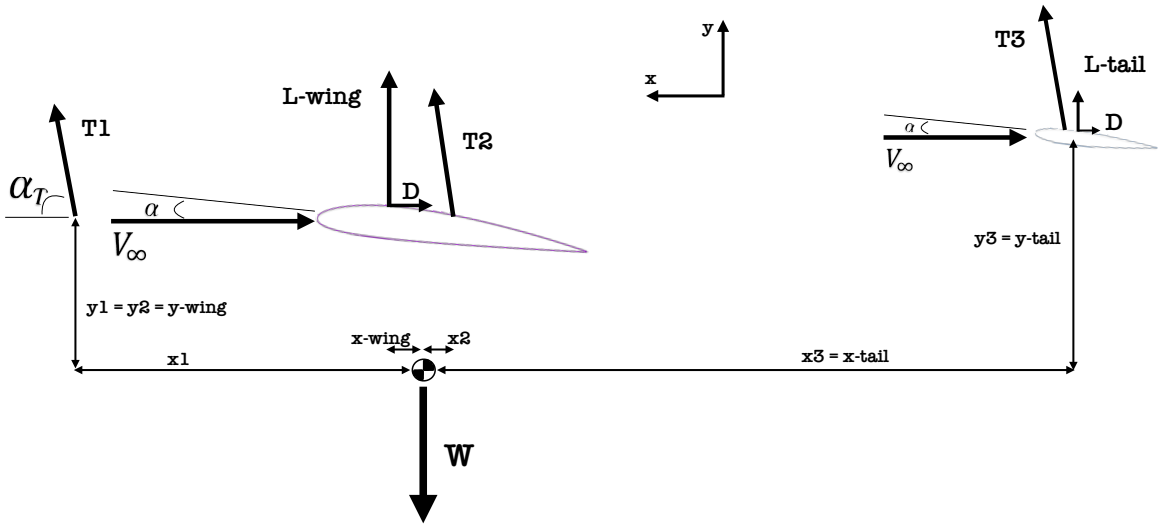

Figure 7.2: *Free Body Diagram for transition to climb*

Phase 1: Propeller angle: 90 [deg] At the start of phase 1, the aircraft has a rate of climb of 2 [m/s] and a x-velocity of zero. After reaching an altitude of 30.5 [m], the whole aircraft will tilt back about 0.8 [deg]. This is because the trim angle of the wings is 4.2 [deg] while the optimum climb angle is 5.0 [deg], calculated by finding at which angle C_L^3/C_D^2 is maximum (Subsection 7.2.2). After that the propellers will start tilting: Phase 2.

Phase 2: Propeller rotation After the wings are tilted for optimum climb angle, the propellers start tilting up. For this model the transition time for the propellers to be fully rotated from 90 [deg] to 4.2 [deg] is set at 30 [sec]. This is faster than current eVTOL transition times which are between 30 [sec] and 1 [min][26] [1]. The turning rate of the propellers is thus a constant variable, and the angle of the propellers is calculated using Equation 7.5.

$$\alpha_T = \frac{\pi}{2} - \frac{t}{t_{end}}\left(\frac{\pi}{2} - \alpha_{climb}\right) \text{ [in radians]} \tag{7.5}$$

[1] Accessed May 9th 2023, https://www.youtube.com/watch?v=cuJEf4v05Z0&t=31s

The final climb rate V_y follows from the climb velocity for the most efficient climb in horizontal configuration, as explained in [1]. A climb gradient of 0.125 is most efficient, thus the V_y should become this value after the Phase 2. The vertical acceleration can then also be computed using Equation 7.7, where V_{y_0} is the starting climbing rate, which is 2 [m/s].

$$V_{y_{end}} = 0.125 \cdot V_{climb} \tag{7.6}$$

$$a_y = \frac{V_{y_{end}} - V_{y_0}}{t_{end}} \tag{7.7}$$

The thrust can be calculated using Equation 7.8. Since the fuel mass is roughly 1% of the total mass, the mass is assumed to be the maximum take-off mass (and thus constant). This will slightly overestimate the thrust required. Using the calculated thrust, the horizontal acceleration can be found (Equation 7.9). As the thrust angle will become smaller, its contribution to the horizontal acceleration will increase, however, so will the lift and drag.

$$T = \frac{(mg_0 - L\cos\alpha_{climb} + ma_y)}{\sin\alpha_T} \tag{7.8}$$

$$a_x = \frac{T\cos\alpha_T - L\sin\alpha_{climb} - D}{m} \tag{7.9}$$

The power is calculated using Equation 7.10 and Equation 7.11, where P_h is the hover power and P_c is the climbing power. κ is an efficiency factor which is 1.2 [1]. The total power is then computed by using the angle of the propellers: At 90 [deg] the power is calculated using the hover power equation, while at 5 [deg], it is the climb power.

$$P_h = T\cdot ROC + \kappa T\left(-\frac{ROC}{2} + \sqrt{\frac{(ROC)^2}{4} + \frac{T}{2\rho A_{\text{disk}}}}\right) \tag{7.10}$$

$$P_c = mg_0 \cdot \left(ROC + \sqrt{\frac{W}{S}\frac{2}{\rho}}\left(\frac{C_D}{C_L^{3/2}}\right)_{opt}\right)\cdot\frac{1}{\eta_{prop}} \tag{7.11}$$

Phase 3: Climb configuration After the propellers have rotated fully to the wing angle, the velocity will be 70 [m/s]. The final phase is accelerating to the climb velocity, which is 77 [m/s].

The results of the simulation can be seen in Figure 7.3.

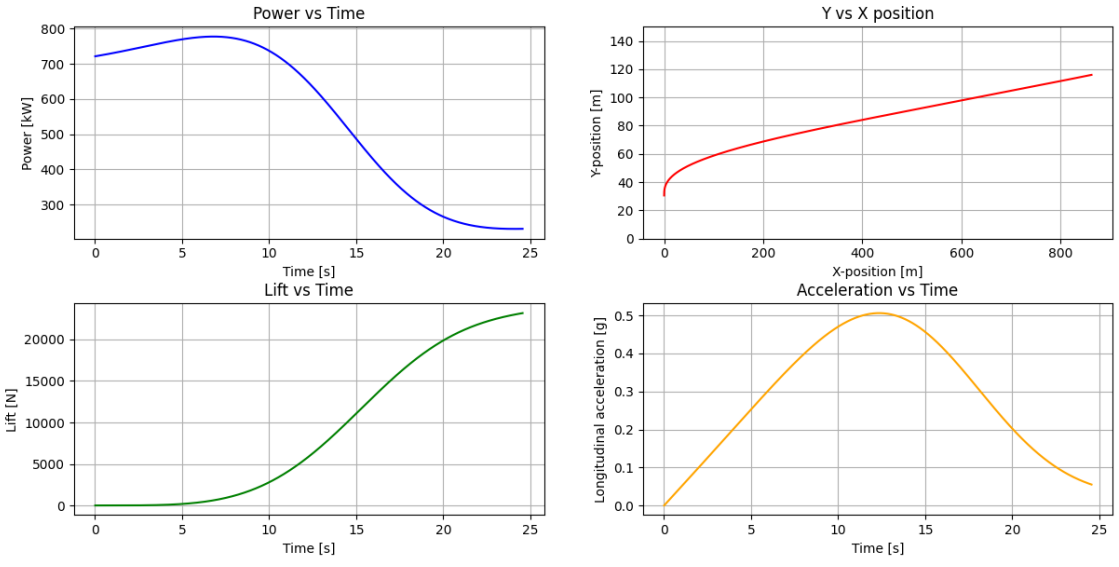

Figure 7.3: *Performance parameters of the transition to climb configuration*

As can be seen in the figure, the power required will slightly increase at the start of the transition. This is because the lift is still zero (bottom-left) while the propellers are angled. As soon as the

aircraft starts gaining horizontal velocity the lift the wing produce increases and the power of the propellers decrease to climbing power. The acceleration is steadily increasing till a g-force of 0.5. In case the passengers want to experience a Tesla-like feel (1.1 g's), this can be made possible as the power can be increased.

7.2.2. Climb angle

To optimize the climb section Equation 7.11 has been used to calculate the power. From this equation is can be seen that the C_D over $C_L^{3/2}$ should be minimized. To achieve this, the values for C_D and C_L can be calculated using Equation 7.12 and Equation 7.13.

$$C_L = \sqrt{3C_{D_0}\pi Ae} \tag{7.12}$$

$$C_D = 4C_{D_0} \tag{7.13}$$

This gives a C_L of 1.05 and a C_D of 0.082. The climb angle is however taken as a variable. The climb gradient is 0.125 as this is a requirement by EASA [25], which is only after takeoff. After transition the climb gradient will become 0.065. This has the advantage that the climbing velocity is 77 m/s.

7.2.3. Descent to Landing Simulation

The descent to landing model has been expanded more than the hovering to climb model to also include the landing phase. The start of the model consists of the aircraft in descent. The optimal descent angle has been found to be about 2.2 [deg]. Similar to the transition to climb, this transition can also be split up in 3 phases. The EOM are shown in Equations 7.14, 7.15 and 7.16. Again, the moment equation is assumed to equal zero such that the aircraft shall not experience any angular accelerations in the longitudinal axis. Also, the total moment due to lift is assumed to be zero again as well and the α_T is assumed to be the same for all propellers. The FBD for this transition phase is illustrated in Figure 7.4.

$$\Sigma F_x : (T_1 + T_2 + T_3)\cos\alpha_T - L_{total}\sin(\alpha - \gamma) - D\cos\gamma = ma_x \tag{7.14}$$

$$\Sigma F_y : (T_1 + T_2 + T_3)\sin\alpha_T + L_{total}\cos(\alpha - \gamma) - D\sin\gamma - W = ma_y \tag{7.15}$$

$$\Sigma M_{@c.g.} : T_1(-\sin\alpha_T \cdot x_1 + \cos\alpha_T \cdot y_1) + T_2(\sin\alpha_T \cdot x_2 + \cos\alpha_T \cdot y_2) + T_3(\sin\alpha_T \cdot x_3 + \cos\alpha_T \cdot y_3) = I\ddot{\theta} = 0 \tag{7.16}$$

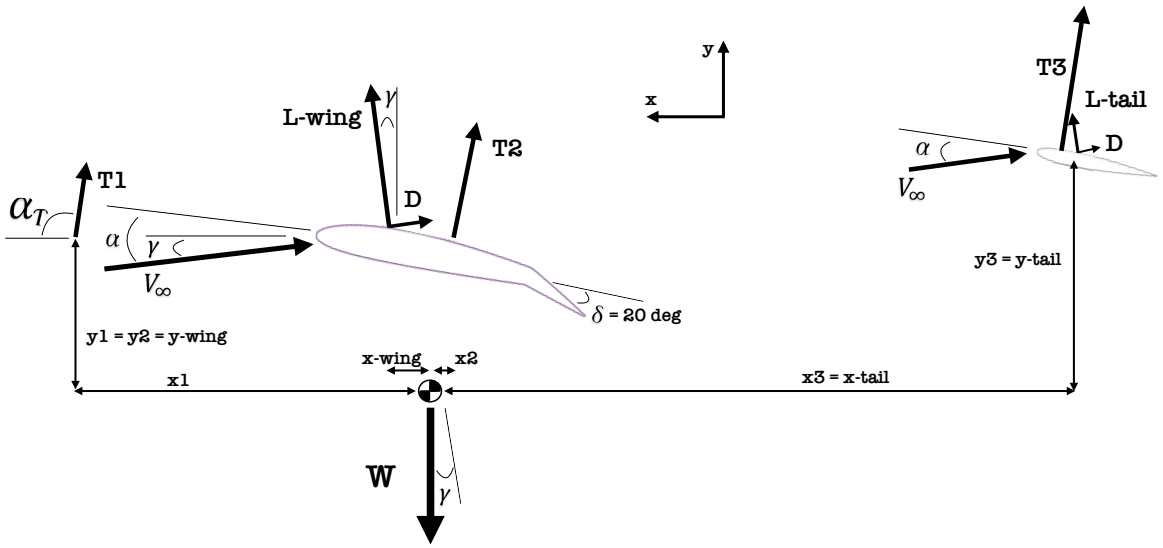

Figure 7.4: *Free Body Diagram for the transition from descent*

Phase 1 In phase 1, the thrust is zero and the propellers rotate to vertical configuration 90 [deg] in 5 [s]. This will cause a decrease in horizontal velocity due to the drag and an increase in vertical velocity due to lift decreasing. This phase will only take 5 [sec] as the vertical velocity will become too large otherwise.

$$a_y = \frac{L\cos\alpha - m \cdot g_0}{m} \tag{7.17}$$

$$a_x = \frac{-L\sin\alpha - D}{m} \tag{7.18}$$

α is the angle of attack during descent, which is 12 [deg].

Phase 2 After 5 [sec] phase 2 begins. The propellers are angled at 90 [deg] and start providing thrust in order to level out the aircraft. The goal of phase 2 is to have the propellers in vertical position and to achieve an y velocity of 0 [m/s]. There is no positive horizontal component of the thrust so the aircraft's horizontal velocity will keep decreasing.

$$T = \frac{-L\cos\alpha + mg_0 + ma_y}{\sin\alpha_T} \tag{7.19}$$

$$a_x = \frac{T\cos\alpha_T - L\sin\alpha - D}{m} \tag{7.20}$$

Phase 3 Phase 3 starts when the aircraft has leveled out. The propellers will be angled slightly backward at 3.1 [deg] (this is also the lift direction as the wing has an angle of attack of 3.1 [deg]). The aircraft will start descending to reach a vertical velocity of -2 [m/s]. At 30.5 meters altitude, the horizontal velocity will be zero thus the aircraft will land vertically.

The results of the landing transition can be seen in Figure 7.5.

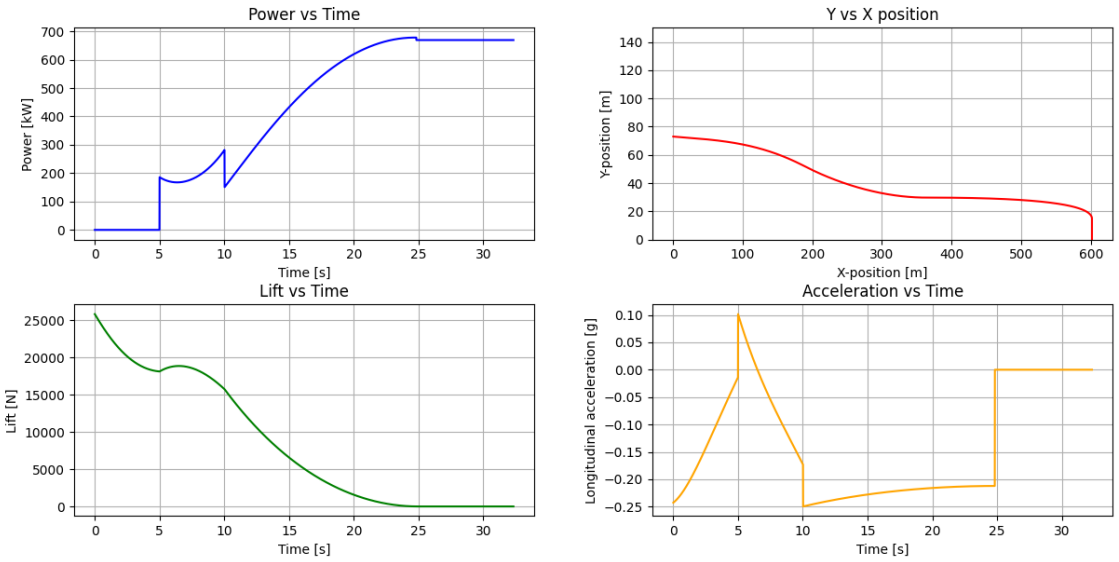

Figure 7.5: *Performance parameters of the landing transition simulation*

From the figure, a number of results can be obtained. First of all, it can be noted that the power suddenly changes at certain moments in time. This is due to the assumption that power can be provided instantly, which might not be the case. The power increases due to the decreased velocity, which reduces the lift meaning the propeller thrust is needed to keep the aircraft level, of which the acceleration is very small. In comparison, road cars experience a deceleration of about 0.1 g on average. The aircraft shall be just outside that range.

7.2.4. Maximum Thrust Simulation

During the transition period, the thrust of the separate propellers should not exceed the maximum thrust of each propeller. To calculate this, the propellers were split up into 3 groups: The inboard propellers positioned in front of the wing (with thrust T1), the outboard propellers on the wingtips (with thrust T2) and the propellers on the V-tail (with thrust T3). Since the angular velocity of the aircraft is kept at zero during the transition, the moments around the center of gravity should be zero as well. A moment equation was then set up to calculate the thrust of each propeller during the transition using Figure 7.2. The aerodynamic forces have been neglected due to the low speed of the transition manouvre. After reaching the stall speed, the aerodynamic control surface will be used to control the aircraft thus simulation of individual thrust is run until the stall speed is reached. The T2 (outboard propellers) are assumed to provide half of the total thrust since they are located only 7 cm from the cg (in the longitudinal direction) and will therefore lower the thrust of the inboard and V-tail propellers. The results of the simulation can be found in Figure 7.6. The figure indicates that the thrust from the propellers stays below the maximum thrust available. The V-tail thrust is low, due to the large moment arm it has around the c.g.

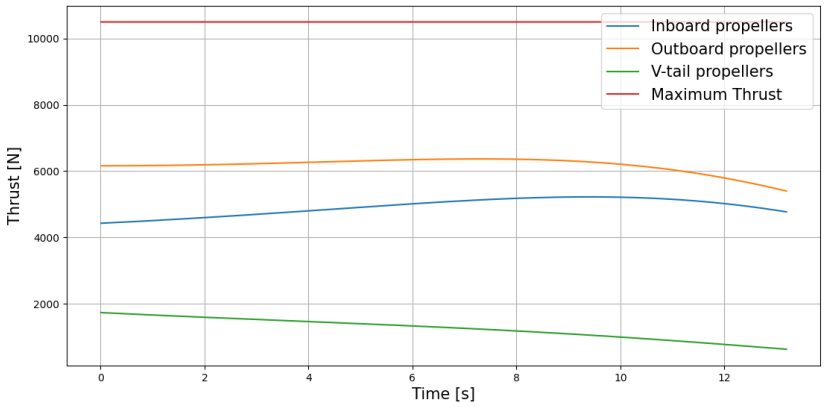

Figure 7.6: *Thrust Per Engine During Transition Until V-stall*

7.3. Mission Energy

The total mission energy can be found in Table 7.1. The maximum power is found during the transition phase after takeoff (Figure 7.3). Compared to the previously calculated mission energy of 199 [kWh] [1], an increase of 15% mission energy has occurred due the detailed design phase. This is mainly due to the weight increase.

Table 7.1: *Energy Of Mission Segments*

Segment	Altitude [m]	Time [s]	Max Power [kW]	Energy [kWh]
B Takeoff	0 - 30.5	15.3	715	3.0
C Transition	30.5 - 116	45	777	3.2
D Climbing	116 - 2400	466	238	20.8
E Cruise	2400	3638	122	135
F Descend	2400 - 73	800	25	5.5
G+H Transition & Landing	73 - 0	45	678	10.2
E' Loiter Horizontal	2400	1200	122	41.7
H' Loiter Vertical	20	20	715	4.6
Total	2400	83.5 [min]	777	219

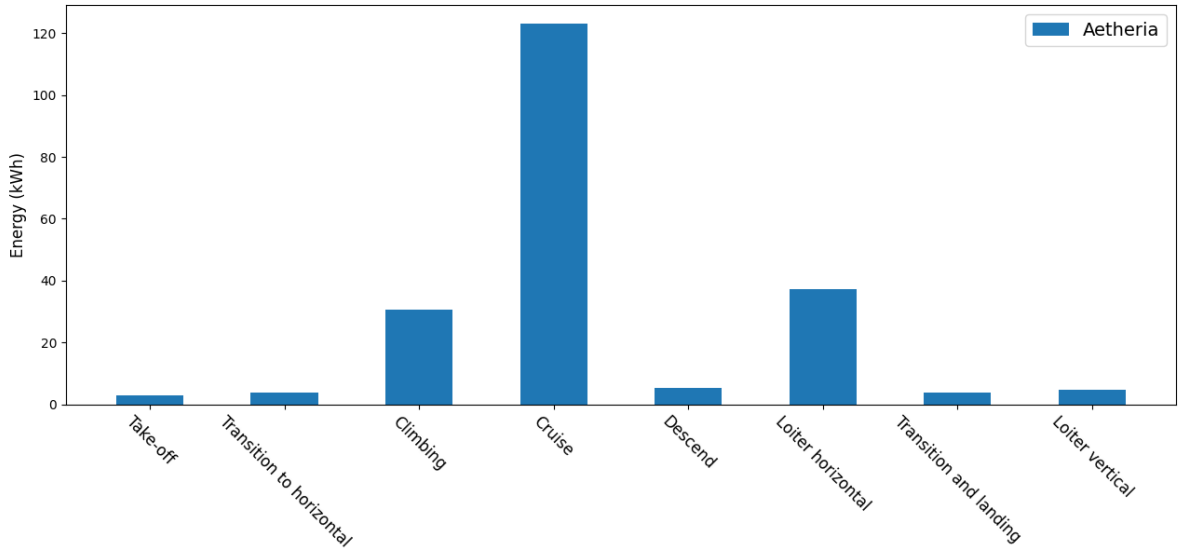

Figure 7.7: *Mission Energy Aetheria*

7.4. Sensitivity Analysis

In this section, a sensitivity analysis of the cruise altitude has been performed to investigate its effect on the mission energy. Furthermore, the effect of wind on the range of the mission will be investigated, as this is a common occurance in flight.

7.4.1. Cruise Altitude Analysis

The last phase of the mission profile to be optimized is the cruise phase. When investigating how the cruise energy could be decreased, the altitude was determined as a factor which could be optimized. Increasing the cruise altitude required a longer climbing phase, but the density is lower at higher altitudes, thus less power is required. In Figure 7.8 the total mission energy can be seen against the cruise altitude. From this figure, an optimum cruise altitude of 3500 [m] is derived. However, due to the requirement that the cabin shall not be pressurized [4] and the fact that pressurized aircraft keep the cabin pressure at an equivalent pressure for an altitude of 2400 [m] [2]. Hence, this is chosen as the new cruise altitude.

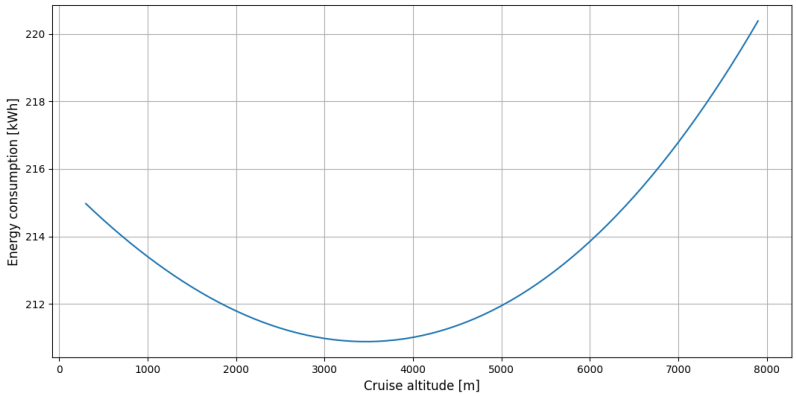

Figure 7.8: *Cruise Altitude Optimization*

[2] Accessed June 16th 2023, https://www.skybrary.aero/articles/cabin-altitude

It can be seen however that the cruise altitude does not impose large affects on the mission energy since the difference from an altitude of 300 [m] to the optimum 3500 [m] is less than 2.5%. However, social aspect such as noise can also be taken into account. This would prefer a higher altitude as the noise levels at zero altitude would be insignificant, while at 300 [m] they do play a role.

7.4.2. Wind

To perform a sensitivity study on the impact of wind, the effect on range (assuming equal mission energy) and time have been investigated. The results can be found in Figure 7.9. A negative wind speed indicates a tailwind, while a positive means a headwind.

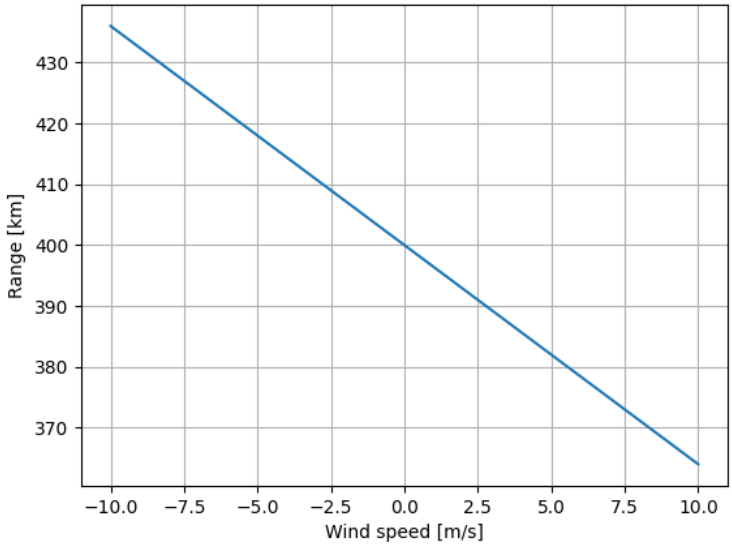

Figure 7.9: *Wind Influence on Range*

From the figure it can be deducted that the wind does have a large effect on the range, since a 10 [m/s] head wind causes a range decrease of 7.5%. When flying against a stronger headwind at maximum range, it should certainly be taken into account.

8

Control and Stability Design

In this chapter, the stability and control of the aircraft is assessed. In Section 8.1, the stability and control relevant components is visualized, and the CG excursion is found. In Section 8.2, the vertical flight stability and control is examined. Based on it, the rotors are located and a vertical flight control system is designed. Section 8.3 presents the horizontal flight static stability and control, in which the tail and control surfaces are sized and determined. In Section 8.4, the dynamic stability and control of the aircraft is assesed during horizontal flight, and the necessary SAS systems are designed. Lastly, in Section 8.5, the landing gear is positioned, in order to provide ground stability and control.

8.1. General Layout for Stability and Control

The 3-view drawing of Aetheria can be found in Chapter 13. According to this, the general layout of stability and control affected components can be determined and sized for. This general layout follows from an in-depth trade-off exercise performed in [1].

Static Loading Diagram & CG Limits

A static loading diagram is created to determine the CG excursion in which the aircraft must be stable and controllable, using the individual weights and locations of all aircraft elements. The plot is created by first loading the cargo, composed of five 25 kg suitcases. Then, the loading of the pilot and passengers is plotted when the aircraft is loaded back to front, and front to back. When loading back to front, the passengers are loaded first, starting from the rearmost row, and then the pilot is loaded. When loading front to back, first the pilot is loaded and then the passengers are loaded starting from the front row. The mass of the fuel is ignored in the CG excursion plot, as it corresponds to less than 0.5% of the MTOM. The resulting CG excursion diagram looks as depicted in Figure 8.1.

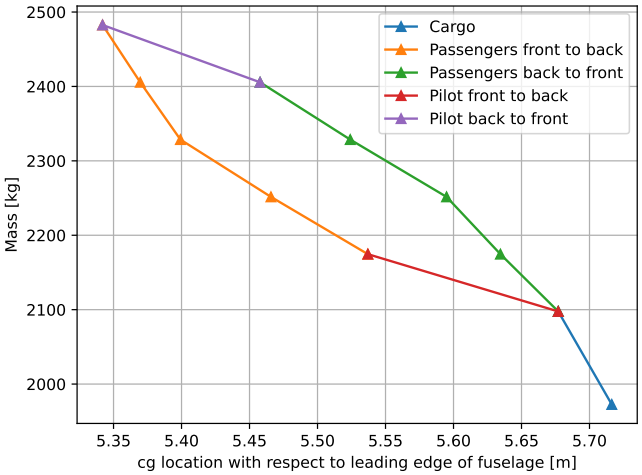

Figure 8.1: *Static loading diagram*

The foremost and rearmost CG locations are determined from the loading diagram. When designing the tail, control surfaces and choosing the rotor locations to ensure stability and control during both horizontal and vertical flight, the aircraft is designed to be stable and controllable at a CG range

that is 20% larger than the CG travel determined from the loading diagram. In other words, a contingency margin of 10% has been added to both the rear and forward CG limits. This corresponds to the following CG excursion limits, with margins applied within which the aircraft is designed to be statically stable and controllable: $x_{cg_{fr}} = 5.308m$ $x_{cg_r} = 5.711m$, as measured from the nose.

8.2. Vertical Flight Static and Dynamic Stability & Control

In this chapter, the aircraft is designed for vertical flight stability and control. In Subsection 8.2.1, the vertical flight controllability of the aircraft is ensured under one engine inoperative condition with gusts and crosswinds by choosing the positions of the rotors. In Subsection 8.2.2, a vertical flight stability and control augmentation system is developed to compensate for the fact that a multicopter is inherently unstable, since it does not provide a naturally counteracting force or moment to disturbances.

8.2.1. Rotor Locations Based on Vertical Flight Controllability

The rotor locations affect the vertical flight controllability, as this determines the CG range in which the aircraft is controllable during vertical flight. In this subsection, the rotor locations are chosen such that the forces and moments of the aircraft can be balanced ($T = W$, $L = M = N = 0$) even under the one engine inoperative condition in the presence of a gust and crosswind. Vertical flight controllability is evaluated by using the Available Control Authority Index (ACAI) function [27]. For a given set of rotor locations, engine failure, CG location, gust and a crosswind magnitude, if ACAI=0, then this means that the aircraft can achieve a balance of forces and moments [27]. When ACAI > 0, there is available control authority beyond being able to balance forces and moments indicating that the aircraft can perform maneuvers during vertical flight [27].

The aircraft contains 6 rotors, in a similar arrangement to that of Joby S4. Each of these rotors are powered by two motors. These rotors are placed such that ACAI is greater than 0 within the CG excursion and the 20% contingency margin determined using the loading diagram. ACAI must be greater than 0 even if any one of the engines fail and there is a gust and crosswind upto the limit defined in CS-27. This means that the aircraft shall be controllable under a crosswind of 31 km/h and vertical gust of 9.1 m/s [28] with one engine failure [28]. Since there are 2 engines per rotor, failure of one engine limits the available maximum thrust to half of its nominal value for a certain rotor. Hence, rotor placement must ensure that the aircraft is controllable during vertical flight (ie: ACAI > 0) even in the worst-case scenario, in which extreme external loads are acting on the aircraft, while one engine is inoperative. This condition is then used for placing the rotors, together with structural constraints and a comprehensive systems engineering design approach.

The case of one propeller inoperative is not assessed, as the aircraft cannot be stable vertically under (almost) any conditions. It is assumed that propellers will not fail during vertical flight, as the main cause of propeller failure is due to birdstrike, and the probability of a birdstrike at the altitudes that vertical flight is performed is negligible according to EASA [1]. Additionally, it is highly unlikely for a bird to fly into a quasi-stationary object which is the case when hovering where ground speed is usually negligible.

The rotor locations vary in the x- and y-axes. Regarding the y-positions, it is established that, for stability and control, and aerodynamic reasons, the outermost rotors at the wing are placed at the wingtip. Similarly, the rotors located at the tail are placed at the tail's wingtip. The inboard rotors at the main wing are located as far outboard as possible, while keeping a propeller-propeller clearance, to avoid wake disturbances.

Regarding the x-positions, the outermost rotors in the main wing are placed at 20% of the wingtip

[1] Accessed on 20 June 2023, https://www.easa.europa.eu/community/topics/rotorcraft-birdstrikes

chord, and the tail rotors are placed at 50% of the tail's wingtip chord. The inboard main wing propellers are placed in front of the wing, using pylons. A dedicated optimisation code has been used to find the shortest pylon length required to attain sufficient stability and control in vertical flight. This reduces the structural weight of the pylons. The final x-location of the inboard rotors is 2.6 meters in front of the leading edge of the wing at the y-location. This value has been found through a balance between the pylon structural weight, and the propeller sizing, while ensuring vertical flight stability. The use of pylons of this size, while maintaining the limit conditions defined previously, corresponds to a required available maximum thrust per rotor 2.25 times as large as the nominal hovering thrust per rotor. The final rotor locations are displayed in Table 8.1 and Figure 8.2.

Table 8.1: *Rotor locations from nose (x, y) = (0, 0), y=0 is the center line of the aircraft. For each engine pair one is on the positive side and one on the negative*

Rotors	X-position [m]	Y-position [m]
Inboard	2.7113	±2.6025
Outboard	5.5775	±4.7977
Tail	11.3937	±2.4594

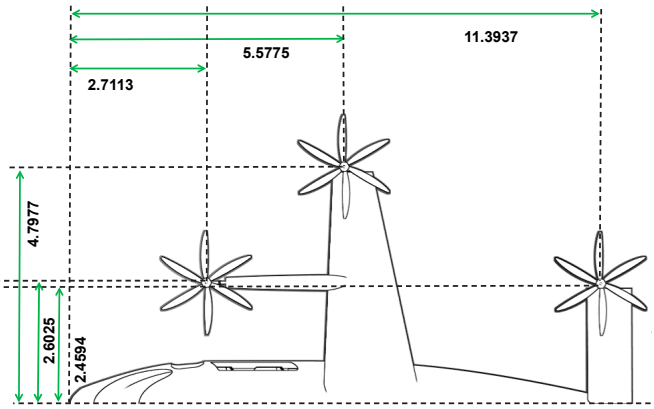

Figure 8.2: *Rotor locations w.r.t. aircraft's nose, lengths in metres*

8.2.2. Vertical Flight Controller Design for Dynamic Stability and Control

Having positioned the rotors for vertical control, a stability and control augmentation system is required in order to safely perform vertical flight maneuvers such as take-off and landing. This stability and control augmentation system serves two functions. Firstly, it needs to provide dynamic stability and damp oscillations. Secondly, it needs to allow the pilot to control state variables that are important for vertical operation by giving inputs. The input variables controlled by the pilot were defined as altitude h, velocities v_x and v_y (which are the forward and span-wise velocities respectively) and the yaw angle ψ. The variables that are measured and fed back to the control system are altitude h (based on a pressure sensor), the velocities v_x and v_y in the plane of the hexacopter (obtained from a camera on the eVTOL or fed to the aircraft from vertiport's measurements) and ψ, θ, and ϕ angles obtained from gyroscopes. Based on these variables, the dynamic equations of motion of the hexacopter eVTOL were developed and linearized for the horizontal hover condition. In this linearization, small velocities are assumed allowing neglection of drag. Secondly, small roll and pitch angles are assumed ($\sin\theta = \theta$ and $\sin\phi = \phi$). In addition, the rotational velocities are

neglected ($\omega_x \simeq \omega_y \simeq \omega_z \simeq 0$). All these assumptions are realistic as small roll and pitch angles and angular velocities are necessary to maintain passengers' comfort, leading to the following equations [29]:

$$x'' = -g\theta \quad y'' = g\phi \quad z'' = \frac{-\Delta T}{m} \quad \theta'' = \frac{\Delta M}{I_{yy}} \quad \Delta N = \psi'' \cdot I_{zz} - \phi'' \cdot I_{zx} \quad \Delta L = \phi'' \cdot I_{xx} - \psi'' \cdot I_{zx} \tag{8.1}$$

It is assumed that $I_{xy} \simeq I_{yz} \simeq 0$ [30]. ΔT, ΔL, ΔM, and ΔN respectively indicate the additional thrust, roll, pitch, and yaw moment exerted by the propellers compared to the hover condition. In Equation 8.1, the variables are defined in the right-handed body axis with the centre of the coordinate frame at the location of the cg. The z-axis points downward and x-axis points in the direction of the nose.

The controller was adapted from [31] with modification to input states. The vertical flight controller is comprised of 6 individual controllers, as labelled in Figure 8.3.

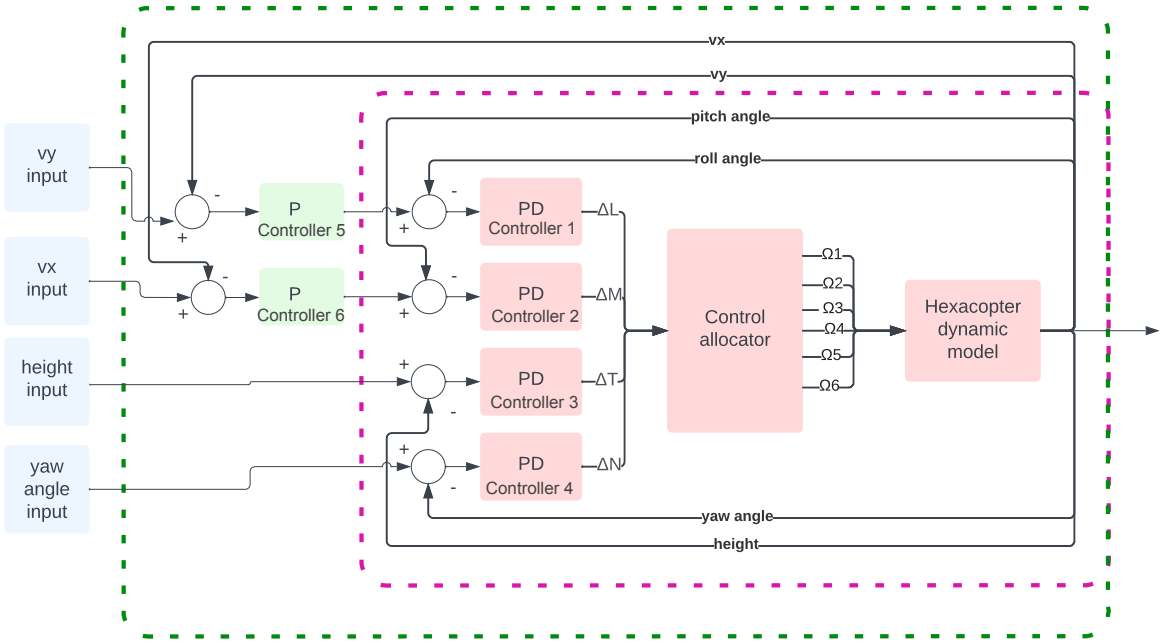

Figure 8.3: *Vertical flight controller*

As seen in Figure 8.3, the inner loop, indicated with pink dashed lines, allows the pilot to control the yaw and the altitude of the VTOL. Additionally, it serves as a stability augmentation system (SAS) for the pitch and roll angle. The outer loop (indicated with green dashed lines) serves as a CAS for the control of planar velocities. Not only a gain but a PD controller in the inner loop was used to reduce overshoot. An 'I' controller was not used as no steady-state error to step control inputs was identified. It was observed that a simple gain in the outer loop (green controllers) allowed for sufficient tracking of reference velocities. Adding a derivative controller resulted in a non-minimum phase system, which is difficult to control.

In the control system, a maximum limit on the additional thrust (ΔT) and moments ($\Delta M, \Delta L, \Delta N$) was imposed to simulate the non-linearity caused by possible actuator (engine) saturation due to limitation of available thrust on each engine. The maximum available thrust (ΔT) was calculated by subtracting the aircraft weight from the maximum thrust. The maximum limit of the roll moment

(ΔL) was calculated assuming engines on one side of the aircraft being idle and the three engines on the other side working at maximum thrust. The maximum yawing moment (ΔN) was calculated considering the proportionality between the torque of an engine and its thrust to be $\frac{Torque}{Thrust} = 0.1$ [27]. The maximum pitching moment (ΔM) was calculated by assuming that either the two front most or the two rearmost engines are put to idle mode while the remaining four engines operate at maximum thrust. The available thrust and moment values are presented in Table 8.3.

The control system was built in Simulink. During the gain tuning process, a rise time of below 3 seconds and an overshoot less than 10% was aimed for when a step input was given to v_x, v_y and altitude. The rise time and the overshoot can be seen from the control system's response to step inputs in Figure 8.4, Figure 8.5, and Figure 8.6. Having a low rise time and overshoot led to high proportional and derivative gains for controllers 1,2 and 3. With these high gains, acceptable tracking quality for these inputs (v_x, v_y and h) was achieved, which is crucial for a safe landing. This can be said based on the controller's ability to track the reference speed (v_y) as presented in Figure 8.7. The input v_y in Figure 8.7 is varied abruptly to test the performance of the control system under stress, and to prove that the control system can follow the abrupt inputs that a pilot may give to prevent a possible crash. However, it is important to keep in mind that high gains could lead to amplification of noise in the system so where possible, the gains were kept low. An example of this is the yaw controller. Since controlling yaw control is not safety critical (unlike v_x, v_y and altitude), lower gains in controller 4 were used which led to a slow response. These gains for the different controllers are presented in Table 8.2. Lastly, to meet the CS-27 requirements, the PID controllers damp oscillations with periods equal to or less than 10 seconds to half amplitude in less than one time period. However, this requirement was not driving for any of the controllers. The damping of the pitch angle after a step input can be seen in Figure 8.6.

Table 8.2: *Controller gains*

Controller	K_p	K_d
1	-10000	-7000
2	120000	50000
3	100000	100000
4	10900	18800
5	0.21	N/A
6	-0.21	N/A

Table 8.3: *Thrust and Moment Limits*

Force/Moment	Maximum Value
ΔT	36000 N
ΔL	93457 Nm
ΔM	20120 Nm
ΔN	3018 Nm

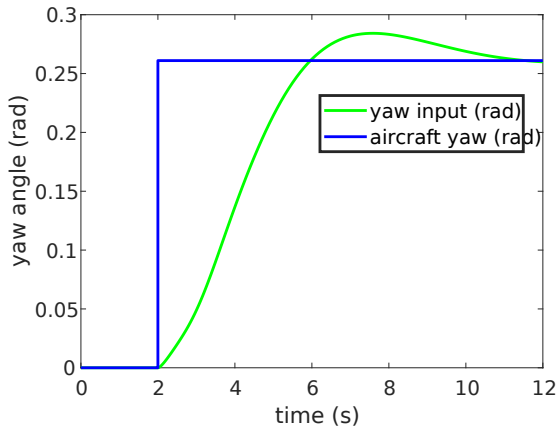

Figure 8.4: *System reference tracking of yaw angle input*

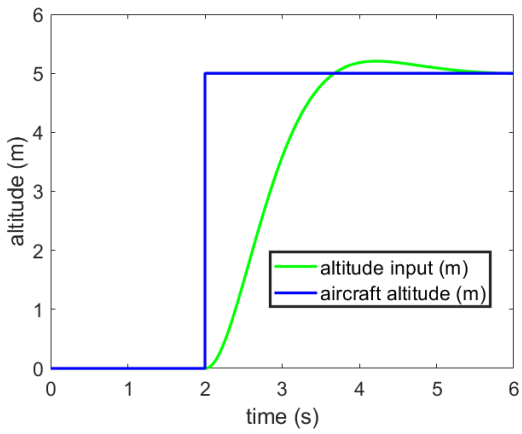

Figure 8.5: *System reference tracking of altitude input*

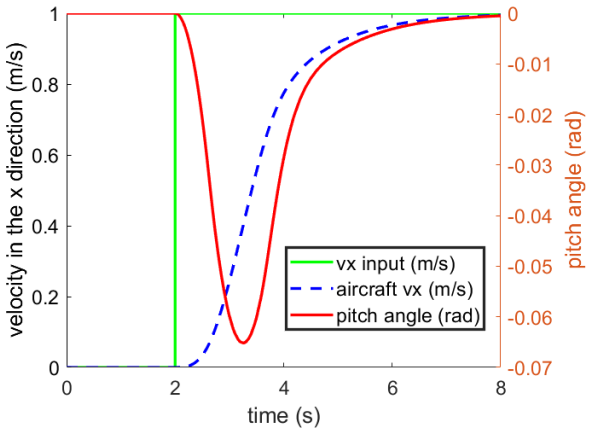

Figure 8.6: *System reference tracking of a step x-velocity input*

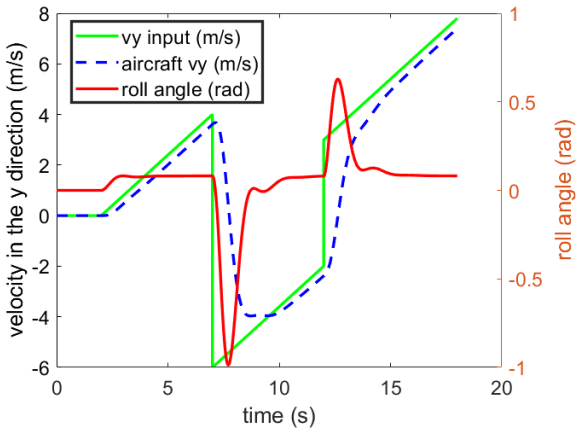

Figure 8.7: *System reference tracking of an abrupt y-velocity input*

8.3. Horizontal Flight Static Stability and Control

In this section, the design of the subsystems affected by horizontal flight stability and control is performed. Firstly, the requirements on these subsystems and design outcomes are presented. Then, a discussion follows on the desired empennage configuration, followed by its design procedure. Following this, the control surface sizing is performed. Lastly, the design optimisation procedure is explained and the final values of the affected design are displayed.

8.3.1. Control and Static Stability Requirements Regarding Horizontal Flight

The wing placement, control surface and tail sizing is made such that the horizontal flight control and stability requirements are met:

- Positive weather vane stability (C_{n_β}): The vertical tail needs to be added so that the C_{n_β} derivative of the aircraft becomes positive. It is recommended by Roskam that the C_{n_β} of the aircraft equals 0.0571 [rad/s] for good directional stability characteristics [32].
- Sufficient roll rate (p): Small aircraft must meet a roll rate of 60° per 1.3 seconds to ensure level 1 ('good') flying qualities [33]. Hence the ailerons need to be sized to ensure that this roll rate is achievable.
- Cross-wind requirement: The aircraft has to have to be certified for a landing with a cross-wind 20% of the stall speed, as per CS-23 regulations [34], to be able to land horizontally. During this landing, the yaw moments around the aircraft must be neutralized. The equilibrium under this cross-wind condition is used to size the rudder. For conventional aircraft, the one engine inoperative condition is set to size the rudder. However, for Aetheria, if one of the engines fails, the rotor can still provide 50% of its thrust due to two engines powering one rotor. The rotor on the opposite side of the aircraft can also be reduced to 50% power and the yawing moment on the aircraft can be nullified without a rudder deflection. Since the rotors are sized to provide hover thrust, there is a very large thrust surplus in horizontal flight making it possible to reduce the power of the opposing engine.
- Longitudinal control and stability: Due to the use of an airfoil with a positive camber, it was determined that the tail needs to produce a downforce to balance the pitching moments around the aircraft ($C_m = 0$), highest during horizontal landing. Hence, the elevators must be sized for longitudinal landing control. In addition, the aircraft must be longitudinally stat-

ically stable (C_{m_α}<0). The stability requirement is the most stringent during cruise. Both the longitudinal controllability during landing and static stability during cruise is used to determine wing location, and horizontal tail area.

8.3.2. Chosen Tail Configuration: V-tail

Since Aetheria is a high-wing design, the considered options for empennage are a T-tail or a V-tail to reduce aerodynamic interference. Since the rear rotors are attached to the tips of the tail to provide sufficient clearance between the propellers and the fuselage, a T-tail would require significant stiffening at the center to resist the bending moments imposed by any minor amount of differential thrust provided by the rear rotors. Hence, a V-tail configuration was chosen.

In order to size a V-tail, a virtual horizontal tail and a vertical tail has to be sized first [35]. The virtual horizontal and vertical can be combined into a V-tail as explained in Subsection 8.3.3.

Virtual Horizontal Tail Sizing

A methodology has been created, that relates the wing location with respect to the fuselage length to the ratio of surface areas of the horizontal tail and wing. This is such that the combination of wing location and horizontal tail size provides stability and control within the CG excursion plus margin, as dictated by the static loading diagram. It is important to note that the CG excursion varies with the wing location and horizontal tail size. The wing location for which the horizontal tail size is the smallest is preferred, as a lower horizontal tail size yields a lower V-tail size, which yields a lower trim drag, as shown in Subsection 8.3.5.

In order to do size the V-tail, a wing location with respect to the fuselage is selected, for which the static loading diagram is created. From this static loading diagram, the CG excursion is determined with a 10% margin on both the front and rear CG limits.

The scissor plot is then created, by setting the CG limits imposed by stability and control performance. Equation 8.2 and Equation 8.3 are used, that relate the ratio of surface areas of the virtual horizontal tail and main wing to the most limiting location of the CG. Equation 8.2 shows this relationship for stability reasons, and Equation 8.3 for control[36].

$$\frac{S_h}{S} = \frac{1}{\left(\frac{C_{L_{\alpha_h}}}{C_{L_{\alpha_{A-h}}}}\left(1-\frac{d\epsilon}{d\alpha}\right)\frac{l_h}{\bar{c}}\left(\frac{V_h}{V}\right)^2\right)}\bar{x}_{cg} - \frac{\bar{x}_{ac}-0.05}{\left(\frac{C_{L_{\alpha_h}}}{C_{L_{\alpha_{A-h}}}}\left(1-\frac{d\epsilon}{d\alpha}\right)\frac{l_h}{\bar{c}}\left(\frac{V_h}{V}\right)^2\right)} \tag{8.2}$$

$$\frac{S_h}{S} = \frac{1}{\frac{C_{L_h}}{C_{L_{A-h}}}\frac{l_h}{\bar{c}}\left(\frac{V_h}{V}\right)^2}\bar{x}_{cg} + \frac{\frac{C_{m_{ac}}}{C_{L_{A-h}}} - \bar{x}_{ac}}{\frac{C_{L_h}}{C_{L_{A-h}}}\frac{l_h}{\bar{c}}\left(\frac{V_h}{V}\right)^2} \tag{8.3}$$

From these equations, the lowest $\frac{S_h}{S}$ ratio that satisfies the required CG excursion is found. The process is looped for different wing positions. This creates a relationship between the wing position and the smallest $\frac{S_h}{S}$ ratio that allows stability and control of the aircraft during horizontal flight.

In order to estimate the C_{L_α} value of the horizontal tail, Equation 8.4 has been used [37]. This value has to be estimated in order to assess the horizontal stability of the aircraft.

$$C_{L_{\alpha_h}} = \frac{2\pi A_h}{2+\sqrt{4+\left(\frac{A_h\beta}{\eta_{af}}\right)^2\left(1+\frac{\tan^2\Lambda_{0.5C_h}}{\beta^2}\right)}} \tag{8.4}$$

In the equation above, η_{af} is assumed to be 0.95, according to [37], and the virtual horizontal tail's sweep angle at half-chord is 0 since the aircraft operates in the incompressible flow region.

The resulting wing location and virtual horizontal tail size are as follows: the leading edge of the root chord is placed 5.178m behind the nose, and ratio of virtual horizontal tail surface area to main wing surface area is 0.3037. The location of the virtual horizontal is the same as the location of the V-tail.

Virtual Vertical Tail Sizing
The vertical tail has to be sized such that the required C_{n_β} (0.0571) can be achieved. The two main contributors to C_{n_β} are the tail and the fuselage. This leads to [38]:

$$C_{n_{\beta_{vt}}} = C_{n_\beta} - C_{n_{\beta_f}} = -C_{Y_{\beta_{vt}}}(1 - \frac{d\sigma}{d\beta})\frac{S_v l_v}{Sb} = C_{n_\beta} - (-\frac{2v_{fuse}}{Sb}) \tag{8.5}$$

Neglecting the contribution of the fuselage to the sideslip gradient ($\frac{d\sigma}{d\beta}$), the vertical tail area can be determined as:

$$S_v = \frac{C_{n_\beta} + \frac{2v_{fuse}}{Sb}}{-C_{Y_{\beta_{vt}}}\frac{Sb}{l_v}} \tag{8.6}$$

The term $-C_{Y_{\beta_{vt}}}$ in Equation 8.6 is defined in Equation 8.11.

8.3.3. V-tail Sizing

Having mentioned that the V-tail is a combination of a virtual horizontal and vertical tail, it must be enforced that the pitch moment coefficient with respect to angle of attack of the tail ($C_{m_{\alpha_t}}$) remains the same in a conversion between the horizontal tail and the V-tail. This condition is enforced by Equation 8.7 [39]:

$$S_h C_{L_{\alpha_h}} = S_{vee} C_{L_{\alpha_{vee}}} = S_{vee} C_{L_{\alpha_{vee_N}}} \cos^2(\Gamma_{vee}) \tag{8.7}$$

The $\cos^2(\Gamma_{vee})$ factor comes from the fact that an increase in angle of attack experienced by the V-tail is only $\cos(\Gamma_{vee})$ times the increase of angle of attack experienced by a horizontal tail. In addition, the component of the additional lift (due to an increase in aircraft angle of attack) that contributes to pitching moment is a factor $\cos(\Gamma_{vee})$ less compared to a horizontal tail.

Similarly, if the V-tail has to provide the same C_{n_β} as a vertical tail, the following condition has to be satisfied [39]:

$$S_v \cdot -C_{Y_{\beta_{v_t}}} = S_{vee} \cdot -C_{Y_{\beta_{vee}}} = S_{vee} K C_{L_{\alpha_{vee_N}}} \sin^2(\Gamma_{vee}) \tag{8.8}$$

The factor 'K' takes into account the fact that the effective aspect ratio of the vertical tail is reduced due to the aerodynamic interference between the two sides of the V-tail. Under sideslip, at the root of the V-tail, is when the circulations of the two sides of the V-tail are opposing each other. This leads to vortices at the root of the V-tail that reduce the effective aspect ratio. The taper ratio of the V-tail was chosen to be equal to 1 to be able to store the nacelle rotational mechanism and provide enough structural stiffness to support the rotors. At a V-tail taper ratio of 1 ($\lambda_{vee} = 1$), the value of K as a function of the V-tail aspect ratio is defined as follows [39]:

$$K = 0.1035 \ln(A_{vee}) + 0.5618 \tag{8.9}$$

$$C_{L_{\alpha_{vee_N}}} = C_{L_{\alpha_h}} \tag{8.10}$$

$$-C_{Y_{\beta_{vt}}} = K C_{L_{\alpha_{vee_N}}} \tag{8.11}$$

If the virtual horizontal and the vee-tail have the same aspect ratio ($A_h = A_{vee}$), then this results in Equation 8.9. Similarly, knowing that the effectiveness of the virtual vertical tail is reduced by a

factor 'K' once it is converted to a V-tail, the term $-C_{Y_{\beta_{vt}}}$ in Equation 8.6 can be defined as in Equation 8.10. Hence, the virtual vertical tail surface S_v designed using Equation 8.6 is over-designed purposefully such that the loss 'K' is taken into account. Substituting Equation 8.11 and Equation 8.10 into Equation 8.7 and Equation 8.8, yields Equation 8.12

$$S_h = S_{vee}\cos^2\Gamma_{vee} \qquad S_v = S_{vee}\sin^2\Gamma_{vee} \tag{8.12}$$

Equation 8.12 can be rearranged to determine the dihedral angle and the surface area of the V-tail [39]:

$$S_{vee} = S_h + S_v \qquad \Gamma_{vee} = \arctan\left(\sqrt{\frac{S_v}{S_h}}\right) \tag{8.13}$$

8.3.4. Control Surface Sizing

For a V-tail aircraft, two different aerodynamic surfaces need to be sized. The aileron is sized to meet the roll rate requirement. In addition, the ruddervators need to be sized such that the required C_{m_α} and the $C_{n_{\delta_r}}$ can be provided.

Aileron Sizing

Small aircraft (of class I) require a roll rate of 60 degrees per 1.3 seconds (0.8055 rad/s). Hence, an aileron that can provide this roll rate (p) must be designed. The roll rate of an aileron is sized for the stall speed (V_s) where the roll authority is the least. The roll rate that can be provided is given by [38]:

$$p = \frac{C_{l_{\delta a}}}{C_{l_p}} \cdot \delta_{a_{max}} \frac{2V_s}{b} \tag{8.14}$$

30° is a common limit for $\delta_{a_{max}}$ according to [38] and shall hence be used. The rear spar of the wingbox forms a natural strong attachment point for the aileron. Thus, this means that the aileron chord to wing chord ratio (c_a/c) is fixed at 0.25. The ailerons are placed as outboard as possible to provide maximum roll moment. This leaves only one design parameter; the spanwise location of the inboard end of the aileron (y_{inner}). Hence, for a particular y_{inner}, the C_{l_p} and $C_{l_{\delta a}}$ need be determined. $C_{l_{\delta a}}$ is given by [38]:

$$C_{l_{\delta a}} = -C_{L_a}\tau_a \frac{c_r}{Sb}\left(\left(\frac{y_{inner}^2}{2} + \frac{2}{3}y_{inner}^3\frac{\lambda-1}{b}\right) - \left(\frac{b^2}{8} + \frac{2}{3}\left(\frac{b}{2}\right)^3\frac{\lambda-1}{b}\right)\right) \tag{8.15}$$

The aileron effectiveness (τ_a) in Equation 8.15 is given by [38]:

$$\tau_a = -6.624\left(\frac{S_a}{S}\right)^4 + 12.07\left(\frac{S_a}{S}\right)^3 - 8.292\left(\frac{S_a}{S}\right)^2 + 3.295\frac{S_a}{S} + 0.004942 \tag{8.16}$$

The area of wing covered by the ailerons ($\frac{S_a}{S}$)compared to wing surface is given by:

$$\frac{S_a}{S} = 2\frac{c_a}{c}\frac{\left(\frac{b}{2} - y_{inner}\right)\left(\frac{c_r}{b}(\lambda-1)\right)\left(\frac{b}{2} - y_{inner}\right)}{S} \tag{8.17}$$

The roll rate derivative of the roll moment in Equation 8.14 is given by Equation 8.31.

Ruddervator Sizing

In a V-tail, the rudder and the elevator must share the allowable deflection, for which a 20° is used based the design procedure proposed by NASA [39]. Hence:

$$\delta_{r_{max}} + \delta_{e_{max}} = 20° \tag{8.18}$$

The rudder deflection is sized to provide sufficient yawing moment to counter a cross wind of 20% stall speed during horizontal landing. Hence, the required $C_{n_{\delta_r}}$ required from the horizontal tail can be determined using:

$$C_n = C_{n_\beta}\beta_{max} + C_{n_{\delta_r}}\delta_{r_{max}} = 0 \qquad \beta_{max} = \arctan\left(\frac{0.2V_s}{V_s}\right) \tag{8.19}$$

Similarly, the V-tail must be able to provide a down force equivalent to that would have been provided by a horizontal tail, which was specified in Equation 8.3 to size the virtual horizontal tail by choosing a C_{L_h} value. Hence, the required $C_{L_{\delta_e}}$ that had to be provided by the tail was:

$$C_{L_{\delta_e}} = \frac{C_{L_h} - C_{L_{\alpha_h}}(\alpha - \epsilon)}{-\delta_{e_{max}}} \tag{8.20}$$

This would have been equivalent to a pitch moment coefficient derivative with respect to elevator deflection as given by :

$$C_{m_{\delta_e}} = -C_{L_{\delta_e}}\left(\frac{V_h}{V}\right)^2\left(\frac{S_h l_v}{Sc}\right) \tag{8.21}$$

In a typical V-Tail, the ruddervator covers the whole span of the V-Tail making the ruddervator control surface chord to V-tail chord ratio ($\frac{c_c}{c_{vee}}$) the design parameter that influences τ_e and τ_r, the elevator and rudder effectiveness. Since the same control surface is used by both the rudder and the elevator, the $\frac{c_c}{c_{vee}}$ has to be sized for the highest of τ_e and τ_r. Allocating the rudder a larger portion of the available 20° deflection means that the rudder requires a lower effectiveness (lower τ_r) to provide a given yawing moment. As a consequence, the smaller available elevator deflection means that the elevator effectiveness (τ_e) would need to be higher to provide a given pitching moment. Thus, the 20° is distributed between the rudder and the elevator such that τ_e= τ_r leading to minimum ruddervator chord. The required elevator and rudder effectiveness is given as [39]:

$$\tau_e = \frac{C_{m_{\delta_e}}}{\left(\frac{V_h}{V}\right)^2 \frac{l_v S_{vee}}{\bar{c}S}\cos(\Gamma_{vee})C_{L_{\alpha_N}}} \qquad \tau_r = \frac{C_{n_{\delta_r}}}{\left(\frac{V_h}{V}\right)^2 \frac{l_v S_{vee}}{bS}\sin(\Gamma_{vee})KC_{L_{\alpha_N}}} \tag{8.22}$$

The tail to wing speed ratio $\frac{V_h}{V}$ ratio takes into account the aerodynamic interaction between the main wing and the tail and the propeller tail interaction (since a rotor is placed at the tip of the tail):

$$\left(\frac{V_h}{V}\right)^2 = 0.95(1+a)^2 \tag{8.23}$$

The value of 0.95 can be used for a V-Tail [36]. The term in Equation 8.23 'a' is the averaged induction factor of the propeller to model the propeller's acceleration of the axial velocity. The rotational induction of the propeller was neglected due to the tangential induction factor (a') being low.

Finally, the value of τ can be related to $\frac{c_c}{c_{vee}}$ to size the ruddervator by using [40]:

$$\tau = -2.7552\left(\frac{c_c}{c_{vee}}\right)^2 + 2.703\left(\frac{c_c}{c_{vee}}\right) + 0.0048 \tag{8.24}$$

8.3.5. Design Optimisation & Sensitivity Study

A loop is created to optimise the design of the V-tail that determines the optimum V-tail design under different values of V-tail aspect ratio. Different approach C_{L_h} values are also optimised. The cruise $C_{L_{vee_N}}$ value is calculated for each iteration with Equation 8.25.

$$C_{L_{vee_{cr_N}}} = \frac{C_{m_{ac}} + C_{L_{vee_{cr}}} \Delta \bar{x}_{cg}}{\left(\frac{V_h}{V}\right)^2 \frac{S_{vee}}{S} \cos\Gamma_{vee} \frac{l_{vee}}{\bar{c}}} \tag{8.25}$$

This value, when squared and multiplied by the V-tail surface area, and then divided by the aspect ratio, is used as a value to minimise, as it is proportional to the cruise drag created by the V-tail. This makes the assumption that the Oswald efficiency factor would remain constant. The final V-tail consists of the V-tail design that yields the lowest cruise drag.

In Figure 8.8a, an analysis can be observed for the sensitivity of the ratio of the surface areas of the virtual horizontal tail and main wing against the wing location. This is relevant as the surface area of the virtual horizontal tail is a major component of the calculation of the V-tail's surface area. Next, in Figure 8.8b, the sensitivity of the trim drag (proportional) component is analysed against the V-tail's aspect ratio. The trim drag component consists on $C^2_{L_{vee_{trim}}} \frac{S_{vee}}{A_{vee}}$, which assumes $C_{D_{0_{vee}}}$ to be included in the aircraft's C_{D_0} term, making the V-tail's drag force a function of $C_{L_{vee_{trim}}}$, A_{vee}, and S_{vee}.

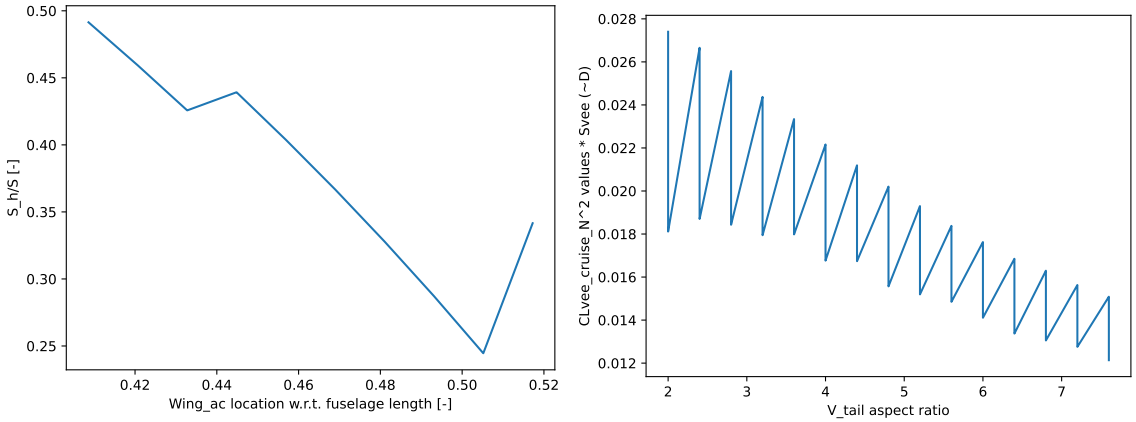

(a) $\frac{S_h}{S}$ *against wing location sensitivity analysis*

(b) *Drag against V-tail's aspect ratio sensitivity analysis*

As observed, the $\frac{S_h}{S}$ ratio is very sensitive to the wing location, as a strong minimum is observed at a specific wing location. Fortunately, the x-axis is very long, as an only 2% difference in wing location w.r.t. the fuselage corresponds roughly to a 20cm difference in position. This is a very big difference in this context. Additionally, from Figure 8.8b, it can be observed that the trim drag component reduces, as the aspect ratio increases. The aspect ratio of the V-tail should not be too large either, and a limit of 8 has been determined based on the stall characteristics of the tail.

8.3.6. Stability & Control Determined Sizes

In this subsection, a summary of the sizes determined by stability and control criteria can be found. These sizes are displayed in Table 8.4.

Table 8.4: *Horizontal stability and control determined sizes*

Parameter	Value	Unit	Parameter	Value	Unit
x_{lewing}	5.179	m	$C_{D_{0_{vtail}}}$	0.008684	-
S_{vee}	4.446	m^2	$C_{L_{vee_{cr_N}}}$	0.11096	-
Γ_{vee}	0.33035	rad	$\frac{c_{ctrl}}{c_{vee}}$	0.2893	-
l_{vee}	5.368	m	$\eta_{ruddervator}$	0.5357	-

8.4. Dynamic stability design for horizontal flight

In this section, the dynamic stability of the aircraft is determined and designed for. Firstly, the requirements on the dynamic stability are presented. Then, a method is presented to estimate the stability derivatives, from which these are calculated and displayed. Lastly, the dynamic stability is assessed, and the required SAS systems are designed, such that the requirements are met.

8.4.1. Stability Requirements

Regarding dynamic stability, the CS23 requirements that address the aircraft eigenmotions are enough to guarantee safe operation. But an aircraft with dynamic response characteristics that meets the CS requirements does not necessarily have 'good' handling qualities. For this reason, when it comes to eigenmotions, even passenger aircraft are usually designed to meet military aircraft eigenmotion standards [41], which are more stringent. These are outlined in MIL-F-8785c Category B, level 1, military standards [41]. Level 1 indicates 'good' handling quality. Category B indicates gradual maneuvers, as performed by a passenger aircraft.

The eigenmotion response requirements are found to be as follows. The damping ratio for short period shall be between 0.3 and 2. Additionally, the phugoid damping ratio shall be greater than or equal to 0.04. The roll mode time constant shall be less than 1.4s. The spiral mode is allowed to be unstable, as long as the time to double the amplitude is greater than 20s. Lastly, the following criteria apply for the dutch roll motion: the damping ratio shall be greater than or equal to 0.08, the natural frequency shall be greater than or equal to 0.4, and the product of the damping ratio and natural frequency shall be greater than or equal to 0.15.

Regarding the requirements on the stability derivatives, the following apply. C_{n_β} shall be positive, in order to obtain weather-vane stability. Additionally, C_{Y_β} shall be negative, as an aircraft that is pulled towards the wind direction is inherently unstable. Lastly, C_{l_β} shall be negative in order to provide a counteracting action to sideslip perturbations.

The requirements for the SAS design are the following. When designing a SAS system, a 9.5dB gain margin and 35 degree phase margin shall be used. The SAS shall provide damping at resonant frequencies. Lastly, the SAS shall avoid PIO, in accordance with Gibson's criteria.

8.4.2. Stability Derivatives

The stability derivatives taken from the book Flight Vehicle Aerodynamics [42]. These equations are based on proven theories such as lifting line theory, on simplifications, such as C_{n_r} being affected only by the V-tail, and on empirical formulas. The resulting estimation equations are in accordance with the equations found in the AE3212-II Flight Dynamics course reader [43], and can be found in Equations (8.26) to (8.33). The stability derivatives of the aircraft can be observed in Tables 8.5 to 8.7. The stability derivatives with respect to $\dot{\alpha}$ are given as:

$$C_{Z_{\dot{\alpha}}} = -C_{L_{\alpha_h}} \frac{S_h}{S} \left(\frac{V_h}{V}\right)^2 \frac{d\epsilon}{d\alpha} \frac{l_h}{\bar{c}} \quad C_{m_{\dot{\alpha}}} = -C_{L_{\alpha_h}} \frac{S_h}{S} \left(\frac{V_h}{V}\right)^2 \frac{d\epsilon}{d\alpha} \left(\frac{l_h}{\bar{c}}\right)^2 \tag{8.26}$$

The stability derivatives with respect to α are given as:

$$\begin{gathered} C_{X_\alpha} = C_{L_0} - C_{D_\alpha} \quad C_{Z_\alpha} = -C_{L_\alpha} - C_{D_0} \quad C_{m_\alpha} = C_{L_\alpha} \frac{l_{cg}}{\bar{c}} - C_{L_{\alpha_h}} V_h \left(1 - \frac{d\epsilon}{d\alpha}\right) + C_{m_{\alpha_{fuse}}} \\ C_{D_\alpha} = \frac{2C_{L_0} C_{L_\alpha}}{\pi A} \quad C_{m_{\alpha_{fuse}}} = 2\frac{V_{fuse}}{S\bar{c}} \end{gathered} \tag{8.27}$$

The stability derivatives with respect to q are given as:

$$C_{X_q} = 0 \quad C_{Z_q} = -2C_{L_{\alpha_h}} V_h \quad C_{m_q} = -2C_{L_{\alpha_h}} V_h \frac{l_h}{\bar{c}} + C_{m_{q_{fuse}}} \quad C_{m_{q_{fuse}}} = 0 \tag{8.28}$$

The force coefficient at trim condition are given by:

$$C_{X_0} = \frac{W \cdot \sin\theta_0}{\frac{1}{2}\rho V^2 S} \quad C_{Z_0} = -\frac{W \cdot \cos\theta_0}{\frac{1}{2}\rho V^2 S} \tag{8.29}$$

The stability derivatives with respect to β are given as:

$$C_{Y_\beta} = -C_{n_\beta}\frac{b}{l_v} \quad C_{l_\beta} = -C_{L_\alpha}\frac{\Gamma}{6}\frac{1+2\lambda}{1+\lambda} \quad C_{n_\beta} = 0.0571 \tag{8.30}$$

The stability derivatives with respect to p are given as:

$$C_{Y_p} = 0 \quad C_{l_p} = -C_{L_\alpha}\frac{1+3\lambda}{12(1+\lambda)} \quad C_{n_p} = -\frac{C_{L_0}}{8} \tag{8.31}$$

The stability derivatives with respect to r are given as:

$$C_{Y_r} = 2V_v C_{L_{\alpha_v}} \quad C_{l_r} = \frac{C_{L_0}}{4} \quad C_{n_r} = -2C_{L_{\alpha_v}} V_v \frac{l_v}{b} \tag{8.32}$$

The stability derivatives with respect to δr are given as:

$$C_{Y_{\delta r}} = -C_{n_{\delta r}}\frac{b}{l_v} \quad C_{l_{\delta r}} = C_{Y_{\delta r}}\frac{z_{vee}}{b} \quad z_{vee} = z_{cg-vee_r} + \sin\Gamma_{vee}\frac{b_{vee}}{2} \tag{8.33}$$

Table 8.5: *Longitudinal stability derivatives*

Derivative w.r.t.	C_X	C_Z	C_m
$\dot{\alpha}$	N/A	-2.237	-8.114
α	0.09166	-4.643	-1.666
q	0	-10.782	-39.116
0	0.03028	-0.5529	N/A

Table 8.6: *Lateral stability derivatives*

Derivative w.r.t.	C_Y	C_l	C_n
β	-0.09995	0	0.0571
p	0	-0.6053	-0.02034
r	0.1889	0.04068	-0.1079

Table 8.7: *Control surfaces stability derivatives*

Control derivative	**Value**
$C_{m_{\delta e}}$	-2.617
$C_{Y_{\delta r}}$	0.1809
$C_{l_{\delta a}}$	-0.09777
$C_{n_{\delta r}}$	-0.1033
$C_{l_{\delta r}}$	0.03098

The stability derivatives that are not displayed in the tables above are not relevant for the necessary applications or are assumed to be 0. This includes, but is not limited to, $C_{Z_{\delta e}}$ or $C_{n_{\delta a}}$.

8.4.3. Dynamic Stability

In this subsection, the aircraft eigenmotions are explored, and based on them, the required SAS systems are designed.

Aircraft Eigenmotions

Based on the stability derivatives, and the moments of inertia of the aircraft, a state-space system of the aircraft can be created, following the form of Equation 8.34.

$$\dot{\mathbf{x}} = A\mathbf{x} + B\mathbf{u} \tag{8.34}$$

The moments of inertia have to be defined in order to create a dynamic model. The values of I_{XX}, I_{YY}, I_{ZZ}, and I_{XZ} are derived from Class I estimations from Roskam part V [30], and can be found in Table 8.8.

Table 8.8: *Values of moments of inertia following Class I estimations*

Parameter	Value [kg · m^2]
I_{XX}	10437
I_{YY}	12082
I_{ZZ}	21722
I_{XZ}	1264.5

$$P = \begin{bmatrix} -2\mu_c \frac{\bar{c}}{V_0} & 0 & 0 & 0 \\ 0 & \left(C_{Z_{\dot{\alpha}}} - 2\mu_c\right)\frac{\bar{c}}{V_0} & 0 & 0 \\ 0 & 0 & -\frac{\bar{c}}{V_0} & 0 \\ 0 & C_{m_{\dot{\alpha}}}\frac{\bar{c}}{V_0} & 0 & -2\mu_c K_Y^2 \frac{\bar{c}}{V_0} \end{bmatrix} \quad Q = \begin{bmatrix} -C_{X_u} & -CX_\alpha & -C_{Z_0} & 0 \\ -C_{Z_u} & -C_{Z_\alpha} & C_{X_0} & -\left(C_{Z_q} + 2\mu_c\right) \\ 0 & 0 & 0 & -1 \\ -C_{m_u} & -C_{m_\alpha} & 0 & -C_{m_q} \end{bmatrix} \quad R = \begin{bmatrix} -C_{X_{\delta_e}} \\ -C_{Z_{\delta_e}} \\ 0 \\ -C_{m_{\delta_e}} \end{bmatrix} \tag{8.35}$$

$$P = \begin{bmatrix} \left(C_{Y_{\dot{\beta}}} - 2\mu_b\right)\frac{b}{V} & 0 & 0 & 0 \\ 0 & -\frac{1}{2}\frac{b}{V} & 0 & 0 \\ 0 & 0 & -4\mu_b K_X^2 \frac{b}{V} & 4\mu_b K_{XZ}\frac{b}{V} \\ C_{n_{\dot{\beta}}}\frac{b}{V} & 0 & 4\mu_b K_{XZ}\frac{b}{V} & -4\mu_b K_Z^2 \frac{b}{V} \end{bmatrix} \quad Q = \begin{bmatrix} -C_{Y_\beta} & -C_L & -C_{Y_p} & -\left(C_{Y_r} - 4\mu_b\right) \\ 0 & 0 & -1 & 0 \\ -C_{l_\beta} & 0 & -C_{l_p} & -C_{l_r} \\ -C_{n_\beta} & 0 & -C_{n_p} & -C_{n_r} \end{bmatrix} \quad R = \begin{bmatrix} -C_{Y_{\delta_a}} & -C_{Y_{\delta_r}} \\ 0 & 0 \\ -C_{Y_{\delta_a}} & -C_{Y_{\delta_r}} \\ -C_{Y_{\delta_a}} & -C_{Y_{\delta_r}} \end{bmatrix} \tag{8.36}$$

$$A = P^{-1}Q \quad B = P^{-1}R \tag{8.37}$$

From the A matrices above [43], the eigenvalues of the aircraft were determined shown in Table 8.9 in the form $\xi + \eta j$. Since the returned eigenvalues are non-dimensional, they were multiplied by the cruise speed and divided by the mean aerodynamic chord, for the longitudinal, and by the span length, for the lateral ones.

However, the CS-23 requirements on the eigenmotions are vague. In aircraft design, the military standards 'MIL-F-8785c' category B, and Level 1 standards are sought to give the aircraft 'good' handling qualities. These requirements are more stringent than in CS. A comparison of the desired values and the aircraft parameters are provided in Table 8.11.

Table 8.9: *Eigenvalues of Symmetric and Asymmetric Motions*

Eigenmotion	Phugoid	Short Period	Aperiodic Roll	Dutch Roll	Spiral
Value	$-0.0015 \pm 0.0767\,j$	$-1.4760 \pm 1.1777\,j$	-0.7299	$-0.0409 \pm 0.5620\,j$	0.0043

Based on these eigenvalues, the dynamic stability parameters of the aircraft can be determined using Equation 8.38:

$$\omega_d = \eta \qquad \zeta = \frac{\xi}{\sqrt{\xi^2 + \eta^2}} \qquad \tau = -\frac{1}{\xi} \qquad T_2 = \frac{ln(2)}{\xi} \tag{8.38}$$

Table 8.10: *Eigenmotion MIL-F-8785c Category B Level 1 requirements versus actual aircraft values*

Source	Phugoid	Short Period	Aperiodic Roll	Dutch Roll	Spiral
Requirement [41]	$\zeta > 0.04$	$0.3 < \zeta < 2$	$\tau < 1.4s$	$\zeta > 0.08$, $\omega_d > 0.4$, $\zeta \cdot \omega_d > 0.15$	$T_2 > 20$
Aircraft	$\zeta = 0.0193$	$\zeta = 0.7817$	$\tau = 1.3701$	$\zeta = 0.072$, $\omega_d = 0.5620$,$\zeta \cdot \omega_d = 0.0408$	$T_2 = 160.45s$

SAS System

Since phugoid motion and dutch roll do not meet the MIL-F-8785c Category B Level 1, two stability augmention systems (SAS) need to be designed; a phugoid damper and a yaw damper. In this architecture, the yaw rate gyro and the speed sensor are assumed to have a transfer function of $H(s) = 1$ meaning that sensors measure states without error and without delay. This is a good assumption as according to [44]. The elevator and the rudder servos (which is the ruddervator servo in the V-tail) are assumed to have a transfer function of $H(s) = \frac{1}{0.05s+1}$ [44] to model the phase delay introduced by the actuators. Besides meeting the MIL-F-8785c requirement, two other things need to be considered during the SAS design and choosing the damper tranfer function. Firstly, both the stability augmentation seen in Figure 8.9 and Figure 8.10 require at least a 9.5dB gain margin and a 35° phase margin to be robust [44]. Secondly, the possibility for a pilot induced oscillation (PIO) needs to be minimized by abiding by Gibson's phase rate criteria [45] that sets a minimum limit for the cross-over frequency (1 rad/s) and maximum limit for the rate of change of the phase at this frequency (of 50 $\frac{deg \cdot s}{rad}$) as seen in Equation 8.39 though it was later seen that this consideration did not drive SAS design.

$$\omega_{\phi_{sys}=-180°} \geq 1 \frac{rad}{s} \qquad -\left(\frac{\delta \phi_{sys}}{\delta \omega}\right)_{\phi_{sys}=-180°} \leq 50 \frac{deg \cdot s}{rad} \tag{8.39}$$

The architectures of the yaw and phugoid damper are presented in Figure 8.9 and Figure 8.10.

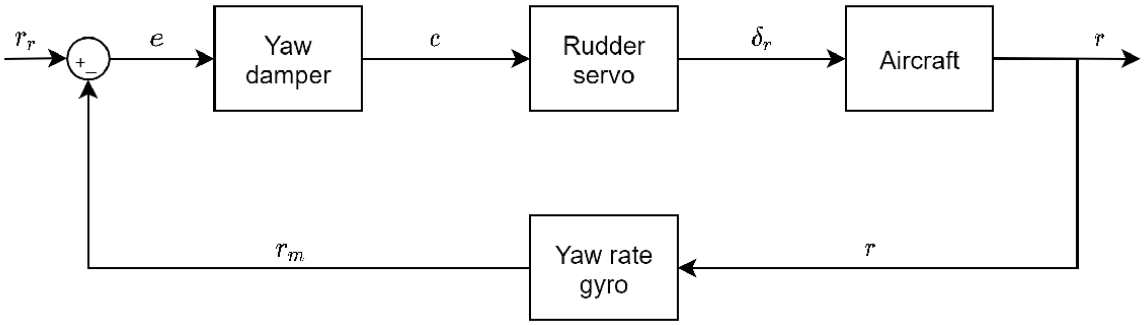

Figure 8.9: *Phugoid Stability Augmentation System Architecture [44]*

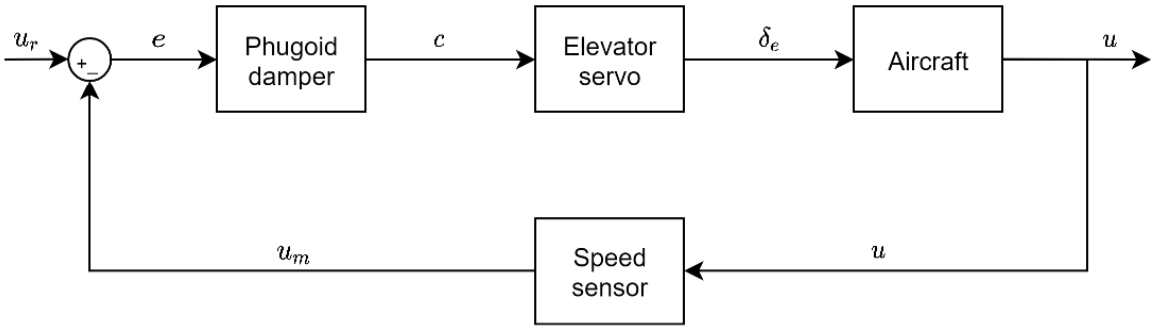

Figure 8.10: *Dutch Roll Stability Augmentation System Architecture [44]*

The yaw damper works by returning a rudder deflection based on the reference yaw rate. This damps the dutch roll motion. It was determined that a steady state error in tracking a reference yaw rate was present. Hence, a 'PI' controller was used in the yaw damper with transfer function $H_{yd} = \frac{-1.7}{s} - 1$. The phugoid is also damped with a 'PI' controller. The transfer function of the phugoid damper is $H_{pd} = \frac{0.2}{s} + 0.2$. However, in this case, the integrating component is added not to eliminiate steady state error but to meet the required gain margin of 35° to make sure that the controller is robust. Since the phugoid motion leads to an oscillation in velocity, a reference velocity is used to damp the phugoid motion. It is important to note that the reference velocity in the phugoid damper and the reference yaw rate in the yaw damper are fed to the aircraft by the control augmentation system (CAS) [44] which is another control loop outside the stability augmentation system (SAS). The CAS system is not designed for horizontal operation as the aircraft is comprised of many different modes (eg: pitch hold, altitude hold, etc.) and designing this intricate system goes beyond designing the aircraft and proving that it can be sufficiently stabilized and safely operated.

Table 8.11: *Eigenvalues and corresponding parameters of aircraft after addition of yaw and phugoid damper*

Value	Phugoid	Short Period	Aperiodic Roll	Dutch Roll	Spiral
Eigenvalue	$-0.3379 \pm 0.4896\,j$	$-1.0874 \pm 1.5380\,j$	-0.740	$-0.2956 \pm 1.1073\,j$	0.0011
Parameter	$\zeta = 0.5680$	$\zeta = 0.5773$	$\tau = 1.3514$	$\zeta = 0.2579$, $\omega_d = 1.1073$,$\zeta \cdot \omega_d = 0.2856$	$T_2 = 630.1s$

Figure 8.11 and Figure 8.12 compare the aircraft's phugoid and dutch roll eigenmotion before and after the implementation of SAS. It is evident that adding SAS significantly increased damping.

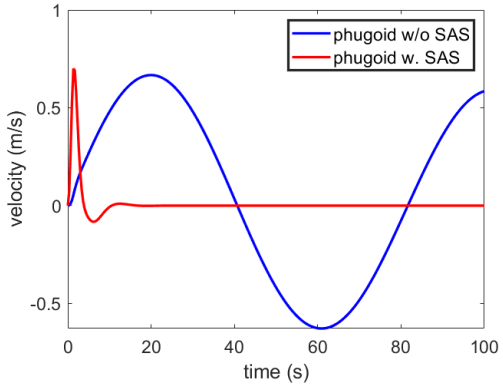

Figure 8.11: *Phugoid motion of aircraft with and without SAS*

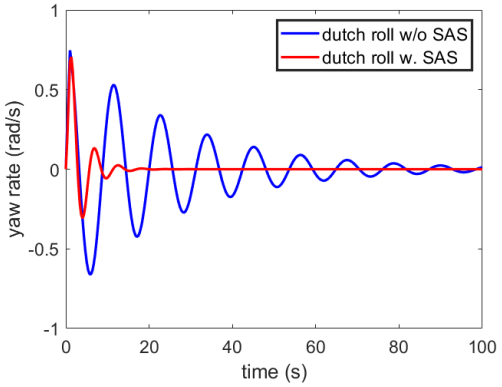

Figure 8.12: *Dutch roll motion of aircraft with and without SAS*

8.5. Landing Gear Design

Aircraft of similar weight to Aetheria use the Michelin Air X, Goodyear Flight Custom III and McCreary Air Hawk tyres which have diameters between 14 to 15 inches [2]. Hence, 14.5 inches (≃ 37cm) can be used as the the tyre diameter. The landing gear configuration is decided to be a tricycle. The landing gears are retractable due to the high speed and range of the aircraft. The longitudinal and spanwise positions of the landing gears as well as the landing gear strut height are constrained by several considerations:

1. The nose gear does not carry more than 15% of the weight for structural reasons and not less than 8% of the weight for sufficient steering capability [35].
2. During horizontal landing which may need to be performed in case of an emergency, a tail strike should be avoided. It is recommended that tail strike should be avoided up to a pitch angle of 15° [35]. This is a conservative estimate given that the stall angle of attack at 20° flap deflection is 12° and further deflecting the flaps would only reduce the stall angle.
3. The aircraft should also avoid tip back. Hence, the main landing gear sized and positioned such that at the highest pitch angle during landing (taken as 15°), the most aft CG position does not fall behind the main landing gear [35].
4. To prevent the aircraft from being susceptible to turnover, the most aft CG location should lead to a turnover angle (ψ_{to}) of less than 55° [35]. The definition of this angle is shown in Figure 8.13. The turnover consideration limits the maximum height of the landing gear strut and sets a minimum limit on the spanwise position of the main landing gear.
5. Propellers should have sufficient ground clearance. Due to the high wing configuration used, the ground clearence consideration was not driving the landing gear position and height.

It was determined that the biggest constraint was the turn-over angle. Because of this, no possible landing gear positioning and strut height could be found that satisfies all 5 of these constraints unless the MLG track width was 2.6 [m]. Since the fuselage width is 1.8 [m], the main landing gears was attached to the fuselage. The landing gear configuration can be seen in Figure 13.3 and Figure 13.4, with its parameters displayed in Table 8.12.

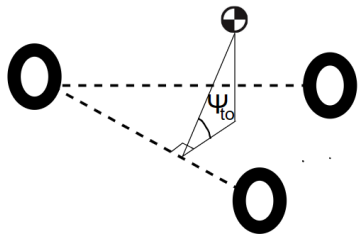

Figure 8.13: ψ_{to} *Turnover angle definition with respect to landing gear*

Table 8.12: *Landing gear dimensions*

Dimension	Value (m)
MLG track width	2.6
NLG strut length	0.74
MLG strut length	0.65
x_{MLG}	0.05
x_{NLG}	6.16

[2] Accessed May 13th, https://shop.boeing.com/aviation-supply/p/M08301=3T#:~:text=Size%2C%20225%20mph-,MICHELIN%C2%AE%20AIR%20X%C2%AE%20M08301%20Radial%20Aircraft%20Tire%2C%2014.5,R6%20in%20Size%2C%20225%20mph

9

Structural Design

This chapter will talk about the works of the structure department, the work and calculations were done using models of structural parts. These codes optimize weight while maintaining structural integrity. This chapter starts with the crashworthiness considerations in Section 9.1, this is followed by the determination of the flight loads in Section 9.2 which is then followed by the wing box design in Section 9.3. After this, the pylon for the inboard engines is modeled in Section 9.4, after which the crash energy absorption structure is described in Section 9.5, and the fuselage and tail are sized in Section 9.6. The aircraft is subject to a vibrational analysis in Section 9.7, the resulting masses are broken down in Section 9.8, and the sensitivity analysis is shown in Section 9.9. The section is finished with Section 9.7.

9.1. Crashworthiness considerations

Crashworthiness is crucial to consider in the development of eVTOL aircraft, which demands careful attention. Ensuring passenger safety and the integrity of the hydrogen system drives the fuselage design which is further described in Section 9.6.

9.1.1. Emergency landings

Designing with emergency landings in mind is crucial for the safety of hydrogen-powered eVTOL aircraft, considering the public view of hydrogen's danger. By prioritizing crashworthiness, the project aims to address the concern of the customers, promote a positive public image and guarantee the safety of the passengers.

Horizontal Emergency Landing

In case of a bird strike during horizontal flight the propellers might break off, in such an event the eVTOL can still land horizontally with one-propeller-inoperative as described in Subsection 8.2.1. However, another is that the propeller might damage the fuselage, wiring and hydraulics. This would cause the pilot to lose control of the aircraft and its subsystems. To mitigate this risk, the hydraulics and wiring will follow two separate paths on both sides of the fuselage hull to make sure one path still functions properly in case one is cut or damaged. This method is chosen since designing the fuselage to resist a cut from a propeller is unfeasible and this would result in an unnecessarily heavy aircraft.

Vertical Emergency Landing

Loss of power during vertical flight mode would have more severe consequences, as the wing is not able to generate enough lift to support the weight. The aircraft will decelerate rapidly toward the ground and crash on impact. The kinetic energy is related to the square of impact velocity, which is in turn related to the height where power loss occurs. The structure of the eVTOL aircraft will not be able to make each vertical emergency landing survivable, but the majority shall be. Guidelines are therefore necessary, which are defined by EASA based on empirical data of rotorcraft crashes. To accommodate these requirements, a crash absorbing structure is designed to be placed below the fuselage. This structure will absorb most of the energy and increase the safety of the passengers, the sizing of this structure is described in Section 9.5.

9.1.2. EASA crashworthiness regulations

EASA has compiled Crashworthiness Requirements for Special Condition VTOL, based on requirements for small aircraft (CS-23) and rotorcraft (CS-27). The requirements are divided into three paragraphs and serve as a baseline for the design of the fuselage and the packaging of the systems within it. The requirements and their description are listed below.

SC-VTOL.2270

"Occupant protect systems shall include seat belts and shall not cause secondary injury to an occupant. Baggage items shall not move during an emergency landing, preventing it from injuring occupants or damaging flight controls."

The baggage compartment will therefore be placed aft of the last seat row, and all luggage will be secured. Furthermore, ultimate load factors are imposed on occupants and other items of mass during emergency landings, including dynamic conditions. The Means of Compliance for this requirement are based on CS-23/27.561, which describes that the downward occupant load shall not exceed 20 g during a 9.1 [m/s] impact, which covers 95% of rotorcraft crashes. The design of the energy-absorbing structure to satisfy this requirement is presented in Section 9.5.

SC-VTOL.2325

"Fire initiation shall be minimized by implementing an effective cooling system and by developing, testing, and maintaining leak-tight tanks and tubes. Furthermore, no component shall ignite automatically after a survivable emergency landing. Fire propagation shall be minimized by adapting fire extinguishing systems and by placing fire retardant material between the cabin and designated fire zones."

Due to this requirement, it was chosen to locate all fuel cell related systems aft of the cabin. An additional benefit of storing the power system in the rear fuselage is the prevention of rollover. A firewall is placed between the power system and the cabin to protect the occupants against potential fire from this system.

SC-VTOL.2430

"Hazards to the cabin caused by the energy storage system shall be minimal during a crash that is otherwise survivable. The hydrogen tank shall be completely leak-tight and self-insulated, and any projectile release shall not injure any occupants or critical components."

This is an important consideration while designing and locating the hydrogen system component, especially the connection of tubes, which have the highest risk of releasing hydrogen. Furthermore, the hydrogen tank shall survive an impact velocity of 15.2 [m/s], which covers 99% of all rotorcraft crashes. This requirement is based on CS-27.952. To stay conservative, it was decided to use the crashed diameter coefficient to safely place the hydrogen tanks in the tail cone. By designing it and placing it to resist above mentioned impacts, it is assured that the tank will not impose safety hazards. The crashed diameter coefficient and its application to the tail cone sizing will be explained in Section 9.6.

9.2. In-flight loads

The maximum loads on an aircraft are determined by constructing a manoeuvre and gust envelope, this procedure is thoroughly described in [1] but will be shortly explained here. The equations are the same but the values will have to be updated due to our design. The maximum load factors for the manoeuvre diagram are set by EASA to be no higher than 2.5 and not lower than -1. The gusts at V_b, V_c and V_d are given by EASA to be 20.12, 15.24 and 7.62 [m/s] respectively. V_b is the design velocity for maximum gust velocity and is obtained from requirements from EASA [46] and Introduction to Aerospace Flight Vehicles [47]. The dive velocity V_D is given by multiplying the cruise velocity V_C by 1.25. Mirroring the points in $n = -1$ gives the entire gust diagram and completes the load diagram.

$$n = \frac{\rho v^2 C_{L,max}}{2W/S} \tag{9.1}$$

$$n = 1 + \frac{\rho V C_{L_\alpha} u}{2W/S} \tag{9.2}$$

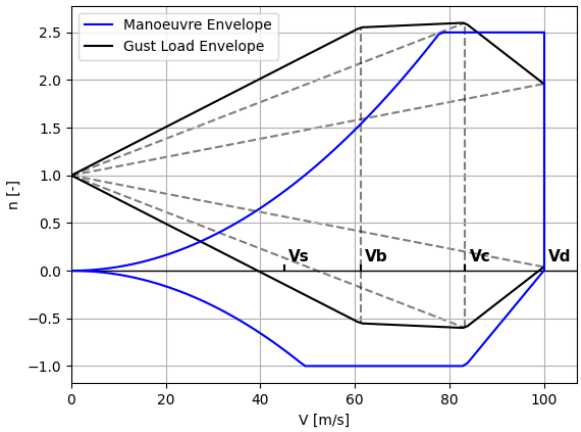

Figure 9.1: *Load diagram for the flight envelope of Aetheria*

This results in a maximum load factor of $n_{max} = 2.6$ which give the ultimate load factor by multiplying it by a safety factor of 1.5, $n_{ult} = 3.9$. This will also be used in designing the wingbox.

9.3. Wingbox Design

To come up with an optimized design, a Python model was used[48]. The model determines the geometry, loads and stresses on the wingbox after which it checks these loads with the constraints set on them by certain failure modes. A genetic algorithm is used to map the design space after which an optimization algorithm is used to determine the values for which the wingbox passes the criteria and has the lowest weight. First the assumptions are listed, then the geometry calculations are described, then the load and stress calculations, after which the constraints are given and then the resulting wingbox will be shown and described. The ultimate load factor is derived from Section 9.2 and the safety factor is set by regulations at 1.5.

Assumptions

- **Symmetric Cross-Section:** The wing cross-section is assumed to be symmetric about the longitudinal axis of the aircraft.
- **Thin-Walled Assumption:** The wing structure is considered to be thin-walled, implying that the thickness of the wing components is significantly smaller than their characteristic dimensions.
- **Shear Load Distribution:** Only the skin panels and spar webs are responsible for carrying the shear loads acting on the wing.
- **Euler-Bernoulli Beam Theory:** The wing is modeled as a clamped beam at the root using the Euler-Bernoulli beam theory. This assumption implies that the wing experiences only small deflections, and the theory may not be valid for large deflections.
- **Negligible Drag**: The wing is designed primarily for lift and torsion, assuming that the drag contribution is negligible.
- **Rectangular Wing-Box**: The wing-box structure is simplified as a rectangular shape and does not precisely follow the contour of the specific airfoil shape.
- **Constant Stringer Pitch and Size:** The pitch (spacing) and size of the stringers remain constant throughout the wing structure.

- **Rib Function:** Ribs are utilized to prevent buckling of the stringers and maintain the integrity of the skin.
- **Z-Stringers:** Z-shaped stringers are employed in the wing structure.
- **Aircraft Coordinate System:** The aircraft body coordinate system is adopted, with the x-axis aligned in the nose direction, the y-axis in the span direction, and the z-axis pointing downward.
- **Single-Wing Model:** Only one wing (the left wing) is modeled due to the assumption of symmetry between the wings.
- **Point Load Representation:** Engine forces are simplified as point loads acting on the wing structure.
- **Analysis Scenarios:** Two flight scenarios are considered: vertical flight and horizontal flight.
- **Horizontal Flight:** In horizontal flight analysis, no torsion is considered, and the lift generated by aerodynamic forces is the primary load.
- **Vertical Flight:** In vertical flight analysis, torsion is introduced from the root to the inboard engine due to the pylon, while aerodynamic lift is assumed to be absent.

It is important to note that these assumptions help simplify the analysis and may introduce certain limitations to the model. The design variables were chosen to be the spar thickness, the stringer height, the stringer width, the stringer thickness and the skin thickness. This were chosen since they had the biggest effect on the different constraints. The input vector is thus $X = [t_{sp}, h_{str}, w_{str}, t_{str}, t_{sk}]$

9.3.1. Wingbox geometry

The wingbox is modelled as a rectangle with half of an ellipse in the front and a triangle in the back (as seen in Figure 9.2), this is done to greatly simplify the calculations. The chord length, chord height, stringer area and stringer moment of inertia were calculated respectively with Equation 9.3, Equation 9.4 , Equation 9.5, Equation 9.6. Where y is the spanwise location with 0 taken at the chord root.

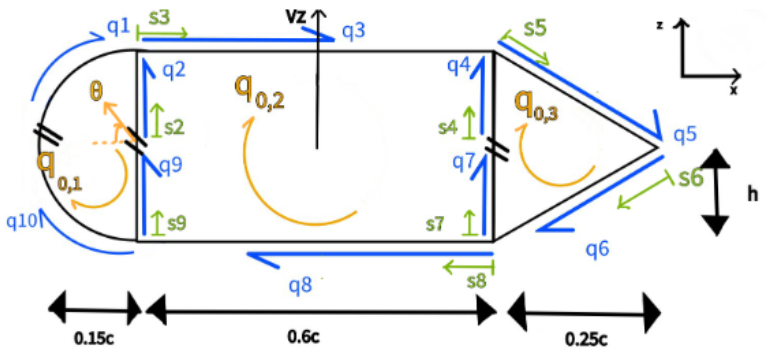

Figure 9.2: *Simple drawing of the wingbox and the shear flow through each member.*

$$c(y) = c_r - c_r(1-\lambda)\frac{y}{b/2} \tag{9.3}$$

$$h(y) = (t/c)_{airfoil} \cdot c(y) \tag{9.4}$$

$$A_{str} = (w_{str}\, t_{str}) + (h_{str} - 2t_{str}) \cdot t_{str} \tag{9.5}$$

$$I_{str_{xx}} = \frac{t_{st} h_{st}^3}{12} + \frac{w_{str}\, t_{str}^3}{12} + 2A_{str}\left(\frac{h_{str}}{2}\right)^2 \tag{9.6}$$

Throughout this design Z-stringers are used because of the ease of manufacturing and their accessibility. The size of the stringers are parameterized in the model to come up with the strongest design and the lowest weight. The other values that are parameterized are the spar thickness and the wing skin thickness. The spars are modeled as I-beams where the width of the flange is 30% of the spar height which is the same as the wingbox height. The first spar is located at 15% of the chord and the rear spar is located at 75% of the wingbox to keep room for high lift devices and to keep the rectangular shape. The ribs are modeled as rectangles with the same size as the wingbox, there will be 10 ribs spaced uniformly along the wingbox. This number was chosen for ease of calculation since the wing is divided up into 10 sections where the stresses were calculated. This number of ribs also optimized the stringer buckling behavior, the rib thickness was chosen to be 3 mm since research from NASA determined this to be an optimal thickness for aeroelasticity [1].

9.3.2. Load calculations

The loads are calculated for both the horizontal- and vertical flight situations, these procedures are described below.

Weight

First the mass of the wingbox along the span is calculated, this is the same in both horizontal- and vertical flight. The mass of each individual component was calculated using the following formulas, the skin mass was calculated using Equation 9.7 for the top and bottom, Equation 9.8 was used to calculate the mass of the half ellipse of the leading edge, Equation 9.9 was used to calculate the mass of the skin of the trailing edge, the rib mass was calculated using Equation 9.10, stringer mass was calculated using Equation 9.11 and the spar mass was calculated using Equation 9.12.

$$m_{skinwingbox} = \left[\left(0.6c(y) + 0.6c(b/2)\right) * (b/2 - y)/2\right] \cdot 2 \cdot t_{skin} \cdot \rho \tag{9.7}$$

$$m_{skinLE} = \pi \cdot \left(3(0.15c(y) + h(y)) - \sqrt{(3 \cdot 0.15c(y) + h(y)) \cdot (0.15c(y) + 3h(y))}\right)/2 \cdot t_{skin} \cdot \rho \tag{9.8}$$

$$m_{skinTE} = \sqrt{(0.25 \cdot c(y))^2 \cdot (h(y))^2} \cdot 2 \cdot t_{skin} \cdot \rho \tag{9.9}$$

$$m_{rib} = 0.6c(y) \cdot h(y) \cdot t_{rib} \cdot \rho \tag{9.10}$$

$$m_{stringer} = A_{stringer} \cdot y \cdot \rho \tag{9.11}$$

$$m_{spar} = A_{spar} \cdot y \cdot \rho \tag{9.12}$$

$$W_{total} = (m_{skinwingbox} + m_{skinLE} + m_{skinTE} + m_{rib} + m_{stringer} + m_{spar} + 2m_{engine}) \cdot g \tag{9.13}$$

Shear forces

The aerodynamic loads during horizontal flight are taken from AVL as described in Section 6.5. These loads are multiplied by the ultimate load factor to design the wing structure for all cases. The thrust force is taken as the maximum thrust that can be delivered by the engine multiplied by the safety factor (1.5) to account for gusts. During horizontal flight the shear force in the wingbox is equal to the lift on the wingbox minus the weight of the wingbox and the engines. For vertical flight, the shear along the wingbox is the thrust (or lift) supplied by the engines minus the weight of the wingbox. Both situations are plotted in Figure 9.4.

[1] Accessed on 17 June 2023, https://ntrs.nasa.gov/api/citations/20140007307/downloads/20140007307.pdf

Torsion

For the vertical flight case, the displacement of the inboard engine from the wingbox centerline causes a torsional moment. The outboard engine of the eVTOL is placed at 20% of the tip chord (as described in Subsection 8.2.1) this creates only a very small torsional moment. However, for the inboard section, this is not the case, the torque is calculated in Equation 9.14 where l_{pylon} is the length of the pylon, F_T is the thrust force of the engine and W_{eng} is the weight of the engine.

$$T = l_{pylon} \cdot (F_T - W_{eng}) \tag{9.14}$$

9.3.3. Stress calculations

Shear flow

The shear flow in the wingbox is in both situations caused by the shear forces. However, during vertical flight the inboard engine is positioned on a pylon which causes a big torsional moment around the wingbox. In the calculations below the shear flow in each member of the wingbox due to the shear force is calculted. At the end the torsion is also calculated for the vertical flight case and super positioned onto the previous problem.

First the base shear flow in each member is calculated using Equation 9.15 while assuming a cut at the leading edge of the wingbox (the direction of the flows can be seen in Figure 9.2). Then the redundant shear flow is determined by setting the rate of twist to zero as in which is applied in each cell in order to provide a consistent twist of the entire cross-section (one cell can not have a different twist from the other cells). The numerical values of the redundant shear flow can be calculated using $A \cdot \bar{q_{0,x}} = -\bar{b_x}$. Here the indices of A indicate the geometry integrals $\oint \frac{ds}{t}$. The index indicates the geometry. For example, index 11 shows the geomtry integral corresponding to the shear present in cell 1 only, whereas index 12 corresponds to the region that is exposed to the shear flow in both cell 1 and cell 2 (thus the spar web). The total base shear flows are calculated below. Once the base and redundant shear flow are superimposed, the maximum shear flow in the cross-section can be identified.

$$q(s) = \int_0^s \frac{\delta q}{\delta s} ds = -\frac{V_z t}{I_{xx}} \int_0^s z ds - \frac{V_x t}{I_{zz}} \int_0^s x ds = -\frac{V_z t}{I_{xx}} \int_0^s z ds \tag{9.15}$$

$$T_{total} = \sum_{i=1}^{3} 2 q_i A_i \tag{9.16}$$

However, for the vertical flight the shear flow due to the torsion also has to be calculated. Since the left wing is modeled, the torsion is positive in clockwise direction so it is assumed the torsion of each cell is positive in the same direction as the redundant shear flow from the previous calculation. The shear flow is calculated for each section with Equation 9.16 where the i indicates which cell is analyzed. This shear flow is then added to the previously calculated shear flow to determine the maximum shear flow in the section. These are plotted below in Figure 9.4.

Bending moment and stress

The bending moments in both cases are caused by both the wing weight and the lift on the aircraft. The only difference is that in the vertical flight case this lift is supplied by the thrust of the engines and the outboard engine thrust causes a big moment due to the long moment arm. Both are calculated with Equation 9.17. This moment causes a bending stress which is calculated using Equation 9.18.

$$M_x(y) = \int_0^y V(y) dy + \sum W_{rib,i} \cdot [y - y_{rib}] + \sum W_{eng,i} \cdot [y - y_{eng,i}] \tag{9.17}$$

$$\sigma_{x,max}(y) = \frac{M_x(y) h(y)/2}{I_{xx}(y)} \tag{9.18}$$

9.3.4. Constraints

Now that all the stresses, loads and geometries are calculated the constraints can be added. Each constraint checks the current maximum stresses and compares them to the stress constraints as listed below. The model interprets this as the ratio between the actual maximum load with a safety factor and divides this by the maximum stress associated with this constraint. Then one is subtracted from this ratio since the optimizer wants to minimize all these ratios.

Combined compression and shear buckling

The skin between the stringers can buckle when loaded in compression and shear,. The critical buckling stress for both shear and compressive stress are calculated respectively in Equation 9.19 and Equation 9.20. Here b_{st} is the stringer pitch, k_c is the buckling coefficient which depends on the size of the skin panel and the boundary conditions it is subjected to. This k_c is shown in Figure 9.3a for different boundary conditions and skin aspect ratio's. For this situation, it has been assumed the skin is simply supported by the stringers, so following curve C leads to a conservative estimate of 4 for the skin buckling coefficient k_c. There is also a k_s for the shear buckling equation which is shown in Figure 9.3b, here the same procedure is followed and simply supported edges are assumed. This leads to a value of 5.35 for k_s. Now the optimizer has to check the constraint shown in Equation 9.27 where it checks the ratios.

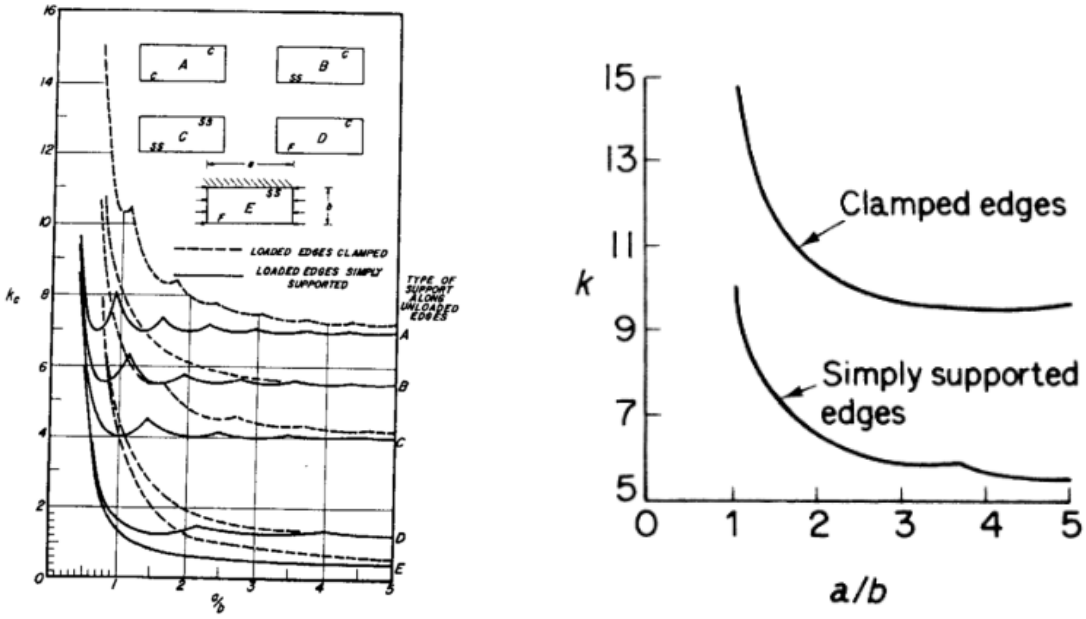

(a) *Compressive buckling coefficient* **(b)** *Shear buckling coefficient*

Figure 9.3: *Buckling coefficients*

$$\sigma_{cr,x} = k_c \frac{\pi^2 E}{12(1-\nu)} \left(\frac{t_{sk}}{b_{st}}\right)^2 \tag{9.19}$$

$$\tau_{cr,xy} = k_s \frac{\pi^2 E}{12(1-\nu)} \left(\frac{t_{sk}}{b_{st}}\right)^2 \tag{9.20}$$

$$\frac{\sigma_x \cdot SF}{\sigma_{cr,x}} + \left(\frac{\tau_{xy} \cdot SF}{\tau_{cr,xy}}\right)^2 \leq 1 \longleftrightarrow \frac{\sigma_x \cdot SF}{\sigma_{cr,x}} + \left(\frac{\tau_{xy} \cdot SF}{\tau_{cr,xy}}\right)^2 - 1 \leq 0 \tag{9.21}$$

Von Mises

Yield stress is dangerous for aluminium wingboxes, for composites the program will use it's com-

pressive strength since this is the expected failure mode. This constraint checks if the maximum stresses defined by the material properties are not exceeded. Equation 9.22 shows the formula and Equation 9.23 shows the constraint.

$$\sigma_{VM} = \sqrt{\frac{1}{2}[(\sigma_{xx}-\sigma_{yy})^2+(\sigma_{yy}-\sigma_{zz})^2+(\sigma_{zz}-\sigma_{xx})^2]+3(\tau_{xy}^2+\tau_{yz}^2+\tau_{xz}^2)} = \sqrt{\frac{1}{2}\sigma_{zz}^2+3\tau_{xz}^2} \quad (9.22)$$

$$\sigma_{VM} \cdot SF/\sigma_{yield} - 1 \leq 0 \quad (9.23)$$

Stringer buckling

Stringer buckling occurs when the compressive forces become too great due to the bending moments. The actual compressive stress is converted to a force by multiplying it by the stringer area, the constraint is shown in Equation 9.24 and Equation 9.25where L is taken as the rib pitch since these constrain the stringers and divide it up into sections.

$$P_{crit} = \frac{\pi^2 E I_x x}{L^2} \quad (9.24) \qquad \frac{\sigma_x \cdot A_{str} \cdot SF}{P_{crit}} - 1 \leq 0 \quad (9.25)$$

Global skin buckling

Despite the stiffening effect of the stringers, a panel can still buckle. Here the entire skin width is taken instead of the stringer pitch, the stringers still have some supporting effect so this is taken into account in $t_{smeared}$. This factor is determined by smearing their thickness to the skin thickness which is shown in Equation 9.26. With this the global buckling stress can be calculated in the same way as in Equation 9.20, one just has to replace t_{sk} by $t_{smeared}$. This new constraint is shown in Equation 9.27.

$$t_{smeared} = \frac{t_{sk} \cdot b + n_{str} \cdot t_{str} \cdot (h_{str} - t_{sk}}{b} \quad (9.26) \qquad \frac{\sigma_x \cdot SF}{\sigma_{x,cr,global}} - 1 \leq 0 \quad (9.27)$$

Fatigue

One constraint that has been omitted from this section is the crippling or fatigue constraint. Crippling and fatigue occur when a structure is submitted to a large number of load cycles with loads that do not exceed the failure limit. However, the recurring load cycles can weaken a structure. The reason this was left out of the report is that cripple and fatigue analyses are quite inaccurate, these types of analyses are better done by testing. Using formulas gives a rough estimate but this is still difficult for composite structures because of their novelty. One thing that can be taken into consideration is that studies have shown that composites often have higher fatigue strength than their aluminium and titanium counterparts [2]. This helps in the material choice and gives some confidence in the fatigue life of composites.

9.3.5. Material selection

The structural components will make up the largest part of the total weight, so their selection is of utmost importance. For long, aluminium alloys have been the optimal material due to their high strength-to-weight ratio. However, the use of composites has emerged in the aerospace sector, especially in the upcoming eVTOL market[3]. For battery powered aircraft, reducing structural weight by using composites is crucial to achieve range requirements. Composites come with disadvantages however, their environmental sustainability is not as good as aluminium. This is mainly due to the

[2] Accessed on 17 June 2023, https://doi.org/10.1016/j.proeng.2013.12.128

[3] Accessed on 17 June 2023 https://www.compositesworld.com/articles/composite-aerostructures-in-the-emerging-urban-a

novelty of carbon fibre parts, the process of recycling these parts is quite new as well so this might improve in the future. Composite production also emits more greenhouse gasses, however, the use of a lighter structure requires less propellant which in turn reduces the required energy during the operation life. Therefore, the team has decided to consider composite structures because of their lightweight characteristics. The material will be chosen based on their resulting wing weights.

Three materials were considered for the wingbox elements, the first is an aluminium and titanium alloy (AA7075-T6). It is one of the aluminium alloys with the highest strength-to-weight ratios [4] which is why its often used in wingboxes. Two composites were considered as these materials are currently emerging in the eVTOL market, they are both fabric composites with quasi-isotropic properties. The specifications of these materials are shown below in Table 9.1. The resulting wing weights will be given for each material, and the material with the lowest resulting weight will be chosen. This is because the lower weight results in less required fuel which greatly impacts the sustainability of the aircraft.

Table 9.1: *Material properties*

Materials	**MAT01** [49] **Solvay CYCOM 977-2A HTA**	**MAT05** [49] **Toray M46J Fabric**	**AA7075-T6** [5]
Longitudinal E-mod [N/m^2]	5.96×10^{10}	1.26×10^{11}	7.17×10^{10}
Transverse E-mod [N/m^2]	5.61×10^{10}	1.26×10^{11}	7.17×10^{10}
Shear modulus G [N/m^2]	3.1×10^{9}	4.00×10^{9}	2.69×10^{10}
Poisson's ratio v [-]	0.064	0.3	0.33
Density [kg/m^3]	1522	1600	2810
Tensile strength [MPa]	722.6	689	572
Compressive strength [MPa]	810	407	503[6]

9.3.6. Results

The optimizer was set up to make sure the constraints were met and the weight of the wing was minimized, this did include the engine weight but the results in Table 9.2 do not include these weights. The input vector was $X = [t_{sp}, h_{str}, w_{str}, t_{str}, t_{sk}]$, limits were set on these variables to ensure feasibility. The upper limit for the stringer height was the height of the wingbox at the tip divided by two. this to make sure everything would fit inside the wingbox since the space at the wing tip is limited. The lower bounds were taken to be 5mm for the spar thickness, 1.5 [cm] for both the stringer height and the stringer width, 2 [mm] for the stringer thickness and 0.8 [mm] for the skin thickness. This was chosen since stringers smaller than this are difficult to manufacture. It was also noted that the optimizer tended to minimize the stringer size since this was more effective than increasing the skin thickness. But this would often result in stringer heights of 2 [mm] so the 1.5 [cm] was chosen as a limit to make sure the stringers would have realistic proportions and still be manufacturable.

The three materials mentioned in Subsection 9.3.5 are all considered by the optimizer, it will minimize the weight for all three materials and a set number of stringers. With these results the configuration with the lowest wing weight can be chosen.

[4] Accessed on 18 June 2023, https://www.aircraftaluminium.com/a/the-strongest-aluminum-alloys-used-in-aircraft.html

Table 9.2: *Effects of materials and stringer number on wing mass*

No.str[-]	**MAT01**[kg]	**MAT05**[kg]	**AA7075-T6**[kg]
0	556.4	440.6	893.3
8	199.5	191.1	366.6
13	184.4	171.5	319.0
14	183.0	**169.0**	319.5
15	182.9	169.4	318.3
18	188.2	172.2	321.8
20	185.89	174.6	325.6

Table 9.3: *Resulting configuration*

Property	**value**
Weight	173.7$[kg]$
t_{spar}	5$[mm]$
$h_{stringer}$	15$[mm]$
$w_{stringer}$	15$[mm]$
$t_{stringer}$	2.2$[mm]$
t_{skin}	1.6$[mm]$
Material	MAT05
No. stringers	14

As seen above in Table 9.2, the lowest weight is reached by using material 1 (Solvay CYCOM 977-2A HTA) and 14 stringers. With this design, the following stresses and forces are experienced in both horizontal and vertical flight, they are shown in Figure 9.4 and the stresses at the root are given in Table 9.4.

Table 9.4: *Loads experienced at the root for both horizontal and vertical flight.*

Load	**Horizontal**	**Vertical**
Lift/Thrust[kN]	46.5	17.4
Weight[lN]	2.78	2.78
Shear force[kN]	43.8	14.7
Moment[kNm]	100.6	51.6
Axial[MPa]	97.3	43.1
Shear flow[kN/m]	142.6	48.5

Table 9.5: *Constraint ratio's for both horizontal and vertical flight.*

Constraint	**Horizontal**	**Vertical**
Local buckling	0.498	0.759
Von Mises	0.396	0.161
Stringer buckling	0.249	0.611
Global skin buckling	0.958	0.978

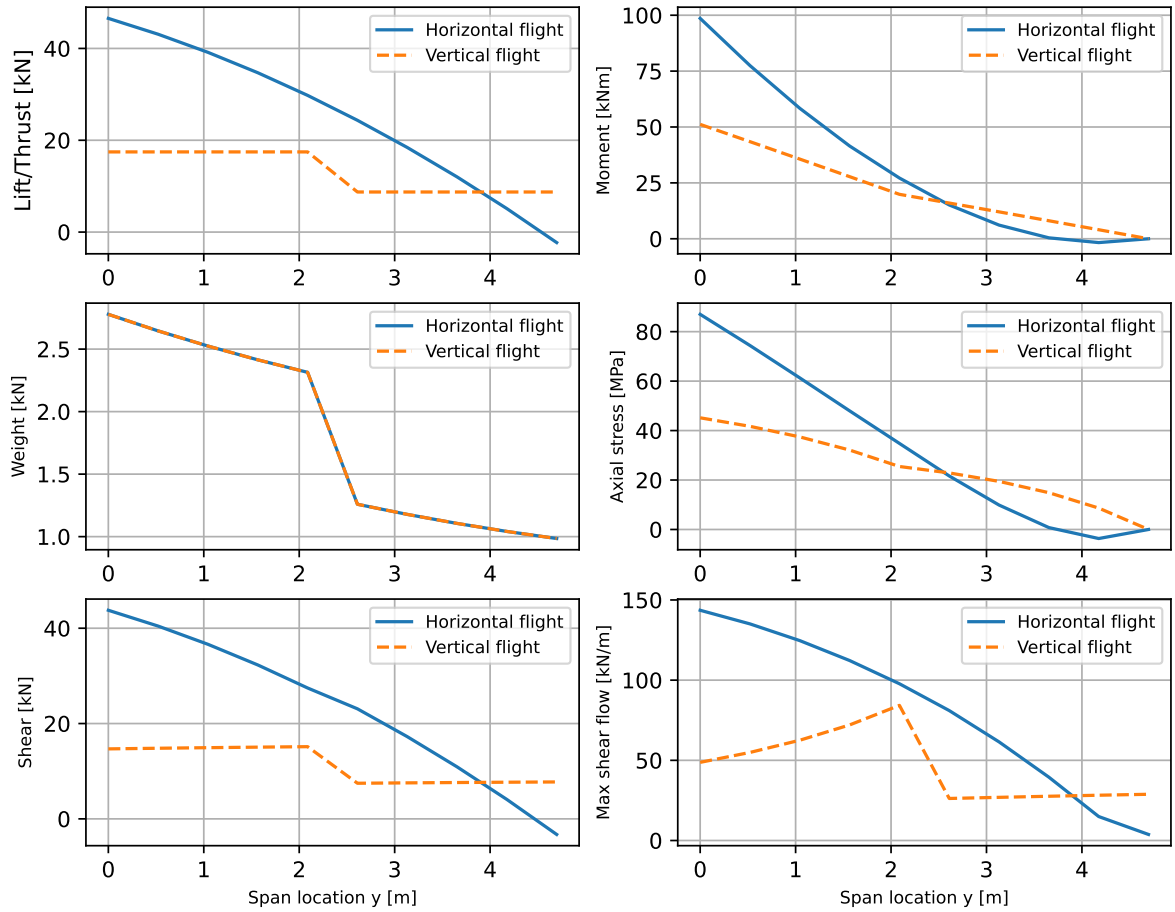

Figure 9.4: *Loads experienced by the final wingbox design*

As can be seen above, the shear flow is quite high, this is to be expected with the ultimate load factor applied to the lift. This causes the high shear force which in turn causes the high shear flow. Also, the optimizer has shown that it hasn't fully reduced a constraint to zero, this is the case because of the limits on the design variables. This does show that the model would even further lower these design variables but this is not always feasible. The model would like to have a high number of very small stringers since these have a lower contribution to the weight and a high contribution to the bending resistance. The effect of changing the different constraints can be further analyzed with a sensitivity analysis but this is not included due to lack of time.

All in all, the model has optimized the wingbox design to meet the structural requirements and constraints while maintaining a minimal weight. This model can be used in the future and can be expanded with more failure modes, especially for composite structures the failure modes can be more thoroughly analyzed. But for the scope of this project the model has worked as required and will also be used to design the wingbox of the v-tail.

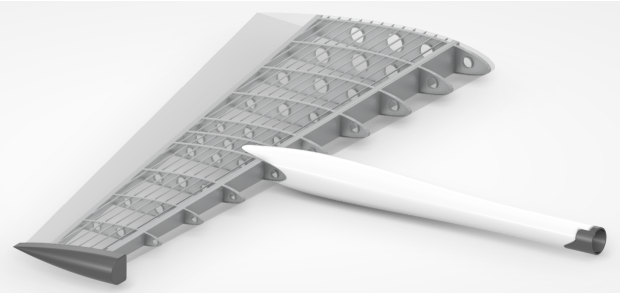

Figure 9.5: *Right wingbox design with outboard nacelle and inboard pylon*

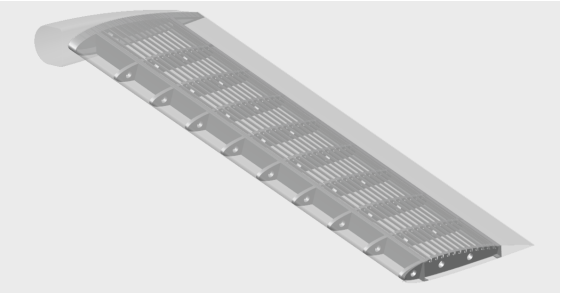

Figure 9.6: *V-tail right wingbox design (with top stringers) with outboard nacelle*

9.3.7. V-tail wingbox design

For this design the same procedure was used as for the wingbox of the main wing, this is described in the Section 9.3. The only difference is that the weight and thrust loads are now under an angle. For simplification it is now assumed the thrust acts as an upward pointload at the center of the wingbox and the weight acts as downward distributed load along the centerline of the wingbox. The lift is modelled as a distributed load pointing perpendicular to the center line. The frame of reference is still the face of the wingbox so the thrust and weight forces now result in a compressive and tensile force respectively, a sketch of the situation is shown in Figure 9.7. The loads for the tail are retrieved from AVL as described in Section 6.5. The design variables are also $X = [t_{sp}, h_{str}, w_{str}, t_{str}, t_{sk}]$ and the same composite material is used.

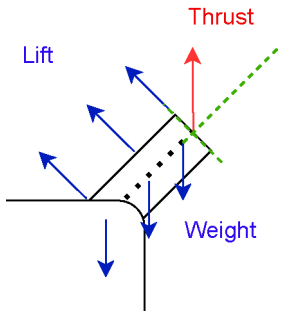

Figure 9.7: *Front view: sketch of the V-tail wingbox analysis*

Table 9.6: *Resulting configuration*

Property	Value
Weight	45.4$[kg]$
t_{spar}	5.0$[mm]$
$h_{stringer}$	15.0$[mm]$
$w_{stringer}$	15.0$[mm]$
$t_{stringer}$	2.0$[mm]$
t_{skin}	1.3$[mm]$
Material	MAT01
No. stringers	8

9.4. Pylon Design

To accommodate the requirements for the x-location of the inboard engines as described in Subsection 8.2.1, a pylon has been designed. This pylon's length has been optimized in Subsection 8.2.1 to guarantee stability and control in case of one-engine-inoperative. This pylon has been sized using a code that checks the same constraints as described in Section 9.3. The ones applicable are the von mises yield and the column buckling constraint, the pylon's eigenfrequency was also determined and set to be above 20$[Hz]$. It was modeled as a hollow tube and the dimensions are listed in Table 9.7, the same carbon material was used in the wingbox because of its low density and high strength. The tube will primarily have to deal with torsion due to the rotation of the propeller and bending due to the weight and the vertical flight thrust. A tube was chosen over other shapes such as I-beams since they offer the best overall performance in both torsion and bending [50].

Table 9.7: *Pylon properties*

Property	Value
Pylon length	2.6[m]
Moment of Inertia	$9.4e^{-5}$[m^4]
Tube inner radius	121.8[mm]
Tube thickness	14.0[mm]
Material	MAT05 (9.3.5)

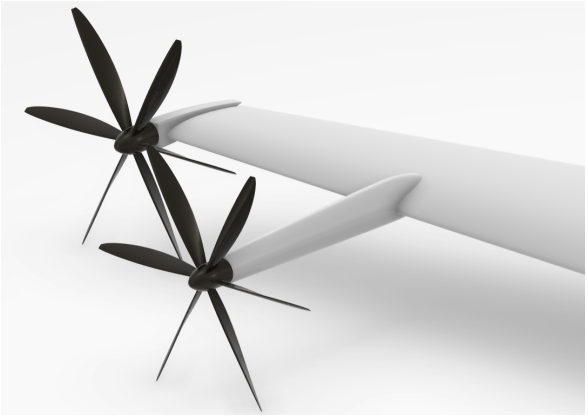

Figure 9.8: *Pylon design*

9.5. Crash Energy Absorbing Structure Design

As discussed in Section 9.1, the occupants shall be protected in the case of an emergency landing. This section provides the design of a Crash Energy Absorbing Structure, that shall mitigate the impact forces during a crash event to minimize the accelerations felt by the occupants. An optimal crash structure maximizes the deceleration distance and time, thereby lowering the instantaneous velocity change felt by the human body, which in turn reduces injuries and prevents fatalities. This is achieved by absorbing the kinetic energy while plastically deforming the structure.

The preliminary design of the crash structure will be presented in this section. It is important to acknowledge that comprehensively modeling the complete dynamics of the frame, skin, crash structure and seats during a crash impact entails high complexity that cannot be performed with simple equations. It has therefore been chosen to size the crash structure as if it crashes independently with presence of the aircraft mass on top. This sizing will yield the external dimensions of structure necessary for compliance with the regulations.

The crash structure is designed with SC-VTOL.2270 in mind [51]. This requirement states that the downward acceleration should not exceed 20 g during a crash that covers 95% of rotorcraft crashes (9.1 [m/s]). Furthermore, the peak acceleration shall be 30 g minimum and not occur no later than 0.031 [s] after impact.

The crash structure deformation is modelled with the conservation of energy. The kinetic energy of the aircraft is absorbed by the crushing of the honeycomb structure below the cabin. The formulas for the kinetic and absorbed energy are displayed in Equation 9.28 and Equation 9.29 respectively.

$$E_k = \frac{1}{2} m \left(\frac{ds}{dt} \right)^2 \tag{9.28}$$

$$E_{cr} = \sigma_{cr} A s \tag{9.29}$$

Here, E_k is the kinetic energy, m the aircraft mass, s the deceleration distance, E_{cr} the absorbed crash energy, A the crash structure area and σ_{cr} the crushing stress. This stress is dependent on the strain and this relation can be displayed in a stress-strain curve. The curve can be divided into three segments. The first is the elastic region, where the slope of the curve is determined by the Young's Modulus. The stress region culminates in a stress peak, after which the stress reduces to the plateau stress. Lastly, at high strain levels, densification takes place, signifying the near-complete crushing of the honeycomb structure. During this segment, the stress increases rapidly as the opposing cells in the structure start to press against each other. The structure shall be designed in such a way that densification will not that place, as the acceleration will quickly reach unacceptable levels that could severely injure passengers. The total height of the crash structure will therefore need to be higher

than the deformed height after a crash.

The deceleration experienced by the occupants can be obtained by differentiating, equating and rearranging Equation 9.28 and Equation 9.29:

$$\frac{d^2s}{dt^2} = \sigma_{cr}(\epsilon)\frac{A}{m} \tag{9.30}$$

The material properties of the honeycomb structure can be modified by altering key design parameters, such as ply thickness and cell size. These modifications enable control over the stiffness and strength to make the crash structure satisfy to comply with the regulations.

In this phase of the design, it has been chosen to only size the external dimensions of the crash structure by specifying its stress and strain characteristics. The complete internal design of the honeycomb structure can be performed in a more detailed design phase. The optimisation of the crash structure has yielded the acceleration response as displayed in Figure 9.9.

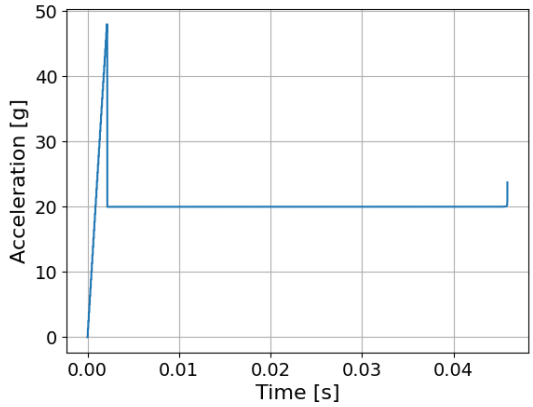

Figure 9.9: *Acceleration overtime after a crash with an impact velocity of 9.1 [m/s]*

As can be seen, the requirements from SC-VTOL.2270 are met. The initial period is characterised by the elastic region and peak stress. The peak acceleration during this impact is 48 g, which human bodies can survive for periods of one millisecond [52]. The acceleration is only above 20 g for one millisecond. During the rest of crash, the acceleration at 20 g is determined by the plateau stress. The peak and plateau stress and peak and densification strain are displayed in Table 9.8 and were adapted from existing honeycomb structures to align with the requirements [53].

Table 9.8: *Stress and strain values for the crash structure*

Peak Stress [MPa]	**Plateau Stress [MPa]**	**Peak Strain [-]**	**Densification Strain [-]**
1.2	0.50	0.038	0.89

The optimised crash structure has a height of 0.23 [m] and an area 0.98 [m^2] and can be observed below the cabin in Figure 9.15. As stated above, it is essential to recognize that the current model only models the crash structure as a standalone unit subjected to a crash. Consequently, is not an exact representation of the final crash structure. However, these dimensions can be used as an input for the fuselage design.

9.6. Fuselage Design

The fuselage is split up into three sections, the cockpit, the cabin and the tail cone. Since the flight altitude is only 2400 [m] there will be no need for a pressurized cabin, this causes the fuselage to be designed as a rectangle with curved edges to minimize drag and reduce unneeded volume. The cockpit and cabin space have fixed lengths, therefore in order to size the fuselage the length of the tail cone has to be determined.

9.6.1. Cockpit and Cabin

A comprehensive design of the cockpit has not been performed. Instead, the cockpit length has been set to 2 [m], based on the Lilium Jet and small business jets. The cabin section has been sized based on business jet dimensions found in Airplane Design Part III [54]. One Type IV door is placed on the left of the fuselage. The seats are 660 [mm] long and have a pitch of 1020 [mm]. The space behind the seats is allocated to cargo storage. It can hold 5 standard carry-on suitcases that are 25 [cm] deep. The total cabin length is 2700 [mm]. These dimensions are displayed in the fuselage side view in Figure 9.15.

9.6.2. Tail Cone

As explained in Subsection 9.1.2, the hydrogen tank will be placed in the tail cone of the aircraft. The tail cone will hence be sized with the use of crashed diameter coefficient, β. The crashed diameter coefficient, a novel method introduced by the DSE tutor Dr.Ing. S. Giovani Pereira Castro, relates the fuselage diameter (D_{fus}) to the maximum allowed diameter of the LH2 vessel considering post-crash deformations after a crash. For example, the crashed diameter of an A320 crash test is visualized by Dr.Ing.S.G.P Castro in Figure 9.10 for an A320.

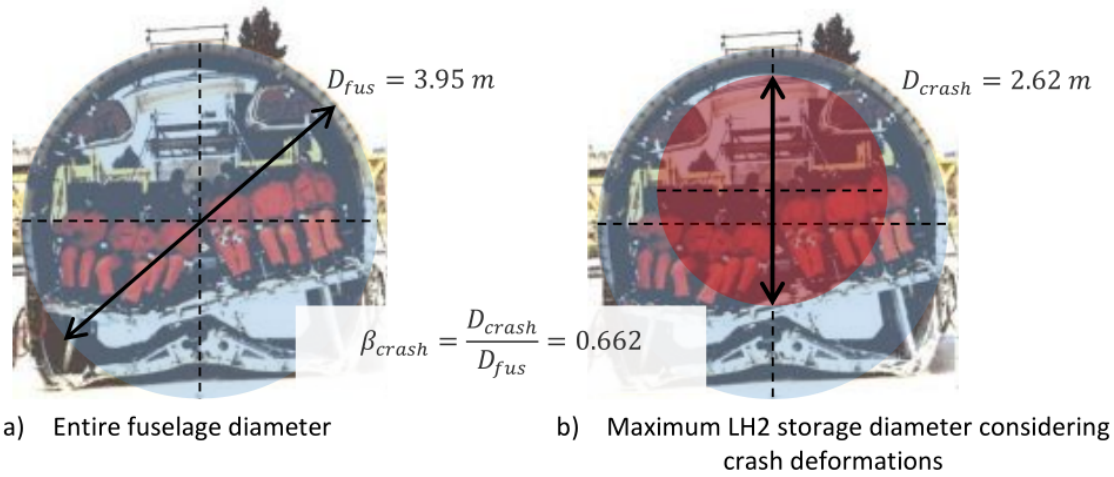

Figure 9.10: *Crashed diameter coefficient β_{crash} for the A320, modified from [55]. Figure provided by DSE tutor Dr. Ing. S. Giovani Pereira Castro.*

As Aetheria will have a rectangular cross-section, it is not possible to derive β from the fuselage diameter. The formula for β is therefore adapted to the cross-sectional area of the fuselage as shown in Equation 9.31:

$$\beta^2 = \frac{A_{crashed}}{A_{fuselage}} \tag{9.31}$$

$$AR = \frac{b}{h} \tag{9.32}$$

This is of interest since, it directly relates available volume to the fuselage dimensions. The crash area has been visualized for $\beta = 0.5$ in Figure 9.12. The assumption was that the crash cross sec-

tional area would have the same aspect ratio as the original fuselage as visualized in Figure 9.12. Where the fuselage aspect ratio is defined as shown in Equation 9.32, let b be the width of the fuselage and h the height of the fuselage.

Width and height is used as the tail cone will be modeled as a polyhedron as illustrated in Figure 9.11, which is a conservative approach as the actual shape is curved. This increases the vertical crumple zone below the hydrogen tanks. The aspect ratio of the tail-cone is varied linearly along the tail cone. At the start, the aspect ratio is determined by the cabin cross-section. The aspect ratio at the end of the tail is a variable that is optimised in order to minimize the fuselage length.

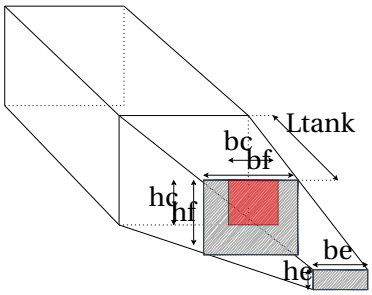

Figure 9.11: *The model used for the shape of the tail cone.*

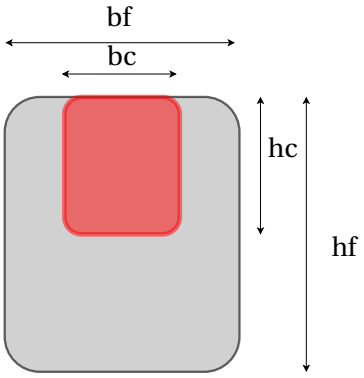

Figure 9.12: *Cross sectional visualization of how the the crashed diameter coefficient translates to a cross sectional fuselage.*

Two hydrogen tanks will be stored in the top tail section to allow for the largest crumple zone and two tanks will be placed beside each other to allow for redundancy for the hydrogen tanks. The location of storage can be seen in Figure 9.11. With a selected β of 0.5, it ensured that the hydrogen tank is not penetrated or crushed in a survivable emergency landing. Note that no stiff elements will be allowed to be placed under the hydrogen tanks as these could then penetrate the tank.

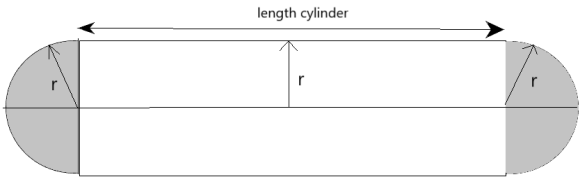

Figure 9.13: *The model of the hydrogen tank used to size the fuselage.*

Then finally, the hydrogen tank is modeled as shown in Figure 9.13. It is a cylinder with length l_{cyl} and two half spheres that have a radius equal to that of the cylinder.

Using this model and its assumptions, the following steps are used to obtain the limit fuselage length:

1. Set a L_{tank} and calculate the tank radius from the required hydrogen volume. There are two tanks, so the volume per tank is half the total volume. The volume can be computed by finding

the roots of the equation as shown in Equation 9.33.

$$\begin{aligned} V &= \pi r^2 l_{cyl} + \frac{4}{3}\pi r^3 \\ l_{cyl} &= l_{tank} - 2r \\ -\frac{2}{3}\pi r^3 + \pi l_{tot} r^2 - V &= 0 \end{aligned} \tag{9.33}$$

2. From the radius of the tank, the minimal required crash cross-section can be obtained by considering that two tanks have to fit side by side. So the width of the crash area has to be at least 4 times the width, thus leading to the simple equation Equation 9.34:

$$b_c = 4r \tag{9.34}$$

3. The tail cone cross-sectional area at the end of the hydrogen tanks can be obtained by combining equation Equation 9.31 and Equation 9.32, the result being Equation 9.35:

$$A_f = \frac{b_c^2}{AR_f \cdot \beta^2} \tag{9.35}$$

Where AR_f is the aspect ratio of the fuselage at the limiting cross-section. Which is determined by the length of the hydrogen tank, AR_{cabin} and AR_e. It is crucial to note however that AR_f is not known and no explicit solution exists as it is dependent on the tail cone length. Hence, an initial estimate is made on the aspect ratio from which a tail cone length can be computed. This new tail cone length is then used to compute an updated aspect ratio. This is repeated until an error of lower than 0.5% is achieved between AR_{f_i} and $AR_{f_{i+1}}$. Please reference Figure 9.11 for a spatial illustration of the problem.

4. The tail cone length can then be obtained using similar triangles leading to the equation shown in Equation 9.36. The assumption is that the cross-sectional surface area at the end of the tail cone approaches zero.

$$l_{tail} = \frac{h_0}{h_f} l_{tank} \tag{9.36}$$

This process is iterated for a range of L_{tank} values to find the minimal tail cone length. Thus a formal expression of the optimization is shown in Equation 9.37:

$$\begin{aligned} &\textit{Minimize: } l_{tail}(AR_e, l_{tank}, V) \\ &\textit{subject to: } 4 \cdot r(V) < b_c(AR_e, l_{tank}) \\ &\qquad\qquad 2 \cdot r(V) < h_c(AR_e, l_{tank}) \end{aligned} \tag{9.37}$$

In this optimization the volume, V, is a variable imposed by the power department and hence can not be varied. However, the length of the tank and the aspect ratio at the end of the tail AR_e can be chosen such that the length of the tail is minimized. The solution space can be plotted to visualize the optimum solution for a fixed β of 0.5. This value was chosen such that is reasonably conservative. However, there is a degree of arbitrariness in this assumption, hence a sensitivty analysis on β is performed in Section 9.9. The result is shown in Figure 9.14.

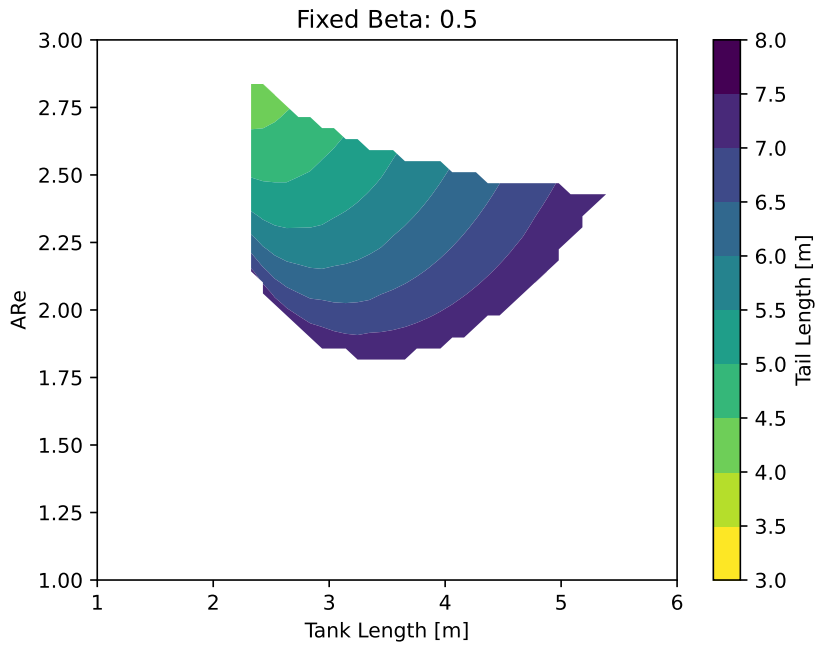

Figure 9.14: *The solution space of the optimization problem illustrated in Equation 9.37 for a fixed β of 0.5.*

Table 9.9: *Final results of the fuselage sizing*

Parameter	Value
l_{tank}	2.38 [m]
r_{tank}	0.194 [m]
AR_e	2.75 [-]
V	0.533 [m^3]
b_c	0.79 [m]
h_c	0.42 [m]
l_{tail}	4.34 [m]
Limit $l_{fuselage}$	9.50 [m]

As can be seen from the figure, the shortest fuselage length possible is for comparatively wide tail cones with a short tank length. This is sensible as a short tank length logically leads to a shorter tail cone. The wide aspect ratio follows from the fact that two tanks side by side are utilized. The sharp line on the left hand side results from the fact that not feasible design is possible below a tank length of 2.38 [m]. Based on Figure 9.14, it was decided to use an AR_e of 2.75. The analysis then results in the values as shown in Table 9.9. Resulting in a hard requirement on the crash worthy volume of 2.38 x 0.79 x 0.42 [m] in the tail cone.

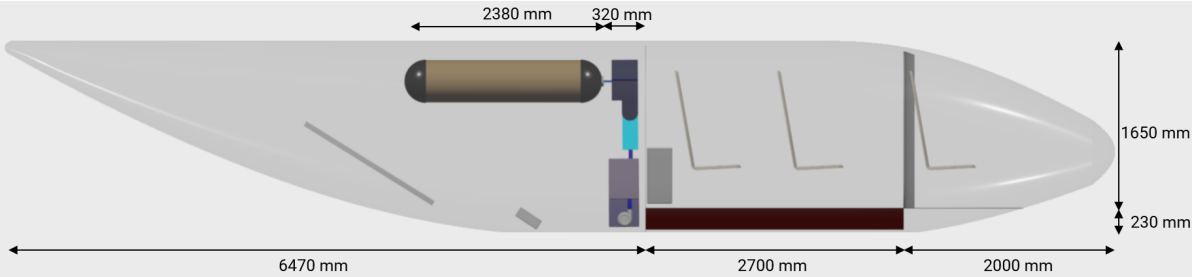

Figure 9.15: *Side view of fuselage with subsystems*

9.7. Modal analysis of the airframe

The Aetheria has six propellers each on long structural members, this inhibits the vibrational performance of the airframe. To ensure safety, reliability and performance of the airframe a modal analysis of the airframe will be performed. Specifically, the coupling between wing and tail vibrations have to inspected as it could cause catastrophic failure of the airframe. In this manner, risk TR-ST-12 is mitigated and accounted for.

The modal analysis will be performed using a Finite Element Method (FEM) implemented with the

pyfe3d library [56]. The mesh used is as shown in Figure 9.16. The beam elements used are Consistent Timoshenko beam elements [57]. The wing is modeled using 4 elements, the engine pylon is also modeled. Then finally the V-tail is simply modeled using a single element for each side. This is a valid assumption as the V tail has no taper. Additionally, the properties of the elements of the wing are taken to be the average between the nodes.

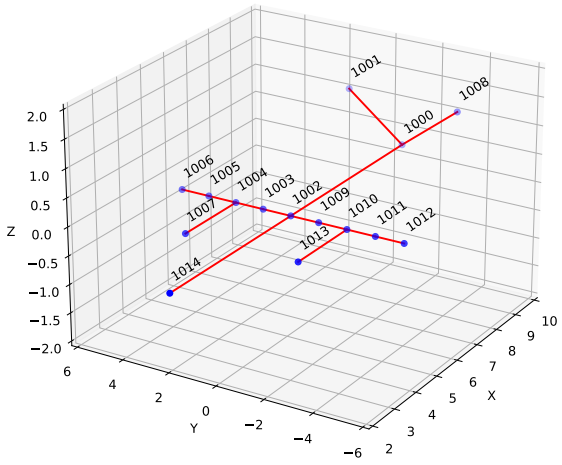

Figure 9.16: *The mesh implemented for the modal analysis of the Aetheria. The wings, V-tail and pylons are modeled within the mesh.*

Table 9.10: *Placement of the concentrated masses and boundary conditions of the model*

Node ID	**Mass** [kg]
1001	98.4
1008	98.4
1006	98.4
1007	98.4
1012	98.4
1013	98.4
1009	51.3
1010	51.3
1003	51.3
1004	51.3
Constrained Node ID	
1000	1002
1014	-

The main concern for the Aetheria is the effect of the engine and battery weight on the extremities of the aircraft. Thus concentrated masses were added as shown in Table 9.10 to model these weight. Additionally, the constrained nodes are also shown. These nodes belong the fuselage and follows from the fact that the fuselage is assumed to be sufficiently stiff.

The result of the analysis is as shown in Figure 9.17. The fundamental oscillation is the most prominent mode shape with a natural frequency of 2.7 [Hz]. It can be said with certainty this frequency would be too low to avoid resonance of various causes within the flight envelope. Examples which could excite the wing structure could be the periodic loading due to the short period eigenmotion or the engines throttling the propellers in order to keep the aircraft hovering in a stable configuration. Furthermore, mode shapes 2 and 3 have a natural frequency in the direct vicinity of mode 0 and mode 1. This is problematic as a coupling between the wing and v-tail could be excited. Twisting the fuselage and increasing the inertia of the vibration thus decreasing the effectivenss of dampening. The twisting motion of the fuselage and the oscillations of the wing and V-tail could lead to catastrophic failure of the airframe. In a best case scenario it would severely increase the process of fatigue of the materials.

The final two mode shapes, mode 4 and mode 5, describe one of the harmonics of the vertical oscillation of the wing. It has a natural frequency of 12.0 [Hz], this frequency is unlikely to be reached within the flight envelope. However, it's important to consider that flutter is a complex phenomenon influenced by a multitude of factors outside the scope of the current analysis such as control system dynamics, wing divergence and control reversal [58]. Thus, the confidence level in the fact that 12 [Hz] is a sufficiently safe frequency is relatively low.

As a final note, it can be seen that mode couples 0,1 and 4,5 differ slightly in their natural frequency even though they have identical properties. The cause of this model behaviour is unknown and the

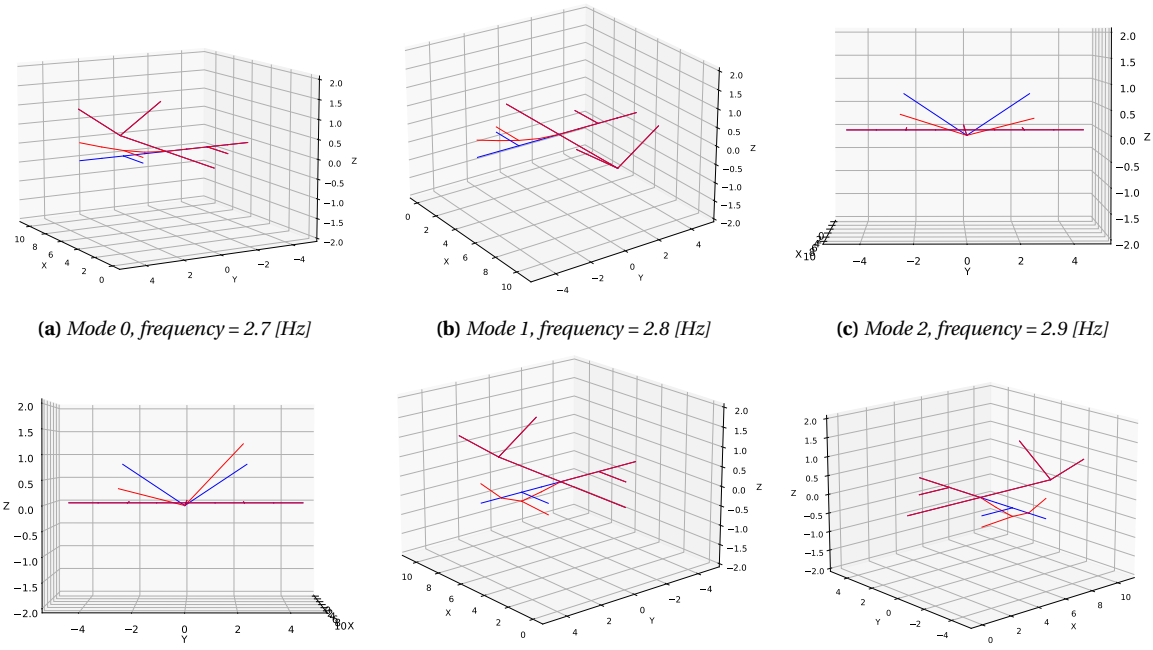

(a) *Mode 0, frequency = 2.7 [Hz]*

(b) *Mode 1, frequency = 2.8 [Hz]*

(c) *Mode 2, frequency = 2.9 [Hz]*

(d) *Mode 3, frequency = 2.9 [Hz]*

(e) *Mode 4, frequency = 12.0 [Hz]*

(f) *Mode 5, frequency = 12.3 Hz]*

Figure 9.17: *The first 6 mode shapes of the model and their respective natural frequency.*

model has been checked thoroughly for any differing properties but none have been found. Due to the limited time no further investigation could be performed and the decision was made to use the model as is.

9.8. Mass Breakdown

As Aetheria's design is more detailed, a detailed mass breakdown can be made for the components that are already designed. For the components that have yet to be designed, a class two mass estimation was used to estimate the mass of the components. The equations used for these can be found in the midterm report [1].

Table 9.11: *Mass budget*

Component	**mass [kg]**	**% OEM**	**% MTOM**	Estimation method
Wing	173.7	8.6	6.9	Detailed design
Horizontal Tail	84.3	4.2	3.3	Class 2
Fuselage	287.9	14.3	11.3	Class 2
Landing gear	102.9	5.1	4.1	Class 2
Powertrain	486.0	24.12	19.3	Class 2
Power system	510.1	25.3	20.2	Detailed design
Nacelles	104.4	5.2	4.1	Detailed design
Miscellaneous	262.8	13	10.4	Class 2
OEM	2012.1	-	-	-
Payload	510	-	20.2	-
Total	2522.1	-	-	-

9.9. Sensitivity Analysis

To perform the structural design of the aircraft numerous assumptions were made. Grasping the effect of these assumptions is essential to identifying areas of attention for further detailed design. The crucial assumption made regarding the crashworthiness of the design is the fact that a crashed diameter coefficient of 0.5 was chosen. Limited research has been performed on the crashed diameter and to accurately predict a value for it, an intricate finite element analysis would have to be performed. The time-frame of the project did not allow for this. Thus, a sensitivity analysis is performed on the crashed diameter coefficient. The result can be seen in Figure 9.19 and Figure 9.18, for an aft fuselage aspect ratio of 2.5 and 2.75, respectively.

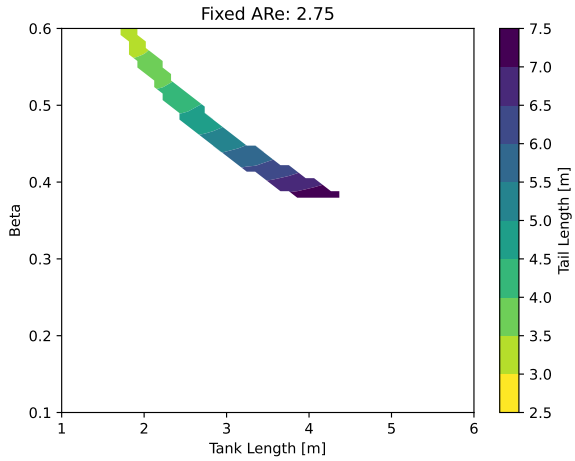

Figure 9.18: *Tail length vs Tank Length for various crashed diameter coefficients for a fixed AR_e of 2.75.*

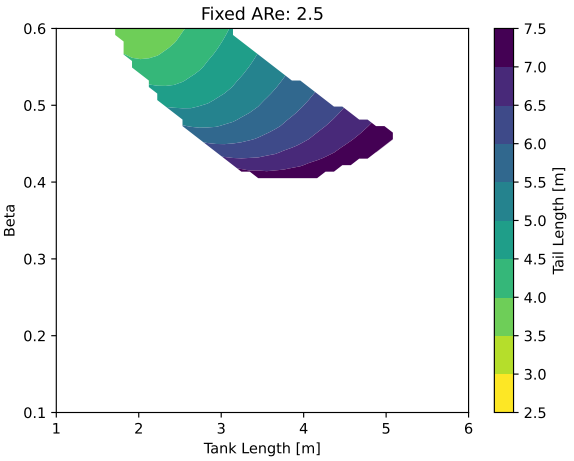

Figure 9.19: *Tail length vs Tank Length for various crashed diameter coefficients for a fixed AR_e of 2.5*

As can be seen from the figure on the left, a decreasing crashed diameter coefficient results in longer tail length limits as expected. More importantly, it can be seen that no crashworthy solution exists below a β of approximately 0.38. Furthermore, using a high AR_e of 2.75 results in a small range of solutions, the reason being that the height of the crash area becomes limiting tanks rather than the width of the fuselage. However, a lower AR_e results in the crashed diameter becoming more constraining to the design as can be seen from Figure 9.19 which only has a feasible solution above $\beta = 0.4$.

Concluding from the observations, the limit length of the tail and fuselage is severely affected by the crashed diameter coefficient. Altering the starting assumption of $\beta = 0.5$ to $\beta = 0.4$ would result in an increase of 2.2 [m] in fuselage length, resulting in the current design being unfeasible as the current length is 11.17 [m]. However, the probability of β being 0.4 is unlikely, as Figure 9.10 illustrates the A320 having a crashed diameter coefficient of 0.662. Additionally, smaller variations in β would not translate to the design. The reason is that due to the V - tail sizing it is more beneficial to have a longer fuselage than required by the crashworthiness. Thus, in the current design, there is more space available than required. A slight decrease in the crashed diameter than expected would therefore not be problematic and it can be said with confidence that the hydrogen is implemented in crashworthy manner.

10

Power System

This chapter is about the power system and its consequent subsystems. The subsystems that will be looked at and analysed in detail are the battery, fuel cell, hydrogen storage and cooling and finally, the integration of all these subsystems will be looked at in depth. For the sizing of these subsystems, first, the trade-offs performed in the Midterm report [1] will be discussed shortly, followed by an analysis of the power budget. Finally, the different subsystems will be sized and integrated with each other.

10.1. Power system configuration

Before the different subsystems can be sized, first, the various configurations used should be mentioned. From the Midterm report, the power system mass sizing showed that the optimum option for the flight was a hybrid cruise configuration in which 82% of the energy will come from hydrogen while the other 18% will be supplied by the batteries [1]. Furthermore, the batteries will also be used for the hovering stages both in take-off and landing.

From the subsystem trade-offs performed previously [1], it was decided that lithium-ion batteries, polymer electrolyte membrane (PEM) fuel cells and a 350-bar compressed hydrogen storage system would be used. More details about the trade-off procedure can be seen in the Midterm report [1]. Following, these chosen configurations, each subsystem can be analysed and designed in more detail regarding their mass, volume, integration and more. These will be done, once a more in-depth analysis of the power distribution throughout the Aetheria systems has been done.

10.2. Design Power and Energy

The different power consumptions of secondary systems and the power and energy requirements for the power subsystems will be derived in this section.

10.2.1. Power and Energy Distribution

The power needed for the different systems except for propulsion-related content also has to be analysed. A summary of the power requirement for the different systems can be seen in Table 10.1.

The rotor rotation mechanism power requirement was assumed to be equal to the power necessary to tilt the rotors of Joby due to the similarity of the tilt-rotor design. This was found to be 2.5kW for one rotor of Joby by performing rough calculations, thus, for the 6-rotor design of Aetheria, the power requirement for the mechanism was found to be 15kW as stated in Table 10.1.

The power necessary by each system in Table 10.1 was calculated by using the values from Wigeon [38] and performing linear extrapolation by scaling the values for Aetheria. In addition, a 30% contingency factor was applied to these estimates in order to account for possible uncertainties and inaccuracies while performing the linear extrapolation method. Furthermore, since the total power for these secondary systems (30.2 kW) is only 4.3% of the battery power (700 kW) seen in Table 10.2, the influence of these systems is relatively small. Therefore, the estimates in Table 10.1 are sufficient for the current design stage of the eVTOL. Since the power necessary for the secondary systems will be supplied by the batteries, the power budget was compared to the power of the batteries only. Furthermore, the power consumption of the secondary power systems was included in the sizing for the

Table 10.1: *Power of secondary systems*

System	Power[W]	Contingency [%30]
Avionics	179.8	233.8
Air-con	2140.9	2783.1
Battery temperature management	263.7	342.8
Auto-pilot	107.8	140.1
Trim	38.5	50.1
Passenger power	285.5	371.1
Lighting	83.5	108.5
De-icing	2140.9	2783.1
Landing gear mechanism	35.7	46.4
Rotor rotation mechanism	15000	19500
Cooling Pump	-	97
Cooling Fan	-	3720
Total	**20276.2**	**30170**

batteries in Subsection 10.3.2. In addition to the non-flight performance-related power-consuming systems, the power and energy requirements for flight performance are also necessary for sizing. These are discussed in Subsection 10.2.2.

10.2.2. Power and Energy Requirements

The power requirement for the battery can be sized using the maximum power requirement stated in Table 7.1. This maximum power requirement is 777 [kW] during the transition, where both batteries and the fuel cell will be used. Therefore, to obtain the actual power requirement from the battery, Equation 10.1 can be used where the power generated by the fuel cell is subtracted and the power requirements for the air subsystem and secondary systems are included.

$$P_{req_{bt}} = P_{tot} - P_{max_{FC}} + P_{air} + P_{budget} \tag{10.1}$$

Here, P_{tot} is the total maximum power from Table 7.1, $P_{max_{FC}}$ is the maximum power of the fuel cell, which is the rated power seen in Table 10.6, P_{air} refers to the power consumption of the air subsystem seen in Table 10.16 and P_{budget} refers to the power consumption of secondary systems seen in Table 10.1. This gives a value of 700 [kW] requirement for the battery. This is the limiting case since the battery can also be sized for the sum of the power required during the cruise and during hovering. These power requirements can be calculated using Equation 10.2 and Equation 10.3. However, these only resulted in a battery power requirement of 660 [kW]. This is less than 700 [kW], thus if this method was used to size the batteries, then the batteries would have been undersized.

$$P_{req_{cruise}} = P_{cruise} \cdot (1 - \nu) + P_{air} + P_{budget} \tag{10.2}$$

$$P_{req_{hover}} = P_{hover} - P_{max_{FC}} \tag{10.3}$$

Here, ν is the fraction of cruise in which hydrogen will be used which was determined to be 80%, in which batteries will supply the rest 20%, also used for hovering [1]. However, once again, this method is discarded due to not being the limiting case. In addition, the energy requirement for batteries is calculated using Equation 10.4.

$$E_{req} = E_{mission} \cdot (1 - \nu) \tag{10.4}$$

With $E_{mission}$ being the mission of the energy which is 218.6 [kWh]. This results in an energy requirement for batteries of 43.7 [kWh]. Furthermore, the power requirement for the fuel cell can be calculated by Equation 10.5.

$$P_{req_{FC}} = P_{cruise} \cdot \nu \tag{10.5}$$

This yields a value of 97.9 [kW] for $P_{req_{FC}}$. Finally, to calculate the energy requirement from hydrogen, Equation 10.6 can be used.

$$E_{req_{H2}} = E_{mission} \cdot \nu \tag{10.6}$$

This gives a hydrogen energy requirement value of 174.9 [kWh]. An overview of the power and energy requirements for the different subsystems can be seen in Table 10.2

Table 10.2: *Power and Energy Requirements Table*

Requirement	Battery	Fuel Cell	Hydrogen
Power [kW]	700	97.9	-
Energy [kWh]	43.7	-	174.9

10.3. Battery

In this section, the chosen battery will be discussed and will be sized for the design. The mass, volume, number of cells and cost will all be calculated. The methods used will be the same as the ones previously mentioned in the Midterm report [1].

10.3.1. Battery characteristics

From the trade-off performed in the Midterm report, a conclusion was drawn to use lithium-ion batteries [1]. A literature study was conducted to find the best and most suitable type of lithium-ion batteries for Aetheria. It was found that Ionblox Launch batteries[1] would be the best option since they offer high power during the initial and final stages of flight (i.e. take-off and landing). These are the stages where hovering is performed which is extremely power-demanding. Furthermore, this battery is specifically designed for eVTOLs as these type of aircraft have requirements that differ from regular EVs. These batteries are also used by the Lilium design, showing the high potential batteries indicate. The reason for the desire for high specific power and energy, as well as energy density and cycles were mentioned in the Midterm report [1], for which reason it shall not be repeated here again. Therefore, the characteristics of the most suitable battery for this design, Ionblox, can be seen in Table 10.3 and Table 10.4 obtained from the product data-sheet [59].

Table 10.3: *Technical Battery Characteristics*

Criteria	Value
Specific energy [Wh/kg]	340
Specific power [W/kg]	3800
Energy density [Wh/L]	850
Depth of Discharge (DOD) [%]	100
End of life capacity (EOLC) [%]	90
Cycles	500
Efficiency	0.9

Table 10.4: *Dimensional Battery Characteristics*

Criteria	Value
Cell Weight [kg]	0.121
Cell Volume [L]	0.056
Cell Dimensions [m]	0.145 x 0.064 x 0.006
Cell Capacity [Ah]	12
Cost [$/kWh]	225
Operating Temperature [°C]	-20-55

The cell weight, volume and capacity were also included in order to find the number of cells that will be needed once the batteries have been sized to obtain the total mass needed and volume oc-

[1] Accessed May 30th 2023 https://www.ionblox.com/air

cupied. Whichever is the limiting factor, either mass or volume is used to compute the number of cells. Furthermore, the capacity of the battery towards its end of life (EOLC) is also an important consideration. According to Ionblox [59], the capacity of the battery remains above 90% towards 500 discharge cycles with 100% DoD. The product manufacturer, Ionblox, does not state the efficiency of its batteries, however, lithium-ion batteries have efficiency ranging between 90% and 99%[2]. For contingency reasons, the lower bound was taken to be the efficiency in the design of Aetheria, which was also the design choice of Wigeon [38]. In terms of composition, the cell chemistry consists of an 811 NCM (Nickel, Cobalt and Manganese) cathode and an anode with a composition of more than 90% silicon oxide (SiOx)[59]. The 811 value refers to the ratio of composition of Nickel, Cobalt and Manganese as 8:1:1 respectively.

Finally, to size the battery, the power, P_{req}, and energy, E_{req}, required from the battery are necessary. These are obtained using the method previously discussed in Subsection 10.2.2, and are tabulated in Table 10.5 once more for clarity reasons.

Table 10.5: *Battery Requirement*

Required Power [kW]	Required Energy [kWh]
700	43.7

10.3.2. Battery Sizing

To determine the final mass of the batteries that will be needed for the design, sizing both for energy and power requirements should be done from which the higher battery mass obtained will be the critical value to be considered. These energy and power requirements are based on hovering rather than cruising since hovering is more power-demanding compared to cruising. Furthermore, batteries will only be used for 18% cruise, therefore, this will not be the limiting factor. From Table 10.5, the required power, P_{req} [kW], and energy, E_{req} [kWh] requirements for the battery obtained can be seen. Using the method stated in the Midterm report, the battery mass if sized for energy turns out to be 179 [kg], whereas, if sized for power the mass turns out to be 205 [kg]. The higher mass value is taken as the final battery mass to comply with the requirements. Logically, since the batteries are mainly used in and sized for hovering, the critical case being the power requirement deduced mass makes sense. Furthermore, the volume of the battery can also be computed using the volumetric energy density and battery mass, which yielded a volume of 72.3 [L].

Furthermore, the battery is not 100% efficient. With the power it generates, heat is also produced as a by-product. This generation of heat will increase the temperature of the batteries outside their operating temperatures of -20°C to 55°C [59]. This can cause thermal runways and other problems, therefore, to prevent this a cooling system will be necessary to cool the batteries down. This is analysed and designed for in Subsection 10.6.5. Moving on, the cost of batteries can also be calculated, as well as the number of cells that will be necessary for the design. The cost is simply calculated using Equation 10.7.

$$C_{bat} = C_{kWh} \cdot \frac{E_{sp}}{1000} \cdot m_{bat_p} \tag{10.7}$$

C_{kWh} refers to the cost of the batteries in [$/kWh], E_{sp} refers to the specific energy of the batteries [Wh/kg] and m_{bat_p} is the mass that the batteries have been sized for previously. This results in a battery cost of 15682.5 $. Furthermore, to calculate the number of cells necessary, the mass and volume needed of the total battery system are divided by the mass and volume of each cell as can be seen in Equation 10.8 and Equation 10.9.

[2] Accessed June 16th 2023, https://news.energysage.com/lithium-ion-vs-lead-acid-batteries/

$$n_{cells_V} = \frac{V_{bat}}{V_{cell}} \tag{10.8}$$

$$n_{cells_m} = \frac{m_{bat_p}}{m_{cell}} \tag{10.9}$$

Performing these calculations using results from Table 10.4 and Table 10.5 results in the total number of cells of 1299 and 1695 to meet volume and mass requirements respectively. The higher number of cells is the limiting case, which is obtained by sizing the number of cells according to mass. Since the number of cells necessary to meet mass is higher than that for volume, the volume will be higher than before. Therefore, the total volume of the batteries has to be updated. The new volume occupied by the batteries can be calculated using Equation 10.10, which gives a final volume of 94.4 litres for the battery subsystem.

$$V_{bat_{final}} = n_{cells_m} \cdot V_{cell} \tag{10.10}$$

Finally, the total energy stored in the battery cells can be computed, this can be done by multiplying the battery mass by the energy and end-of-life capacity (EOLC). Thus, the batteries can store 62.7 [kWh] of energy at their End-of-Life towards 500 cycles, whereas, they can store 69.7 kWh initially.

10.4. Fuel Cell

In this section, the chosen fuel cell will be sized for the design. All the necessary calculations to size the fuel cell, including, mass, volume and cost will all be touched upon. The methods used will be the same as the ones previously mentioned in the Midterm report [1].

10.4.1. Fuel Cell Characteristics

From the Midterm report trade-off, it was found that the most optimum fuel cell type for this design would be Polymer Electrolyte Membrane (PEM) [1]. From a conducted literature study, it was obtained that the best PEM fuel cell for this design will be the P-Stack fuel cell stack manufactured by the Power Cell Group[3]. As stated in the trade-off performed in the Midterm report [1], high power and volumetric densities, as well as high efficiencies, are desired, which was the case with P-stack compared to the rest. Furthermore, a high coolant outlet temperature is also desired as it reduces the power necessary from the cooling system to cool the fuel cell. The characteristics of the P-stack fuel cell can be seen in Table 10.6 and the fuel cell stack can be visualised in Figure 10.1.

Table 10.6: *P-Stack PEM Fuel Cell Characteristics*

Criteria	Value
Rated power [kW]	125
Cell count	455
Stack Mass [kg]	42
Coolant temp [C]	90
Stack Volume [L]	38.1
Efficiency [%]	0.55
Lifetime [hours]	20000
Dimensions [m]	0.42 x 0.582 x 0.156
Operating Temperature [C]	-30-70

Figure 10.1: *Power Cell Group P-stack Fuel Cell* [4]

[3]Accessed June 5th 2023, https://powercellgroup.com/product/p-stack/

10.4.2. Fuel Cell Sizing

From the fuel cell characteristics in Table 10.6, the gravimetric, $P_{SP_{FC}}$ and volumetric, E_V, power densities of the fuel cell stack can be calculated by simply dividing the rated power [kW] by the mass [kg] and volume [L] respectively. The densities obtained using the method were 3 [kW/kg] and 3.25 [kW/L] respectively. Finally, to size the mass and volume of the fuel cell necessary to generate the required power, Equation 10.11 and Equation 10.12 can be used along with the power requirement the fuel cell has to be compliant with, which was obtained in Subsection 10.2.2.

Finally, to size the mass and volume of fuel cell necessary to generate the required power, Equation 10.11 and Equation 10.12 can be used along with the power requirement the fuel cell has to be compliant with, which was obtained in Subsection 10.2.2.

$$m_{FC} = \frac{P_{req}}{P_{SP_{FC}}} \tag{10.11}$$

$$V_{FC} = \frac{P_{req}}{E_V} \tag{10.12}$$

Once the mass and volume needed for the fuel cell are calculated, they have to be rounded up to the mass and volume characteristics per fuel cell since a proportion of the fuel cell cannot be used. As a result, the required fuel cell mass and volume are below that of one P-stack, therefore, rounding up results in a fuel cell mass and volume of 42 [kg] and 38.1 [L], which are the same as the ones stated in Table 10.6. Furthermore, the cost of the P-stack fuel cell stack can also be computed. According to some assessments [5], the PEM fuel cells are priced at a cost of 75$, resulting in a total cost of 9375$.

10.4.3. Fuel Cell System

Simply sizing the mass and volume of fuel cells that will be required is not enough. The fuel cell system also has to be designed for the hydrogen and air supply systems as well as the output power and water. The hydrogen supply should be provided directly to the anode of the fuel cell where the catalyst will help split the hydrogen into protons and electrons. The electrons are output towards a circuit which they can enter to provide electricity and subsequently heat, whereas, the protons continue through the electrolyte until they reach the second catalyst at the cathode. Here, they bond with the oxygen molecules being supplied in order to produce water, which flows out of an outlet. A schematic of this system can be seen in Figure 10.2.

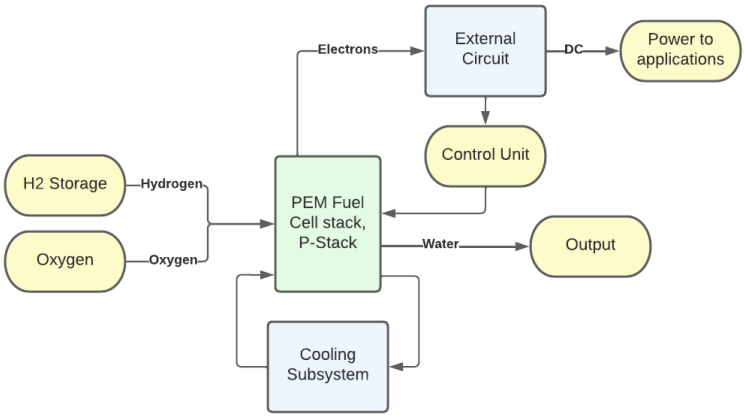

Figure 10.2: *Fuel Cell System*

From Figure 10.2, it can be seen that the direct current (DC) electricity generated from the external

[5] Accessed 2nd June 2023, https://www.pnas.org/doi/10.1073/pnas.1804221116

circuit is provided to the power-requiring applications, such as propeller engines in propulsion. Furthermore, the generated current is also supplied into a control unit which is used to regulate the operation of the fuel cell. The generated water has to be output, which can be used stored in a container and extracted at the vertiport or it can also be provided as water for drinking for the passengers. In case the water generation is too high, the excess water can be either evaporated or expelled. Finally, the cooling system is used to keep the fuel cell at ideal operating conditions and prevent it from overheating. The sizing of this cooling subsystem is performed in Section 10.6.

10.5. Hydrogen Storage

There are four different types of hydrogen tanks that can be used for this design; namely, Type I, Type II, Type III and Type IV. The first 2 tanks are used to store hydrogen of pressure up to 300 bars, which makes them unsuitable for this design since it was determined that 350 bars of pressure will be used [1]. Therefore, either Type III or Type IV tanks will be used for this design. However, Type IV tanks are preferred over Type III due to the higher gravimetric density [% weight] and lower costs [$/kg] they provide [60]. Thus, Type IV tanks are preferred for the design of Aetheria.

Type IV tanks, are made up of composite resins such as carbon fibres with polymer-based liners [60]. The carbon fibres are mainly used to form the overwrap (the body of the tank), whereas, a polymer-like material, HDPE (high-density polyethylene), is used as a liner [60]. Since these tanks use composite materials in contrast to Type III tanks which use metals, they are significantly lighter which makes them perfect for applications in vehicles where lower mass is preferable. These Type IV tanks allow for pressures up to 700 bars, which will be unnecessary for this design since only 350 bars are required, therefore the pressure valves will be adjusted accordingly.

From a discussion with a Fuel Cell engineer at ZeroAvia, it follows that a Type IV tank has a gravimetric density of 7-9% [6]. However, taking contingency factors of 20% into account, a 5.4% gravimetric density shall be designed for, which is a gravimetric density that also includes contingency factor from 5.7% stated in another source [60]. This value represents the percentage of the mass of hydrogen [kg] that can be stored with respect to the total mass of the tank. The efficiency of the tank is also taken into account within this value. The energy requirement for hydrogen is 174.9 [kWh], however, implementing the efficiency of the fuel cell, which is 55% [1], in this energy requirement, increases the requirement to 320 [kWh]. Therefore, it is found that 9.6 [kg] of hydrogen will be necessary to supply this much energy. Thus, performing calculations using Equation 10.13, leads to a total tank mass of 176.7 [kg], including hydrogen.

$$m_{tank} = \frac{100}{\eta_{storage}} \cdot m_{H2} \tag{10.13}$$

Here, $\eta_{storage}$ refers to the gravimetric density [%], and m_{H2} refers to the mass of the hydrogen [kg]. Another source states that a 350-bar compressed Type IV hydrogen tank has a gravimetric density of 1.8 [kWh/kg system] [61]. Since the mass of H2 necessary is 9.6 [kg] and the energy of hydrogen is 33.33 [kWh/kg], this means that the 9.6 [kg] of hydrogen provides an energy of 320 [kWh]. Dividing this by the gravimetric density of 1.8 yields a tank mass (including Hydrogen) of 177.8 [kg]. These 2 values obtained for the hydrogen tank mass (including H2) are almost the same, thus making the estimate for the hydrogen mass reliable, verifying the method to small uncertainties. Furthermore, DOE states that the volumetric density of the entire system for a 350-bar compressed hydrogen storage tank is 0.6 [kWh/L][62]. Dividing the 320 [kWh] hydrogen energy by this value yields a system volume of 533 litres. This was obtained using Equation 10.15. Whereas, calculating the volume necessary for 350-bar compressed hydrogen using Equation 10.14 resulted in a volume of 368 litres.

[6] P. de Boer, Fuel cell Engineer at Zeroavia. Technical Meeting

Therefore, this difference of 165 litres, suggests that the difference in the 2 volumes calculated refers to the volume of the tank excluding hydrogen storage volume within it and pressure valves.

$$V_{H2} = \frac{m_{H2}}{\rho_{350-bar}} \tag{10.14}$$

$$V_{sys} = \frac{E_{H2}}{\rho_{sys}} \tag{10.15}$$

Here m_{H2} is the mass of hydrogen necessary which is 9.6 [kg] and $\rho_{350-bar}$ is the density of hydrogen when compressed at 350 bars, which is 0.0261 [kg/L] [7]. E_{H2} is the energy provided by the 9.6 kilograms of hydrogen, 320 [kWh], and ρ_{sys} is the volumetric density of the system, 0.6 [kWh/L] [8]. Therefore, this concludes that to store the gaseous hydrogen, only 368 litres of volume is necessary, however, with the whole storage system (tank, hydrogen, valves and thermal pressure relief device (TPRD)), this value adds up to 533 litres. In terms of cost, Type IV tanks are approximated at a price of 633 [$/kg] of hydrogen [60]. This results in a total tank cost of 6076.8$. A summary of the sized hydrogen tank can be seen in Table 10.7.

Table 10.7: *Hydrogen Tank System*

H2 Mass [kg]	Tank+H2 Mass [kg]	H2 Vol [L]	Tank System Vol [L]	Cost System [$]
9.6	176.7	368	533	6076.8

The total volume and mass of the hydrogen storage tank are obtained, however, the dimensions of the tank have not yet been decided. This dimension sizing is important as the storage of hydrogen within the eVTOL is crucial both in terms of safety and crashworthiness, and allocation of space for the design. For redundancy, 2 tanks of hydrogen will be used, so that in case of leakage in one of the tanks, there is no leakage in the other. Therefore, there will be no complete leakage of hydrogen resulting in insufficient energy for landing. Thus, using 2 equivalent tanks results in a volume of tank system of 266.5 litres and a volume of tank of 82.5 litres per tank.

According to the fuselage architecture, in the storage of the 2 tanks, the limiting factor is the diameter. Therefore, since the diameter is the limiting factor, the tank dimension will be sized according to an arbitrarily chosen preferred diameter. First, the length of the tank has to be calculated by using the 266.5 litres system volume per tank and the arbitrarily chosen diameter. This can be done using Equation 10.16. The volume of a cylinder can not be simply used since the tank storage contains a dome with a radius, of R.

$$V_{sys_{per-tank}} = \frac{4}{3} \cdot \pi \cdot R^3 + \pi \cdot R^2 \cdot (L - 2R) \tag{10.16}$$

Here, L is the length [m], R is the outer tank radius [m] which is 0.1938 due to the crashed diameter considerations Section 9.6, and $V_{sys_{per-tank}}$ is the volume of the tank system per tank which is 266.5 litres. Re-arranging and calculating provide a total tank length of 2.38 [m], including the domes of the tank. If the domes of the tank were to be excluded, the pure length of the cylindrical part of the tank would be 2 [m]. Finally to calculate the thickness of the tank, t [m], Equation 10.17 can be used.

$$V_{per_{tank}} = \frac{4}{3} \cdot \pi \cdot (R^3 - (R-t)^3) + \pi \cdot L \cdot (R^2 - (R-t)^2) \tag{10.17}$$

Here, V_{tank} is the volume of the sole tank which is 77.5. This provides a thickness of 0.0275 [m]. This concludes the sizing of the dimension of the tanks and a summary can be seen in Table 10.8. Finally, an example of the structure of the hydrogen tank system can be seen in Figure 10.3.

[7] Accessed May 29th 2023, https://demaco-cryogenics.com/blog/energy-density-of-hydrogen/
[8] Accessed June 5th 2023, https://demaco-cryogenics.com/blog/energy-density-of-hydrogen/
[8] Accessed June 5th 2023,https://powercellgroup.com/product/p-stack/

Table 10.8: *Storage Tank Dimensions*

Length [m]	Outer Diameter [m]	Inner Diameter [m]	Thickness [m]
2.38	0.3876	0.3626	0.025

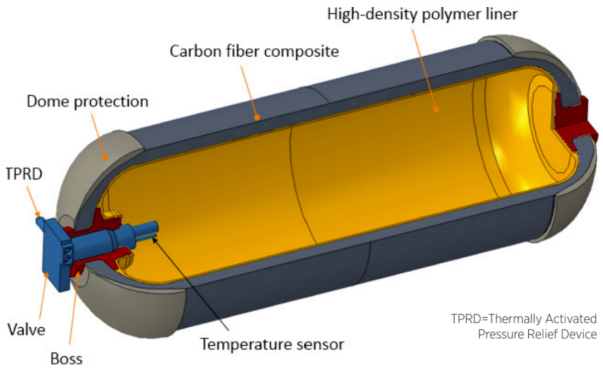

Figure 10.3: *Hydrogen Storage System [60]*

10.6. Fuel cell & Battery Cooling

Thermal management of the fuel cell and batteries is necessary in order to ensure the safe operation of the eVTOL. As the fuel cell and batteries will be bought off-the-shelf, it is assumed that all the heat generated in both systems can be fully extracted from the fuel cell and battery respectively. Therefore, this section will only discuss the release of heat from the heat exchangers to the air.

The method used to model the heat exchanger is the $\epsilon - NTU$ method [63]. The exchange effectiveness is defined, ϵ, is defined in Equation 10.18.

$$\epsilon = \frac{\dot{Q}}{\dot{Q}_{max}} \tag{10.18}$$

The heat capacity rate of a fluid, C, is defined in Equation 10.19 where c_p is the heat capacity and $\dot{m}$ is the mass flow.

$$C = c_p \dot{m} \tag{10.19}$$

The theoretical maximum heat exchanged can be calculated with Equation 10.20. It is dependent on the minimum heat capacity rate and the input temperature difference of the hot coolant (C_{hot}, $T_{h,in}$) and the outside air (C_{cold}, $T_{c,in}$). Furthermore, the heat capacity ratio, C_r is introduced in Equation 10.21.

$$\dot{Q}_{max} = C_{min}(T_{h,in} - T_{c_{c,in}}) \tag{10.20}$$

$$C_r = \frac{C_{min}}{C_{max}} \tag{10.21}$$

ϵ is dependent on the geometry and the configuration of the heat exchanger used. The cross-flow configurations will be used as it is a common configuration for compact heat exchangers [64]. The geometry will be discussed in Subsection 10.6.3. The exchange effectiveness for cross-flow can be calculated with Equation 10.22. [65].

$$\epsilon = 1 - exp\Big[\frac{1}{C_r}(NTU)^{0.22}\{exp[-C_r(NTU)^{0.78}] - 1\}\Big] \tag{10.22}$$

The number of transfer units NTU required to satisfy cooling requirements have to be found iteratively. The NTU is dependent on the overall heat transfer coefficient and the heat transfer area. It

can be thought of as capturing the geometry of the heat exchanger and can be calculated with [65] Equation 10.23.

$$NTU = \frac{UA}{C_{min}} \tag{10.23}$$

The hydraulic diameter, D_h which is an important parameter used in the calculation of Nusselt numbers and heat transfer coefficients can be calculated using Equation 10.24. Furthermore, the mass flux which is used in the calculation of the Reynolds number in Equation 10.27, can be calculated using Equation 10.25 [64].

$$D_h = 2\frac{W_{Channel} \cdot H_{Channel}}{W_{Channel} + H_{channel}} \tag{10.24}$$

$$G = \frac{\dot{m}}{A_{cross}} \tag{10.25}$$

Once these parameters have been calculated, the Reynolds number can be calculated using Equation 10.27 which is dependent on both parameters and μ, the dynamic viscosity of the fluid. Along with the Reynolds number, the Prandtl number is also calculated using Equation 10.26 which is not dependent on either, but rather on the properties of the flow of the corresponding side. Here μ is the dynamic viscosity of the fluid, c_p is the specific heat capacity of the fluid and κ is the thermal conductivity of the fluid.

$$Pr = \frac{c_p\,\mu}{\kappa} \tag{10.26}$$

$$Re = \frac{G \cdot D_h}{\mu} \tag{10.27}$$

Finally, Equation 10.28 can be used to calculate the heat transfer coefficient h_c for a laminar flow. This equation depends on the Nusselt number calculation of each corresponding side which can be calculated using Equation 10.30 for the air side and Equation 10.31 for the coolant side. However, if the flow is turbulent (Re > 3000), Equation 10.28 [64] is not used, and Equation 10.32 is used instead.

$$Nu = \frac{h_c D_h}{\kappa} \tag{10.28}$$

10.6.1. Air side

The method used to size the air side of the heat exchanger was based on the analysis of compact heat exchangers performed by Ranganayakulu et al. [66]. The Nusselt number and consequently the heat transfer coefficient calculations for the air and coolant sides vary. For the air side, first, the Colburn factor, j, has to be found which is a non-dimensional parameter used in further calculations. This factor can be found using the empirical relation shown in Equation 10.29 [67]. The individiual parameters, α, δ and γ can be seen in Figure 10.4b.

$$\begin{aligned} j = {} & 0.6522 \cdot Re^{-0.5403}\alpha^{-0.1541}\delta^{0.1499}\gamma^{-0.0678} \\ & \times \left(1 + 5.269 \times 10^{-5} Re^{1.340}\alpha^{0.504}\delta^{0.456}\gamma^{-1.055}\right)^{0.1} \end{aligned} \tag{10.29}$$

Once the Colburn factor has been determined, the Nusselt number can be deduced using Equation 10.30 [67]. It is important to note that the Reynolds number on this cold air side is different than the Reynolds number on the hot coolant side due to the difference in temperatures of the intakes, as well as their corresponding speeds and viscosities. This difference in Reynolds number can be calculated using Equation 10.27. The Prandtl number, Pr, also differs for both sides for the aforementioned reasons.

$$Nu = j \cdot Re \cdot Pr^{1/3} \tag{10.30}$$

After the calculation of the Nusselt number by re-arrangement of Equation 10.30, the heat transfer coefficient for the cold air side, $h_{c_{cold}}$ can be calculated using Equation 10.28.

10.6.2. Coolant side

For the hot coolant side, the approach is different. The method used differs according to the Reynolds number of the incoming coolant flow. If the Reynolds number is less than 3000, then the method used is based on Equation 10.31 [65]. However, if the Reynolds number is larger than this value, then the approach taken is based on Equation 10.32.

$$Nu = 7.54 + \frac{0.03(D_h/L)Re\,Pr}{1+0.016[(D_h/L)Re\,Pr]^{2/3}} \quad \text{for } Re \leq 3000 \tag{10.31}$$

Here, D_h refers to the hydraulic diameter calculated from Equation 10.24 and L to the length, making their division, the aspect ratio of the duct. Once the Nusselt number has been computed using this relation, since the Reynolds number is less than 3000, the flow is still laminar and thus, Equation 10.28 can used for the heat transfer coefficient calculation for laminar flow. However, the thermal conductivity, κ, and the hydraulic diameter D_h will be different compared to the air side. However, if the Reynolds number is above 3000, then the flow enters a turbulent state requiring Equation 10.32 [65] to be applied to directly calculate the heat transfer coefficient $h_{c_{hot}}$.

$$h_c = \frac{(Re-1000)\cdot Pr\cdot(f/2)\cdot(k/Dh)}{1+12.7\cdot(Pr^{2/3}-1)\cdot(f/2)^{0.5}} \quad \text{for } 3000 \leq Re \leq 10^4 \tag{10.32}$$

Here f, refers to the friction factor, calculated using Equation 10.33[65].

$$\begin{aligned} f =& 9.6243\,\mathrm{Re}^{-0.7422}\,\alpha^{-0.1856}\delta^{0.3053}\gamma^{-0.2659} \\ &\times\left[1+7.669\times10^{-8}\,\mathrm{Re}^{4.429}\,\alpha^{0.920}\delta^{3.767}\gamma^{0.236}\right]^{0.1} \end{aligned} \tag{10.33}$$

Furthermore, the pressure drop and associated pump power needed resulting from friction within the cooling channels can be calculated using Equation 10.34 and Equation 10.35. Δp_{ch} is the pressure drop per channel and P_{pump} is the pump power.

$$\Delta p_{\mathrm{ch}} = \frac{2fG^2L_{\mathrm{ch}}}{D_h\rho} \tag{10.34}$$

$$P_{pump} = \frac{\Delta p_{\mathrm{ch}} N_{\mathrm{ch}}}{\rho\eta_{pump}}\dot{m} \tag{10.35}$$

Here f is the friction factor, G is the mass flux of the channel cross-section, L_{ch} is the length of the channel and ρ is the density of the fluid. η_{pump} is assumed to be 0.75 [64] and is the pump efficiency. Once, the heat transfer coefficients have been calculated for the hot and cold sides, the overal heat transfer capacity of the heat exchanger can be deduced using Equation 10.36.

10.6.3. Heat exchanger Geometry

The heat exchanger consists of a cuboid-like geometry with 2 different entries, one for the coolant (hot) and one for the air (cold). For the air side, an offset fin geometry will be used, like the one seen in Figure 10.4b. The reason for this geometry is that offset fin strips provide the most optimum balance of pressure drop in the air-side and heat transfer coefficient [67]. On the coolant side, the structure used is the flat mini-channel tube. The main reason behind this choice was that flat tubes are easy to b extruded and manufactured, as well as resistant to high pressures. Furthermore, mini-channel diameters can be made extremely small (around 2mm). This limits the thickness of the tube and consequently reduces the blockage of air, thus increasing the surface area to volume ratio [64].

The heat transfer areas on the coolant (hot) and air (cold) sides can be calculated using the methods described in the thesis by A. Scoccimarro [64]. For simplicity reasons, it is assumed that the width

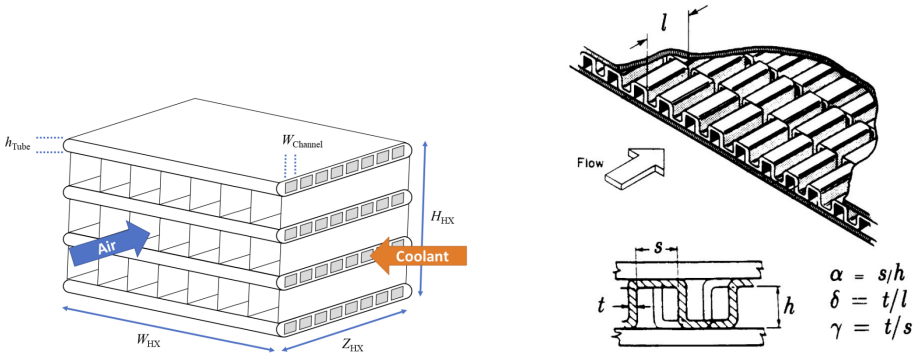

(a) *heat exchanger Geometry [64]* **(b)** *Geometry of the fin, cold Air side [67]*

and height of the coolant channels are equal. However, they are kept separate in the equations to possibly investigate rectangular channels in the future. The corresponding calculated areas, along with the calculated heat transfer coefficients, h_C by each side, hot using Equation 10.32 and cold using Equation 10.28, can be used to calculate the overall heat transfer capacity of the heat exchange, UA, by using Equation 10.36.

$$\frac{1}{UA} = \frac{1}{h_{c,hot} \cdot A_{hot}} + \frac{1}{h_{c,cold} \cdot A_{cold} \cdot \eta_{surf}} \tag{10.36}$$

Here η_{surf} is the surface efficiency of the extended offset strip fins, which can be calculated using couple relations stated by Scoccimarro [64].

Finally, the volume of the heat exchanger can be calculated using the geometric details of the structure, along with the weight of it. The material the heat exchanger is composed of is Aluminium 3003. In addition, an extra 20% of mass is added on top of the calculated initial mass to account for extra applications such as header tanks, mounting points and fittings [64].

10.6.4. Cooling system integration

The cooling system will use fans in order to ensure airflow through the heat exchangers during vertical flight and transition. The airflow would otherwise be problematic due to the lack of the speed Aetheria would have which would limit the mass flow through the radiators. Furthermore, the geometry of the duct where the radiator is placed will be a diffuser - heat exchanger - nozzle to reduce drag.

The duct geometry is visualized in Figure 10.5. The fan will be placed in front and at the same orientation as the heat exchanger in order to increase the disk area of the fan as this decreases the fan power required. A diffuser and nozzle are used to decrease the drag of the heat exchanger.

The power that the fan would have to supply is modelled with actuator disk theory. It can be derived that the fan power is related to the mass flow it has to produce and the disk area as can be seen in Equation 10.37.

$$P_{fan} = \frac{\dot{m}_{air}^3}{(2\rho_{air} A_{disk})^2} \tag{10.37}$$

$$A_{disk} = \frac{\pi}{4}(0.8 W_{HX})^2 \tag{10.38}$$

The disk area is calculated based on the minimum frontal diameter (width and height). In Aetheria's case, this will be the width of the heat exchanger. The diameter of the fan will be 80 % of this dimension to ensure sufficient clearance between the duct and the fan which results in Equation 10.38.

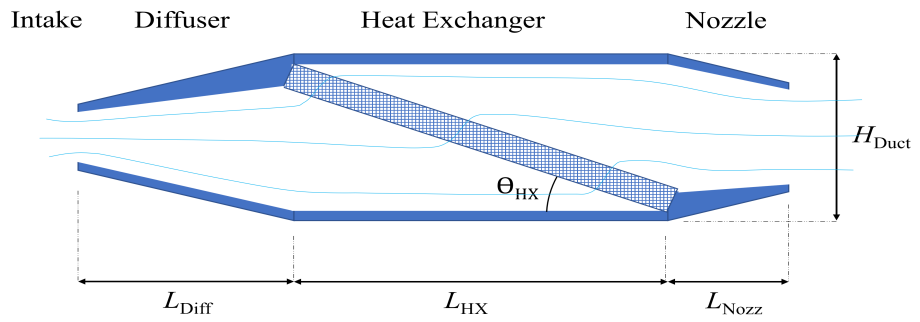

Figure 10.5: *Cooling duct geometry [64]*

10.6.5. Heat Exchanger Design

Due to time constraints, it was chosen that the fin and channel dimensions will not be optimized. Therefore the parameters found in A. Scocciroco's master's thesis were used [64] found in Table 10.9.

Table 10.9: *Heat exchanger surface dimension [64]*

$W_{channel}$	l_{fin}	s_{fin}	h_{fin}	t_{fin}
2.5 mm	2 mm	1 mm	2 mm	0.1 mm

Furthermore, the fuel cell and battery will have a separate cooling cycle. This is needed due to the different operating temperatures.

Fuel Cell

Fuel cell cooling is crucial for safety, especially considering the nature of hydrogen. Therefore, it has to be ensured that the heat exchanger can remove the heat produced by the fuel cell. The Pstack fuel cells maximum rated electrical power output is 125 kW and it has an efficiency of 55%. Therefore, the maximum amount of heat generated would be 103 kW according to the following relation.

$$\dot{Q} = \frac{1-\eta}{\eta} P_{el} \tag{10.39}$$

The fuel cell heat exchanger is sized for stall conditions and the coolant is for simplicity assumed to be water. A 10% contingency factor is taken into account to dispose of heat from auxiliary components such as pumps. The design points for the fuel cell heat exchanger are shown in Table 10.10. In reality, the needed dissipated heat in the heat exchanger would be less as some of the fuel cell heat evaporates some wastewater [64]. However, this is not taken into account in order to stay conservative. Lastly, the outlet temperature of the coolant from the fuel cell is a maximum of 90°C. Therefore, to remain on the safe side the inlet temperature of the fuel cell is chosen to be 85°C.

Table 10.10: *Fuel cell heat exchanger design point*

P_{el}	$\dot{Q}_{FC}$	$\dot{m}_{air}$	$\dot{m}_{coolant}$	T_{air}	$T_{coolant}$
125 kW	113.3 kW	5.5 kg/s	2.45 kg/s	45 °C	85 °C

The fuel cell has a width of 38 cm, a height of 60 cm and a depth of 10 cm. These dimensions satisfy the cooling requirement from the fuel cell. This results in a heat exchanger mass of 9.7 kg and it expels 114 kW of heat which meets the requirement. Furthermore, as can be seen in Table 10.12, the

coolant pressure drop is 56.3 kPa over the heat exchanger which results in a pumping power required of 1.84 kW due to the heat exchanger. This pumping power poses no problem for the feasibility. Lastly, the fan power is 3.72 kW which also does not pose a problem with feasibility.

Table 10.11: *Fuel cell heat exchanger dimensions*

W_{HX}	H_{HX}	Z_{HX}
38 cm	45 cm	10 cm

Table 10.12: *Fuel cell heat exchanger properties*

$\dot{Q}_{expelled}$	mass	Δp	P_{pump}	P_{fan}
113 kW	11.1 kg	56.3 kPa	1.84 kW	3.72 kW

Battery

The battery operating temperature is considerably lower than the operating temperature of the fuel cell of 55°C [59]. However, before thermal runaway occurs it is possible that the temperature of the battery will be slightly higher [68] to 65°C. This increased temperature allows to be more heat expelled from the system due to a larger temperature difference with the ambient air.

The battery can provide 780 kW of power. From Equation 10.39 and a 10 % contingency, it follows that with a 90 % efficiency the heat that has to be expelled from the system is 95.1 kW as can be seen in Table 10.13. Furthermore, the assumed airflow through the radiator is 7.35 kg/s and the coolant flow is calculated to be 2.07 kg/s.

Table 10.13: *Battery heat exchanger design point*

$\dot{Q}_{bat}$	$\dot{m}_{air}$	$\dot{m}_{coolant}$	T_{air}	$T_{coolant}$
95.1 kW	7.35 kg/s	2.07 kg/s	45 °C	65 °C

It was found that the heat exchanger needs a width of 50 cm, a height of 150 cm, and a depth of 5 cm. It is interesting to note that the depth of the heat exchanger is half the depth of the fuel cell heat exchanger. This comes at a cost of reduced exchanger effectiveness however it results in an overall mass reduction for the heat exchanger. This is due to an increased depth increase in the number of fins which increases the mass.

Table 10.14: *Battery heat exchanger dimensions*

W_{HX}	H_{HX}	Z_{HX}
50 cm	150 cm	5 cm

Table 10.15: *Battery heat exchanger properties*

$\dot{Q}_{expelled}$	mass	Δp	P_{pump}	P_{fan}
95.5 kW	37.0 kg	62.7 kPa	1.73 kW	5.96 kW

The battery heat exchanger can expel 95.5 kW of heat with these operating parameters and has a mass of 37 kg. The large mass compared to the fuel cell heat exchanger is mainly due to the smaller temperature difference compared to the fuel cell cooling cycle. The pressure drop of the coolant is 74.2 kPa which results in a pumping power of 1.73 kW which is manageable [64]. Lastly, the power that has to be supplied to the fan is 5.96 kW.

10.7. Air-Subsystem

The air subsystem is important for fuel cell integration. It consists of different parts such as water separators, air filters, compressors, intercoolers, humidifiers, turbines and purge valves. An overview of the air subsystem can be seen in Figure 10.6.

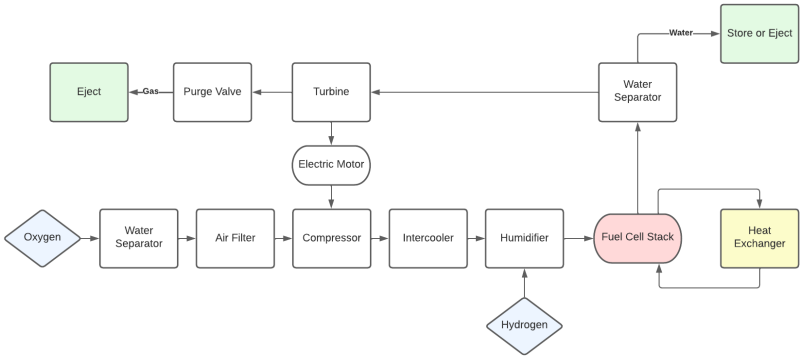

Figure 10.6: *Air System Schematic*

Initially, the oxygen supply from the outside air that enters the system has to go through the water separator in order to remove any water vapour that the air may contain which can damage other components by forming liquid water when due to compression and cooling. Later the dry air that comes out of the water vapour has to be filtered in order to remove any particles and contaminants present to prevent fuel cell damage and degradation. The filtered air is compressed in order to increase the air pressure for the fuel cell. This improves the power output and efficiency of the fuel cell by improving the oxygen transport within the fuel cell. The heated air due to compression passes through the intercooler for cooling. In this way, high air temperatures entering the fuel cell are avoided which reduces the degradation and additional overheating of the fuel cell. Finally, a humidifier is used prior to the fuel cell to moisturise the air to improve proton conductivity, as well as to prevent membrane dehydration.

The humidifier used is an external passive humidifier, thus the hydrogen supplied can also be circulated through this before entering the fuel cell in order to obtain the optimal hydration of the fuel cell membrane [9]. The heat exchanger was sized for and explained in Section 10.6. The water and exhaust air generated by the fuel cell stack first flows through the water separator in which water and air are separated. The water that is separated is then either stored or ejected. Whereas, the air is first passed through a turbine from which used air (from the fuel cell cathode) can be expanded and supplied back to the compressor for re-circulation. The electrical motor between the compressor and the turbine thus decides the net power consumed by the compressor using the difference between the power consumption of the compressor and the power supplied by the turbine. According to Bosch Mobility, this is in the range of 50% [10], therefore the power consumption of the compressor in Table 10.16 is halved if only a compressor was used. This reduces the power consumption of the compressor since the turbine supplies some power by doing this process. A summary of all the components used can be seen in Table 10.16.

The power for the air-system is supplied by the batteries during the cruising stage, as it is then when

[9] Accessed June 13th 2023, https://www.nature.com/articles/s41586-021-03482-7
[10] Accessed June 13th 2023, https://www.bosch-mobility.com/en/solutions/powertrain/fuel-cell-electric/electric-air-compressor/
[11] Accessed June 6th 2023, https://www.fischer-fuelcell-compressor.com/fileadmin/user_upload/02_FFCC/DOKUMENTE/Wasserabscheider_EN.pdf
[12] Accessed June 6th 2023, https://shop.mann-hummel.com/en/e-mobility/entaron-fc-7-5-filter-system-1.html
[13] Accessed June 6th 2023, https://www.fischer-fuelcell-compressor.com/en/products
[14] Accessed June 6th 2023, https://www.fumatech.com/en/products/humidifier-modules-ecomate/
[15] Accessed June 13th 2023, https://www.fischer-fuelcell-compressor.com/fileadmin/user_upload/02_FFCC/DOKUMENTE/FISCHER_Broschuere_FFCC_Compressor_EN.pdf

Table 10.16: *Air system components*

Component	Mass [kg]	Volume [L]	Power Consumption [W]
Water Separator [11]	8	15	0
Air filter [12]	3	13	500
Compressor [13]	11	14	11250
Intercooler [69]	7.2	9.5	2000
Humidifier [14]	6.2	16	1
Turbine [15]	3	10	0
Total	**38.3**	**76.9**	**13751**

this system is used to supply air to the fuel cells. A more detailed component analysis will not be done at this stage. Furthermore, the air subsystem was also a deeper than necessary analysis of the power system, therefore, this will be the design of it at this stage and will not be looked at in more detail currently as it is sufficient for the current design stage.

10.8. Final Power System

In this section, an overview of the power system will be provided. A powertrain showing the distribution of power, as well as the integration of the different subsystems within the eVTOL will be presented. Finally, the power system sizing overview will be shown.

10.8.1. Powertrain

The fuel cell and battery both generate power for all the systems of the eVTOL. For the output voltage of the fuel cell stack, a DC/DC converter is used in order to boost the output voltage of the fuel cell stack in order to meet the desired voltage level [16]. This is also done for the battery so that the DC/DC converter can step up or down the voltage according to the application the power is being supplied to. This converter is also used for regulatory purposes. This can maximise the efficiency and performance of the fuel cell which will be desired. Following this conversion, the power from the fuel cells and batteries can be distributed to each rotor. As opposed to the initial J1 design in the Midterm report [1], 2 engines per rotor are used which are connected in parallel for redundancy reasons. The power produced by the battery is also used to supply power to the secondary power systems such as the ones mentioned in Table 10.1. An overview of the whole powertrain can be visualised in Figure 10.7.

[16] Accessed 9th June 2023, https://www.infineon.com/cms/en/applications/automotive/fuel-cell-ev-drivetrain/dc-dc-boost-converter/

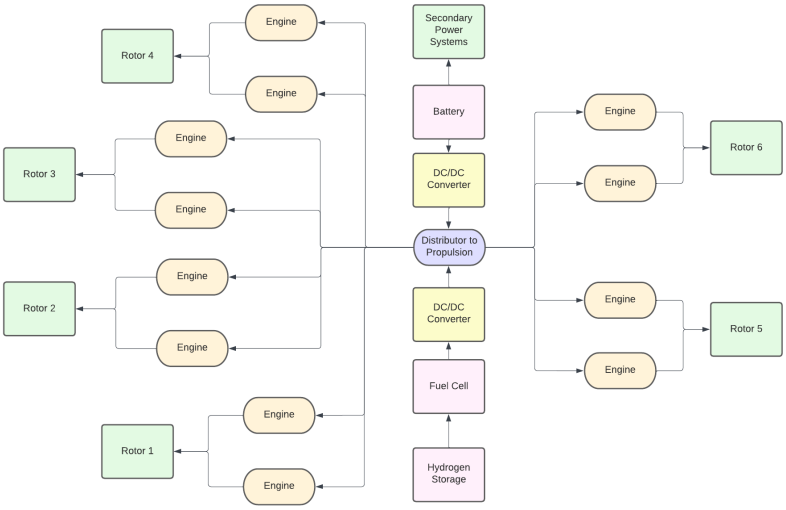

Figure 10.7: *Powertrain Schematic*

10.8.2. Subsystem Integration

Battery

The batteries will be placed throughout the span of the wings. Doing this has advantages such as a reduction in the structural weight of the aircraft. The battery placement in the wings reduces the bending moment and the torsional load on the spars, thus reducing their thickness and decreasing the overall weight of the eVTOL. Furthermore, placing the batteries this close to the rotors decreases the wiring distance between the two, thus, losses because of resistance and wiring are decreased [17]. In addition, placing the batteries in the wing, as far away from the hydrogen tanks as possible, decreases the probability of an explosion in case of battery failure and fire. During the cruise, batteries can be cooled by the flow of air over the wings, however, since batteries are mainly used for hovering, they will heat up most during this phase. However, in this phase, the flow of air will not align with the airfoil shape and thus it will not be sufficient to provide the necessary cooling. Therefore, a separate cooling system is also used for the batteries. This cooling system will be placed in the tail section of the eVTOL next to the cooling system of the fuel cell. Furthermore, the aircraft will have implemented 'side-pods' beneath the wing right next to the fuselage for the intake of air that will be directly supplied to the heat exchanger, which is placed in the tail section next to the fuel cell heat exchanger as can be seen in Figure 10.8.

Fuel Cell and Hydrogen Storage

The fuel cell and the hydrogen tanks will be integrated into the rear part of the fuselage behind the cabin wall, in the tail. The hydrogen tanks will be attached to the ceiling, within the crash structure which has been adjusted according to the crashed diameter coefficient in Section 9.1. The fuel cell will be placed below the tanks with pipes connecting the hydrogen storage to the fuel cell to ensure the flow of hydrogen from the tanks. Furthermore, the air intake from the 'side-pods' will flow through pipes and the air subsystem to be finally connected to the fuel cell. Furthermore, the cooling system for the fuel cell, the heat exchanger, will be placed within close proximity to the fuel cell in the tail section. This close integration of these subsystems increases efficiency and provides easier maintenance and repair. Figure 10.8 shows the placement of the tanks, fuel cell, air subsystem and cooling systems within the tail section of the fuselage.

[17] Accessed June 12th 2023, https://www.aviationtoday.com/2020/09/08/batteries-behind-electric-aircraft-revolution/

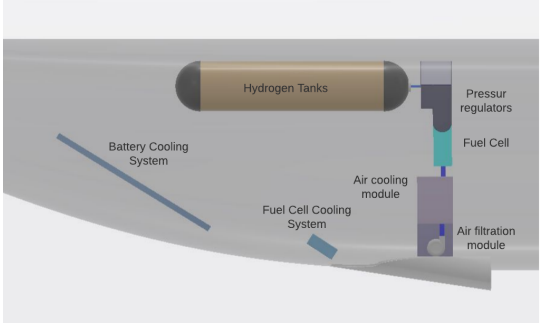

Figure 10.8: *Side view of Tail Section*

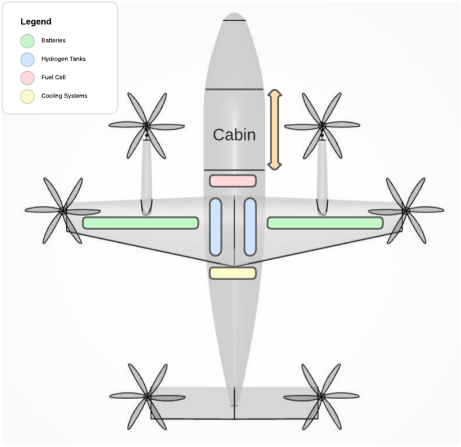

Figure 10.9: *Overview of Subsystem Integration*

The air filtration and cooling, and pressure regulators are all part of the air subsystem. Where, the air filtration module consists of air filters and water separators, whereas, the air cooling module consists of a humidifier, intercooler, compressor and turbines. Finally, a complete overview of the integration of the different subsystems can be seen from the top view of the design in Figure 10.9. In this figure, green refers to batteries, blue to hydrogen tanks, pink to fuel cell and air subsystem, and yellow to cooling systems. Although the tanks and batteries seem in close proximity in this figure, in reality, they are quite far since the batteries are within the wings, whereas, the tanks are in the fuselage. In addition, although there is a lot of space in the rear tail section of the eVTOL, hydrogen tanks can not be placed there to be further away from the batteries as it would result in the centre of gravity (cg) to shift too aft, resulting in an extremely difficult, or even impossible, to control eVTOL.

10.8.3. Power System sizing overview

Following the sizing of individual subsystems, a summary of the whole power system can be provided. This can be applied by the addition of individual subsystems to provide the overall mass and volume of the power system as well. An overview can be seen in Table 10.17.

Table 10.17: *Power System Sizing Overview*

Subsystem	Mass [kg]	Volume [L]	Power [kW]	Energy [kWh]
Battery	205	94.4	778	61.4
Fuel Cell	42	38.1	125	
Hydrogen Storage	176.7	533		319
Cooling Fuel Cell	11.1	17.1	- 5.56	
Cooling Battery	37	37.5	- 7.69	
Air	38.3	76.9	-13.8	
Total	510.1	797	872.95	380.4

It can be concluded that the overall fuel cell subsystem mass, including the cooling and air subsystem, is 91.4 kg. This results in a power density of the fuel cell subsystem of 1.35 kW/kg as the Pstack max rated power is 125 kW. This aligns with the system power density of around 1.5 kW/kg mentioned by a Fuel cell engineer at Zeroavia [18].

[18] P. de Boer, Fuel cell Engineer at Zeroavia. Technical Meeting

11

Propulsion

In this chapter, the design process of the propeller blades is discussed. First, the necessary derivations are given, followed by the design process for cruise. This is ensued by the derivations of the hovering conditions, and finally the results. Lastly, the noise emissions are presented.

11.1. Design Process Source

To begin designing the propellers, Larabee's method was chosen. This method presents a straightforward process of optimising a propeller in both cruise, and off-design (hovering) conditions. However, the paper that is referenced in this chapter is by Adkins and Liebeck [2], two authors that improve on Larabee's method by alleviating some of the constraints that Larabee previously applied. In this chapter, every piece of information and all formulas have been taken from this paper, unless otherwise specified.

11.2. Blade Geometry

To start designing the blades, the blade geometry, and velocity acting on the blades should be defined. These are depicted in Figure 11.1.

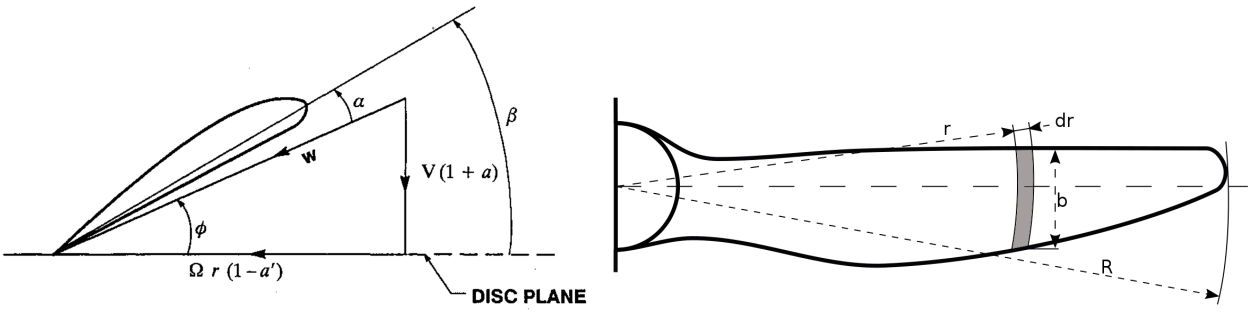

(a) *Side View [2]*

(b) *Top View* [1]

Figure 11.1: *Blade Geometry*

Here, α is defined as the blade angle of attack, β is defined as the blade pitch angle and ϕ is the blade flow angle, which is the angle at which the flow hits the blades. The blade pitch angle can also be expressed as $\beta = \alpha + \phi$.

In Figure 11.1, the velocities are also given. The resultant velocity, W, experienced by the propeller, can be broken down into two components; axial and tangential. The axial velocity is given by $V(1 + a)$. Here, V is the freestream velocity, and a is an axial interference factor. This factor follows from the fact that the rotating propellers have an upwind impact on the flow which can increase the freestream velocity. The tangential velocity is $\Omega r(1 - a')$, where Ω is the rotational speed of the propellers and r is the propeller radius. Likewise, the tangential velocity also has a component, a', that adjusts for the propeller effect on the flow.

[1] Accessed on June 1st 2023, https://en.m.wikipedia.org/wiki/File:Propeller_blade_BET.svg

11.2.1. Introduction of Momentum Equations

Momentum theory, or actuator disk theory, is used to build equations based on a simplified model of propellers. Here, the propeller blade is sectioned into annuli, and the thrust per unit radius, acting on each annulus can be determined. To do this, a fluid element of mass dm must be considered, moving far upstream towards the propeller disk, with a velocity V. The mass flow can be expressed as ρAV, where ρ is the air density, A is the area of the annulus, and V is the freestream velocity with an adjustment factor, as explained in Section 11.2. The area of the annulus is found using Figure 11.1b, where the area of the shaded part (representing each annulus) can be expressed as $2\pi r dr$, r being the local radius at the annulus measured from propeller hub. This means that the mass flow per unit radius can be expressed as $2\pi r\rho V(1+a)$. When said fluid element moves through the propeller into the wake, its velocity is further increased to $V(1+b)$ in the far wake. According to [2], the value b can be approximated as $2a$, which is further supported by another source [2]. To find the thrust per unit radius, the difference in velocity between the slipstream and freestream must be found, and multiplied with the mass flow per unit radius. Also taking into account a parameter F, which considers the loss of momentum due to radial flow (also known as the Prandtl tip loss factor), the thrust per unit radius can be calculated as:

$$T' = 2\pi r\rho V(1+a)(2VaF) \tag{11.1}$$

Using the same principles, the torque per unit radius can be found too.

$$Q'/r = 2\pi r\rho V(1+a)(2\Omega r a'F) \tag{11.2}$$

where Ω is the angular velocity in radians per second.

11.2.2. Circulation to Reduce Induced Power

By optimizing the blade geometry, the circulation can be modeled as a function of the radius such that it minimizes the power required to provide enough lift, called the induced power [3]. This begins with the Kutta-Joukowski theorem, which states that the lift per unit span is the product of air density, freestream velocity, and circulation; $L' = \rho V_\infty \Gamma$.

This can be adapted for a propeller by doing two things; multiplying it by the number of blades, therefore, making it the lift per unit radius of the entire propeller, and replacing the freestream velocity by W, the local total velocity, found in Figure 11.1a. Similarly, the circulation behind each corresponding annulus can also be calculated. These are shown in Equation 11.3 and Equation 11.4.

$$L' = B\rho W\Gamma \tag{11.3}$$

$$B\Gamma = 2\pi r F w_t \tag{11.4}$$

Here, the only previously undefined variable is w_t. This is the tangential velocity of the local total velocity, W, called the swirl velocity of the slipstream. This is made more clear in Figure 11.2a.

[2] Accessed on June 1st 2023, http://www-mdp.eng.cam.ac.uk/web/library/enginfo/aerothermal_dvd_only/aero/propeller/prop1.html

[3] Accessed on June 1st 2023, https://www.usu.edu/math/powell/ornlab-html/node7.html

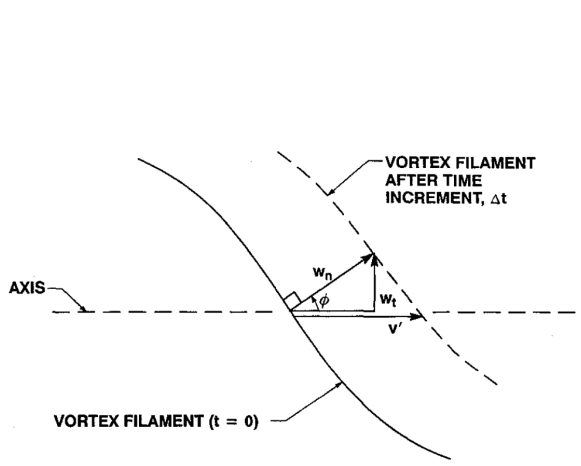

(a) *Vortex Filament Velocity Components*

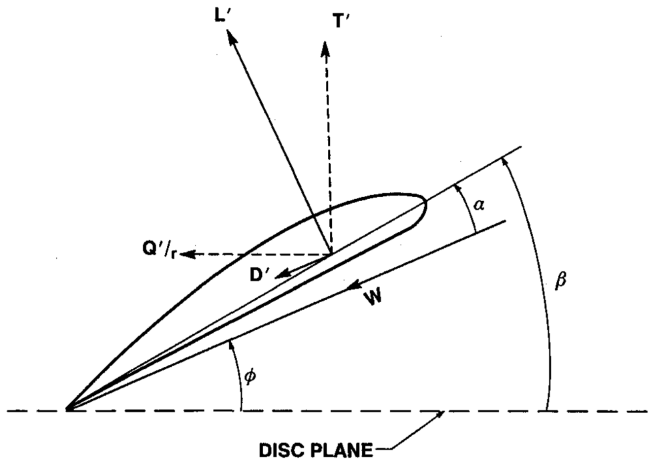

(b) *Blade Force*

Figure 11.2a depicts the vortex filaments in the wake, together with its velocity breakdown. This is shown, as to be able to find the circulation distribution, $\Gamma(r)$, w_t must be converted into a more measurable velocity. It is known that the motion of the fluid must be normal to the vortex sheet, meaning the equality $w_t = w_n \sin\phi$ can be found from Equation 11.3, where w_n is the normal component of the local total velocity, relative the to vortex filament. However, using a coordinate system that is fixed to the propeller disk is more conventional. Therefore, the relation $v' = w_n/\cos\phi$ is used, where v' represents the axial velocity of the vortex filament. Using this, the swirl velocity can be rewritten as $w_t = v' \sin\phi\cos\phi$. Finally, a new variable is introduced, called the displacement velocity ratio, $\zeta = v'/V$, and is implemented so that the swirl velocity is expressed as:

$$w_t = V\zeta \sin\phi\cos\phi \tag{11.5}$$

Next, a new variable G is introduced, where $G = F\sin\phi\cos\phi$. Using this, Equation 11.5, and $r = V/\Omega$, Equation 11.4 can be rewritten as:

$$\Gamma = \frac{2\pi G V^2 \zeta}{\Omega B} \tag{11.6}$$

Now that the circulation has been expressed using the desired variables, Equation 11.1 and Equation 11.2, expressing the thrust per radius and torque per radius respectively, can be modified to be expressed in a simpler manner. For this Figure 11.2b is used. The forces acting on the blade, as seen in Figure 11.2b, are:

$$T' = L'\cos\phi - D'\sin\phi \tag{11.7}$$

$$Q'/r = L'\sin\phi + D'\cos\phi \tag{11.8}$$

These can also be rewritten as:

$$T' = L'\cos\phi(1 - \epsilon\tan\phi) \tag{11.9}$$

$$Q'/r = L'\sin\phi(1 + \epsilon/\tan\phi) \tag{11.10}$$

Where D' is the drag per unit radius, and ϵ is the drag over lift ratio. Using these, the interference factor, a, discussed in Section 11.2 can be found. Adkins and Liebeck specify that here, a deviation is made from Larrabee's method. This is because Equation 11.9 and Equation 11.1 are required to be equivalent, combining blade element and momentum theory. Knowing this, and by considering from Figure 11.1 that $V(1+a) = W\sin\phi$, the interference factor is shown as:

$$a = \frac{\zeta}{2}\cos^2\phi(1 - \epsilon\tan\phi) \tag{11.11}$$

It should be noted that the $\tan\phi$ can also be written as:

$$\tan\phi = (1+\zeta/2)\lambda/\xi \;\Rightarrow\; r\tan\phi = (1+\zeta/2)\lambda R \tag{11.12}$$

Where λ is the speed ratio, $V/(\Omega R)$, and ξ is the nondimensional radius, r/R. Equation 11.12 is imperative as it shows that $r\tan\phi$ is constant. This is referred to as the Betz condition, and it proves that for the vortex sheet to be considered a regular screw surface, this condition must hold, as it ensures that the energy loss is minimum.

11.2.3. Constraining Equations for a Specific Thrust

Adkins and Liebeck specify that at this stage, either a thrust value or a power value must be specified for the design. Although a power requirement has been calculated in the Midterm Report [1], this is a preliminary estimate. Using a thrust value is more beneficial since the current cruise thrust estimate is more reliable than the available power estimate, besides the fact that the thrust values are more relevant for this context. For the design, the nondimensional versions of thrust and power are used, namely T_C and P_C. They are given by:

$$T_C = \frac{2T}{\rho V^2 \pi R^2} \tag{11.13}$$

$$P_C = \frac{2P}{\rho V^3 \pi R^2} \tag{11.14}$$

Using Equation 11.9, Equation 11.13 can be rewritten as:

$$T_C' = I_1'\zeta - I_2'\zeta^2 \tag{11.15}$$

Where,

$$I_1' = 4\xi G(1-\epsilon\tan\phi) \tag{11.16}$$

$$I_2' = \lambda(I_1'/2\xi)(1+\epsilon/\tan\phi)\sin\phi\cos\phi \tag{11.17}$$

Considering that ζ is a constant value, a specific thrust produces these constraint equations:

$$\zeta = (I_1/2I_2) - [(I_1/2I_2)^2 - T_C/I_2]^{1/2} \tag{11.18}$$

$$P_C = J_1\zeta - J_2\zeta^2 \tag{11.19}$$

Where,

$$J_1' = 4\xi G(1+\epsilon/\tan\phi) \tag{11.20}$$

$$J_2' = (I_1'/2)(1-\epsilon\tan\phi)\cos^2\phi \tag{11.21}$$

The values for I and J in Equation 11.18 and Equation 11.19 are integrated expressions, evaluated from ζ_0 to 1, where ζ_0 is the propeller hub radius.

11.2.4. Determining Blade Geometry

The blade geometry can be calculated, considering what has been discussed above. Using the lift equation, the lift per unit radius of an element, dr, of a single blade can be expressed as:

$$0.5\rho W^2 c C_l = \rho W\Gamma \tag{11.22}$$

Where c is the chord length, and C_l is the local lift coefficient. Using Equation 11.6, and $r = V/\Omega = \lambda R$, this equation can be rewritten as:

$$Wc = \frac{4\pi\lambda G V R\zeta}{C_l B} \tag{11.23}$$

This value can also be multiplied by the air density, and divided by viscosity to find the Reynolds number so that each station can be analyzed at its respective Reynolds number. Equation 11.23 can also be used to find the chord, c, by dividing it by W. As mentioned before, W can be found by using the equation $V(1+a) = W\sin\phi$. Finally, the momentum loss factor can also be defined, so all parameters in Equation 11.23 are defined (since G is a function of F).

$$F = \frac{2}{\pi}\arccos(e^{\frac{B(1-\xi)}{2\sin\phi_t}}) \tag{11.24}$$

Where $\tan\phi = \tan\phi_t/\xi$

11.3. Design Procedure for Cruise

This design procedure is primarily used for one single given condition, which in this case, is cruise, as most of the time is spent in this phase. For the design procedure, many iterations will be performed to be able to maximize the efficiency. The procedure depends on certain flight conditions and atmospheric parameters. It is expected that the number of blades, the rpm, and the blade radius is known. An airfoil for the propellers also needs to be determined beforehand. In the procedure, the propulsive efficiency will be maximised.

This process begins with an initial estimate for ζ, the velocity ratio. Adkins and Liebeck suggest using 0 as an initial value. Once this is established, ϕ must be found at each blade station. Using Equation 11.12, and the fact that $\xi = 1$ turns ϕ into ϕ_t (tip angle ϕ), $\tan\phi_t$ can be found. Following this the Betz condition, $r\tan\phi = R\tan\phi_t$, can be used, giving ϕ. The momentum loss factor, F, is also found by using Equation 11.24 since all the variables are known.

Once F is known, G is also known. Since V, R, and B are known, and λ is dependent on variables that are all known, this means the only unknown is C_l. To find this, the airfoil of the propeller must be determined. Due to certain time constraints, an extensive airfoil trade-off was not performed. Instead, research was done to see the common airfoils being used for propellers, and among these, the Wortmann FX 63-137 and the NACA4412 were considered, due to their high lift-to-drag ratios. Once these airfoils were put in XFOIL, and the design procedure was run, it seemed that the Wortmann had a slightly higher propulsive efficiency when compared to the NACA4412, meaning the Wortmann was selected, as shown in Figure 11.3 [4].

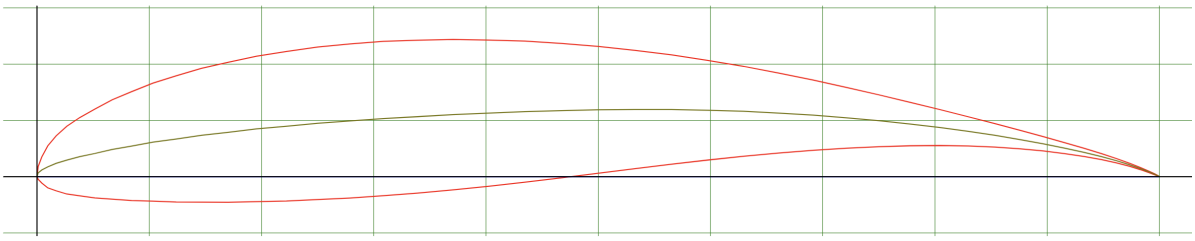

Figure 11.3: *Wortmann FX 63-137*

Therefore, the Wortmann airfoil was simulated using XFOIL, for Mach 0, with Reynolds numbers ranging from 100,000 to 5,000,000.

The airfoil selection being complete means that the optimal lift-to-drag ratio of each blade station can be determined. To begin this, an array of C_l's was made, using a step size of 0.05. These values were used to determine Wc at each blade station, using Equation 11.23. Following this, the Reynolds number per station is found by:

$$\text{Re} = Wc\cdot\rho/\mu \tag{11.25}$$

[4] Accessed on June 14th 2023, http://airfoiltools.com/airfoil/details?airfoil=fx63137-il

where ρ is the air density, and μ is the dynamic viscosity of the air. The XFOIL simulation of the Wortmann corresponding to the Reynolds number was then opened, and the Cd and α were found for every C_l value. Next, the minimum D/L was found. This meant that the optimum C_l value, and following this, α for each station was found.

The flow angle still needs to be found to find the optimal blade geometry. To do this, Equation 11.12 is used to find the flow angle per station. Following this, the interference factor is found using Equation 11.11, and finally, the local flow velocity W can be found.

At this point, the entire blade geometry can be determined. Since the angle of attack, and the flow angle are known, the pitch angle per station is determined as $\beta = \alpha + \phi$. Since each station has its own pitch angle, this also gives the blade twist. Before, Wc was also found per station, and since W is now known too, the chord length per station is also determined.

Now, the derivatives I_1' and I_2' can be calculated using Equation 11.16 and Equation 11.17, which allows for the calculation of ζ, the displacement velocity ratio. The entire procedure listed is iterated until the consecutive zetas found are within 0.1% of one another, meaning the procedure has converged on a value.

Now, with all the values found, T_C, the derivatives J_1' and J_2', and P_C can be calculated. Finally, the propulsive efficiency of the configuration is determined by T_C/P_C.

11.4. Analysis of Configuration in Off-Design Conditions

Although the blades can be designed, this configuration must be evaluated for off-design conditions, namely hovering. This procedure assumes that a blade geometry has already been defined, and analyzes it, to see if the blade can meet the conditions of hover. This process is also from the same paper by Adkins and Liebeck, described above.

The process begins by defining coefficients for the propeller force, which are defined from the airfoil coefficients; these are C_y and C_x and are defined as is seen in Figure 11.4.

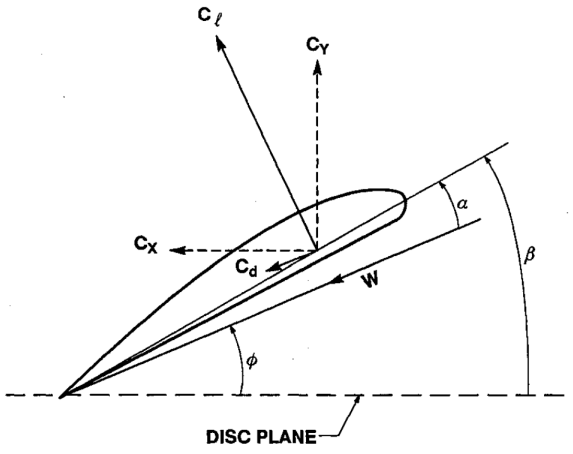

Figure 11.4: *Propeller Force Coefficients*

From this, it follows that:

$$C_y = C_l \cos\phi - C_d \sin\phi = C_l(\cos\phi - \epsilon \sin\phi) \tag{11.26}$$

$$C_x = C_l \sin\phi + C_d \cos\phi = C_l(\sin\phi + \epsilon \cos\phi) \tag{11.27}$$

Now, the thrust and torque per unit radius can be expressed as:

$$T' = 0.5\rho W^2 BcC_y \tag{11.28}$$

$$Q'/r = 0.5\rho W^2 BcC_x \tag{11.29}$$

As was the case for the cruise design procedure, Equation 11.28 and Equation 11.29 must be equal to T' and Q'/r in the momentum equations, Equation 11.1 and Equation 11.2. Setting these equal gives the new interference factors:

$$a = \frac{\sigma K}{F - \sigma K} \tag{11.30}$$

$$a' = \frac{\sigma K'}{F + \sigma K'} \tag{11.31}$$

Where,

$$K = \frac{C_y}{4\sin^2\phi} \tag{11.32}$$

$$K' = \frac{C_x}{4\sin\phi\cos\phi} \tag{11.33}$$

and $\sigma = Bc/2\pi r$. σ represents the solidity, which is a ratio of the total blade area, to the disk area.

11.4.1. Iterative Process

The iterative part of the process requires a solution for the flow angle at each blade station. This is done by having an initial estimate of it by assuming ζ is 0. Following this, since the blade pitch angle is known, the angle of attack is found by subtracting the flow angle from the blade pitch angle. If the angle of attack is known, an initial estimate of the Reynolds number must be found too so that the airfoil characteristics such as C_l and Cd can be found. Normally, the Reynolds number is calculated as $\rho Vc/\mu$, yet, in this case, the speed is replaced with the rotational velocity, Ωr to find an initial Reynolds number. Now, C_l and C_D can be found, and since the flow angle is known too, C_y and C_x can be calculated.

Following this, the interference factors can be found using Equation 11.30 and Equation 11.31. From Figure 11.1a, the local flow velocity can be calculated using:

$$W = \sqrt{(V(1+a))^2 + (\Omega r(1-a'))^2} \tag{11.34}$$

Since all these parameters are known, the Reynolds number can be updated using the local flow velocity. Finally, ϕ can be found using:

$$\tan\phi = \frac{V(1+a)}{\Omega r(1-a')} \tag{11.35}$$

This procedure is iterated until a final ϕ has been found, which leads to the final calculation of C_y, C_x, and W. Now, the thrust per unit radius can be calculated using Equation 11.28.

Lastly, the efficiency of the propellers can be determined in this off-design condition, which can be calculated using $\eta = C_T J/C_P$. Here, C_T is the thrust coefficient, C_P is the power coefficient, and J is the advance ratio, defined as V/nD (n is the rotational speed in revolutions per second, and D is the rotor diameter). C_T and C_P are:

$$C_T = \frac{T}{\rho n^2 D^4} \tag{11.36}$$

$$C_P = \frac{P}{\rho n^3 D^5} \tag{11.37}$$

In this case, the thrust is specified meaning that the thrust coefficient can be found, but the power coefficient cannot be found due to the absence of P. For this, another equation can be used:

$$C'_P = \frac{C'_T \pi^4 \sigma \xi^2 F^{32}}{4((F+\sigma K')\cos\phi)^2} \tag{11.38}$$

This equation can be integrated from the hub radius to the tip to find C_P, so that the efficiency can be found.

11.5. Final Propulsive Characteristics

Once all the design procedures have been set in place, the final values can be obtained through iteration. Designing a propeller that works for both cruise and hover proved to be quite difficult, as the goal is to optimize for cruise, but to be able to meet the conditions of hovering. To do this, the "design" thrust must be determined, by multiplying the required cruise thrust by a certain T-factor. This design thrust is what the propellers will be sized for, and must be as small as possible so that the design thrust is close to the cruise thrust. Then, by varying the rpm and pitch angle, the hover requirements can be met. Another issue is that to meet the requirements set in Subsection 8.2.1, the propellers have to supply 2.25 times the nominal thrust required in hover.

Keeping this in mind, the required cruise thrust per engine is 258.5 [N]. This follows from dividing the MTOW by the aircraft C_L/C_D and splitting it per engine. The hovering requirement is the MTOW multiplied by the maximum thrust-to-weight ratio, as found in the midterm report [1], and splitting it per engine. This value will is relevant for any vertical flight, and resulted in a thrust requirement of 4680 [N]. The same was done for the hover controllability, yet multiplied by 2.25 to reach 10,530 [N] per engine.

Following this, multiple iterations and optimizations were done to find the right balance of the blade number, T-factor, and cruise rpm. The reason cruise rpm was important was that this affected the geometry of the design. For example, if the cruise rpm was too high, this would lower the blade chords, which would mean that they cannot meet the hover controllability thrust.

As for the radius, it was known that the higher the radius, the better it is for the propulsive efficiency. However, increasing the radius too decreased the blade chord length, which had a negative effect, as will be discussed in the sensitivity analysis in Section 11.6. A value based on the sensitivity analysis was chosen, ensuring that the disk loading was at a value close to 120, one that was chosen in the midterm report [1].

This resulted in design thrust conditions of 1000 rpm, a T-factor of 10, with 6 blades, and a radius of 1.05 [m]. This means that at the design condition, at a nominal blade pitch angle, each propeller can produce 2,585 [N]. The resulting propeller operates at 83% efficiency. This value seems lower than was desired, yet the propellers have to accommodate for an extremely large range of thrusts because propulsive efficiency was considered less compared to ensuring that the required thrust could be reached. Once the design conditions were set, the sizing conditions' parameters were found, as seen in Table 11.1. In this table, $\Delta\beta$ represents the change in pitch angle necessary in a phase to reach the required thrust values.

Table 11.1: *Propulsive Settings*

	Max Thrust (for Controllability)	**Hover Thrust**	**Cruise Thrust**
RPM [-]	2331	1585	302
$\Delta\beta$ **[deg]**	-40	-40	0
Thrust Produced [N]	10,666	4,689	259

Here, the propellers will be oriented at their nominal pitch angle, and spin at 280rpm to produce the cruise thrust. It is clear that 280 rpm is a very low number compared to other aircraft. Since the max thrust requirement is much higher compared to cruise, this creates a propeller that is, in a way, too large for cruise, yet is the only way that the aircraft can be controllable during one engine inoperative vertical flight with gust and crosswind defined by CS27. Therefore, this rpm is required for cruise. For the maximum thrust and hover thrust, the rpm is raised to the values seen in Table 11.1. The

hover rpm was optimal for that mission phase, but the rpm for the max thrust was limited by the tip Mach number. This was limited to 0.75, to avoid shockwaves, since a relatively thicker airfoil is being used. The maximum thrust configuration is only in case of emergencies, as specified in Subsection 8.2.1. The overall blade geometry, for the mission phases, is as follows:

(a) *Cruise Configuration* **(b)** *Hover Configuration*

Figure 11.5: *Propeller Side View*

Figure 11.6: *Propeller Top View in Hover*

11.6. Sensitivity Analysis

To see how each result of interest is affected by the inputs of the design procedure, a sensitivity analysis can be performed.

Firstly, the input parameters' effect on the propulsive efficiency should be considered. These are the radius, cruise velocity, blade number, and rpm. The radius was expected to affect the results tremendously, as every single parameter has a link to the radius. The cruise velocity was also shown as this value could have been changed to fly at a more optimal propulsive efficiency, yet this affects other technical departments too, therefore was more difficult to change. The blade number was more difficult to change, as increasing this number significantly resulted in decreased blade chords, which led to the blade chord being too short to be able to have structural integrity. Finally, the cruise RPM also had an enormous effect, as this determined the blade geometry, which then determined the hover RPM and T-factor to be used. The results are depicted in Figure 11.7a and Figure 11.7b. The design point of the Aetheria has been marked on each figure.

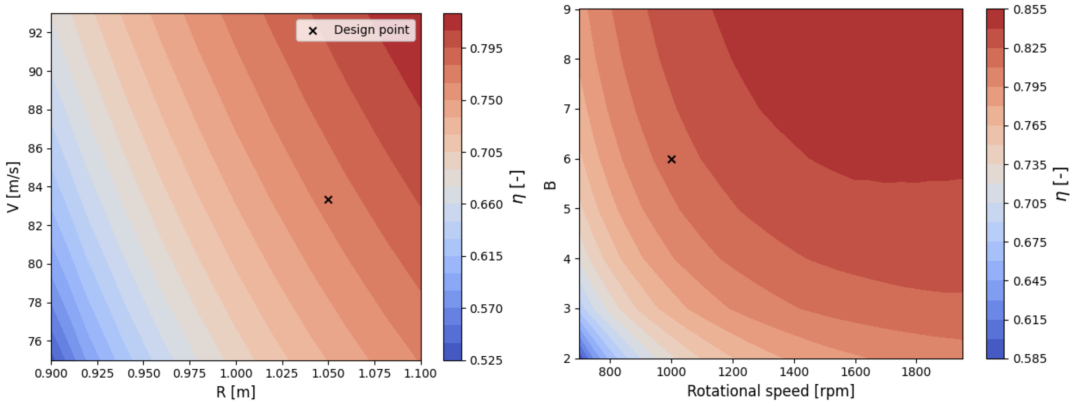

(a) *Cruise Velocity and Radius vs. Propulsive Efficiency* **(b)** *Blade Number and RPM vs. Propulsive Efficiency*

Figure 11.7: *Input Sensitivity*

As can be seen, a design point that is close to the maximum possible within these bounds has been picked. In both figures, reaching the top right corner (highest efficiency) becomes more difficult, as the spacings of the color contours increase, showing that there are diminishing returns on increasing the input values further than the design point. The cruise velocity was not increased further, as a large increase in the cruise velocity resulted in a small increase in the propulsive efficiency. As this value affected other departments more, the given value was chosen. The radius and number of blades were maximized as much as possible without it decreasing the chord length too much. Finally, the cruise rpm could have been increased more, but that would have meant that a much larger T-factor would be required, meaning the propeller would have been designed for a point further away from cruise conditions. This is shown in Figure 11.8.

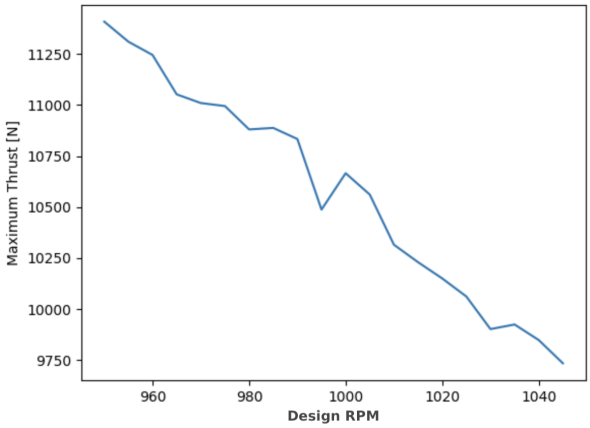

Figure 11.8: *Maximum Thrust Delivered vs. Design RPM*

Here, it is possible to see that increasing the design RPM has a negative impact on the maximum amount of thrust possible. Therefore, the design RPM that corresponds to the maximum thrust requirement was chosen. It should be noted that this graph should be completely straight, but since the thrust depends on C_l values taken from XFOIL, there are some irregularities that prohibit the line from being straight.

Besides the input values, the hover requirements also had to be met. This was done by adjusting the blade pitch angle, T-factor, and hover rpm to see how the thrust could be provided. Their sensitivity is shown below. It should be noted this shows the available thrust.

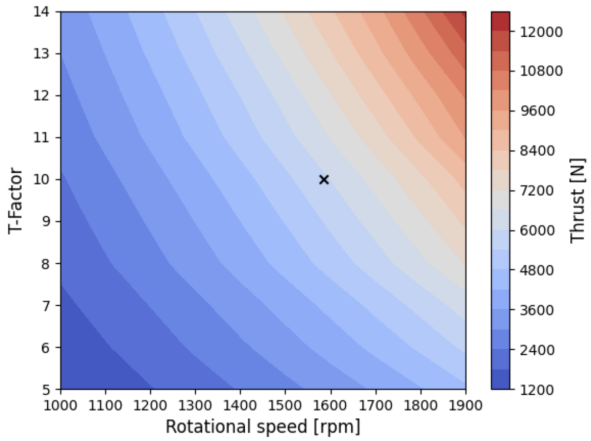

(a) *T-Factor and Hover RPM vs. Hover Thrust*

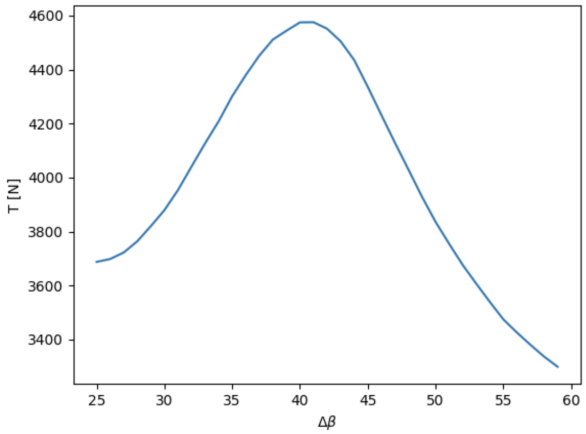

(b) *Pitch Angle Variation Effect on Thrust*

Figure 11.9: *Hover Requirements*

It is evident from Figure 11.9a, that the thrust provided in hover is extremely sensitive to the T-factor and the rotational speed in hover. Here, the aim is not to maximize, but to just barely reach the maximum thrust required. For this, the thrust required is the colour gradient that the design point is in. Therefore, any configuration that can place the point in that gradient would work. Lowering the T-factor would have had benefits, but this would also affect the maximum thrust requirement; the design point chosen was carefully picked to meet all the requirements of each mission phase while maximising efficiency.

Finally, Figure 11.9b depicts how the variation in blade pitch angle can affect the thrust produced. As to not overdesign, the propulsive configuration that is able to just barely meet the thrust requirements by a variation of the blade pitch angle should be picked.

11.7. Noise

Since the propulsive characteristics have been found, the noise emissions of the total configuration can also be determined. For this, a complex empirical method has been used, as outlined in "A Review of Aerodynamic Noise From Propellers, Rotors, and Lift Fans" by Jack E. Marte and Donald W. Kurtz [70]. To predict the noise of a single propeller, this equation was produced:

$$\text{SPL} = L_1 + 20\log(\frac{4}{B}) + 40\log(\frac{15.5}{D}) + CF_{MACH} + CF_{\theta} - 20\log(r-1) \tag{11.39}$$

Equation 11.39 gives the noise level at any distance by inputting that distance in feet, for r, at the end of the equation. This equation, being empirical, considers all forms of noise produced by a

propeller, whether it be turbulent air noise, vortex noise, exhaust air noise, etc.

From the terms, L1 is a general noise estimation, based on the propeller horsepower. At cruise, this value was picked to be 108, and at hover, 117. This value was found in a figure within the source, yet by extrapolation, the equation was found to be $L_1 = 6.3407\ln(P) + 85.872$, where P is given power in the desired mission phase. The second term accounts for the fact that the more blades there are, the less noise is produced. This is due to the fact that the loads on the blades are reduced, since each blade is required to produce less lift, meaning the pressure differences are less. The number of blades was an optimization parameter, and the noise emissions were taken into account. The third term is a correction that is based on the propeller size.

The fourth term is a noise metric based on the rotational tip speed of the propellers. This was obtained from Figure B-3 in the paper, and since the tip Mach speed at cruise is roughly 0.1, this resulted in a correction factor of -17 [dB]. The fifth term considers the angle at which the sound is being measured. For this factor, the angle that corresponded to the loudest noise level was taken, meaning it was 4 [dB].

For cruise, the value r was taken at 2400 [m], which is the cruise altitude, and for hover, it was taken to be 30 [m]. The 30 [m] is an estimation of the closest distance between the Aetheria, and the people surrounding the vertiports. To find the total noise, a basic logarithmic summation was taken for the 6 propellers. This resulted in a noise of **34.42 [dB]** at cruise, and **79.57 [dB]** at hover distance.

It should be noted that using electric propulsion would lower the noise, however, most of the propeller noise comes from vortex shedding and the propeller blade noise. The electric engine would be quieter than its piston engine counterpart, but at the high rpm of hover, this difference becomes negligible. Therefore this estimation of the noise was deemed to have enough accuracy [5].

[5] Accessed on June 18th 2023, https://www.drivingtests.co.nz/resources/are-electric-cars-quieter-than-petrol-or-diese

12

Verification & Validation

Verification and validation play a paramount role in ensuring the reliability and quality of the software. They serve as crutial steps to evaluate and confirm the performance of the code. In Section 12.1 the verification of the system is outlined, explaining firstly the unit testing and secondly the module tests. In Section 12.2 the validation of the product is explained.

12.1. Verification

In the verification section the unit tests and module tests are explained.

12.1.1. Unit tests

Unit tests were conducted as the initial step to verify the code, focusing on examining small code components within the repository. A total of 138 unit tests were developed, some covering different scenarios for the same functions. Details of these tests, including passing and failing rates, can be found in Table 12.1. Notably, an asterisk (*) indicates that tests may not have failed entirely but were skipped upon encountering an error, based on the established setup. Additionally, a double asterisk (**) signifies tests that previously passed but are currently non-functional due to lack of updates in the repository structure. Unfortunately, insufficient time was available to address these updates. Consequently, the coverage report of the unit tests was omitted as it does not accurately represent the functionality of the repository.

Table 12.1: *Summary of all modules and their unit tests. An asterisk(*) indicates that tests may not have failed entirely, but Python proceeds to the next test upon encountering an error, as per the setup. Double asterisk (**) indicates tests passed ran successfully before integration but are currently not working due to lack of update*

Module	Amount of Unit Tests	Passed	Failed
test_lift.py	1	1	0
test_avl_access.py	3	3	0
test_drag.py	17	6	11*
test_prop_wing_interaction.py	12	6	6*
test_coolingsystem.py	21	19	2
test_powersystem.py	6	6	0
test_wing_power_loading	1	1	0
test_mission_energy.py	9	0	9
test_aileron_sizing.py	1	1**	0
test_stability_derivatives.py	27	27**	0
test_control_surface_sizing.py	4	4**	0
test_wing_loc.py	11	11	0
test_fuselage_sizing.py	1	1	0
test_weight_estimation.py	1	1	
test_geometry_forms.py	7	7	0
test_stress_forms.py	8	8	0
test_wingbox.py	8	8**	0

Based on the findings presented in Table 12.1, it can be concluded that the current verification process lacks robustness. This limitation arises from the highly dynamic nature of the repository, which is a consequence of the restricted time span of 10 weeks. The dynamic nature necessitates regular

updates to the tests, which unfortunately could not be addressed before the conclusion of the Design Synthesis Exercise (DSE) due to time constraints. However, it is important to note that all tests were successfully executed at some point in the commit history. The main challenges were encountered during the process of achieving successful implementation of the functions, where most mistakes were identified. Consequently, the repository has been verified to a certain extent, and several modules can be deemed reliable with a high level of confidence.

12.1.2. Module tests

Aerodynamics

For verifying the aerodynamic parameters, XFLR5 [22] has been used. Certain parameters like C_L/C_D ratio and climb C_L^3/C_D^2 have been compared to the XFLR5 outputs. The output values were in the range of 10%, which could be due to empirical methods used and the neglection of the fuselage in XFLR5.

Flight Performance

To verify the flight performance chapter, a number of methods are used. First of all, the model is supposed to calculate the mission energy of the entire flight segment. Thus the distances of each segment should add up to the total mission distance of 400 [km]. This was checked and this was indeed the case. Furthermore, the total time was calculated as well by adding the times of each segment. The total time was 83 min, which gives an average speed of 80 [m/s]. Since the climbing speed is 77 [m/s] and cruise speed is 83 [m/s], this is verified.

Control and Stability

For engine placement, the controllability limits of the aircraft during vertical operation were determined using the Available Control Authority Index (ACAI) method, which has undergone peer review. The ACAI results defining the controllability limits were cross-verified against the limits determined by the equilibrium of forces and moments.

In horizontal flight, eigenvalues obtained from symmetric and asymmetric flight matrices were compared to those computed analytically based on the aircraft's stability derivatives. The comparison confirmed the match between the matrix-derived eigenvalues and the analytical method, validating their accuracy. Furthermore, stability derivatives and control derivatives were compared to similar derivatives, and unit tests were conducted on the functions responsible for generating these derivatives.

Finally, a SIMULINK-based flight simulator was employed to visually simulate the aircraft's response to various inputs such as height, yaw angle, and reference velocity during vertical flight. This simulation included assessments before and after the implementation of the vertical flight controller. The simulations served as a visual verification of correct flight physics modeling and the effective functioning of the vertical flight controller.

Structural Design

Module tests were conducted for the wingbox optimization, Pylon design, and modal analysis of the airframe as part of the structural design. These tests were primarily qualitative in nature. In the wingbox optimization module, plots were generated for the internal moments in the wing, which were manually calculated and verified. The optimization results were also checked to ensure their reasonableness. Similar procedures were followed for the pylon design module, with additional comparison of the pylon size to that of the Joby VTOL for reference. In the modal analysis module, a brief sensitivity analysis was performed. This involved increasing the magnitudes of several concentrated masses to observe the expected result of a decrease in natural frequency of the corresponding component's modal shape.

Propulsion

Firstly, the exhaust velocity of the propellers can be compared. For BEM, this is found by $V(1+\zeta)$, and for actuator disk theory, the method was outlined in the midterm report [1].

In Figure 12.1, the two exhaust velocities are compared. It seems that these two values are quite close, and become closer as the number of blades increases. This is expected, as actuator disk theory assumes the propellers to be a full disk, meaning that the more blades there are in BEM, the more it fits into the assumptions of the actuator disk theory. Still, there is still a difference between the two. It must be considered that actuator disk theory is a simpler method, and does not take into account many forms of energy losses. Since BEM is a more complex and more accurate method, this is reflected in the fact that the exhaust velocity is higher, which translates to a lower efficiency value.

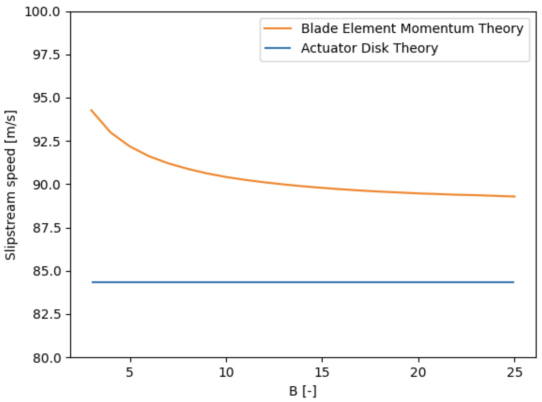

Figure 12.1: *Exhaust Velocity found in BEM vs. Actuator Disk Theory*

Next, the C_T vs. J, and η vs. J graphs can be plotted, to see if these have the correct shape. The propulsive characteristics are very sensitive to C_T and η, so ensuring that the graphs have the right shape can make sure that the code runs in the optimal manner.

As a reference shape, figures 11.28 and 11.29 from an MIT website discussing propeller performance have been used [1]. According to them, the C_T vs. J graph should have a slight increase at low advance ratios, then a gradual fall towards higher advance ratios, when considering propellers at high blade pitch angles. The η vs. J graph should be increasing at a decreasing rate, then reach a maximum, and begin decreasing. Having taken reference graphs into account, the plots produced can be shown:

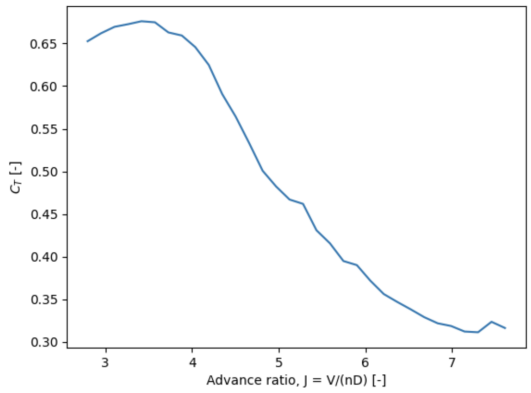

Figure 12.2: *Thrust coefficient vs advance ratio depiction.*

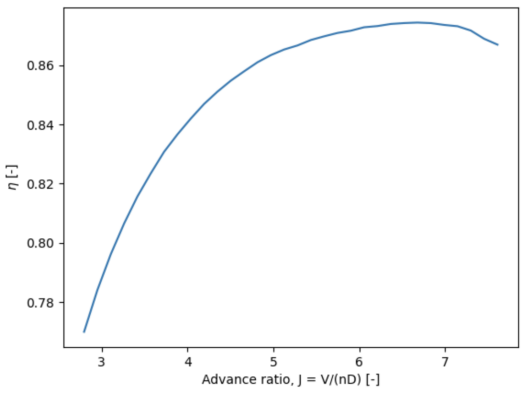

Figure 12.3: *Efficiency vs advance ratio depiction*

The information presented in this section has been deemed good enough to consider the verification as a pass.

[1] Accessed on June 17th 2023, https://web.mit.edu/16.unified/www/FALL/thermodynamics/notes/node86.html

12.2. Validation Plan

The validation can be done in multiple steps. Firstly, by using a balance, the cg travel of the aircraft can be determined and validated. By wind-tunnel measurements, the stability and control derivatives of the aircraft can be validated and improved. Based on these, the gains of the PID controllers can be adjusted. The vertical flight CAS & SAS and the horizontal flight SAS's functions can be validated on the scale model of the aircraft. Lastly, the aircraft can be flight tested to perform system identification and validate the cg travel where the aircraft is stable and controllable and that the CAS and SAS systems function as intended.

For the aerodynamics and flight performance validation, a number of steps have to be performed. First of all, after the DSE CFD analysis should be performed on the Aetheria to validate the lift and drag of the aircraft. Also, the SUAVE conceptual aircraft design tool for new designs can be used to validate the design as it shows similar capabilities in terms of accuracy compared to CFD [71]. Furthermore, the propeller wing interaction can be modelled with wind tunnel test and flow-vis paint to validate how the propellers affect the downwash and airflow around the fuselage. In order for this to succeed, a 3D prototype is required. This can be 3D printed at TU Delft. This prototype will be used to validate the L/D in cruise conditions since this is the main aerodynamic parameter. Finally, a to-scale prototype can be manufactured, to validate the remaining performance parameters not only related to aerodynamics.

To validate that the model generated to perform the necessary calculations within the propulsion system is accurate, the model can be used to generate an output for an adjusted input. The input, in terms of mission energy, will be adjusted according to the Joby design since Aetheria is most similar to Joby. Therefore, the current mission energy of Aetheria which is for a 300 [km/h] speed and 400 [km] range will be scaled down to obtain mission energy for a 320 [km/h] speed and 240 [km] which is that of Joby Aviation [2]. Furthermore, battery specifications in the model were adjusted according to the battery specifications used in the Joby design. Thus, performing these changes in the inputs, resulted in a power system mass of 868 [kg] with only batteries, while for Joby this was 850 [kg] [3]. This overestimation of 1.8% if preferred over a potential underestimation, since it suggests that the final power system mass obtained in Table 10.17 is also an overestimate, thus providing room for contingency.

[2] Accessed June 13th 2023, https://www.jobyaviation.com/

[3] Accessed June 13th 2023,https://www.forbes.com/sites/jeremybogaisky/2020/11/23/joby-batteries-electric-aviation/?sh=692a288576a7

13

Integration & Optimisation

In this chapter, the integration of all subsystems and the overall optimization will be discussed. Integration of all subsystems design is crucial in order to converge to a feasible configuration as most subsystems are heavily intertwined. Furthermore, an overall optimization for mission energy is conducted as this is heavily linked to operational costs.

13.1. Subsystem Integration

The work of all departments was integrated to reach a feasible and consistent design. This is necessary, as at least some output of each department is used as input for work for another department. Therefore, multiple iterations had to be conducted in order to reach a converged design. In the converged design, Aetheria's parameters will approach constant values. This ensures that each department has used the correct parameters.

A high-level overview of the integration can be seen in Figure 13.1. First, initial parameters were estimated by departments in order to initiate the integration scheme. This is followed by the main wing sizing. Based on this, the aircraft's drag was estimated which is used to estimate the mission energy and necessary power. This allows for the power subsystem to be sized. After this, the wing is placed and the v-tail is sized in order to ensure longitudinal static stability. The minimum length for the fuselage is determined for crashworthiness. Finally, the updated maximum take-off mass is estimated with the updated parameters which are checked for convergences.

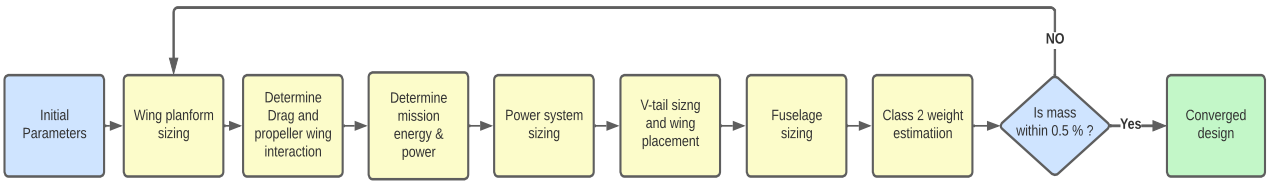

Figure 13.1: *High-level overview of the subsystem integration scheme*

The design was deemed to be converged when the difference between maximum take-off mass for consecutive iterations was below 0.5%. The maximum difference of 0.5% for consecutive iterations was decided based on the engineering judgment of Aetheria's design team. This balances the computational costs and accuracy of the estimation made. This 0.5% iteration error is more strict than the minimum 5% advised in Roskam [30]. However, the team concluded that the absolute error of ĩ60 kg, which is 5% of the 3175 kg limit (*VTOL-CON-MASS-01*), is unsatisfactory. An absolute error of 16 kg was deemed acceptable.

13.2. Overall Design Optimisation

It may be that if all subsystems are optimized individually, the overall design is not the optimal solution. Therefore, after a converged design had been obtained, an optimisation was conducted. This ensures that the overall design is optimized. It was decided that the design is optimized in order to minimize the mission energy, as this would reduce operating costs and increase sustainability.

The design optimisation consist of two parameters: the aspect ratio and fuselage length. The aspect ratio influences the lift-induced drag of the wing and hence the mission energy. A larger aspect ratio results in a reduction of lift-induced drag albeit at the expense of the wing mass.

Additionally, the crashworthiness requirement mentioned in Section 9.6 limits the minimal length of the aircraft fuselage. Using the minimal fuselage length results in a v-tail which is approximately 80% the size of the main wing. This large v-tail causes a substantial amount of drag which is undesirable. The v-tail size can be reduced by increasing the fuselage length. However, this would increase the fuselage friction drag as well as the weight of the fuselage which negatively influences the mission energy.

The optimisation is an extension of the subsystem integration scheme described in Section 13.1. The high-level overview of the can be seen in Figure 13.2. The optimisation algorithm used is the "COBYLA" in the openmdao framework [72]. This algorithm was chosen as it requires no derivatives as input and is compatible with the required constraints.

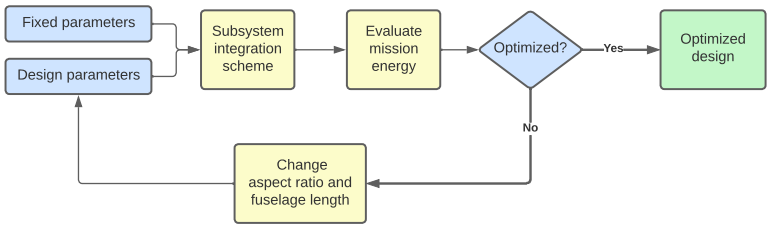

Figure 13.2: *High-level overview of the optimisation scheme*

The optimisation algorithm has to be constrained to ensure requirement compliance. The span and length can not exceed 14m (VTOL-STK-VERT-01) as Aetheria should be able to land on current helipads. The MTOM can not exceed 3175 kg (VTOL-CON-MASS-01), according to EASA requirements. Furthermore, the minimum length of the fuselage, $L_{f,limit}$ is determined by the required length to fit all subsystems as explained in Section 9.6. The constraints are summarized in Table 13.1.

Table 13.1: *Optimisation constraints*

Parameters	min	max
Span [m]	[-]	14
fuselage length [m]	$L_{f,limit}$	14
Mass [kg]	[-]	3175

13.3. Final design

The final design has been obtained following the optimisation procedure, resulting in the following design parameters. The maximum take-off mass (MTOM) is 2483 kg and the mission energy is 218.6 kWh. A summary of other parameters is shown in Table 13.2, where S is the wing surface area, b is the wing span, AR is the aspect ration, l_f is the fuselage length and S_{tail} is the surface area of the the v-tail. This can be seen in the three view drawings in Figure 13.3, Figure 13.4 and Figure 13.5.

Table 13.2: *Optimised result after the mission energy optimization*

MTOM [kg]	Mission Energy [kWh]	S [m^2]	b [m]	AR [-]	l_f [m]	S_{tail} [m]
2522.1	218.6	13.1	9.4	6.7	11.2	4.45

The optimisation resulted in an extended fuselage design with a low aspect ratio. The fuselage is extended as the minimum fuselage length to safely store hydrogen is 8.2 m. This indicates that to optimize mission energy, it is preferred to elongate the fuselage in order to decrease the v tail size. To compensate for the extra mass of the extended fuselage, the aspect ratio was reduced to reduce the wing mass.

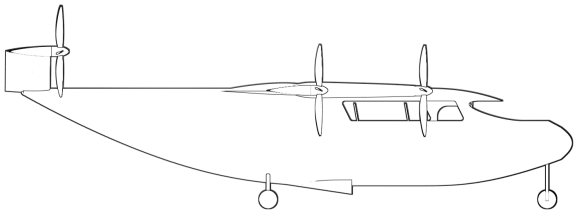

Figure 13.3: *Aetheria side view*

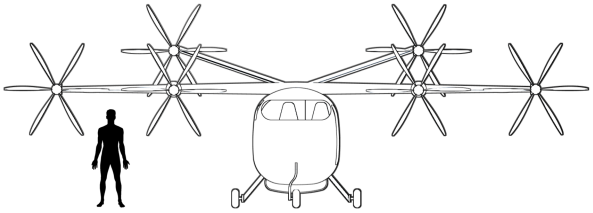

Figure 13.4: *Aetheria front view*

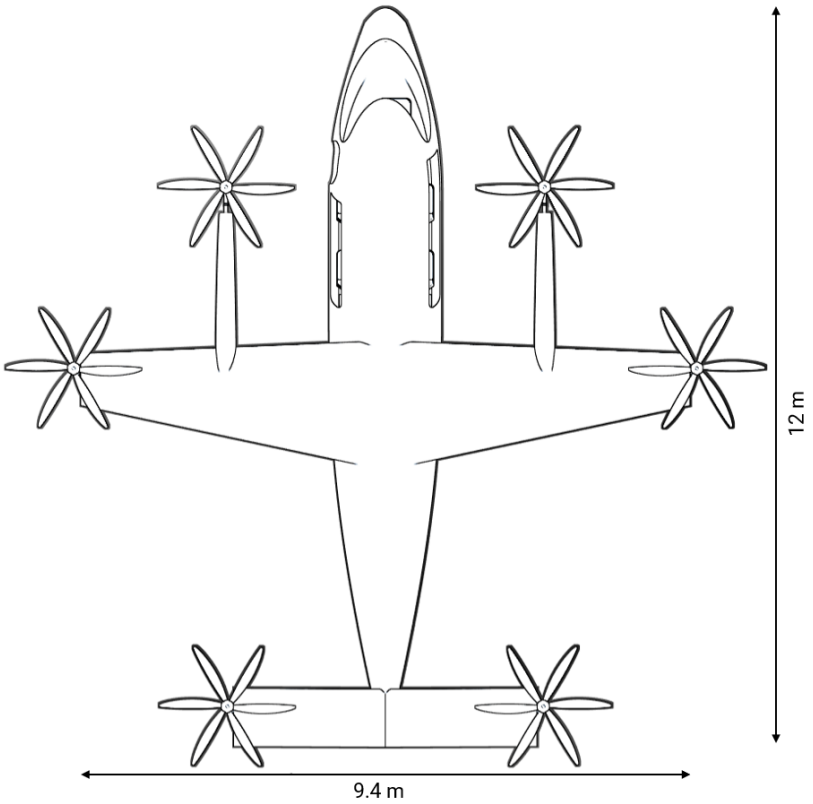

Figure 13.5: *Aetheria top view*

14

Sustainability

In this chapter, the relevance and impact of sustainability on the design shall be discussed. Besides the overarching aspect of the complete life cycle analysis (LCA), the influence of sustainability on the design of each system is critically analysed.

14.1. Life Cycle Analysis

The goal of this life cycle analysis (LCA) is to assess the environmental impact of Aetheria over the course of its entire lifetime, starting from the production and manufacturing phase all the way to the recycling and disposal of the aircraft. An extensive LCA was performed in [4], where the impact of the cradle-to-gate (CTG) and well-to-shaft (WTS) cycles are quantitatively analyzed. The CTG was quantified as Global Warming Potential (GWP) in terms of kilograms of equivalent CO2 emissions per VTOL produced. Next, the WTS determines the impact of the batteries and is quantified using GWP expressed in terms of kilograms of CO2 per kWh. An overview of the GWP breakdown for different types of eVTOLs per segment is illustrated in Figure 14.1.

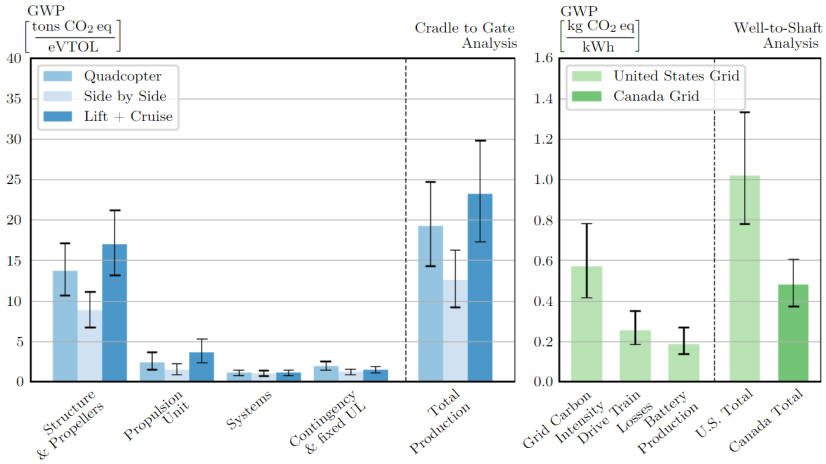

Figure 14.1: *Life Cycle Analysis for Battery Powered eVTOLs between 2200 to 4300kg [73]*

The CTG expressed in GWP should be multiplied by the MTOM of Aetheria to find the final GWP. Considering the GWP for Aetheria is in the range of 15-25 kgCO2/eVTOL, the total GWP shall be approximately 50 tons of equivalent CO2 emissions (for a MTOM of 2500 kg). Then, for the WTS, considering a total energy capacity of 70 kWh for the battery pack in Aetheria, a GWP of approximately 70 kg of equivalent CO2 emissions can be found for the US grid. The values fall within the bounds of the average WTS and GWP.

14.1.1. End-of-Life & Material Choice

After the operational lifetime of Aetheria, the end-of-life phase is the next important phase considering the overall sustainability of Aetheria. Conscientious disposal, recycling and reusing are aspects that should be managed properly to assure a sustainable end-of-life phase. Besides that, as Aetheria will push the boundaries for green transport, sustainability considerations in the material

selection are crucial. The sustainability can be assessed by analysing the life cycle of the product. The phases can be linked to three material properties: material mass index, embodied energy and recyclability. The mass influences the whole life cycle, especially the operational phase. The embodied energy encompasses the material production, product manufacturing and transport phase, while the recyclability only affects the disposal phase (possible end-of-life credit included).

The material index for CFRP is lower compared to aluminum, which is beneficial. However, the embodied energy, which accommodates all energy incorporated in the production of a product, as well as the recyclability is slightly worse for CFRP compared to aluminum. Despite this, the gain in mass reduction currently outweighs the negative sides from a sustainability point of view to attain a feasible design.

14.2. Sustainable Design Choices

In an era of energy revolution, the concept of sustainability has taken a vital role in the design process. From energy consumption and green fuels to material selection and noise minimization, sustainability has become a driving force behind the design. This chapter explains how sustainability has driven design choices over different departments.

14.2.1. Aerodynamics

Environmental sustainability in aviation is significantly influenced by drag. Minimizing the drag reduces energy consumption. Given the lack of fully sustainable hydrogen fuels currently available, this factor directly affects Aetheria's environmental sustainability, as reduced energy consumption leads to reduced carbon emissions. Furthermore, during the airfoil selection, active notice was taken of commonly used airfoils compared to newer, less used ones. The NACA2412 is used in the Cessna 172, a lightweight aircraft with comparable dimensions [1]. This will decrease production costs as existing manufacturing methods can be applied [74]. Besides that, workers will not require extra intensive training, which will also reduce manufacturing costs. The use of the NACA2412 airfoil also affects environmental sustainability, as using existing machinery will limit material loss during development and production.

14.2.2. Flight Performance

Design choices affecting the environmental sustainability regarding the flight performance design aspect are as follows. First of all, the mission profile has been optimized such that the mission energy and maximum power are minimized. This is done by optimizing the cruise and climbing phases and limiting the hover times. While designing the cruise altitude, a maximum and minimum were set regarding social sustainability. The maximum was set at 2400 [m]. This was derived from the cabin altitude, which is set at 2400 [m] and a study by Muhm et al. [75] which indicated that a cabin pressurization equivalent to an altitude of 2400 [m] only lowered the oxygen saturation by 4 percentage points. The study was, however, conducted during a flight duration of 10 [h], while Aetheria's cruise duration is approximately 1 [h]. Furthermore, the passengers did not encounter any significant effects of acute mountain sickness due to the altitude. Then, the minimum cruise altitude was set at 305 [m], as this is the Uber specified requirement [2]. Besides, a higher cruise altitude quickly reduces noise pollution on the ground. Finally, the mission profile has been constructed to minimize the first and last mile segments: Aetheria will take off and land as close as possible to the user's final destination. This will reduce the travel distance compared to a more convenient transportation method such as a train or commercial aircraft. Compared to these transportation methods, Aetheria's mission profile has a sustainability advantage.

[1] Accessed May 15th, https://www.dimensions.com/element/cessna-172-skyhawk-aircraft
[2] Accessed May 15th, https://evtol.news/uber-elevate-ecrm-003/

14.2.3. Power

In the design stage, minimising the use of batteries by maximising the use of hydrogen was a design choice regarding environmental sustainability since lithium-ion batteries contain toxic materials that are harmful if disposed of improperly. In addition, a composite hydrogen tank was preferred over a metal tank in order to reduce the mass of the tank and the overall mass of the aircraft reducing energy consumption. Regarding economic sustainability, the choice of using 350 bars of compressed hydrogen over 700 bars resulted in a cheaper design due to the lower energy necessary to compress and thus the lower cost for it. Furthermore, the system cost of a 350-bar compressed hydrogen storage is lower than that of a 700-bar system [76]. Social aspects considered, a design choice made was to place the batteries in the wings while placing the hydrogen in the tail, keeping both far away from each other, which is a choice regarding the safety of this design. Furthermore, high-technology batteries were also used in order to decrease their mass and thus consequently reduce the mass of the power system and MTOM. This reduces the price of the tickets for Aetheria, making this design available to a larger market.

14.2.4. Propulsion

During the initial design process, the type of propulsion was discussed. Among these, combusting hydrogen in a turbojet-like engine was also considered. This choice was completely disregarded due to its effect on the environment. Instead, using a form of electric propulsion was deemed much better due to its minimal effect on the environment. Moreover, using combustion engines is also extremely expensive. These have high manufacturing costs, and even higher operating costs [3]. Besides this, using a configuration such as tilted ducts would mean the integration of more complex engines and mechanisms, which also costs more to operate. Social sustainability was considered in the form of noise. Reducing the amount of noise present during hovering configuration beyond stated requirements by regulatory bodies is beneficial to society, especially since the vertiports must be in populous locations. The process of the integration of eVTOLs into the current aviation market can be accelerated by attempting to reduce noise, which has a negative impact on society.

14.2.5. Structures

For the structures department, the crashworthiness of the design is important for social sustainability, as an aircraft carrying hydrogen is a novel concept without many applications yet. Therefore, to gain the trust of the general public, serious measures have been taken in making the design crashworthy and ensuring the hydrogen tank shall be within the crashed diameter of the aircraft to prevent catastrophic failure during a small crash. Regarding economic sustainability, making the aircraft as light as possible shall reduce the unit cost per aircraft, together with the material choice. This decision was mainly based on the resulting weight characteristics of the material, as it was determined composite structures would result in a wing box with almost half the weight of aluminium. This weight saving results in lower mission energy which is greatly beneficial to environmental sustainability.

14.2.6. Control & Stability

During the control & stability design, a social sustainability direction was taken as essential, to ensure the safe operation of the eVTOL by making sure that the eVTOL is stable and controllable during both horizontal and vertical flight. It was also ensured that the aircraft exhibits good handling qualities by designing for adequate damping of eigenmotions and response time to inputs. By doing so, the aircraft was made safer to operate which will increase social acceptance. Furthermore, to increase environmental sustainability, the mission energy was minimized by optimizing the wing position, fuselage length, and tail aspect ratio.

15

Operations and Logistics

In this chapter, the operations and logistics of the design will be evaluated. Furthermore, the Reliability, Availability, Maintainability and Safety (RAMS) characteristics of the design will also be discussed.

15.1. In Operation

When the aircraft is in operation, its operational profile consists of multiple steps, as seen in Figure 15.1 obtained from the Midterm report [1].

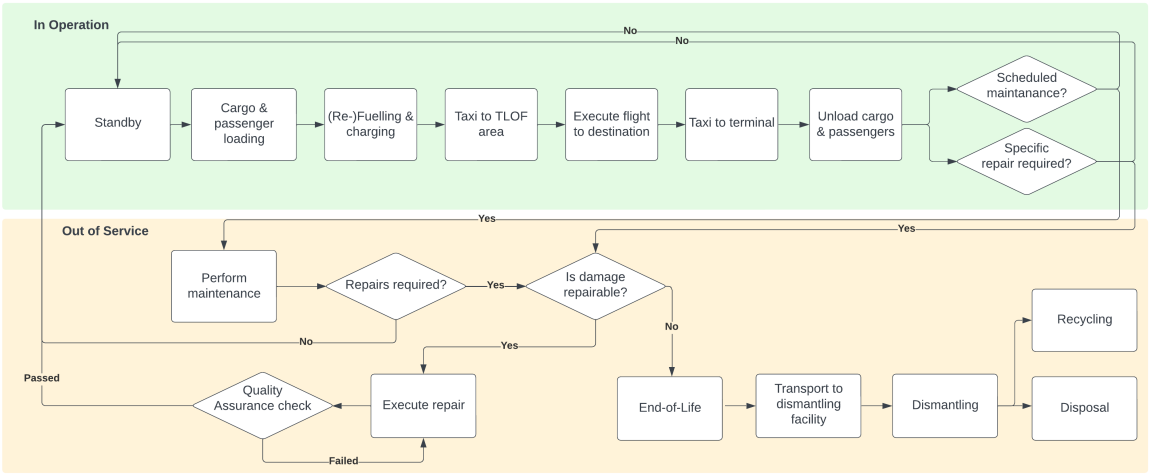

Figure 15.1: *Operations & Logistics Flow Diagram*

1. Standby

While in the standby/parking phase, the eVTOL is waiting for its next mission while not being in use. In this stage, the eVTOL is within a hangar or on a VTOL parking spot. The main stakeholders in this stage are the customer and the vertiport operator [1]. Following standby, the eVTOL can be moved around using a pushback tug.

2. Cargo & passenger loading

During the cargo and passenger loading trade-off, there are several factors to take into account. The main stakeholders are the passengers and the customers, thus, naturally, customers would prefer easily accessible cargo space for shorter turn-around time, while passengers would prefer embarkment to be as smooth as possible. The high-wing configuration provides easy embarkment which is advantageous in this case [1].

3. (Re-)Fuelling & charging Hydrogen

Hydrogen will be refuelled by the vertiport refuelling system that will supply 350-bar compressed hydrogen into the storage tank present in the eVTOL. However, the refuelling system should supply higher pressurised hydrogen, in order to account for compression heating, to achieve a complete fill during rapid refuelling [62]. Compression heating relates to the increase in temperature of the gas

due to increased pressure which results in molecules colliding more increasing the kinetic energy and temperature. This increase in temperature can lead to decreased accuracy in pressure measurements and potential pressure losses. Therefore, to supply 350-bar compressed hydrogen, an overpressure of approximately 440-bars is required to account for this effect [62].

The Department of Energy, DOE, states that H2A projected that approximately 2.2 [kWh/kg H2] is necessary to compress hydrogen from 20 bars to 440 bars at 300K [62]. The required mass of H2 for the mission is 9 [kg], thus, this results in a necessary energy of 19.8 [kWh] for pressurising the hydrogen for refuelling. This results in an additional 0.59 [kg] of hydrogen mass-equivalent to supply this energy.

A possible applicable refuelling station is the Hydrogen Refueling Solutions (HRS) which can supply 6 [kg] of hydrogen in a span of 5 minutes [1]. This would scale to loading the mission required 9 [kg] of hydrogen would take approximately 7.5 minutes of refuelling time. Furthermore, since more than 5 [kg] of hydrogen will be refuelled for a time longer than 5 minutes, pre-cooling of hydrogen will be necessary in order to avoid overheating the tank during the process [62]. This process will further require an additional 0.15 [kWh/kg H2], resulting in a necessary energy of 1.35 [kWh] and a mass equivalent of H2 of 0.04 [kg]. Therefore, the total energy necessary for pressurising the hydrogen and pre-cooling during fueling will add up to 21.15 [kWh] or 0.63 [kg] of equivalent hydrogen.

The refuelling process can be done by transporting the eVTOL to the refuelling station present at the vertiport using a pushback tug similar to the ones used in aircraft. Once at the refuelling station, the process is similar to refuelling a car. The corresponding fuel gun can be chosen from the station (either 350 or 700-bar compressed hydrogen[2]), and placed in the designated location of the eVTOL body (in the tail section where the tanks are placed). In future applications, movable fuelling tanks can also be used so that the fuelling tank goes to the location of the eVTOL rather than the movement of the eVTOL towards the fuelling station. Once refuelling is finished the eVTOL can be prepared for the next mission.

Batteries
To recharge the batteries, an EASA-approved, SKYCHARGE charging station can be used [3]. This is a mobile charging station connected to a power outlet on the ground and can be moved to the location of the eVTOL on the vertiport and charged using a GB/T connector. This connector is placed underneath the wings to access the location of the batteries, located in them. This station also consists of a touch screen displaying the battery health, temperature, voltage and charging status. Upon completion of charging, the mobile station can be unplugged from the eVTOL.

4. Take-off and Landing
For take-off, the eVTOL is initially located at a park station on the vertiport. Here, the passengers and the cargo are loaded. Once this has been completed, the pushback tug can be used to transport the eVTOL to the refuelling station located on the vertiport for refuelling as described previously. The eVTOL is also subject to recharging of batteries during this refuelling process as discussed. Following the completion of these, the eVTOL taxis to the take-off and landing area. Once permission from air-traffic control (ATC) is provided, the eVTOL can start lift-off to execute the mission.

For landing, first, the eVTOL transitions from horizontal flight to vertical flight and then prepares for landing by slowly hovering towards the ground. Upon touchdown, the eVTOL taxis to the park location where the passengers and the cargo are unloaded. Following this, a routine inspection is done to ensure the eVTOL is in a good condition to execute the next mission and repeat the cycle. If

[1] Accessed June 5th 2023, https://www.hydrogen-refueling-solutions.fr/hydrogen-stations/?lang=en
[2] Accessed June 5th 2023, https://www.hydrogen-refueling-solutions.fr/hydrogen-stations/?lang=en
[3] Accessed June 14th 2023, https://www.eaton.com/ch/en-gb/catalog/emobility/skycharge-mobile.html

the inspection is unsuccessful, the eVTOL is grounded and maintenance and repairs are performed on it. After this, the eVTOL can be returned back to operation.

15.2. Out of Service

Following each flight performed by Aetheria, it is assessed whether or not there is scheduled maintenance or whether a specific repair is required. If maintenance is scheduled, Aetheria will be out of service until the required checks and repairs have been done.

1. Perform maintenance

For scheduled maintenance, the complexity and duration may vary significantly depending on the operation that has to be performed. During the maintenance, a record of all the performed activities should be recorded for potential future reference. The aircraft structure, such as the wings, fuselage, tail, propellers and etc. should be inspected to check for damage in terms of corrosion or structural deformation. Functioning components such as batteries, propellers, avionics and sensors should be tested and run to make sure that they all function as intended and comply with the standard requirements set by EASA [24]. In case these components do not function as intended, possible calibration or updates can be performed. If this does not fix the problem the eVTOL is scheduled for repair where they can be replaced or repaired.

2. Repairs

Upon performed maintenance, a decision has to be made whether the eVTOL requires a repair or not. If not, the eVTOL can be returned to service and prepared for the following flight, whereas if repair is necessary, the eVTOL is grounded. The damage is assessed to check if it is repairable without leading to significant costs [1]. If the repair is within an acceptable cost range, the damage will be fixed which will be followed up by a quality assurance before being released back into operation. Should the damage be beyond repair, the aircraft proceeds to the end-of-life phase [1].

3. End-of-life

When arriving at the end-of-life phase, the eVTOL will be transported to a dismantling facility where the aircraft will be dismantled [1]. For sustainability purposes, components that can be reused will be recycled or repurposed. Any components not suitable for recycling should be disposed of in a sustainable manner. [1].

15.3. Emergency Procedures

In case of an emergency, there are several steps that have to be applied in order to ensure the safety of the pilot and the passengers. Most of these procedures are similar to the ones executed in an emergency situation of an aircraft. The emergency procedures can be split up into two categories; for the pilot, and for the passengers.

In case of an emergency, the first thing the pilot should perform is to go over the provided emergency checklist. Then, communication with air traffic control (ATC) should be established to request an emergency landing. The pilot should strive to land safely and promptly evacuate the passengers. Additionally, the pilot must secure the remaining systems to prevent any further damage or explosion before leaving the eVTOL. In the event of a fire, the pilot should be prepared to operate a fire extinguisher to swiftly extinguish the fire. Furthermore, before boarding, the pilot should conduct safety demonstrations for the passengers, similar to those conducted on aircraft, to ensure passengers are aware of the appropriate behaviour in various situations.

The passengers on the other hand should clearly follow the safety demonstrations presented prior to flight. They should wear seatbelts during critical stages of the mission as well as in case of an emergency. Each passenger will be provided with a life vest located under the seat, which should be used in case of an emergency landing in water. Once an emergency landing has been performed

they should move towards the exit as fast as possible.

15.4. RAMS

The Reliability, Availability, Maintainability and Safety characteristics of the three designs are to be maximized to ensure Aetheria will fulfill the mission for which it is designed [4]. Hence, these criteria will be evaluated.

Reliability The reliability is the probability that the system will perform its task[5]. The chances of failure are the highest in the beginning and end-of-life[6], which can be related to the 'bath-tub' curve. Production errors will always cause some failures. Since hydrogen fuel cells are still in an early development stage, their chance of failure is relatively high. Also, in making a design choice on the type of batteries to be used, the Technology Readiness Level (TRL) should be held in high regard and taken as a trade-off criterion for the battery trade-off.

Availability The availability of a product is determined by its likeliness to perform its tasks in the product lifetime[7]. The availability of Aetheria largely depends on the time spent between missions (the turnover time) as well as the time spent in repairs when the aircraft is inoperable. Minimizing the turnover time increases availability. The use of hydrogen is beneficial in this aspect as filling a hydrogen tank with compressed hydrogen can be done in about 7.5 minutes, as explained in Section 15.1. On the other hand, the most powerful electric vehicle chargers can currently deliver up to 400 [kW] of power[8], resulting in a charging time of roughly 10-15 minutes for the 70 [kWh] battery pack of Aetheria. Both these charging times do not seem to constrain with respect to the turnover time as embarking and disembarking will most likely take at least about 10 minutes as well.

Maintainability As discussed in Section 15.2, the difference in maintainability for conventional and tilt-rotor configurations is quite substantial due to the significant increase in complexity of the tilting mechanisms. For this reason, the aircraft should provide easy access for mechanics to inspect and maintain the aircraft and all its complex components. Also, checks should be performed after each flight on the proper functioning of the mechanisms as mechanical failure may result in catastrophic failure of the aircraft during transition.

Safety The safety of the aircraft is crucial, especially when incorporating hydrogen as a power system, given the significant pressure it operates under. The crashworthiness of the aircraft plays a vital role in preventing catastrophic events in the event of a crash. To avoid the most deadly scenario, a post-fire crash, the hydrogen tanks are positioned outside the crumple zone, as explained in more detail in Section 9.1. Furthermore, loads on the passengers in the event of a crash are reduced by implementing a crash structure in the sub-floor structure of the fuselage.

[4] Accessed May 8th 2023, https://www.byhon.it/rams-engineering-analysis/#:~:text=The%20RAMS%20(Reliability%2C%20Availabilitby%2C,availability%20and%20well%2Ddefined%20safety.
[5] Accessed May 8th 2023, https://asq.org/quality-resources/reliability
[6] Accessed May 8th 2023, https://www.code7700.com/aircraft_reliability.htm
[7] Accessed May 22nd 2023, https://www.byhon.it/rams-engineering-analysis/
[8] Accessed June 19th 2023, https://blog.evbox.com/level-3-charging

16

Financial Plan

16.1. Cost-Breakdown Structure

To provide a cost breakdown of Aetheria, many empirical methods can be used to calculate the cost of all the various parameters, such as the production, operational, certification, unit, and research costs. The method used for Aetheria cost calculations will be the Eastlake method, which is a modified version of the DAPCA-IV method, based on a paper to determine the cost of a GA aircraft [3]. The equations based on the Eastlake method [3], will not be displayed in this report as they were previously analyzed in detail in the Midterm report [1]. Instead, a summary of the results will be provided which can be seen in Figure 16.1. Only additional costs which are not included in the Eastlake method, but necessary for the calculation of the costs for Aetheria will be analyzed, such as the battery, fuel cell and hydrogen subsystem costs, therefore increasing the reliability of our financial analysis.

The following equations were determined in order to calculate the costs for the components of our design not covered by [3]. The cost of the fuel cell and the hydrogen storage system that will be used can be calculated using Equation 16.1 and Equation 16.2 [1].

$$C_{FCELL} = C_{kW} \cdot P_{mission} \tag{16.1}$$

$$C_{H2tank} = C_{H2system} \cdot E_{mission} \tag{16.2}$$

"*Here, C_{kW} refers to the cost of fuel cells [$/kW] and $P_{mission}$ refers to the total mission power needed for which the fuel cells will be used [kW]. $C_{H2system}$ is the storage cost system [$/kWh] according to [77]. $E_{mission}$ refers to the total energy mission [kWh]. In addition, batteries and their replacement cost [19] will also be necessary and can be calculated with the equations below*" [1].

$$C_{BAT} = M_{BAT} \cdot C_{BATKG} \tag{16.3}$$

$$C_{BATREP} = \frac{M_{BAT} C_{BATKG} Q_{\text{FLGT}}}{F_{\text{cycle}}\, N_{cycles}} \tag{16.4}$$

Where M_{BAT} refers to the mass of the battery used in the design [kg] and C_{BATKG} refers to the cost of the battery [$/kg] [1]. Storage tanks have a very long lifetime (more than 15 years), thus their replacement will not be necessary during the operational lifetime of the eVTOL. However, fuel cells have a lifetime of 11.1 years, thus, they will have to be replaced once during the operational lifetime. This can be done using Equation 16.5 [1].

$$C_{FC_{REP}} = C_{FCELL} + \frac{C_{FCELL} \cdot Q_{FLGT}}{N_{life}} \tag{16.5}$$

Where C_{FCELL} is the previously calculated cost of the fuel cell, Q_{FLGT} is the number of flight hours per year and N_{life} is the lifetime of the fuel cell in hours. Finally, to calculate the cost of the energy necessary for the batteries, Equation 16.6 can be used :

$$C_{ELEC} = \frac{M_{BAT} C_{kWh} E_{kg} Q_{\text{FLGT}}}{F_{\text{cycle}}} \tag{16.6}$$

"The parameters used in this equation are as follows: C_{kWh} refers to the energy cost [$/kWh], E_{kg} refers to the specific energy density of battery [kWh/kg], Q_{FLGT} is the number of flight hours per year (arbitrarily assumed to be 1800), N_{cycles} refers to the number of battery discharge cycles and F_{cycle} is the number of flight hours per cycle [19]"[1]. These extra equations, combined with the Eastlake method described in [1], can be used to calculate the cost of individual subsystems. Once, these have been determined, Equation 16.7 and Equation 16.8, can be used to calculate the Unit variable and Fixed costs to compute the Break-even point using Equation 16.9. An overview can be seen in Figure 16.1.

$$\text{Unit Variable Cost} = \frac{C_{MFG} + C_{QC} + C_{MAT}}{N} + C_{AV} + C_{CSTPROP} + C_{PP} + C_{LG} + C_{INS} + C_{FCELL} + C_{TANK} + C_{BAT} \tag{16.7}$$

$$\text{Total Fixed Cost} = C_{CERT} = C_{ENG} + C_{DEV} + C_{FT} + C_{TOOL} \tag{16.8}$$

$$N_{BE} = \frac{\text{Total Fixed Cost}}{\text{UnitPrice} - \text{Unit Variable Cost}} \tag{16.9}$$

Figure 16.1: *Aetheria Cost Breakdown*

(a) *Aetheria Cost*

Costs	Aetheria
Flight Test Operations	1,129,746
Development	4,623,271
Tooling	43,029,909
Engineering	64,447,079
Fixed (certification)	113,230,005
Landing Gear Deduction	0
Storage Tank	6,080
Fuel Cell	9,375
Battery	15,683
Avionics	19,500
Liability Insurance	38,000
Engine (power plant)	118,730
Constant Speed Propeller	238,019
Quality Control	57,935,790
Material	65,088,489
Manufacturing	356,527,939
Unit Variable Cost	924,939
Unit Price	2,000,000
Break Even Units	106

(b) *Aetheria Operational Cost Breakdown*

Costs	Aetheria
Annual Inspection	500
Fuel Cell Replacement	920
Storage	3,000
Maintenance	28,080
Annual Insurance	38,000
Energy	41,402
Battery Replacement	42,343
Fuel	64,800
Engine Overhaul Fund	108,000
Yearly Operational Cost	327,045
Yearly flight hours	1,800
Cost per flight hour	181.7
Cost per flight kilometre	0.6

To calculate the yearly operational cost seen in Figure 16.1b, Equation 16.10 can be used. Furthermore, to calculate the costs per flight hour and kilometre, Equation 16.11 and Equation 16.12 can be used respectively to generate the results seen in Figure 16.1b.

$$C_{YEAR} = C_{AP} + C_{FUEL} + C_{INS} + C_{INSP} + C_{OVER} + C_{STOR} + C_{ELEC} + C_{BATREP} + \frac{C_{FC_{REP}} \cdot}{N_{life}} \tag{16.10}$$

$$C_{HR} = \frac{C_{YEAR}}{Q_{FLGT}} \tag{16.11}$$

$$C_{KM} = \frac{C_{HR}}{V_{cruise}} \tag{16.12}$$

16.2. Business Model

Aetheria will begin operation in Europe with the main route being from Paris to London as discussed in the Market Analysis in Section 4.5. In the future, there is a possibility for expansion in North America, to connect rural cities without the present infrastructure in between, as well as on the East Coast to provide fast travel between major metropolitan cities. Aetheria aims to achieve this by first starting out with 5 eVTOLs in Europe to perform the route analysed in Section 4.5, followed by a gradual increase to 1000 units within 6 years, from where an expansion to America can be made.

For this design, the cost per flight hour [$/hr] can be calculated to be 181.7 $ from Figure 16.1b. From this, the cost per flight kilometre was calculated to be 0.6 $. With an increase in technological development within the years leading up to 2030, the cost for hydrogen, fuel cells, high technology batteries and etc. can decrease, eventually leading to a decrease in the yearly operational cost and consequently a decrease in the costs per flight hour and kilometre. However, until this takes action, the projected costs are based on current estimates as mentioned.

16.3. Return on Investment

Based on an update of the values of the Aetheria, the return on investment performed in the midterm report was performed in the exact same way [1]. Based on this, Table 16.1 was generated. Although the profit and loss statement was made for every year from 2030 to 2040, only three "milestone" years are displayed, for conciseness.

Table 16.1: *Return on Investment Table*

	2030	**2035**	**2040**
Units Produced	5	500	1000
Unit Variable Cost	925,000	832,000	749,000
Unit Price	2,000,000	2,000,000	2,000,000
Total Operational Cost	1,635,000	163,522,000	327,044,000
Revenue	10,000,000	1,000,000,000	2,000,000,000
Revenue After Tax	7,500,000	750,000,000	1,500,000,000
Total Unit Variable Cost	4,625,000	416,223,000	749,201,000
Total Cost	3,635,000	165,522,000	329,044,000
Total Profit	1,240,000	170,255,000	423,755,000

This table allows for the return on investment to be found, which is 14%. This is lower than the value found in the midterm, due to the fact that the operational costs are higher, which is a consequence of the more detailed design stage.

17

Manufacturing, Assembly and Integration Plan

The manufacturing, assembly, and integration plan to produce Aetheria will be discussed in this chapter. Building upon the Midterm report [1], the finalized design permits a more detailed plan. Similar to conventional aircraft, Aetheria will undergo line production. The Manufacturing, Assembly, and Integration plan flow diagram can be found in Figure 17.1. It shows a timeline of the production and testing of Aetheria [1].

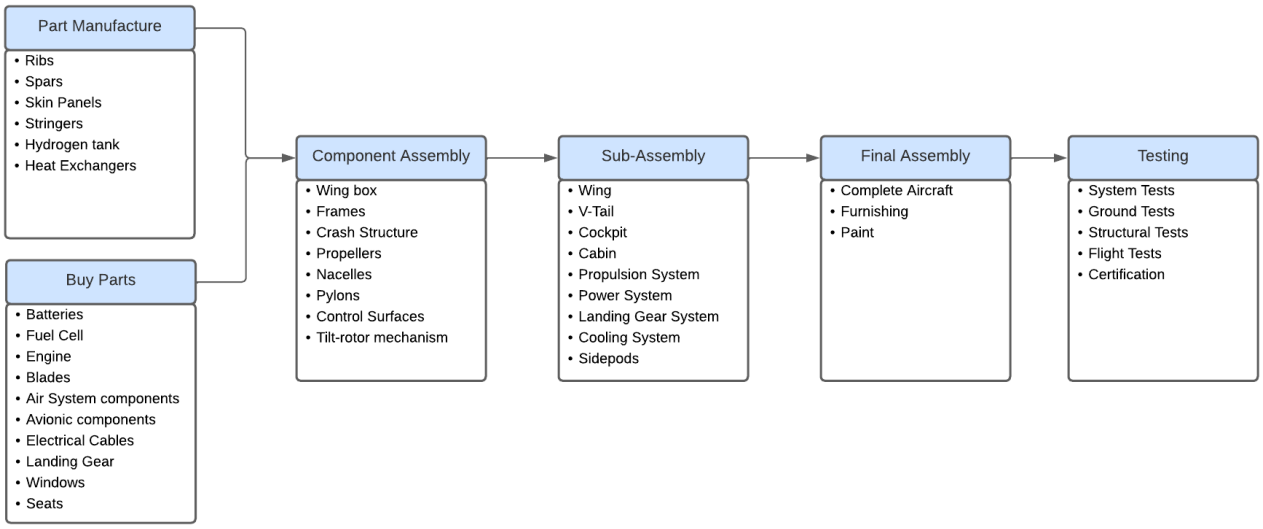

Figure 17.1: *Manufacturing, Assembly and Integration Flow Diagram*

The production process commences by manufacturing parts that are relatively straightforward and specific to the design requirements, whereas complicated, standardised parts and components that require specialised knowledge and labour such as batteries, fuel cells and etc. are bought [1]. To mitigate potential disruptions caused by unforeseen events such as the Suez Canal obstruction or conflicts a just-in-case manufacturing approach will be applied. This entitles an approach of maintaining an inventory of the manufactured and bought parts. This is preferred over Just-in-time manufacturing. The manufacturing process will involve line production like most aircraft manufacturers do. Following part buying and manufacturing, the component assembly line will take place where the parts will be assembled into components. Later, these components will be combined to create larger assemblies in the sub-assembly section. Finally, all these sub-assemblies flow into the final assembly lines where everything is combined into one final product [1]. This line can be seen as the backbone of the production lines and culminates with a complete aircraft [1]. Thereafter, the eVTOL is painted and furnished to be sent for testing where various tests will be performed ranging from (sub) system testing to ground tests to flight tests which make sure the aircraft meets all the performance and safety requirements. Upon successfully passing all required tests, the aircraft can proceed to the certification process, which entails meeting regulatory standards and obtaining the necessary approvals. Subsequently, mass production can commence for commercial use.

18

Requirement compliance

This chapter contains Aetheria's requirement compliance. Only some crucial requirements will be mentioned in this report. A description of the other requirements can be found in the baseline report [4].

Aetheria has to comply with EASA's special document for small-category VTOL aircraft. This document is an extension of the CS-27 small rotorcraft document [28] which limits the maximum take-off mass to 3175kg (*CON-MASS-01*). Failing to meet this requirement would subject Aetheria to more stringent regulations which is undesirable.

Furthermore, Aetheria is intended as a fast point-to-point transportation method that should be able to land on existing helipads. Therefore, the maximum length and span of Aetheria are limited to 14 meters (*STK-VERT-01*), the cruise speed is at least 200 km/h (*FUNC-AERO-02*) and the range is at least 400km (*STK-CUST-01*). Lastly, Aetheria's should be able to carry a payload of 510 kg (*STK-CUST-02*).

Aetheria complies with the above-mentioned requirements for mass, aircraft dimensions, range and payload capacity. As mentioned in Chapter 13, the maximum take-off mass is estimated at 2522 kg and therefore the CS-27 regulations guidelines apply to Aetheria's design. Furthermore, the span and fuselage length does not exceed 14 meters and the cruise speed is 300 km/h. This allows Aetheria to land on current helipads while also allowing for fast travel times. Lastly, the payload capacity for a 400 km mission is 510 kg.

Aetheria complies with most requirements formulated during the baseline report as can be seen in Table 18.1. However, it does not meet the requirement regarding lateral vibrations (STK-PAS-07, FUNC-STR-01) as explained in Section 9.7. These requirements are not met because the design of the wing did not take into account the modal analysis yet. For the next design iterations, the modal analysis will be implemented. This has not been done due to the limited resources available for Aetheria's design team Therefore, it is expected that these requirements will be met in later iterations. Furthermore, multiple requirements can not be verified at this design stage and hence are set to TBD.

Table 18.1: *Aetheria compliance matrix featuring the requirement ID, Compliance Status, and Section Reference. Green signifies requirement compliance, yellow means an unverified requirement, while red indicates unmet requirements*

ID	Section	ID	Section	ID	Section
STK-REG-01	Section 6.3	FUNC-STR-05	Section 9.6	FUNC-GO-04	TBD
STK-REG-02	TBD	FUNC-AERO-01	Section 6.3	MIS-REG-CRSH-01	Section 9.1
STK-REG-03	TBD	FUNC-AERO-02	Section 7.1	MIS-REG-CRSH-02	Section 8.1
STK-REG-04	TBD	FUNC-AERO-03	Section 6.3	MIS-REG-ENV-01	TBD
STK-ENV-01	Section 10.8	FUNC-AERO-04	Section 6.3	MIS-REG-ENV-02	Section 9.2
STK-CUST-01	Section 7.1	FUNC-AERO-05	Section 8.2	MIS-REG-ENV-03	Section 8.3
STK-CUST-02	Section 4.5	FUNC-AERO-06	Section 8.3	MIS-REG-ENV-04	Section 6.3
STK-CUST-03	Section 4.5	FUNC-AERO-07	Section 8.2	MIS-REG-ENV-05	Section 8.3
STK-CUST-04	Section 4.5	FUNC-AERO-08	Section 8.3	MIS-REG-ENV-06	Section 9.7
STK-CUST-05	Section 16.1	FUNC-AERO-09	Section 8.3	MIS-REG-ENV-07	TBD
STK-CUST-06	Section 10.4	FUNC-AERO-10	Section 8.3	MIS-REG-ENV-08	Section 7.1
STK-CUST-07	Section 16.1	FUNC-PROP-01	Section 11.5	MIS-REG-ENV-09	Section 8.2
STK-CUST-08	Section 7.1	FUNC-PROP-02	Section 8.2	MIS-REG-STR-01	Section 9.6
STK-CUST-09	Section 7.1	FUNC-PWR-01	TBD	MIS-REG-STR-02	Section 8.2
STK-PAS-01	Section 9.6	FUNC-PWR-02:	Section 10.5	MIS-REG-STR-03	Section 9.2
STK-PAS-02	Section 9.6	FUNC-PWR-03	Section 10.4	MIS-REG-STR-04	Section 9.2
STK-PAS-03	Section 10.2	FUNC-PWR-04	Section 10.3	MIS-REG-STR-05	TBD
STK-PAS-04	TBD	FUNC-PWR-04-01	Section 10.3	MIS-REG-STR-06	Section 9.3
STK-PAS-05	Section 7.2	FUNC-PWR-04-02	Section 10.3	MIS-REG-STR-07	TBD
STK-PAS-06	Section 7.2	FUNC-PWR-05	Section 10.2	MIS-REG-STR-08	Section 8.5
STK-PAS-07	Section 9.7	FUNC-PWR-06	Section 10.2	CON-MASS-01	Section 13.3
STK-VERT-01	Chapter 13	FUNC-PWR-07	Section 10.8	CON-MASS-02	Section 8.3
STK-INV-01	Section 16.3	FUNC-PWR-07-01	Section 10.4	CON-SUS-01	TBD
STK-INV-02	Section 16.1	FUNC-PWR-08	Section 10.8	CON-SUS-02	Section 14.1
FUNC-STR-01	Section 9.7	FUNC-GO-01	Section 15.1	CON-SUS-03	Section 14.1
FUNC-STR-02	Section 9.3	FUNC-GO-02	TBD	STK-PIL-01	TBD
FUNC-STR-03	TBD	FUNC-GO-03	TBD	STK-PIL-02	TBD

19

Conclusions & Recommendations

In this chapter, the main parameters and findings of the DSE are outlined. The conclusion is explained in Section 19.1 and the recommendations are highlighted in Section 19.2.

19.1. Conclusion

In an era of innovation, Aetheria leads the way, since the usage of hydrogen as a fuel is sustainable as well as more energy efficient. By breaching a gap in the eVTOL branch, it has the possibility to gain an important market share by fulfilling the following mission statement:

Design a safe and sustainable long-range hydrogen eVTOL that can transport four passengers

After a trade-off between the three design configurations, a single high wing combined with a V-tail configuration was chosen. An extensive framework for a multidisciplinary analysis and design optimization (MADO) was set up, leading to the design depicted in Figure 19.1. The design parameters were the aspect ratio and the fuselage length, which were set to minimize mission energy. The main parameters obtained from the current design stage which sum up the characteristics of Aetheria are highlighted in Table 19.1 and Table 19.2.

Figure 19.1: *Isometric view of Aetheria in hover mode*

Table 19.1: *eVTOL Parameters Table 1*

Parameter	Value
MTOM [kg]	2552
OEM [kg]	2042
Range [km]	400
Cruise speed [m/s]	300
Stall speed [m/s]	40
Max. power [kW]	875
Fuel Capacity [kWh]	380.4

Table 19.2: *eVTOL Parameters Table 2*

Parameter	Value
Number of Passengers	4
Wing span [m]	9.4
Wing area [m^2]	13.0
Fuselage length [m]	11.2
Lift to Drag ratio [-]	18.3
Price per eVTOL [million $]	2.0
Unit Variable Cost [thousands] [$]	925

From the final parameters, the conclusion can be drawn that the Aetheria can compete with current eVTOLs. Furthermore, the Aetheria meets the requirements as stated in Chapter 18 and is thus ready for testing.

19.2. Recommendations

Due to the time constraint of 10 weeks, the design team was not able to fully examine all the design options in full depth. Therefore, some aspects of the detailed design were left out. In this section, some recommendations for future designs will be mentioned in order to improve the overall design.

Aerodynamics & Flight Performance

When it comes down to aerodynamics and flight performance, more research into the drag and swirl effects of the propellers could have been performed. Furthermore, a CFD analysis would increase verification of the aerodynamic parameters but this was left out due to time constraints. It would however greatly increase the verification of the aerodynamic analysis methods used. Furthermore, the airfoil selection can be revisited. Due to the high loads of the propellers on the wing, a thicker airfoil is more appropriate for eVTOLs since a thicker wing box will fix inside. The airfoil that is used (NACA2412) is a standard airfoil with a thickness over chord ratio of 0.12. Finally, the drag induced by the downwash on the V-tail has not been investigated and should be looked into before creating a prototype. This could be an explanation why the L/D ratio is relatively high (18.3) compared to similar sized aircraft, which is around 10.

Control & Stability

Regarding control and stability, gain scheduling based on eVTOL speed and air density should be implemented in order to make sure that the controller operation is optimum within the flight envelope of the aircraft. Furthermore, the sensors can be modelled with noise and the control system can be investigated under such circumstances due to the current design being modelled as a transfer function of 1, excluding noise, which in reality is not the case. In addition, the failure tolerance of the control system can be investigated to analyse the effect of a control surface being stuck on the stability and controllability of the aircraft. Finally, a control augmentation system (i.e. autopilot) can be designed for easier, as well as safer operations of the eVTOL during flight.

Power & Propulsion

For recommendations concerning the power system, the implications of solid-state batteries can be investigated. The use of solid-state batteries can result in a lighter and safer design which was not considered during this design due to the low technological readiness level (TRL) of current solid-state batteries. Furthermore, with a longer available design period, the radiator sizing can be implemented in the optimisation loop in order to generate a more optimised power system.

Propulsion recommendations include a more accurate estimation of noise since the current method used relies on a generic empirical method which might not be entirely accurate with eVTOLs which

have not been extensively studied. Furthermore, propeller-propeller interaction was not considered due to time constraints. Prototype testing or CFD can be employed for future applications. Due to controllability requirements that the thrust produced by a single engine should be 2.25 times the nominal thrust, the propellers were not optimised enough for cruise. If another solution were to be found, the T-factor used could be lowered, which would result in a propeller configuration that is more optimal in cruise than the one currently designed.

Structures
To finalize and optimize the structural design further, several recommendations should be considered. The initial step involves enhancing the wing's stiffness to increase the natural frequency of vertical wing oscillations. Moreover, it is crucial to eliminate vibrational coupling between the v-tail and the wing by spacing their respective natural frequencies. Once the structural design is finalized, an aeroelasticity analysis can be conducted to ensure the absence of flutter, divergence, or control reversal. Additionally, it is essential to subject the wingbox material and structure to extensive fatigue testing to validate their strength and fatigue resistance. Similarly, the crash structure must be verified to ensure compliance with regulatory limit loads. The fuselage structure needs to be designed to confirm the assumption of a stiff fuselage and to obtain a more accurate weight estimation. Furthermore, it is necessary to perform further verification of the software implementation. While unit testing has been performed, more comprehensive tests are required to enhance the trustworthiness of the values obtained. In addition, due to time constraints, the external design considerations for emergencies, such as designing for flotation, have not been addressed, but they should be taken into account in future iterations. Lastly, an in-depth design of the firewall is required to ensure its effectiveness and performance.

Next Design iterations
In order to meet all requirements and produce an feasible design an iteration should be conducted. This is not done in the current report due to the limited time resources available for the current design team. The three major recommendations are related to the power system, vertical flight stability and the modal analysis.

For the power system, the cooling system mass estimation should be incorporated into the power system optimisation. During the current design, the mass of the cooling system was evaluated after the mass optimisation for the power system. This is not optimal as the cooling system mass account for 10% of the power system mass and hence mass reduction can be achieved.

Furthermore, the wing placement should also take into account the vertical stability modes as during the current design iteration only the longitudinal stability was accounted for. After this, vertical stability was checked and the engine pylon is sized to make the make Aetheria stable during vertical flight. However, this is not favourable for the wing modal analysis as this resulted in long engine pylons.

Lastly, the modal analysis should be integrated into the global optimization loop. This has to be done as it was found that in the current design, the coupling between the main wing and v-tail is the limiting factor. Therefore, by introducing this in the optimisation, it will be more likely that the design does not have coupling between the wing and v-tail.

Bibliography

[1] van Battum, B., Sarıgöl, B., Karaca, C., Middendorp, L., Albers, W., Keijzer, D. M., de Rijke, S., Hadzhiyski, E., Soria, C. S., and Arends, J., "Midterm Report - Aetheria, hydrogen-based long-range eVTOL designed for crashworthiness," , may 2023. doi:10.5281/zenodo.8056301.

[2] Charles N. Adkins, R. H. L., "Design of Optimum Propellers," *JOURNAL OF PROPULSION AND POWER*, Vol. 10, No. 1, 1994. doi:10.2514/3.23779.

[3] Gudmundsson, S., "General Aviation Aircraft Design - Chapter 2," *Science Direct*, 2014.

[4] van Battum, B. A., Sarıgöl, B., Karaca, C., Middendorp, L., Albers, W., Keijzer, D. M., de Rijke, S., Hadzhiyski, E., Soria, C. S., and Arends, J., "Baseline Report - Aetheria, hydrogen-based long-range eVTOL designed for crashworthiness," , May 2023. doi:10.5281/zenodo.8055976.

[5] Hae Choi, J., and Park, Y., "Exploring economic feasibility for airport shuttle service of urban air mobility (UAM)," *Transportation Research Part A: Policy and Practice*, Vol. 162, 2022, pp. 267–281. doi:10.1016/j.tra.2022.06.004, URL https://www.sciencedirect.com/science/article/pii/S0965856422001574.

[6] Huang, Z., Wu, X., Garcia, A. J., Fik, T. J., and Tatem, A. J., "An Open-Access Modeled Passenger Flow Matrix for the Global Air Network in 2010," *PLoS ONE*, Vol. 8, No. 5, 2013. doi:10.1371/journal.pone.0064317, URL https://www.scopus.com/inward/record.uri?eid=2-s2.0-84877745094&doi=10.1371%2fjournal.pone.0064317&partnerID=40&md5=0e0a578d079f5c63a5619744b079d918, all Open Access, Gold Open Access, Green Open Access.

[7] Gu, H., and Wan, Y., "Can entry of high-speed rail increase air traffic? Price competition, travel time difference and catchment expansion," *Transport Policy*, Vol. 97, 2020, pp. 55–72. doi:10.1016/j.tranpol.2020.07.011, URL https://www.sciencedirect.com/science/article/pii/S0967070X20304029.

[8] Brons, M., Pels, E., Nijkamp, P., and Rietveld, P., "Price elasticities of demand for passenger air travel: a meta-analysis," *Journal of Air Transport Management*, Vol. 8, No. 3, 2002, pp. 165–175. doi:10.1016/S0969-6997(01)00050-3, URL https://www.sciencedirect.com/science/article/pii/S0969699701000503, developments in Air Transport Economics.

[9] Downward, A., Chowdhury, S., and Jayalath, C., "An investigation of route-choice in integrated public transport networks by risk-averse users," *Public Transport*, Vol. 11, No. 1, 2019, pp. 89–110. URL https://www.proquest.com/scholarly-journals/investigation-route-choice-integrated-public/docview/2184227875/se-2.

[10] Blainey, S., Hickford, A., and Preston, J., "Barriers to Passenger Rail Use: A Review of the Evidence," *Transport Reviews*, Vol. 32, No. 6, 2012, pp. 675–696. doi:10.1080/01441647.2012.743489, URL 10.1080/01441647.2012.743489.

[11] Kinjo, H., "Development Trends and Prospects for eVTOL: A New Mode of Air Mobility," Mitsui & Co, June 2018. URL https://www.mitsui.com/mgssi/en/report/detail/__icsFiles/afieldfile/2019/07/18/1906m_kinjo_e.pdf.

[12] Andrade, A. I. d., Vieira, D., Marques, J. L. R., and Babadopulos, M. A. F. d. A., "Operational feasibility to introduce the EVTOL in São Paulo city using the existing infrastructure of helipads and heliports," 2022.

[13] Kai, W., Jacquillat, A., and Vaze, V., "Vertiport Planning for Urban Aerial Mobility: An Adaptive Discretization Approach," *Manufacturing & Service Operations Management*, Vol. 24, No. 6, 2022, pp. 3215–3235. doi:10.1287/msom.2022.1148.

[14] Feldhoff, E., "Simulation-Based Analysis of the Passenger Processing System at Vertiports," *AIAA AVIATION 2022 Forum*, 2022.

[15] López, N., Santamaría, A., and Castro, S., "Preliminary aerodynamic design and load calculation of a long-range eVTOL aircraft," 2022. doi:10.2514/6.2022-1331.

[16] Raymer, D., "Aircraft Design: A Conceptual Approach," , 1999.

[17] R. Vos, J. M., "AE1222-I Lecture 6: Wing and Propulsion System Design," AE1222-I Aerospace Engineering TU Delft, May 2023. Accessed 11-05-2023.

[18] Dr. F. Oliviero, *AE2111-II aircraft part*, September 2021. Academic year 2021/2022.

[19] 06, D. G., "Midterm Report MultiDisciplinary Design and Optimisation of LongRange eVTOL Aircraft," Tech. rep., 2021.

[20] Bouquet, T., and Vos, R., "Modeling the propeller slipstream effect on lift and pitching moment," *55th AIAA Aerospace Sciences Meeting*, 2017, p. 0236.

[21] R. Vos, B. Z., J.A. Melkert, "AE1222-I 2-Class I weight estimation," AE1222-I Aerospace Engineering TU Delft, May 2023. Accessed 11-05-2023.

[22] M.Drela, and H.Youngren, "XFLR5: Analysis tool for airfoils, wings and planes," , 2019.

[23] Sinnige, T., van Arnhem, N., Stokkermans, T. C., Eitelberg, G., and Veldhuis, L. L., "Wingtip-mounted propellers: Aerodynamic analysis of interaction effects and comparison with conventional layout," *Journal of Aircraft*, Vol. 56, No. 1, 2019, pp. 295–312.

[24] EASA, "Second Publication of Means of Compliance with the Special Condition VTOL," *MOC-2 SC-VTOL*, Vol. 3, 2022, pp. 49–62. URL https://www.easa.europa.eu/en/document-library/product-certification-consultations/special-condition-vtol.

[25] EASA, "Means of Compliance with the Special Condition VTOL," Vol. 2, 2021.

[26] Nathen, D. P., "Architectural performance assessment of an electric vertical take-off and landing (e-VTOL) aircraft based on a ducted vectored thrust concept," , May 2023. Accessed 11-05-2023.

[27] Du, G.-X., Quan, Q., Yang, B., and Cai, K.-Y., "Controllability Analysis for Multirotor Helicopter Rotor Degradation and Failure," *Journal of Guidance Control and Dynamics*, Vol. 38, 2015. doi:10.2514/1.G000731.

[28] EASA, "Certification Specifications and Acceptable Mean of Compliance for Small Rotorcraft - Amendment 6," Vol. 1, 2018.

[29] Tahir, Z., Tahirand, W., and Liaqat, S. A., "State Space System Modelling of a Quad Copter UAV," , 2019. URL https://arxiv.org/ftp/arxiv/papers/1908/1908.07401.pdf.

[30] Roskam, J., *Airplane Design Part V: component weight estimation*, Roskam Aviation and Engineering Corporation, Ottowa, Kansas, 1985.

[31] Moussid, M., Medromi, H., and Sayouti, A., "Dynamic Modeling and Control of a HexaRotor using Linear and Nonlinear Methods," , 2015. URL https://www.ijais.org/research/volume9/number5/moussid-2015-ijais-451411.pdf.

[32] Roskam, J., *Airplane Design, Part II : Preliminary Configuration Design and Integration of the Propulsion System*, Roskam Aviation and Engineering Corporation, Ottowa, Kansas, 2018.

[33] Roth, B., "Control Power Design Requirements for Aircraft Flying Qualities," , 2009. URL https://engineering.purdue.edu/~andrisan/Courses/AAE451_F2009/Buffer/Control_Power/flying_qualities_doc_05012009.pdf.

[34] EASA, "Certification Specifications for Normal Category Aeroplanes (CS-23)," 2023.

[35] Oliviero, F., "Lecture 9, AE3211-I, Systems Engineering and Aerospace Design, Design for Lateral-directional aspects, Design for ground operations," , 2023. URL https://repository.tudelft.nl/islandora/object/uuid:21a8ff59-61da-4944-b270-8085214d66d2/datastream/OBJ/download.

[36] Oliviero, F., "Lecture 8, AE3211-I, Systems Engineering and Aerospace Design, Requirement Analysis and Design principles for A/C stability control (Part 2)," , 2023.

[37] Oliviero, F., "Lecture 2, AE2111-II, Aerospace Design and Systems Engineering Elements II, Aircraft aerodynamic analysis - Lift and Drag," , 2019.

[38] 06, D. G., "Final Report MultiDisciplinary Design and Optimisation of LongRange eVTOL Aircraft," Tech. rep., 2021.

[39] Paul E. Pursee, J. P. C., "Experimental verification of a simplified vee-tail theory and analysis of available data on complete models with vee tails," , 1945. URL https://ntrs.nasa.gov/citations/19930091901.

[40] Crandall, S. R. S., Stewart M., "Analysis of available data on the effectiveness of ailerons without exposed overhang balance, report," , 1994. URL https://digital.library.unt.edu/ark:/67531/metadc61635/.

[41] Smeur, E., "Lecture 9, AE4301, Automatic Flight Control System Design," , 2021.

[42] Drela, M., *Flight Vehicle Aerodynamics*, The MIT Press, Cambridge, Massachusets, 2014.

[43] Mulder, J., *Lecture Notes AE3202*, Delft, Netherlands, 2013.

[44] Smeur, E., "Lecture 10, AE4301, Automatic Flight Control System Design," , 2021.

[45] Hendarko, "DEVELOPMENT OF A HANDLING QUALITIES EVALUATION TOOLBOX ON THE BASIS OF GIBSON CRITERIA," 2002. URL http://www.icas.org/ICAS_ARCHIVE/ICAS2002/PAPERS/533.PDF.

[46] Lewis, E., "VTOL Design Loads and Interaction of Systems and Structures," , 2020.

[47] Faisal, N., Ömer Necati Cora, Bekci, M. L., Śliwa, R. E., Sternberg, Y., Pant, S., Degenhardt, R., and Prathuru, A., *Introduction to Aerospace Flight Vehicles*, Springer Aerospace Technology, 2021.

[48] Georgiana Maties, S. G. P. C., "Wigeon: A Python module for urban air mobility studies [Source code]," , 2023. URL https://github.com/saullocastro/wigeon.

[49] A.D.Marano, N. P. e. a., G. Diodati, "Structural Scalability Preliminary Studies for the Next Generation Civil Tiltrotor Composite Wing," , May 2023. doi:10.3390/aerospace10050478, accessed 17-06-2023.

[50] Li, X., Wang, S., and Liang, M., "Modeling and Simulation of Combined Bending-torsion Experiment Based on ABAQUS," , 2022. doi:10.1088/1742-6596/2403/1/012045.

[51] Dühne, A., "VTOL Crashworthiness based on EASA Special Condition," , 2019.

[52] Glaister, D. H., "Human tolerance to impact acceleration," *Injury*, Vol. 9, No. 3, 1978, pp. 191–198. doi:10.1016/0020-1383(78)90006-2, URL https://www.sciencedirect.com/science/article/pii/0020138378900062.

[53] Thomas, T., "Crushing Behaviour of Honeycomb structure: A Review," *International Journal of Crashworthiness*, 2019. doi:10.1080/13588265.2018.1480471.

[54] Roskam, J., *Airplane Design Part III: Layout Design of Cockpit, Fuselage, Wing and Empennage: Cutaways and Inboard Profiles*, Roskam Aviation and Engineering Corporation, Ottowa, Kansas, 1985.

[55] LePage, F., "A320 fuselage section vertical drop test, part 2: Test results," Tech. Rep. N°S95 5776/2, CEAT, 1995.

[56] Castro, S. G. P., "General-purpose finite element solver based on Python and Cython," , 2023. doi:10.5281/zenodo.6573489.

[57] Luo, Y., "An Efficient 3D Timoshenko Beam Element with Consistent Shape Functions," *Adv. Theor. Appl. Mech.*, Vol. 1, No. 3, 2008, pp. 95–106.

[58] Chambers, J. R., *Innovation in Flight: Research of the NASA Langley Research Center on Revolutionary Advanced Concepts for Aeronautics*, NASA SP-2005-4539, 2005. Library of Congress Cataloging-in-Publication Data.

[59] IONBLOX, "IONBLOX Launch (High Energy AV Cell) product sheet," Ionblox, 2023. Accessed 30-05-2023.

[60] Muthukumar, P., Kumar, A., Afzal, M., Bhogilla, S., Sharma, P., Parida, A., Jana, S., Kumar, E. A., Pai, R. K., and Jain, I., "Review on large-scale hydrogen storage systems for better sustainability," *International Journal of Hydrogen Energy*, 2023. doi:10.1016/j.ijhydene.2023.04.304, URL https://www.sciencedirect.com/science/article/pii/S0360319923021584.

[61] U.S Department of Energy (DOE), "Hydrogen Storage," *Multi-Year Research, Development, and Demonstration Plan*, 2012. doi:https://www.energy.gov/sites/default/files/2015/05/f22/fcto_myrdd_storage.pdf.

[62] Department of Energy (DOE), "Energy requirements for hydrogen gas compression and liquefaction as related to vehicle storage needs," *DOE Hydrogen and Fuel Cells Program Record*, 2009. URL https://www.hydrogen.energy.gov/pdfs/9013_energy_requirements_for_hydrogen_gas_compression.pdf.

[63] *Frontmatter*, John Wiley Sons, Ltd, 2003, pp. i–xxxii. doi:10.1002/9780470172605.fmatter.

[64] Scoccimarro, A., "Preliminary design methods for the thermal management of fuel cell powered aeroengines." Master's thesis, Technical University Delft, 2023. URL http://resolver.tudelft.nl/uuid:9a16e0f8-722d-4a17-9f79-96cea2de6906.

[65] Mills, A., Coimbra, C., and Coimbra, C. F., *Basic Heat and Mass Transfer*, Temporal Publishing, 2015. URL https://books.google.nl/books?id=ZFoNswEACAAJ.

[66] Ranganayakulu, S. K. N., C., *Compact Heat Exchangers - Analysis, Design and Optimization Using FEM and CFD Approach*, John Wiley Sons, 2018. URL https://app.knovel.com/hotlink/khtml/id:kt011R5CV1/compact-heat-exchangers/geometric-characteristics.

[67] Manglik, R. M., and Bergles, A. E., "Heat transfer and pressure drop correlations for the rectangular offset strip fin compact heat exchanger," *Experimental Thermal and Fluid Science*, Vol. 10, No. 2, 1995, pp. 171–180. doi:/10.1016/0894-1777(94)00096-Q, aerospace Heat Exchanger Technology.

[68] Ali, H. M., "Thermal management systems for batteries in electric vehicles: A recent review," *Energy Reports*, Vol. 9, 2023, pp. 5545–5564. doi:10.1016/j.egyr.2023.04.359.

[69] Yuan, J., and Sunden, B., "Analysis of Intercoolers in PEM Fuel Cell Systems," 2004, pp. 1–27. doi:10.1115/HT-FED2004-56587.

[70] Jack E. Marte, D. W. K., "A review of aerodynamic noise from propellers, rotors, and lift fans," , January 1970. URL https://ntrs.nasa.gov/api/citations/19700005920/downloads/19700005920.pdf, accessed 17-06-2023.

[71] Botero, E. M., Clarke, M. A., Erhard, R. M., Smart, J. T., Alonso, J. J., and Blaufox, A., "Aerodynamic Verification and Validation of SUAVE," *AIAA SciTech 2022 Forum*, 2022, p. 1929.

[72] Gray, J. S., Hwang, J. T., Martins, J. R. R. A., Moore, K. T., and Naylor, B. A., "OpenMDAO: An Open-Source Framework for Multidisciplinary Design, Analysis, and Optimization," *Structural and Multidisciplinary Optimization*, Vol. 59, 2019, pp. 1075–1104. doi:10.1007/s00158-019-02211-z.

[73] Andŕe, N., and Hajek, M., "Robust Environmental Life Cycle Assessment of Electric VTOL Concepts for Urban Air Mobility," 2019. doi:10.2514/6.2019-3473.

[74] Siedlak, D. J., Pinon, O. J., Schlais, P. R., Schmidt, T. M., and Mavris, D. N., "A digital thread approach to support manufacturing-influenced conceptual aircraft design," *Research in Engineering Design*, Vol. 29, 2018, pp. 285–308.

[75] Muhm, J. M., Rock, P. B., McMullin, D. L., Jones, S. P., Lu, I., Eilers, K. D., Space, D. R., and McMullen, A., "Effect of aircraft-cabin altitude on passenger discomfort," *New England Journal of Medicine*, Vol. 357, No. 1, 2007, pp. 18–27.

[76] Department of Energy (DOE), "On-Board Hydrogen Storage Systems – Projected Performance and Cost Parameters," *DOE Hydrogen and Fuel Cells Program Record*, 2010. URL https://www.hydrogen.energy.gov/pdfs/9017_storage_performance.pdf.

[77] Houchins, C., James, B. D., Huya-Kouadio, J., and DeSantis, D., "Hydrogen Storage Cost Analysis," *Department of Energy*, 2021.